Theoretical Studies of Perovskite Solar Cells

Yecheng Zhou
ResearcherID: O-7658-2014
ORCID: 0000-0001-8222-7193

Submitted in total fulfilment of the requirements of the degree of

Doctor of Philosophy

School of Chemistry
The University of Melbourne

June 2017

Produced on archival quality paper.

Abstract

Perovskite solar cells (PSCs) are solar cells implemented with perovskite absorber. Within 5 years of development, the power conversion efficiency (PCE) of PSCs has reached 22.1%. It has been proposed that the ferroelectric polarization of perovskites may affect the electronic performance of PSCs. $CH_3NH_3PbI_3$ ($MAPbI_3$) is one of the most widely used perovskites in PSCs. Methylammonium ion (MA^+) is believed to be involved in inducing ferroelectric polarization as single MA^+ in vacuum shows a large dipole moment. On the other hand, MA^+ are found to be disordered at room temperature. However, the behavior of MA^+ alignment, and the connection between MA^+ alignment and polarization are not fully understood. A better understanding of these phenomena are crucial in improving the PCE of PSCs. In this thesis, studies of the relationship between the performance and MA^+ alignment, and polarisation have been undertaken.

Band structures and effective masses of $MAPbI_3$ in the α phase and the β phase were calculated with MA^+ orientated differently. It is found that these structures have comparable energies. This is in agreement with the observed disordered MA^+ in experiments. The influence of the orientation of MA^+s on band gap is smaller than 0.1 eV. There is a significant effect of orientation on the effective mass due to the large dipole moment of MA^+. However, overall reduced effective masses of differently orientated MA^+ unit cells are comparable. It is also found that the electronic properties of the α phase are similar to that of the β phase. This is the reason why $MAPbI_3$ PSCs are able to work stably near their phase transition point. These results explained that the orientation of MA^+ and phase transition near room temperature have little influence on solar cell performance.

The energy landscapes for MA^+ reorientations in the α phase and the β phase unit cells and super cells are investigated in detail. The MA^+ reorientation energy barrier depends on the initial and final orientations, it also depends on the orientations of its neighboring MA^+. The energy barrier is smaller for MA^+ rotating from anti-parallel to parallel. This suggests MA^+ prefers parallel alignment. It is also found that the rotational energy barrier in the α phase is lower than that in the β phase. The polarization induced by MA^+ rotation is about 6-8 μCcm^{-2}, which is about

three times higher than that produced by lead ion relaxation. Our work suggests that polarization in $MAPbI_3$ is mainly from MA^+ orientations, which gives us a new understanding of the polarization of perovskite materials.

To study the influence of the specific microscopic characteristics of PSC's on solar cell power conversion performance, setting up of an appropriate transport model for numerical simulations is required. Existing models to simulate solar cell efficiency are unsuitable to study PSCs, as they are developed for silicon solar cells. Also, they tend to be overparameterised, which compromises their predictive capacity. In this thesis numerical models have been developed and implemented in efficient home-made codes. Using these models, it is found that PCEs increase with charge carrier lifetimes, mobilities and diffusion lengths. The open-circuit voltage (V_{oc}) depends on the intensity of the exciting radiation and charge carrier lifetimes. Diffusion length and light intensity determine the saturated circuit current (J_{sc}). Additionally, three theoretical guidelines are proposed for PSC fabrication and optimization. It is theoretically shown that concentrator PSCs may offer advantages. We thus argue that the model developed here provides a framework for numerical modeling of perovskite–based cells and the optimization of their performance.

Hysteresis is the performance difference between the forward and backward measurements. There is considerable debate about the reasons for the observed hysteresis. Polarization and ion migration are two possible reasons causing hysteresis in J-V curves for PSCs. However, there are no quantitative hysteresis simulations, also no theory to show the possibility of hysteresis induced by polarization. By considering two screening relaxation fields in numerical models, I quantitatively reproduced experimental hysteresis in J-V curves. It is theoretically shown that both polarization and ion migration can induce screening fields and then produce hysteresis. Lastly, two possible methods to reduce hysteresis in PSCs are proposed. One consists of reducing defects in thin films and at interfaces; The other consists of using polarisable materials as a charge transfer layer to compensate for the field induced by polarization or (and) ion migration. This work shows for the first time the role of polarization and suggests two ways to eliminate hysteresis.

Our numerical work shows that polarization and ion migration are both possible mechanisms inducing hysteresis in the J-V curves. In order to distinguish between the role of polarization and ion migration in perovskite materials, two-dimensional periodic thin film models for relaxations of ion migration and polarization of MA^+ are investigated. Dynamic simulations show both ion migration and MA^+ polarization are able to build screening fields and promote charge transfer in PSCs. Lifetimes of

these two relaxation mechanisms increase with the thin film thickness and decrease with the initial applied external field. The relaxation lifetime of ion migration obtained with a model using experimental length scale and field strength is estimated to be in the range from 1 ms to 1.5 s, which is comparable to measurement delay times. While, the relaxation lifetimes of MA^+ orientations are estimated to be about several hundred ns to several μs, which significantly differ from experimental delay times. This polarization relaxation lifetime is much shorter than others simulation results. The discrepancy is due to the different model that has been used in this work. Others have used three-dimensional periodic bulk models, which led to longer relaxation lifetimes compared to the two-dimensional periodic thin film models. However, three-dimensional periodic bulk models can not consider surface and interface charges, results from three-dimensional periodic models are thus misleading. Charge behaviors in thin films should be mimicked by two-dimensional periodic thin film models. Our results indicate that the hysteresis in PSCs is induced by ion migration rather than the polarization of MA^+ due to the fast theoretical relaxation time of MA^+ polarization compared to experiments. This finding provides us a better understanding of hysteresis in PSCs.

The influence of the density of the conduction band states (N_c) and the density of the valence band states (N_v) on PSC performance are elucidated. Firstly, N_c and N_v of silicon, CdTe, and typical perovskites are calculated from DFT calculations based on two different methods. It is found that N_cN_v of CdTe and typical perovskites are much lower than that of silicon. Using our developed numerical models, the lower N_cN_v is expected to produce higher output voltage including V_{oc}. The lower N_cN_v in perovskite will result in 100 mV higher V_{oc} and 10% higher PCEs compared to solar cells with the same parameters except for N_cN_v. This provides a new guideline for finding and developing new photovoltaic materials.

This thesis is dedicated to my parents:
ZHENBIAO HE and XINMEI ZHOU
for their patience and effort through difficult times.

Declaration

This is to certify that:

- the thesis comprises only my original work towards the Ph.D except where indicated in the Preface,
- due acknowledgement has been made in the text to all other material used,
- the thesis is less than 100,000 words in length, exclusive of tables, maps, bibliographies and appendices.

Signature:
Date:

Preface

This thesis is comprised of the candidates publications as Chapters. Co-authors included in the publications have signed agreement forms that certifies the following:

- the candidate has contributed more than 50% to the content of the manuscripts including planning, preparation, and execution of the work described in each manuscript
- the candidate is the "primary" or "first" author of the manuscripts
- the manuscripts can be included in the candidates thesis in its published form without redactions or omissions

These agreement forms are found in the Appendices section of this thesis.

Signature:
Date:

Acknowledgements

I would like to thank my principal supervisor Dr. Angus Gray-Weale for his supervision over these three years, especially for the help during the last year after he left Melbourne University. He is a good tutor. He guided me how to learn and how to write as well as how to do research. I have appreciated his feedback on my research work. He also provided me lots of help and suggestions for my thesis and completion talk.

I want to thank Dr. Alessandro Soncini. He is my Ph.D. committee member and also the supervisor after Angus left. I learned a lot from his group meetings. He gives lots suggestion on my final talk and my thesis as well. I also want to thank my committee member Prof. Kenneth Ghiggino. He concerns my research and reminds me to focus on my current research. I very appreciate him for reading my thesis and giving feedback.

We had a strong group. I did enjoy that time. I thank everyone in our group. Dr. Maoyuan Liu took care of machines and made sure everything goes well. The quizze 'Master', Dr. Quinn Besford organized time and people for quizzes. This made our academic life colorful. Mr. Cameron Ritchie is very kind. He helps me almost on everything, especially on paper writing. Ms. Cassandra Lutzko and Mrs. Xinli Zhang shared one office with me and we worked well together.

I want to thank Prof. Yi-Bing Cheng and Dr. Fuzhi Huang from Monash University. My decision to work on perovskite solar cells was because of the talk Prof. Yi-Bing Cheng gave in our building. We have had many discussions about what is important for experimentalists to understand.

I very much appreciate Dr. Mike Towler, University of Cambridge, and Prof. Matthew Foulkes, Imperial College London, for the help in the code developing of dynamic simulations of ion migration and polarization. I thank Prof. Aron Walsh, University of Bath (now in Imperial College London) for discussions on some calculation details and suggestions on my papers. I greatly appreciate Professor Yang Yang at University of

California, Los Angeles, and Professor Qi Chen for providing their initial data in Reference 1. Their initial data, which is used to plot the data "Exp-Zhou" in Figure 4.3, allowed me to compare the experiment and theory in detail.

I thank the National Computational Infrastructure and the VLSCI for High Performance Computing resources. I thank the Chemistry Department, the Faculty of Science and the University for supporting and providing me research and traveling scholarships.

Lastly, I must thank my parents Zhenbiao He and Xinmei Zhou. Thanks for their vision, they continue supporting me even in very difficult times.

List of Publications

During Ph.D candidature duration, besides studies in perovskite solar cells, I also worked on charge transfer in organic materials, solar cells and 2D carbon materials. Publications were produced in all these fields. These are listed herein for reference:

1. **Y. Zhou,** G. Long. "Low Density of Conduction and Valence Band States Contribute to the High Open-Circuit Voltage in Perovskite Solar Cells", *J. Phys. Chem. C,* **12**, 1455–1462(2017*).*
2. **Y. Zhou**,* F. Huang, Y.-B. Cheng, A. Gray-Weale,* "Numerical analysis of a hysteresis model in perovskite solar cells", *Comput. Mater. Sci.* **126**, 22-28(2017). **(*Corresponding Author.)**
3. **Y. Zhou**,* W.-Q. Deng, H.-L. Zhang**,*** "Phonon-electron coupling and tunneling effect on charge transport in organic semi-conductor crystals of C_n-BTBT", *J. Chem. Phys.* **145**,104108(2016). **(*Corresponding Author.)**
4. **Y. Zhou**, A. Gray-Weale, "A Numerical Model for Charge Transport and Energy Conversion of Perovskite Solar Cells", *Phys. Chem. Chem. Phys.,* **18**, 4476–4486(2016).
5. **Y. Zhou**, F. Huang, Y.-B. Cheng, A. Gray-Weale, "Photovoltaic Performance and the Energy Landscape of $CH_3NH_3PbI_3$", *Phys. Chem. Chem. Phys.*, **17**, 22604–22615(2015).
6. G. Long,[+] **Y. Zhou**,[+] M. Jin, B. Kan, *et al.,* "Theoretical Investigation on Two-Dimensional Non-Traditional Carbon Materials Employing Three-Membered Ring and Four-Membered Ring as Building Blocks", *Carbon*, **95**, 1033–1038(2015). [+]**Equal contributions**.
7. H. Xu, **Y.-C. Zhou**, X.-Y. Zhou, *et al.*, "Molecular Packing-Induced Transition between Ambipolar and Unipolar Behavior in Dithiophene-4,9-Dione-Containing Organic Semiconductors", *Adv. Funct. Mater.*, **24**, 2907–2915(2014).
8. J. Zhang, G. Liu**, Y. Zhou**, *et al.*, "Solvent Accommodation: Functionalities Can Be Tailored Through Co-Crystallization Based on 1:1 Coronene-F4TCNQ Charge-Transfer Complex", *ACS Appl. Mater. Interface,* **9**, 1183–1188(2017).
9. Y. Zhang, M. Zhang, **Y. Zhou**, J. Zhao, *et al.,* "Tunable Electronic and Magnetic Properties of Graphene-like ZnO Monolayer upon Doping and CO Adsorption: A First-Principles Study", *J. Mater. Chem. A*, **2**, 13129(2014).
10. K. Liu, C.-L. Song, **Y.-C. Zhou**, X.-Y. Zhou, *et al.*, "Tuning the Ambipolar Charge Transport Properties of N-Heteropentacenes by Their Frontier Molecular Orbital Energy Levels", *J. Mater. Chem. C*, **1**, 3777(2015).
11. G. Long, A. Li, R. Shi, **Y.-C. Zhou**, *et al.*, "The Evidence for Fullerene Aggregation in High-Performance Small-Molecule Solar Cells by Molecular Dynamics Simulation", *Adv. Electron. Mater.*, **1**, 1500217(2015).
12. G. Long, B. Wu, X. Yang, B. Kan, **Y. Zhou**, *et al.*, "Enhancement of Performance and Mechanism Studies of All-Solution Processed Small-Molecule Based Solar Cells with an Inverted Structure", *ACS Appl. Mater. Interfaces*, **7**, 21245–21253(2015).
13. F. Huang, Y. Dkhissi, W. Huang, *et al.*, "Gas-Assisted Preparation of Lead Iodide Perovskite Films Consisting of a Monolayer of Single Crystalline Grains for High Efficiency Planar Solar Cells", *Nano Energy*, **10**, 10–18(2014).

Contents

List of Figures

List of Tables

Chapter 1

Introduction

1.1 The roadmap of solar cells

Clean energy is investigated intensively due to the increasing threat from environment and energy problems over the last few decades. Among renewable energy technologies, solar cells are one of the most realistic and promising. Their working mechanism is the photovoltaic effect, which was first observed by Alexandre Edmond Becquerel about two hundred years ago.[2] A practical solar cell was first invented in Bell labs in 1954.[3] In the very early stage, all solar cells used single crystals. Hence, their costs were extremely high. For example, the cost of the first commercial solar cell was up to $1,785/watt.[2] Too high cost made it impossible to use solar cells in daily life. It only can be used in satellites and space stations. The thought to lower its cost began in the 1980s with thin film solar cells, as shown in Figure 1.1.[4] Thin film solar cells were first made at the University of Delaware. Soon, polysilicon and amorphous silicon solar cells were proposed and produced. After, dye-sensitized solar cells (DSSCs) were invented by Brian O'Regan and Michael Gratzel.[5] This new type of solar cells could be made from solution processes, which avoids the most expensive process – physical vacuum deposition in solar cell fabrications. The DSSC invention was very significant as they gave rise to a new research field. Based on DSSCs, organic solar cells (OSCs), and perovskite solar cells (PSCs) have been developed.

DSSCs lower the fabrication cost. The problem is its very low performance, which limits its application and commercialization. Improving the power conversion efficiency (PCE) became the main goal in the research for optimization of DSSCs. A general solar cell mechanism includes several processes: light absorption, exciton splitting, charge carrier transport to electrodes. As well as these processes, there are non-productive pathways, such as exciton relaxation, charge carrier recombination.

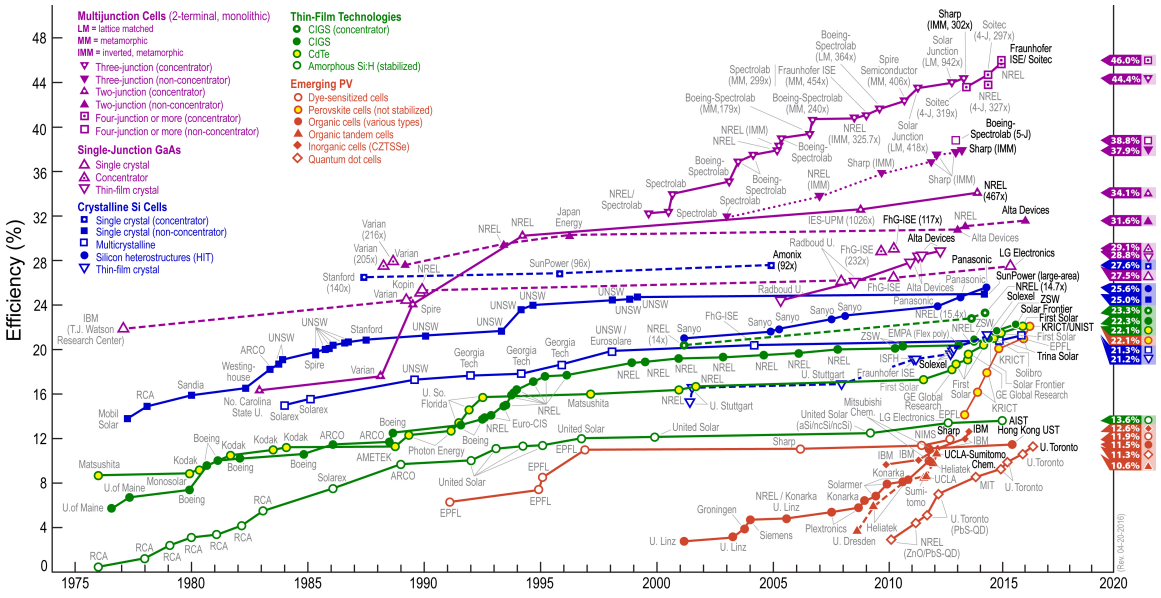

Figure 1.1: Best research-cell efficiencies of various solar cells. PSCs show rapidly growing PCEs. The figure was taken from NREL website.[4]

To enhance PCEs, we could improve light absorption by developing new dyes, increasing exciton splitting rate (same as lowering the exciton splitting energy) and charge carrier mobility. Several feasible methods have been attempted. The first is to lower the exciton splitting energy barrier by introducing organic hosts. The charge transfer is believed to be faster between organic materials. By replacing the TiO_2 hosts in DSSCs with organic materials, such as PCBM, DSSCs become OSCs. The second is to optimize the dye that controls light absorption. A good dye is expected to have high absorption coefficient across a broad wavelength range. In 2009, Kojima *et al.* first introduced a perovskite into a DSSC as a dye.[6] This was the pre-model of PSCs.

1.2 What is perovskite and its solar cells

1.2.1 Perovskite materials

In the narrow sense, perovskite is just a calcium titanium oxide mineral with the chemical formula $CaTiO_3$.[7] It is named after the Russian mineralogist Lev Perovski. The general description of a perovskite is a material with the structure shown in Figure 1.2. A, B and X are three different types of ions. The typical perovskite materials used in solar cells are $MAPbI_3$, $MAPbCl_xI_{3-x}$ and $CH_2(NH_2)_2PbI_3$. In these materials, A is the organic ion, B is the lead ion, and X is the halogen ion. On one hand, perovskite materials usually have several phases[8], for example, $MAPbI_3$ has α phase and β

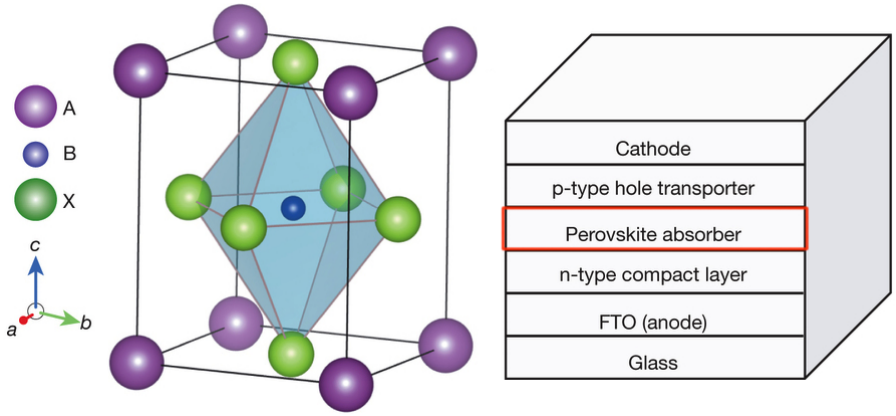

Figure 1.2: The structure of perovskite materials (left) and the structure of its solar cells (right). Original figure was reprinted from Ref. [12]

phase. Its phase transition point is 333 K, which is near its working temperature. On the other hand, it is worth noticing that lots of ferroelectric materials are tetragonal phase perovskite materials, such as $BaTiO_3$, $PbTiO_3$, and $BiFeO_3$.[9, 10, 11] These indicate that the β phase of $MAPbI_3$ maybe ferroelectric.

1.2.2 Perovskite solar cells

A typical PSC has five function layers. They are the anode, the n-type Electron Transport Layer (ETL), the perovskite layer, the p-type Hole Transport Layer (HTL) and the cathode. A classic planar PSC is illustrated in Figure 1.2. The perovskite layer is the core layer, where the light is absorbed, and excitons are formed, separated and transferred. The n-type ETL is used for two reasons. One is for transferring electrons and another is for blocking holes. Electrons are extracted at the interface between the n-type ETL and the perovskite layer. Conversely, the p-type HTL conducts holes and blocks electrons. Generally, photons and excitons are absorbed and formed in perovskite, while electron and hole are separated at interfaces. The glass layer is just the substrate without any other functions. PSCs have three typical structures. Figure 1.2 shows the most common structures where photons impinge through the n-type ETL. Other two are the inverted and the hole-conductor-layer-free solar cells. In inverted solar cells, light comes from the side of p-type HTL.[13, 14, 15, 16] The sequence is glass, cathode, p-type HTL, perovskite, n-type ETL and anode. Inverted solar cells are intensively developed because they are more stable and exhibit less hysteresis.[14, 15, 16] On the other hand, as the p-type HTL material is very expensive, the lack of hole transporter will reduce the cost of solar cell fabrications.[17, 18] PSCs without HTL are called hole-conductor layer free PSCs.[17, 18, 19, 20]

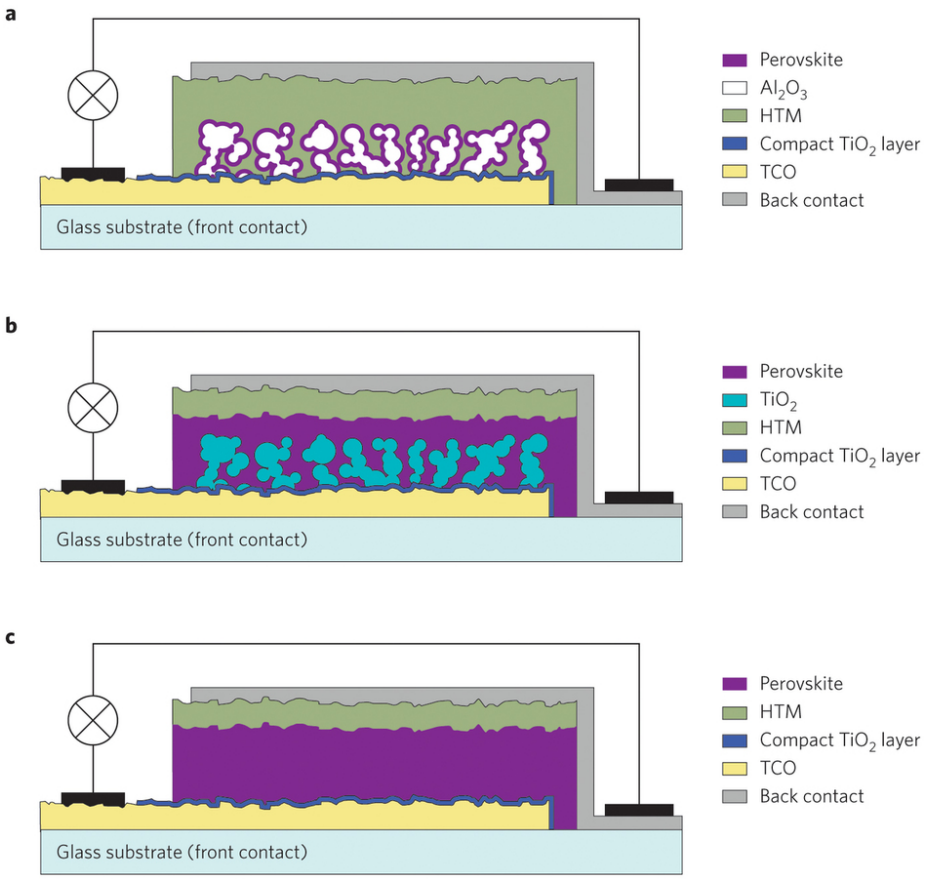

Figure 1.3: The evolution of PSCs: from a mesoscopic to a planar embodiment of the perovskite solar cell. This figure was reprinted from Ref. [21]

1.3 The development of PSCs

1.3.1 PSC's PCE is soaring

Perovskite was first introduced to solar cells in 2009.[6] Its PCE only reached 3.81%. In this solar cell, perovskites replaced the traditional dye in DSSCs. Due to its low PCE, it did not attract much interest. In the next two years, little progress was made. It was reported in 2011 that the solar cell with perovskite as quantum dot sensitizers achieved a maximum PCE of 6.54%.[22] In 2012, significant progress was made in PSCs, its PCE reached 11%.[23, 24] Strictly speaking, these two PSCs were still in the form of DSSC, perovskite was only used as sensitizers, shown in Figure 1.3a.

The current use of PSC was introduced in the second half of 2012.[25, 26] Their PCEs are lower than 10%. Structures of these two solar cells are illustrated in Figure 1.3b, the perovskite was mixed with mesoporous titanium dioxide. In these solar cells, the perovskite layer was used as both absorber and hole transporter. In the

next several years, PCEs of mesoscopic PSCs continued increasing and reached the maximum PCE of 12.3%.[27] As these perovskite materials are ambipolar, they can conduct both electrons and holes. Additionally, they show very high electron and hole mobilities, which have reached several cm^2/Vs.[28, 29] These high mobilities are much higher than the mobilities of most used hole transporting materials in solar cells[30] and the mobilities (≈ 0.02 cm^2/Vs) of most used electron transporting materials in solar cells.[31, 32] Theoretically, it is possible to let all of these processes of light absorbing, electron transport and hole transport happen in the perovskite layer, which will simplify solar cell's structure and lower its costs. Thus, why not use perovskite to replace the hole transporter materials and electron transporter materials? In late 2013, Stranks *et al.* made planar PSCs.[33, 29, 34] In these solar cells, perovskite layers absorb photons and transfer charge carriers. Within one year, PCEs of planar PSCs surpassed mesoscopic PSCs and reached up to 15.7%.[34, 35] In the year of 2014, the PCE increased to 16.2%[36], 16.9%[37] 19.3%[1] and up to 20.5%.[38] After that, it would be no surprise if someone made higher PCE PSCs. The record is being broken again and again, and at the time of writing had reached 22.1 %.[39, 40, 4]

1.3.2 Stability and hysteresis problems

During the rapid development of perovskite, people found that there was an extremely slow photoconductivity response in organic hybrid perovskite materials.[41] Due to this slow response, PCEs of solar cells are increasing and then reach a stable value about 5 – 10 seconds after illumination.[36, 37] It looks like that at the beginning of measurement solar cells are self-improving. Gottesman *et al.* demonstrated that the slow photovoltaic response not only could increase, it also may decrease.[41] This extremely slow relaxation indicates that there are some structure changes under working conditions. In early 2015, Niu *et al.* reported that moisture degrades $MAPbI_3$ materials in solar cells.[42, 43, 44] The normalized PCEs dropped to 20 percent and even to zero compared to the initial PCE. Bryant *et al.* showed that the reduced PCE of solar cells is due to the degradation of $MAPbI_3$, which leads to low absorbance and rough surface.[45, 46, 43]

The other problem of PSCs is the hysteresis in J-V curves. The working J-V curve is determined by the scan direction and scan rate. Due to some slow relaxing processes, the field in perovskite layers lags with respect to the applied field. The hysteresis of PSCs was noticed and investigated since 2014.[36, 47, 48, 49, 50, 51] Because of the presence of hysteresis, it is difficult to determine the real PCE of a solar cell.

The existence of these two problems has encouraged people to find out a way to overcome them. In order to solve these problems, we should know how PSCs were made and how they work.

1.4 Mechanisms in PSCs

1.4.1 Working mechanisms and material requirements of each layer

General working processes of photovoltaic solar cells include light absorption – exciton formation, exciton migration and separation, charge carrier transfer, charge extracting and injection, as shown in Figure 1.4. Light absorption in the donor layer leads to exciton formation. After excitons are formed, there are two possible cases: the first is that if the exciton separation energy in the donor is high, excitons need to be transferred to interfaces between donor and acceptor; the second case is that the exciton separation energy is very small, so that excitons can be split within the donor. The first case includes OSCs, DSSCs, and p-n junction solar cells, for example, silicon solar cells. The second is the case that happens in PSCs. In the light absorption process, the absorber should have a band gap such that it can absorb most photons without losing too much potential. On the other hand, in order to absorb more photons, the absorption coefficient should be high. After absorption, excitons can undergo charge separation. The separation mechanism differs between different solar cells. For p-n junction solar cells, a large built-in field is required. For OSCs, the fast separation rate needs strong coupling between two molecules and small reorganization energy. For PSCs, the exciton separation happens within perovskite. The exciton separation energy in PSCs can be calculated from a hydrogen-like model.[52] It is determined by the effective masses and dielectric constant. The small effective mass and the large high-frequency dielectric constant of perovskite materials contribute to a small separation energy.

After exciton dissociation, two free charge carriers are generated. Hole transport and electron transport occur in the respective layers. Hence, HTL should have high hole mobility and ETL should have high electron mobility. However, in PSCs, both holes and electrons transport in perovskite materials. This indicates that the perovskite material must be ambipolar and have high mobilities for both electrons and holes. The last step is charge collection. Charge carriers will be conducted and injected to electrodes. In the injecting process, energy barriers should be very small or even be negative. Efficient injection requires the corresponding energy levels of

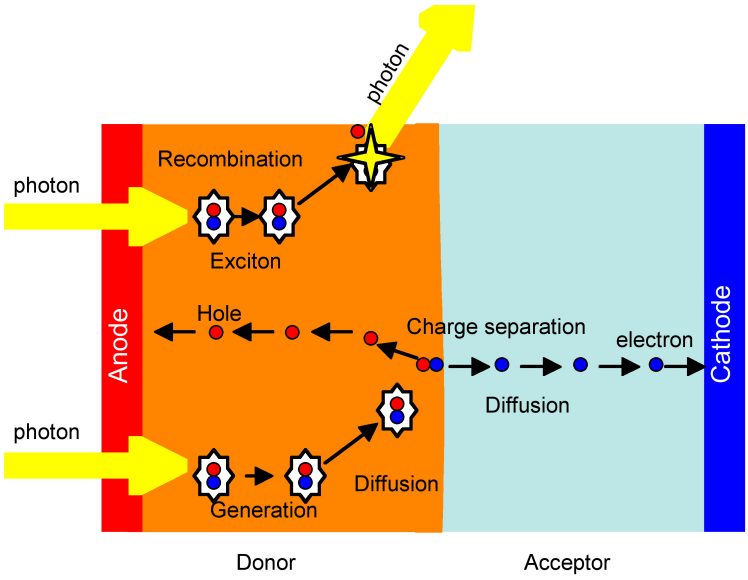

Figure 1.4: Working mechanism of solar cells. The figure was derived from Ref. [53].

transporter and electrodes to be comparable. Ideally, their energy levels should be the same. A high energy barrier leads to poor charge injection. On the other hand, a negative energy barrier leads to lost potential and low voltage output. For PSCs, an additional separation process is required as both electron and hole transfer occur in the perovskite layer. Holes and electrons are separated through blocking. The hole transporter in PSC functions as a hole extractor: conducting holes and blocking electrons. Hence, the HTL is also called the electron blocking layer. The real function of hole transporter or electron transporter is hole extraction or electron extraction rather than charge transfer.

1.4.2 Energy levels and output voltage in PSCs

In PSCs, both electron and hole transfer in the perovskite layer. Electrons transfer on the levels of LUMOs, while, holes transfer on the levels of HOMOs. They are driven by the separate quasi-Fermi levels (E_{fn} and E_{fp}).[54, 55, 56] In a real PSC, the output voltage is the potential difference between the electron Quasi-Fermi level at $x = 0$ and the hole Quasi-Fermi level at $x = d$. $eV = E_{fn}|_{x=0} - E_{fp}|_{x=d}$ (Figure 1.5), where these Fermi levels satisfy: $n|_{x=0} = N_c e^{\frac{E_c - E_{fn}}{-kT}}$ and $p|_{x=d} = N_v e^{\frac{E_v - E_{fp}}{kT}}$, where N_c and N_v are the DOSs of the conduction band and the valence band, respectively. Hence,

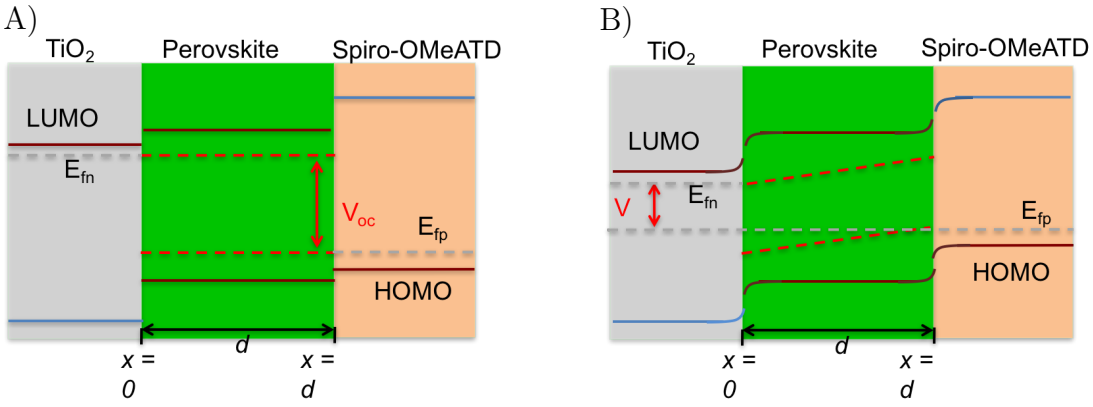

Figure 1.5: A), One grid in simulation compared to the α unit cell. Six possible hopping paths are shown in green arrows and text; B) the simplified grid and possible final locations of six possible hops.

the output voltage can be expressed as:[57]

$$\begin{aligned} eV &= E_{fn} - E_{fp} = E_c + kTln(\frac{n|_{x=0}}{N_c}) - (E_v - kTln(\frac{p|_{x=d}}{N_v})) \\ &= E_{bgap} + kTln(\frac{n|_{x=0}}{N_c}) + kTln(\frac{p|_{x=d}}{N_v}) \end{aligned} \tag{1.1}$$

As shown in Figure 1.5A, at open circuit, the electron quasi-Fermi level in the TiO_2 layer is the same with the electron quasi-Fermi level in the perovskite layer and the hole quasi-Fermi levels in perovskite and spiro-OMeATD (HTL) are the same. There is no charge movement due to the same quasi-Fermi levels. The potential difference between these two quasi-Fermi levels is the open circuit voltage. Under a certain bias, the potential difference between E_{fn} and E_{fp} is narrowed. The lowering of E_{fn} in TiO_2 and the raising of E_{fp} in HTL tilt the quasi-Fermi levels in perovskites, as shown in Figure 1.5B. The gradients of the tilted quasi-Fermi levels drive charge to ETL and HTL.

1.4.3 Why PSCs can achieve high PCEs?

Since the invention of PSCs, their PCEs continue to increase without sophisticated fabrication techniques. The most trusted and broadly believed reason is its good electronic properties. Charge carrier diffusion lengths of PSCs are measured to be as long as 1 μm.[28, 29] Their lifetimes are also estimated to be up to several hundred ns.[19, 1] The long diffusion length means that charge carriers can freely travel a long distance without scattering. Other widely accepted reasons include its appropriate size band gap and large absorption coefficient. Experimental band gaps of $MAPbI_3$

are measured to be 1.45 eV,[58] 1.50 eV,[25] 1.54 eV,[8] 1.55 eV,[1] 1.61 eV[59] and 1.70 eV.[60] These band gaps are near the band gap with maximum efficiency in Shockley-Queisser limit.[61] In experiments, Burschka *et al.* have illustrated that organic hybrid perovskite materials have a very wide absorption wavelength range with high IPCE.[34, 25, 62]

Theory has also found comparable results to experiments. The long diffusion length is confirmed with theoretical small effective masses.[63, 64] The long charge carrier lifetime in experiments is in concert with inert defects and intrinsically benign grain boundaries.[63, 58, 65] Band structures have also been studied by theoreticians.[63, 64, 66, 67] Small exciton separation energy was estimated due to its large dielectric constant and small effective masses.[52]

As perovskite materials often are ferroelectric,[68, 11, 10] there is debate about whether the ferroelectric polarization contributes to the energy conversion process. Frost *et al.* argued that the charge carrier is easier to be transferred along the ferroelectric grain boundary.[69] We find that the polarization screens external hindering fields, promotes charge transfer and improves its PCEs.[52] Our argument is in consistent with the compensated field[70] and screening effect[71] described in references. We will discuss the polarization debate in section 1.5.

1.4.4 What causes hysteresis?

Since the invention of PSCs, it is found that the working J-V curves are different in the backward and forward measurements.[37, 36] The backward scanning produces higher power conversion compared to the forward scan. The difference between forward and backward measurements is called hysteresis. The existence of hysteresis brings about the difficulty in PCE measurement. Very intensive studies have been performed to investigate what causes hysteresis and how to eliminate hysteresis. [70, 51, 50, 72, 73, 74] Proposed reasons include ion migration,[49, 75, 76, 51, 70, 77] ferroelectric polarization,[78, 71] space charge,[74] interface defects.[74] Debates continue.

1.5 Motivation of this research

My research focuses on two main questions: why PSCs can achieve high performance and what causes hysteresis. These general applicational issues can only be addressed if some more fundamental mechanistic questions are answered. These are: Is the polarization of $MAPbI_3$ ferroelectric? How does the polarization contribute to power conversion and hysteresis? In order to answer these questions, we have to

separate them into several parts. We will address these questions using first-principle microscopic simulations, mesoscopic simulations using classic dynamic Monte Carlo simulations, and macroscopic simulations based on numerical models.

1.5.1 What is the origin of electric polarization in $MAPbI_3$, and how does it improve PCEs?

The origin of electric polarization and its impact on PCEs has been discussed in OSCs. It has been proved that the dipole moment of organic molecules increases the charge separation rate and then improves the solar cell PCE.[79, 80] Perovskites are thought to be ferroelectric. Frost *et al.* proposed that excitons may be easier to separate at the internal junctions between ferroelectric domains.[69, 64] This internal junction also may reduce the charge carrier recombination through segregation.[69] We examined the effect of organic ion orientation and possible polarizations from organic ion and lead ion using first-principle methods. We present the evidence for the existence of ferroelectric polarization. This ferroelectric polarization screens external hindering field, promotes charge transfer and PCEs. This part of work is shown in Chapter 2 and published as reference 52.

1.5.2 Problems in numerical PSC models

Numerical simulations are the bridge that connects microscopic properties and macroscopic performance. Numerical models are widely used for silicon solar cell analysis and optimization, such as modeling of free-carrier absorption,[81] enhancement of optical absorption,[82] wafer thickness optimization[83] and optimization of device structure.[84] Numerical models for DSSCs and Bulk Heterojunction (BHJ) OSCs are also developed.[85, 86, 87, 88, 89, 90, 91, 92, 93] With these numerical methods, details of charge transport in solar cells and how this factor affects solar cell's performance are revealed.

However, these models for silicon solar cells and DSSCs are unable to describe the mechanism in PSCs. Silicon solar cells are formed by p-n junctions which are caused by doping. Dopant density and its distribution determine solar cell's performance, especially the output voltage.[93] The model for DSSCs involves solvent, which conducts ions and current. Additionally, its output voltage depends on the redox level in electrolytes.[90] For PSCs, the output voltage depends on the electron and hole quasi-Fermi energy levels at corresponding electrodes, with no relation to dopants nor redox levels. Hence, the model should be adapted to PSCs. In PSCs, most of

the charge carriers are photon-generated holes and electrons, and the output voltage is determined by the difference of quasi-Fermi energy levels at the two perovskites boundaries.

There has been some recent progress in numerical simulations of PSCs. Liu *et al.* using a general solar cell simulation program – AMPS-1D, has shown how the PSC's PCE depends on thickness, defect density and charge mobility of its perovskite layer.[94] As discussed, the general model is unable to describe the charge transfer behavior and mechanism in PSCs exactly. Assuming the electric field in the whole solar cell is constant and using general equations, Sun *et al.* derived an analytical solution.[95] However their assumption contradicts the fact that the electric field in a real solar cell is never constant. Additionally, though they derived analytic solutions, the parameters employed are obtained from the fitting of experimental J-V curves, which is a phenomenological approach that can be severely affected by overparameterisation of the model. Foster *et al.* developed a numerical model with specific parameters and physics for PSCs.[96] It was perhaps the best model, but it has deficiencies. A difficulty with their model is that some parameters are unable to be obtained from experiment directly and this requires solving with physically realistic parameter values. Reenen *et al.* proposed a model to explain the hysteresis in PSCs based on time evolution.[77] Although they could explain the hysteresis, their results are in poor agreement with quantitative measurements in Tress' experiments.[70]

Therefore, a new model is developed here, which uses diffusion equations and has been implemented in a Fortran program. This model has no problem with solving equations with physically realistic parameter values. It is also shown how to use this model to analyze and optimize PSCs. This work was published as reference [57] and presented in Chapter 3.

1.5.3 What is the influence of the screening field on PCE and hysteresis?

In experiments, the compensated screening field was observed and considered to be the reason to induce hysteresis.[70] Juarez-Perez *et al.* found a giant dielectric constant (GDC) phenomenon consisting of a low frequency dielectric constant in the dark of the order of $\epsilon_0 = 1000$.[97] They also found that ϵ_0 further increases under illumination or by charge injection at applied bias. Frost *et al.* reported that the increase at low frequency and under illumination is due to the screening of ion migration and MA^+ polarization.[98] However, how this screening effect will influence the performance

of PSCs has not been much investigated. Using the numerical model developed, I examined the influence of the screening effect in different PSCs.

On the other side, polarization, space charges, and ion migration are other possible causes for hysteresis.[74] Most researchers believe that ion migration is the cause of hysteresis.[49, 75, 76, 51, 70, 77] Very little research supports the possibility of polarization induced hysteresis. There are some reasons to believe that the hysteresis comes from ferroelectric polarization. The first is the possibility of ferroelectricity in the organic hybrid perovskites. The second is that ferroelectric P-E curve shows hysteresis.[68] Ferroelectric materials show a spontaneous polarization and its direction can be reversed by a strong external field. Their polarization states depend not only on the current applied electric field but also on their history, yielding hysteresis loops.[99] Ferroelectric materials often show hysteresis phenomenon.[100, 101, 102] Additionally, there are some theoretical models to simulate the anomalous hysteresis in PSCs,[77] but all of them are qualitative. No quantitative modeling has been made. Therefore, using our developed numerical model implemented with polarization relaxation and capacitive charge relaxation, we reproduced experimental hysteresis J-V curves. Our numerical results demonstrated that polarization is able to bring about hysteresis as ion migration does. To quantitatively reproduce experimental hysteresis J-V curves, two relaxations with different relaxation times are required. Lastly, we proposed some approaches to reduce the hysteresis in PSCs. This work was published as reference [73] and shown in Chapter 4.

1.5.4 Does ferroelectric polarization exist? How do the polarization and ion migration produce hysteresis?

A fundamental question underlying both performance and hysteretic behavior of organic hybrid perovskites concerns their ferroelectric character. If it is ferroelectric, the polarization certainly has effects on power conversion and hysteresis. If it is not ferroelectric, there is no ferroelectric contribution. Theoretically, most people believed that organic hybrid perovskites are ferroelectric.[103, 64] Frost *et al.* assumed the presence of ferroelectric polarization and used it to explain the hysteresis in PSCs.[104, 47] DFT studies demonstrated that organic hybrid perovskites have ferroelectric polarizations.[69, 105, 106, 107] Whereas, there is no certain answer in experiments.

In 2014, Kutes *et al.* claimed that they directly observed ferroelectric domains in $MAPbI_3$ thin films.[108] However in their experiment, they showed the polarization of $MAPbI_3$ thin films under different biases, which can not prove the polarization is

ferroelectric rather than ion migration induced polarization. This polarization may be built by iodine ion migration. In 2015, Beilsten-Edmands *et al.* argued that there is no ferroelectricity in $MAPbI_3$ perovskite-based photovoltaic device.[75] However this argument fails to estimate the intrinsic polarization. They excluded the ferroelectric polarization by assuming the ferroelectric polarization is the intrinsic polarization under extremely high frequency, which was set as the intercept of the line of Q vs $1/f$. All of the ferroelectric polarizations show decreasing trends at very high frequency.[109, 110] Hence, the polarization should be very small at extremely high frequency as electronic orbitals and ions are unable to catch up with the external field and respond. In the same year, Zhao *et al.* reported ferroelectric polarization behaviors in hybrid halide perovskite films.[78, 71] They did not exclude the contribution from ion migration. Fan *et al.* also reported that there should be ferroelectric polarization in theory, but at room temperature they did not observe ferroelectric polarization.[107] They drew the conclusion by comparing the I-E curves of Au/$MAPbI_3$/ PEDOT:PSS/ITO and Au/$BiFeO_3$/$SrRuO_3$. There are two issues in their experiment. The first issue is that they used two different device structures. The second is that they ignored the influence of applied voltage amplitude and frequency. The amplitude and frequency of applied voltage for perovskite are 1 V and 10 Hz, whereas, corresponding values for $BiFeO_3$ are 26 V and 1 kHz. Since ferroelectric polarization is frequency dependent, these two experiments with 100 times difference in frequency cannot be directly compared.

Leguy *et al.* using quasielastic neutron scattering measurements showed that MA^+ ions reorientate with a residence time about 14 ps at room temperature.[111] Their Monte Carlo simulations demonstrated MA^+ ions behave as either anti-ferroelectric or ferroelectric, which depends on the interaction between neighboring MA^+ ions. However, they did not consider the polarization of the inorganic frame, which also could contribute to ferroelectricity, such as $BiFeO_3$. Therefore, we studied the independent and collective movements of MA^+ ions, and also possible polarization coming from inorganic frames. This work is shown in Chapter 2. On the other hand, they used a three-dimensional periodic bulk model, which is not the real case as the thickness of a perovskite layer in solar cells is only several hundred nm. Additionally, the three-dimensional periodic bulk model is unable to model the surface charge, which exists at the interface of PSCs and plays an important role in charge behavior. Hence, charge related behaviors in perovskite layers should be simulated with two-dimensional periodic thin film models. This is also confirmed by our simulations

Table 1.1: Experimental parameters related to band gaps and V_{oc}.

Solar cells	**Band-gap(eV)**	V_{oc} **(V)**	**Deficit (V)**	**PCEs**[4]
Amorphous silicon	1.55[122]	0.98[123]	0.57	13.6%
Multicrystalline silicon[124]	1.12	0.67	0.45	21.3%
CdTe[124]	1.51[125]	0.88;1.04[126]	0.63;0.47	21.1%
$MAPbI_3$[1]	1.57	1.14	0.43	21.1%

that charge behaviors in two- and three-dimensional periodic models are totally different and even show opposite phenomenon. Due to the presence of these issues, we build up two- and three-dimensional periodic models to simulate ion migration and polarization relaxations. This part of the work is presented in Chapter 5.

1.5.5 To understand the high open-circuit voltage in PSCs

Open-circuit voltage of a solar cell is always lower than the band gap of the absorber. The difference between them is called open-circuit voltage deficit. A large open-circuit voltage deficit leads to a low performance. Table 1.1 shows the parameters of different kinds of solar cells. It is worth noticing that the PSC has the smallest open-circuit voltage deficit. This small deficit even surpasses that of silicon solar cells, which have been developed for more than 40 years. I have found that the high V_{oc} in PSCs is not rare, many experiments have achieved V_{oc} higher than 1.1 V.[39, 112, 113, 114] Thus, why PSCs can achieve such a high V_{oc} without sophisticated fabrication methods?

The open-circuit voltage deficit in OSCs,[115, 116, 117, 118] quantum dot solar cells,[119] a-Si:H/c-Si heterojunction solar cells[120, 121] have been discussed. In quantum dot solar cells, it was found that sub-bandgap states are the most likely origin of the high V_{oc} deficit.[119] For bulk heterojunction solar cells, theoretical works showed that the V_{oc} depends on (1) the donor-acceptor energy gap; (2) charge-carrier recombination rates; (3) illumination intensity; (4) the contact work functions (if not in the pinning regime); and (5) the amount of energetic disorder.[120, 121] The V_{oc} in OSCs seems more complicated: Garcia-Belmonte *et al.* found that small tails of DOS distribution will lead to high V_{oc}; Sulas *et al.* showed that the increased density of charge-transfer states causes V_{oc} loss;[116] The same conclusion was also obtained by Collins *et al.*[118]

Do PSCs display similar V_{oc} dependences? The unusual V_{oc} in PSCs hasn't been noticed until 2015.[127, 128, 129] The theoretical study done by Yang *et al.* illustrated that the reduced bimolecular recombination is the origin of high V_{oc}.[127] Chen *et al.* further demonstrated that the limiting of V_{oc} of $MAPbBr_3$ PSCs is due to the interface

loss induced by the charge extraction layer rather than by bulk dominated recombination losses.[129] Hence, we calculated N_c and N_v of different materials including typical perovskites and implemented them into our developed numerical models, it is found that low N_c and N_v in perovskite materials could contribute 100 mV higher V_{oc} compared to PSCs with silicon N_c and N_v. Low N_c and N_v agree with the low DOS tail of conduction band observed by Endres *et al.*[128] This work is reported in Chapter 6 and published as reference [130].

1.6 Outline of the thesis

In this thesis, I employed DFT calculations to study the electronic and polarization properties of $MAPbI_3$ as well as numerical simulations to study the screening effect, ion migration and polarization effect in PSCs. Chapter 1 gives an overview of current PSC research, including the development of PSCs and mechanisms in PSCs. The second half of Chapter 1 discussed the questions and debates in PSCs and stated my research motivation. Two of my research questions are about why PSCs can realize high PCEs and why there is hysteresis. Chapter 2, 5 and 6 are intended to investigate the microscopic origin of high PCEs, while Chapter 2, 3, 4 and 5 investigate the reasons for hysteresis.

Chapter 2

Photovoltaic performance and the energy landscape of $CH_3NH_3PbI_3$

2.1 Introduction

A photovoltaic cell with a perovskite absorbing layer was first made by Kojima *et al.*[6] The first perovskite solar cell (PSC) was made in 2012.[25, 26] The rapid development of PSCs surpasses the understanding of its mechanisms. One year after its invention, PSCs realized power conversion efficiency (PCE) above 15 % although the detailed electronic properties of absorber were unknown.[12, 34] Within 4 years, PCE record of thin film PSCs has reached 22.1%.[24, 25, 62, 34, 33, 131, 12, 1, 4] It is believed that the benign defects, long charge carrier lifetimes and mobilities[28, 29] and very wide wavelength range with high Incident-Photon to Current Efficiency (IPCE)[34, 25, 62] are the reasons for PSCs realizing high PCEs.

$CH_3NH_3PbI_3$ ($MAPbI_3$) and $MAPbI_xCl_{3-x}$ are widely used as light absorbers in PSCs. At room temperature, $MAPbI_3$ adopts a tetragonal structure, its β-phase. It will turn into the cubic α-phase at 333 K.[8] In theory, the structural and electronic properties of its α phase have been discussed by the Aron group.[64] Zhao *et al.* have studied the orthorhombic perovskite $MAPbI_3$ and they show that van der Waals (vdW) interactions are important in DFT calculations.[67] Du has discussed the electronic structure of the β phase of $MAPbI_3$, and reported small electron and hole effective masses, large Born effective charge, and benign traps and recombination centers, all of which contribute to exceptionally good carrier transport properties.[63]

Perovskite materials often exhibit ferroelectricity. Some experiments have reported ferroelectric behavior in $MAPbI_3$ thin films.[8, 108, 78] It is probable that the spontaneous ferroelectric polarization affects the perovskite photovoltaic's performance if ferroelectricity exists. It has been reported that polarizations in dye-

sensitized solar cells (DSCs) and organic solar cells (OSCs) improve their performance.[132, 133] By introducing a permanent electric field in an ultra-thin layer of ferroelectric co-polymer at the interface between the electrode and semiconductor layer of organic solar cells, the interface charge is decreased, and then the Schottky barrier is lowered, which increases charge collection efficiency and PCEs.[134, 80, 135] These studies suggest that polarizations may also affect PSC performance. Frost *et al.* proposed that ferroelectric domains result in internal junctions, which promote the separation of excitons, and reduction of recombination through segregation of charge carriers.[104, 69] The bulk photovoltaic effect related with ferroelectricity and ferroelectric domain wall have been discussed.[136, 66] The links between models and cell performance are not clear.

The first aim of this part is to determine where the ferroelectric polarization may come from and how this polarization influence PSC performance. We examine the methylammonium ion (MA^+) orientation impact on $MAPbI_3$ electronic properties using Density Functional Theory (DFT). We discussed the possible mechanism of polarization, the relative energies of MA^+ structures, and the heights of energy barriers between these structures. Additionally, by using theoretical methods, arguing from three points, we show that the polarization of MA^+ and perovskite unit cell are able to provide the compensated field observed in Tress's and Zhang's experiment.[70, 137] The first point is that the MA^+ in its crystal can be reorientated by the external applied field; the second point is that the rotatable ordered MA^+ can provide overall polarization; The third point is that these polarized MA^+ are able to provide a strong compensated field (we call it the screening field), which promotes the charge transport and improves PCEs in perovskite solar cells.

On the other hand, hysteresis in PSCs behaves anomalously. Hysteresis current-voltage (J-V) curves is observed in silicon solar cells, DSCs and OSCs at high scanning speeds.[138, 139, 140] This hysteresis is explained by capacitive charge, including space charges and trapped charges. When the scanning is faster than the release of traps, or faster than the space charge relaxation, but not so fast that the charges cannot respond at all, hysteresis happens.[141] In hybrid perovskite solar cells, hysteresis behaviors are much slower, and also more complex and anomalous. Most experiments on hybrid perovskite solar cells show stronger hysteresis when scanning speed increases,[36, 37, 142, 50] but Snaith *et al.* also observed that slower scanning could lead to larger hysteresis.[51, 47] They attributed this anomalous hysteresis to a change to the nature of electronic contact between the perovskite and the p- and n-type contact materials, which they verified by removing or changing the hole

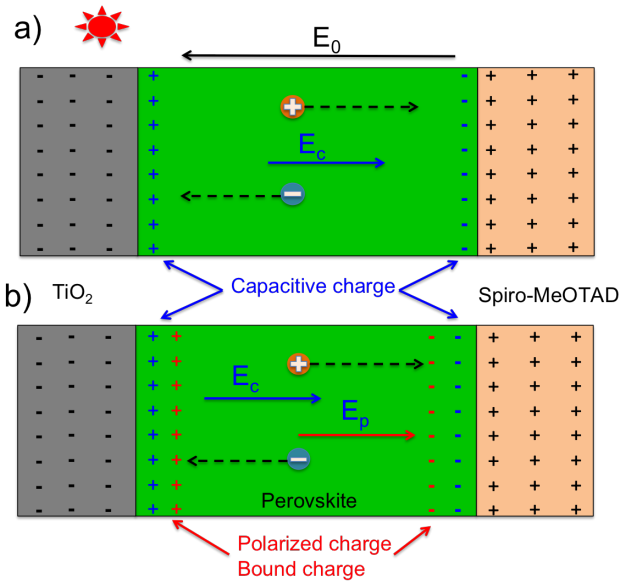

Figure 2.1: The scheme of charge distributions in a normal solar cell without a ferroelectric medium (a), and a perovskite solar cell (b). The gray region on the left is the photo-anode. The excited electrons generated in the absorber layer (the light green region in the center) accumulate here. The dark green region on the right represents the HTL, where holes accumulate. $\mathbf{E}_0$ is the hindering field. Capacitive charges are shown in blue. The field due to polarization and the corresponding bound charges are shown in red.

and electron transfer layer. However, hysteresis in the photovoltaic absorbing layer without charge transfer layers is reported by Tress *et al.*[70] Some have focused on how to reduce or eliminate hysteresis by using a mixed solvent in the deposition process, increasing perovskite crystal size, and using mesoporous-TiO_2.[48, 143] Here, we argue the hysteresis in PSC is very likely due to the hysteresis of ferroelectricity of perovskite materials as the ferroelectricity is defined by the P-E loop, which is a hysteresis loop.

To explain the hysteresis effect in measurements of hybrid perovskite solar cells, lots experiments have been set up. Tress *et. al.* carried out serial experiments and confirmed that there is a compensated field induced by some slow processes. They thought the ion migration is responsible for this slow process.[70] Zhang *et. al.* showed that there is a field in the direction beneficial to charge collection in their solar cells. They also believed this beneficial field is induced by the ionic motion.[137] Chen *et al.* discussed the impact of slow transient capacitive current, trapping and detrapping processes, ion migration, and ferroelectric polarization on the hysteresis behavior and pointed out that ion migration is the most possible reason to induce hysteresis.[74]

Whereas, the experiment done by Gottesman *et al.* refutes this conclusion.[41] In their experiment, three mechanisms have been put forward. They are the migration of MA^+, photo-induced traps for charge carriers in the $MAPbI_3$ and the dipole alignment in films. Their experiment of witnessing two opposite behaviors of decreased/increased photo-conductivity in the same material (different devices), makes the first two mechanisms less possible. Ion migration only can result in one response because ions always migrate towards to the negative electrode. This dismisses the photo-induced traps as there is an increasing photo-conductivity over time.

The second aim of this part is to explain the anomalous hysteresis from first-principles calculations combining with the previous experimental study. The source of hysteresis may be not singular. Figure 2.1 shows the charge distribution in a normal solar cell without a ferroelectric polarization medium (a), and a perovskite solar cell with polarization(b). The left and the right region are electron transfer layer (ETL) and hole transfer layer (HTL) respectively. The center part is absorber, where excitons are generated. After exciton formed, they transfer and separate into a pair of free electron and hole. Electrons go to and accumulate at ETL, while holes go to and accumulate at HTL. These accumulated charges in the charge transfer layer build a potential difference, which is observed as the output voltage. It equals to the applied electric field ($\mathbf{E}_0$) when measures. The direction of this electric field is from HTL to ETL. This field hinders the motion of electrons go to the left, and holes go to the right, therefore reducing solar cell's performance. Charge accumulation also happens at the interfaces of ETL/absorber and absorber/HTL due to energy level differences. These charges always exist in device with interfaces, which called capacitive charges (blue charges). This charge induces a field ($\mathbf{E}_c$), which will partly cancel the hindering external field $\mathbf{E}_0$. For a perovskite solar cell, if polarization exists in perovskite thin film, the polarization of absorber can produce bound charge at interfaces (shown as red charges). The field induced by bound charges ($\mathbf{E}_p$) will further screen $\mathbf{E}_0$ and promote charge transport, and so improve performance. This possible mechanism is consistent with the compensated field in experiments.[137, 70] We based on the quantum calculations analyze the possible polarization from both MA^+ and lead ion. Collective behavior of MA^+ and their orientation distribution under room temperature are also discussed.

2.2 Calculation Methods

The DFT calculations are performed by the Vienna *Ab-initio* Simulation Package (VASP),[144, 145] which implements the projector augmented-wave (PAW) method[146] using a plane-wave basis set. The generalized gradient approximation (GGA) have been used to calculate the exchange correlations. Zhao *et al.* show that vdW interactions are important to DFT calculations on orthorhombic perovskite.[67] Giorgi *et al.* showed that hybrid methods applied on top of the spin-orbit coupling (SOC) calculated structures are not able to open the band gap sufficiently to reproduce the experimental value.[147, 148] More advanced methods give improved results, for example GW+SOC calculations give the best agreement with experimental band gap at 1.5 eV.[149] The GW approximation (GWA) is an approximation made in order to calculate the self-energy of a many-body system of electrons by using the expansion of the self-energy in terms of the single particle Green's function G and the screened Coulomb interaction W. The GW+SOC method, shown to give the band structure closest to experiment, cannot feasibly be used with the nudged elastic band calculations that we use to map out the energy landscape of $MAPbI_3$. We exclude the GW method. In order to get relatively accurate results, we use GGA methods with or without considering the vdW interactions,[150] SOC or both of them. Very small band gaps calculated considering SOC in standard DFT do not agree with experiment, while the standard GGA gives band gap closer to the experimental value.

We optimised the β phase of $MAPbI_3$ with different methods, and then compared these obtained lattice parameters to experiment. As shown in Table A.6, the sequence of lattice parameters and volumes estimated by various methods is: PBE > optPBE-vdW > optB86b-vdW > PBE-vdw > PBEsol > Experimental > PBEsol-vdw. The PBEsol/GGA+vdW calculations will lead to cell vectors about 20 % smaller than that in experiments. In general, for PBE/GGA calculations, vdW helps it to get more accurate lattice parameters. While for PBEsol/GGA calculations, the implement of vdW interactions leads to inaccurate lattice parameters. Parameters calculated by PBEsol are the closest parameters to experiment. Therefore, we chose the PBEsol/GGA method without considering vdW interaction to calculate all the properties reported below.

The exchange-correlation was calculated using the Perdew-Burke-Ernzerhof functional as revised for solids (PBEsol).[151] The GGA PBEsol calculations are done with the PBE-PAW potential considering 14 electrons $5d^{10}6s^26p^2$ for lead. The pseudopotentials with $5s^25p^2$, $2s^22p^2$, $2s^22p^3$ and 1s valence electrons are used for iodine,

carbon, nitrogen and hydrogen, respectively. An energy cut-off was set at 500 eV. A Γ-centerd Monkhorst mesh of 9 × 9 × 9 for the α phase, and 7 × 7 × 5 for the β phase, was used for static calculations, including density of states (DOS) and band structure. The structures were optimized until the maximum force on each atom was smaller than 0.01 eV/Å. For super-cells, 3 × 3 × 3 Γ-centered Monkhorst mesh are used. All the geometries were optimized until the force on each atom is smaller than 0.02 eV/Å. At the beginning, we fully optimized the geometry of all the structure without any constraint, but we found that the optimized structure is not the same with the experiment. This because many local energy minimum configurations exist for $MAPbI_3$, while the phases that we interested are not stable at low temperature. Most of the optimized structures go to γ phase (the phase at lowest temperature) similar structures.[8] Here, we focus on the α and β phase, as both and only α and β phases are possible near room temperature. Therefore, we optimized the structures with the iodide ions fixed, the shape and volume of cells are allowed to change.

To get accurate second derivatives of energy, high-density points band-structure calculations have been performed. 60 points were used between each two high-symmetry points. The second derivative was calculated as twice quadratic coefficient (a) obtained by fitting. The fitting polynomial is,

$$E(\mathbf{k}) = a(\mathbf{k} - \mathbf{k}_0)^2 + c, \tag{2.1}$$

where $E(\mathbf{k})$ is the energy and $\mathbf{k}_0$ is the $\mathbf{k}$ vector where its energy is the minimum (maximum) of the conduction (valence) band. Due to band crossing, the region over which the energy varies quadratically in $\mathbf{k}$ is limited. This limits the data available for the determination of effective mass. Here, we use six points to fit. In the absence of band crossing, the results are very similar for any number of points between 3 and 10.

The polarization of crystals and Born charges were calculated by the Berry phase method, which is widely used to analyze the polarization in crystals.[152, 153, 154, 155] The dielectric constant is estimated by means of density functional perturbation theory.[156] The nudged elastic band (NEB) is a method used to find the minimum energy reaction paths (MEP) when both of the initial and final states are known. It has been implemented in VASP.[157] First, linearly interpolating a set of structures between the known initial and final states gives an initial guess for the path. The energy of this string of images is then minimized. Thus the MEP is revealed. A refined climbing image NEB method calculates not only MEP but also the saddle point. It drives one image to the highest energy up to the saddle point. The force at this

Table 2.1: The energies of $MAPbI_3$ with various MA^+ orientations with or without lead atom relaxed. Structures show in Figure 2.2.

Phase	Orientation	Lead relaxed (eV)	Lead fixed (eV)
α	001	-52.046	-52.046
	$1\bar{1}0$	-52.054	-52.051
	111	-52.060	-52.059
β	$00\bar{1}$	-208.724	-208.360
	$\bar{1}\bar{1}0$	-208.551	-208.338
	$\bar{1}\bar{1}1$	-208.689	-208.328

saddle point along the tangent changes sign. In this way, the image tries to maximize its energy along the band, and minimize in all other directions. When this image converges, it will be at the exact saddle point.[158] In this paper, energy barriers for MA^+ rotations are performed by climbing image NEB (cNEB) calculations. In searching for the saddle points, the relaxation is stopped if all forces are smaller than 0.05 eV/Å.

2.3 Results and discussion

We set out here the properties of structures of the α and β phases, and most importantly, the energy barriers between these states. In this part, we will examine two possible mechanisms for the PCE performance and three points for the explanation of hysteresis we have suggested above.

2.3.1 Structures and energies

The $MAPbI_3$ crystal includes an inorganic lead and iodide framework and MA^+. The disordered MA^+ is associated with the cage of Pb-I atoms as reported in x-ray diffraction.[159, 160, 161] Due to the weak interaction between MA^+ and the inorganic frame, multiple local energy minimum structures exist. MA^+ may point in different directions. In previous theoretical studies, MA^+ orients to different directions in orthorhombic,[67, 162, 163] cubic,[147, 64, 164] or tetragonal structures,[149, 63] which leads to different results, such as band gap, effective mass. Here we systematically compare three representative structures with differently oriented MA^+, in both the α and β phases. The MA^+ ion oriented along [001] direction is denoted 100-$MAPbI_3$ (Figure 2.2(a) and (d)), in which MA^+ ion (C-N bond) is parallel to c axis. The other two cases are MA^+ ion oriented to [110] (110-$MAPbI_3$, Figure 2.2(b)) and [111] (111-$MAPbI_3$, Figure 2.2(c)). The unit cell of the β phase has four MA^+,

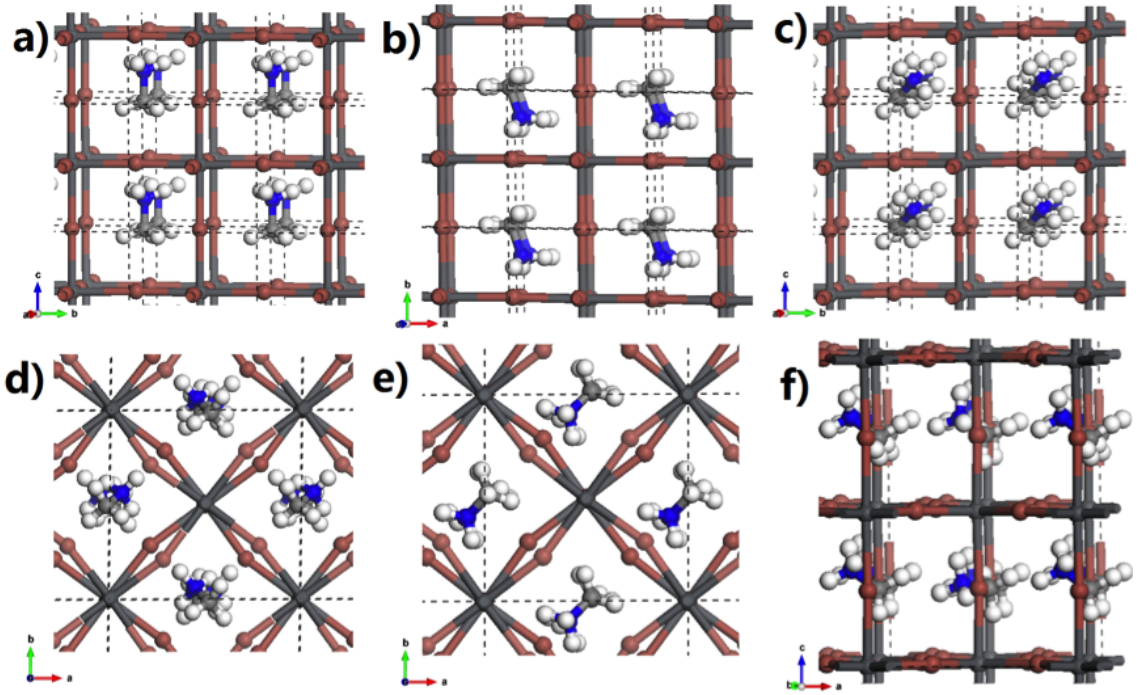

Figure 2.2: The optimized structure of $MAPbI_3$ with lead ions fixed, MA^+ were initially oriented along direction (a) [001]; (b) $[1\bar{1}0]$; (c) [111] in $2 \times 2 \times 2$ super cells of α phase. The unit cell of the β phase with MA^+ were initially oriented along direction (d) $[00\bar{1}]$; (e) $[\bar{1}\bar{1}0]$; (f) $[\bar{1}\bar{1}1]$ in a single unit cell. The carbon and nitrogen coordination difference was defined as the direction. The dash brown lines are the boundaries of unit cells.

we start energy minimizations with all of the MA^+ oriented to $[00\bar{1}]$, $[\bar{1}\bar{1}0]$ and $[\bar{1}\bar{1}1]$. These oriented MA^+ change their orientations little on energy minimization. Two different methods have been used to optimize its structure. The first method keeps the inorganic component fixed during geometry optimization; the other method keeps the iodide ions fixed, while relaxing lead ions and MA^+. For α phase, the 111-$MAPbI_3$ always has the lowest energy (Table 2.1). The energy differences between structures are about 10 meV for the α phase, so that, barriers permitting, MA^+ are able to rotate at room temperature. This difference becomes about 100 meV (25 meV for each MA^+ ion) in the β phase, so that it is a little less thermodynamically favoured for MA^+ to rotate in β phase than that in α phase, but still possible.

2.3.2 Band structure of $MAPbI_3$

Figure 2.3 shows the first Brillouin zone of the α and β phase $MAPbI_3$. Since both of them are tetragonal, the shape of their reciprocal unit cells and the high-symmetry K

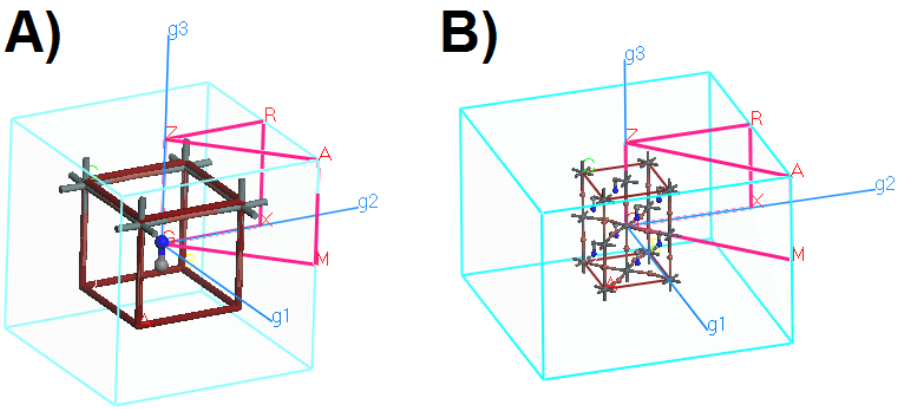

Figure 2.3: The first Brillouin zone of the α phase and the β phase $MAPbI_3$.

points are the same. The band structure of the α and β phases with lead relaxed, are shown in Figure 2.4. The valence band maximum (VBM) and the conduction band minimum (CBM) are shown at R point in the α phase. This K point is Γ in the β phase.

Borriello *et al.* have shown that the electronic properties of tin-halide perovskitic compounds are strongly dependent on the structure of the inorganic cage, as the valence and conduction bands are dominated by the inorganic cage.[165] This view is confirmed with our calculation that band gaps with differently oriented MA^+ are similar, but we found that the shape at the bottom and top of the conduction and valence band changes as the MA^+ ion rotates. The band gaps are about 1.2 eV (α phase) and 1.3 eV (β phase), due to the normal DFT underestimation of band gaps, these are lower than the experimental value of 1.5 eV [159]. There is little difference among these structures with differently oriented MA^+. In the α phase, the band gap of 110-$MAPbI_3$ (1.21 eV) is smaller than that of 001- (1.24 eV) and 111-$MAPbI_3$ (1.29 eV). The band gaps for the structures optimized with lead fixed are 1.22 eV, 1.15 eV, and 1.26 eV for 001-, 110- and 111-$MAPbI_3$, shown in Figure A.1.

The band structures of the β phase are shown at the bottom of Figure 2.4. Band gaps are 1.42 eV, 1.30 eV, 1.27 eV for 001-, 110- and 111- $MAPbI_3$. They are 1.39 eV, 1.28 eV and 1.31 eV for lead-relaxed 001-, 110- and 111- $MAPbI_3$. The band gaps of the structures with lead fixed are about 3% different from that of the lead relaxed β phase, shown in Figure A.1. Those theoretical band gaps are close to the experimental value of 1.5 eV.[159] The electron DOS is shown in Figure A.2. The band divergence of different oriented MA^+ agrees with Brivio's work on the α-phase.[64]

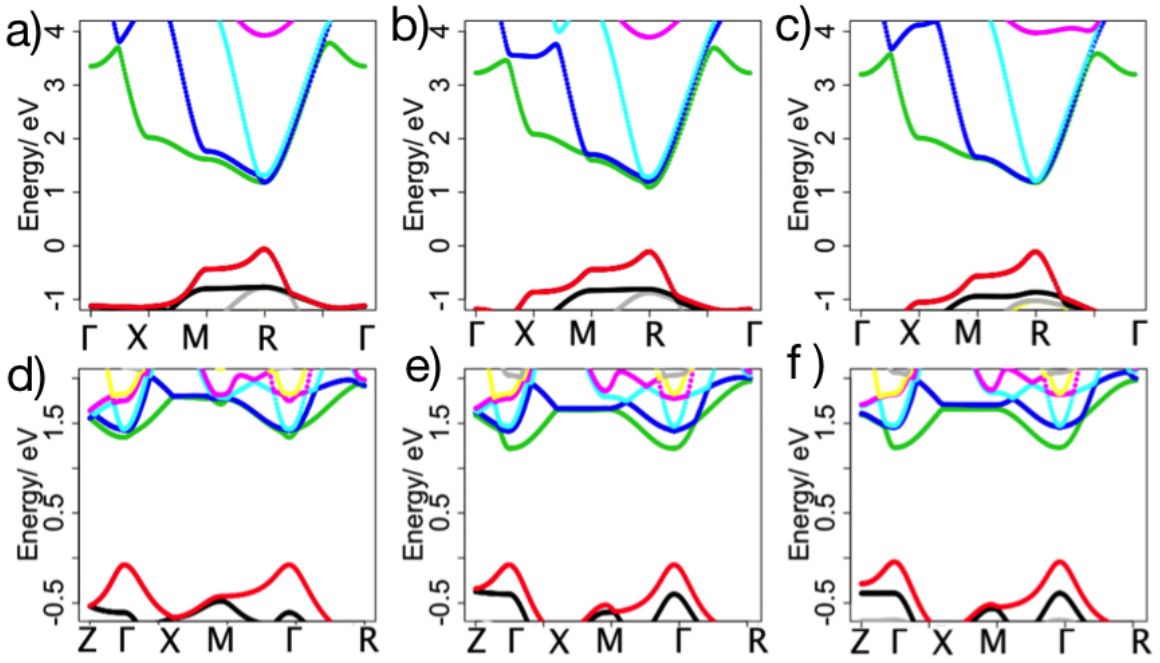

Figure 2.4: The band structure of α phase and β phase optimized with lead relaxed. The (a), (b) and (c) are the band diagrams of α phase, corresponding to 001-, 110- and 111-$MAPbI_3$, respectively. The band diagrams of β phase are shown as (d), (e) and (f) corresponding to 001-, 110- and 111-$MAPbI_3$, respectively).

We find that orientation of MA^+ has a relatively weak effect on the band gap, too small to have any significance consequences for photovoltaic performance.

2.3.3 The effective masses

We estimate the effective mass based on its definition,

$$\frac{1}{m^*} = \frac{1}{\hbar}\frac{d^2E(\mathbf{k})}{d\mathbf{k}^2}, \tag{2.2}$$

where the $E(\mathbf{k})$ is the energy of a band and $\mathbf{k}$ is the wave vector. The method to calculate the second derivative of energy is illustrated in Method.

For the α phase, estimated masses are shown in Table 2.2. The effective hole masses are about 0.16 m_0. This hole effective mass in changes as the MA^+ ion rotates by about 10%. For electron transport, effective masses are anisotropic, and individual values differ greatly between different MA^+ ion orientations. There are three conduction bands with very little energy difference, which suggests all of them could contribute to charge transport. The harmonic mean electron effective masses are 0.174 m_0, 0.180 m_0 and 0.171 m_0 for $[00\bar{1}]$, $[1\bar{1}0]$ and [111] directions, respectively.

Table 2.2: Effective hole and electron masses of the α phase with lead atoms relaxed. These results were fitted with six points near the R point. The effective mass unit is m_0 (the static mass of a free electron).

MA^+ orientation	**Bands**	**M-R**	**R-Γ**	**Harmonic Mean**
001		-0.172	-0.149	-0.160
$1\bar{1}0$	VB	-0.197	-0.154	-0.173
111		-0.150	-0.144	-0.147
	CB1	0.325	0.156	
001	CB2	0.079	0.176	0.174
	CB3	0.655	0.198	
	CB1	0.402	0.155	
$1\bar{1}0$	CB2	0.223	0.179	0.180
	CB3	0.106	0.207	
	CB1	0.069	0.129	
111	CB2	1.044	0.192	0.171
	CB3	0.480	0.219	

The extrema of band structure are at the Γ point in the β phase. For hole transport, effective masses differ little among reciprocal space directions, and change little as the MA^+ ion rotates. We find again in the β phase anisotropic band structure for electron transport. The electron effective masses are very sensitive to the direction of the crystal momentum **k**. For the first conduction band in the β phase (the lowest energy conduction band), they have very small effective masses (lighter than 0.1 m_0) in the direction of the Z point. While the band bottom becomes very flat in the direction of the X point, especially for the 100- and 111-perovskite (Table 2.3). Due to its highly anisotropic transport properties, we also calculated the effective masses in the directions of other high symmetry **k** points, as shown in Table 2.3. The calculated effective masses are about 0.1 m_0. The inequivalence of the M and M2 points for the configuration $[00\bar{1}]$, is due to symmetry breaking by the hydrogen atoms, and the MA^+ ion not aligning exactly in the direction of $[00\bar{1}]$. The harmonic mean electron effective masses are 0.199 m_0, 0.192 m_0 and 0.195 m_0 for $[00\bar{1}]$, $[1\bar{1}0]$ and [111], respectively.

We find effective masses for some one-electron states are very sensitive to the orientations of MA^+, while the Harmonic mean effective hole masses change little. This raises the possibility that in certain directions in the β-phase, for one electron state, the electron mobility responds strongly to polarization. But the overall effective masses and mobility have no much difference.

Table 2.3: Effective hole and electron masses of the β phase along with different directions with lead relaxed. These results were fitted with 6 points near the Γ(0, 0, 0) point. The effective mass unit is m_0. The directions in **k**- space are: M (0.5, 0.5, 0), R (0.5, 0.5, 0.5), Z (0, 0, 0.5), X (0, 0.5, 0), M2 (0.5, -0.5, 0), R2 (0.5, 0.5, -0.5).

MA^+ Direction	Band	Z-Γ	Γ-X	M-Γ	Γ-R	M2-Γ	Γ-R2	Harmonic Mean
$00\bar{1}$	CB3	0.08	0.12	0.15	0.15	0.07	0.14	0.199
	CB2	0.22	0.74	0.71	0.60	3.22[a]	0.51	
	CB1	1.28	0.23	0.18	0.15	0.93	0.20	
	Mean[b]	0.53	0.36	0.35	0.30	1.41	0.28	
$\bar{1}\bar{1}0$	CB3	0.73	0.10	0.08	0.10	0.09	0.10	0.192
	CB2	0.89	0.18	0.45	0.51	0.30	0.50	
	CB1	0.07	1.81	1.40	0.29	1.49	0.34	
	Mean[b]	0.56	0.70	0.64	0.30	0.63	0.31	
$\bar{1}\bar{1}1$	CB3	0.78	0.11	0.08	0.10	0.08	0.10	0.195
	CB2	1.01	0.18	0.62	0.67	0.62	0.67	
	CB1	0.07	1.02	0.94	0.29	0.95	0.29	
	Mean[b]	0.62	0.44	0.55	0.35	0.55	0.35	

[a] is the effective masses calculated from fitting to 10 points around the numerically determined minimum just off the Γ point. [b] is the Harmonic mean.

2.3.4 Born effective charge

For lead atoms in both the α and β phases, the diagonal elements are close to 4.6 e, where e is the magnitude of the elementary charge, while non-diagonal elements are smaller than 0.5 e. In optimized structures, the MA^+ are not at the center of inorganic cages, carbon atoms of MA^+ are always closer to the cage boundary. The zz component of the Born charge of the lead atom reduces from 5.15 e to 5.01 e to 4.78 e, as MA^+ ion rotates from [001] to [101] and to [111] for the α phase, as shown in Table 2.4. Carbon atoms are strongly coupled to lead ions. The Born charges of iodide ions are dependent on their position and coordination geometry around lead atoms. In the α phase, the iodide Born charge is about -4.5 e in the Pb-I bond direction, and almost zero in other directions. Trends are similar in the β phase, but two types of iodides are present: one is apical, located at the center of two lead ions, the other is equatorial.[63] The apical iodides behave as in the α phase, but for the equatorial iodides, the Born charges in the plane of its two Pb-I bonds are about -2.6 e, the direction out of plane is very small. More Born charges of the α and β phases are listed at Table A.2-A.5. The Born effective charges are roughly twice as large as the corresponding formal charge (2.0 e). The large Born effective charges are

Table 2.4: Born charges of the lead ions in α phase. They vary as the MA^+ ion vectors.

MA^+ orientation	Direction	X	Y	Z
[001]	X	4.688	0.007	-0.064
	Y	0.007	4.682	-0.060
	Z	-0.063	-0.059	5.146
[101]	X	4.995	0.007	-0.030
	Y	0.008	4.515	0.360
	Z	-0.030	0.372	5.010
[111]	X	4.863	0.021	0.072
	Y	0.021	4.882	0.073
	Z	0.071	0.073	4.776

related to the large static dielectric constant, or the ferroelectric character if there is. The large dielectric constant and the resulting screening of defects and impurities may promote transport properties.[166, 63] These results show modest changes in the behavior of electrons in the inorganic framework with MA^+ rotation. That argues for the important of the 'macroscopic' mechanism of Figure 2.1 over the possibility of changes in electronic structure with MA^+ rotation.

2.3.5 Exciton separation energy

The energy needed for exciton separation is the energy difference between the lowest and highest energy levels of the two-charge system. The n-th orbital energy of two-charge system is,

$$E_n = -\frac{1}{n^2}\left(\frac{e^2}{4\pi\varepsilon\varepsilon_0}\right)^2\frac{m_{ex}}{2\hbar^2} + \frac{\hbar^2\mathbf{k}^2}{2M}, \tag{2.3}$$

where $m_{ex} = \frac{m_e * m_h}{m_e + m_h}$, $M = m_e + m_h$, where, m_e and m_h are the effective electron and hole masses. $\hbar$ is the reduced Plank constant, ε is the relative dielectric constant and ε_0 is the vacuum permittivity. The last term is the kinetic energy of the exciton. The first term is the orbital energy of different states. The maximum energy for charge separation is to excite a two-charge system from the ground state (n=1) to the highest excited state (n=∞). For $MAPbI_3$ the harmonic mean effective hole and electron masses are about 0.16 m_0 and 0.20 m_0 (shown in Table 2.2 and 2.3), respectively, and the static dielectric constant describing the response of electrons with ions fixed is about 6.0, shown in Table 2.5, calculated from density functional perturbation theory. Using these parameters, we estimated the binding energy to be 30 meV, which agrees with experiment (37 meV,[167] 45 meV[168] and 50 meV[169]).

Table 2.5: Dielectric tense including local field effects in DFT for the α and β phases with representative MA^+ ion orientations.

MA^+ orientation	**Direction**	**X**	**Y**	**Z**
α [001]	X	5.90	-0.00	0.01
	Y	-0.00	5.88	0.02
	Z	0.01	0.02	6.26
α [110]	X	6.20	-0.00	-0.01
	Y	-0.00	5.73	0.19
	Z	-0.01	0.19	6.21
α [111]	X	5.74	0.06	0.08
	Y	0.06	5.74	0.07
	Z	0.08	0.07	5.70
β [001]	X	5.70	-0.03	0.04
	Y	-0.03	5.70	0.04
	Z	0.04	0.04	6.97
β [110]	X	5.95	0.06	0.09
	Y	0.06	5.95	-0.09
	Z	0.09	-0.09	6.49
β [111]	X	5.90	0.00	-0.10
	Y	0.00	5.88	-0.05
	Z	-0.10	-0.05	6.78

The reduced mass (m_{ex}) calculated from our *ab initio* calculation is 0.09 m_0, close to the experimental value (0.12 m_0[167], 0.11 m_0[168], and 0.15 m_0[169]). The small exciton separation energy will promote charge separation, and increase their solar cell's working current.

The static dielectric constant, and effective mass averaged over different directions change little on rotation of the MA^+ ion, so we expect little change in the exciton binding energy across the energy landscape. More importantly, our results are consistent with experimental evidence that the formation of exciton is not a significant performance limiting process.

2.3.6 Polarization due to motion of the lead ions

A typical perovskite material has a formula expressed as ABX_3. B is the atom at the center of the octahedron, whose movement is usually considered as the mechanism of polarization for a ferroelectric perovskite. For $MAPbI_3$, B is the lead ion. First, we discuss the possible polarization due to lead atoms, which is estimated from the change in dipole moment of the unit cells as the lead atom relaxes from the center of its iodide coordination octahedron. The energy of the relaxed structure is slightly lower than

Table 2.6: The lead ions displacement ($\Delta\mathbf{r}$) and the dipole moment differences ($\Delta\mathbf{M}$) between the structures with or without lead ion relaxed for β phase $MAPbI_3$.

Initial MA^+ orientation	$\Delta\mathbf{r}$ (Å)	$\Delta\mathbf{M}$ (e Å)	$\lvert\Delta\mathbf{P}\rvert$ ($\mu C/cm^2$)
$\beta[00\bar{1}]$	(0.15,0.20,0.07)	(-0.01,0.18,-1.86)	3.0
$\beta[\bar{1}\bar{1}0]$	(0.04,0.18,0.15)	(-0.70,-1.11,-0.65)	2.3
$\beta[\bar{1}\bar{1}1]$	(0.21,0.07, -0.02)	(-1.03,-0.47,-0.86)	2.3

Table 2.7: Average MA^+ vector changes ($\Delta\mathbf{r}$) and dipole moment difference ($\Delta\mathbf{M}$) for the β phase $MAPbI_3$, MA^+ ion orientating from $[\bar{1}\bar{1}0]$ or $[\bar{1}\bar{1}1]$ to [001]

Initial MA^+ orientation	$\Delta\mathbf{r}$ (Å)	$\Delta\mathbf{M}$ (e Å)	$\lvert\Delta\mathbf{P}\rvert$ ($\mu C/cm^2$)
$[\bar{1}\bar{1}0]^{a)}$	(-0.94,-0.32, 1.19)	(1.43,-1.44,-3.44)	6.40
$[\bar{1}\bar{1}1]^{b)}$	(-1.02, 0.22, 1.84)	(2.12, 0.49,-4.54)	8.06

[a)]Calculated with center at (0.35, 0.86, 0.50); [b)]Calculated with center at (0.35, 0.85, 0.50).

that of the structure with lead fixed. Table 2.6 shows the average displacement of the four lead atoms and the dipole moment difference between geometries with or without lead atom relaxed in the β phase $MAPbI_3$, with different MA^+ ion orientations. The polarization change on the relaxation of the lead ions is roughly a half or a third of that obtained by rotation of MA^+ (see below). There is no obvious relation between the polarization direction and the average lead atoms displacement. This effect is due to the coupling of MA^+ to the inorganic component of the crystal.

2.3.7 Polarisation due to rotation of the MA^+ ion

MA^+ ion has a dipole moment in its gas phase of 2.29 Debye,[104] and we can not rule out the possibility that the crystal polarization is mainly contributed by the MA^+ ion. To study its polarization properties, the Berry phase of these crystals with differently oriented MA^+ have been investigated. Table 2.7 shows the dipole moments of these unit cells. In this part of calculation, lead atoms are fixed in order to eliminate their influence. As four MA^+ are on the boundary of the β phase unit cell, to calculate the dipole moment change, we need to choose a boundary not crossed by any ion. Generally, if we select a center so that there is not much electron cloud or ions crossing the cell's boundary, the dipole moment change of the cell is proportional to change in the MA^+ ion carbon-nitrogen bond vector. As shown in Table 2.4 Born charges on the inorganic frame change as MA^+ ion rotates. This coupling between inorganic

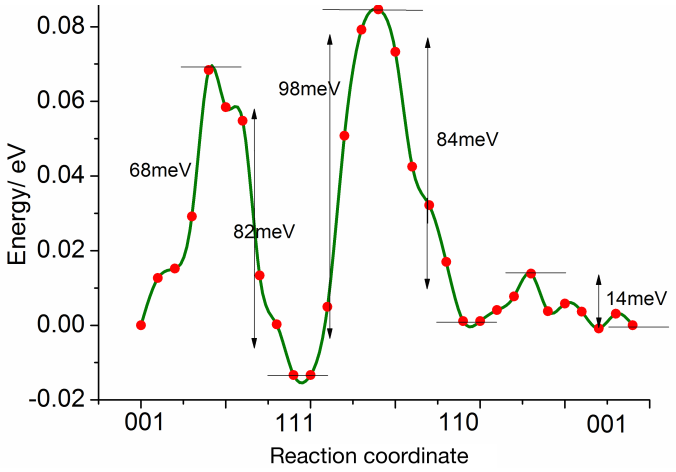

Figure 2.5: The energy landscape of MA^+ ion rotates in representatives orientations in the α unit cell.

and MA^+ make it impossible to get a perfect linear relationship between the MA^+ ion orientations and the dipole moments of their unit cells. The polarization induced by MA^+ ion rotation is two or three times larger than the polarization induced by the lead atom. Therefore, we can draw a conclusion that the polarization of $MAPbI_3$ is controlled by the MA^+ ion, but the coupling between these two is strong, and the role of the inorganic frame cannot be neglected. This is the second point of the argument that the rotation of MA+ is able to polarize the material.

2.3.8 Barriers to methylammonium ions rotation

The direction of spontaneous polarization in a ferroelectric depends not only on the field but also on polarization history. As energy differences between structures in the energy landscape with differently oriented MA^+ are about the thermal energy at room temperature (25 meV), MA^+ can rotate at room temperature (see Figure 2.5 and Table 2.1). If the energy barrier for rotating MA^+ ion is high, the rotation will be slow, and then the polarization of MA^+ ion cannot in a practical period of time be tuned by external electric field. To determine the energy barrier for MA^+ ion reorientation, cNEB calculations have been performed.[158] We estimated energy barriers for the MA^+ ion rotated between [001], [110] and [111] directions in the α phase at first. The α phase unit cell only has one MA^+ ion. When it rotates, the neighbouring MA^+ in the periodic images of the cell are also rotated. For α phase, the energy barrier is about 14 meV for a MA^+ ion rotates between [001] and [011], which is lower than kT. The largest two energy barrier are for [111]-MA^+ ion rotation to [001] and [011], 82 meV or 98 meV, respectively, shown in Figure 2.5. Even the largest

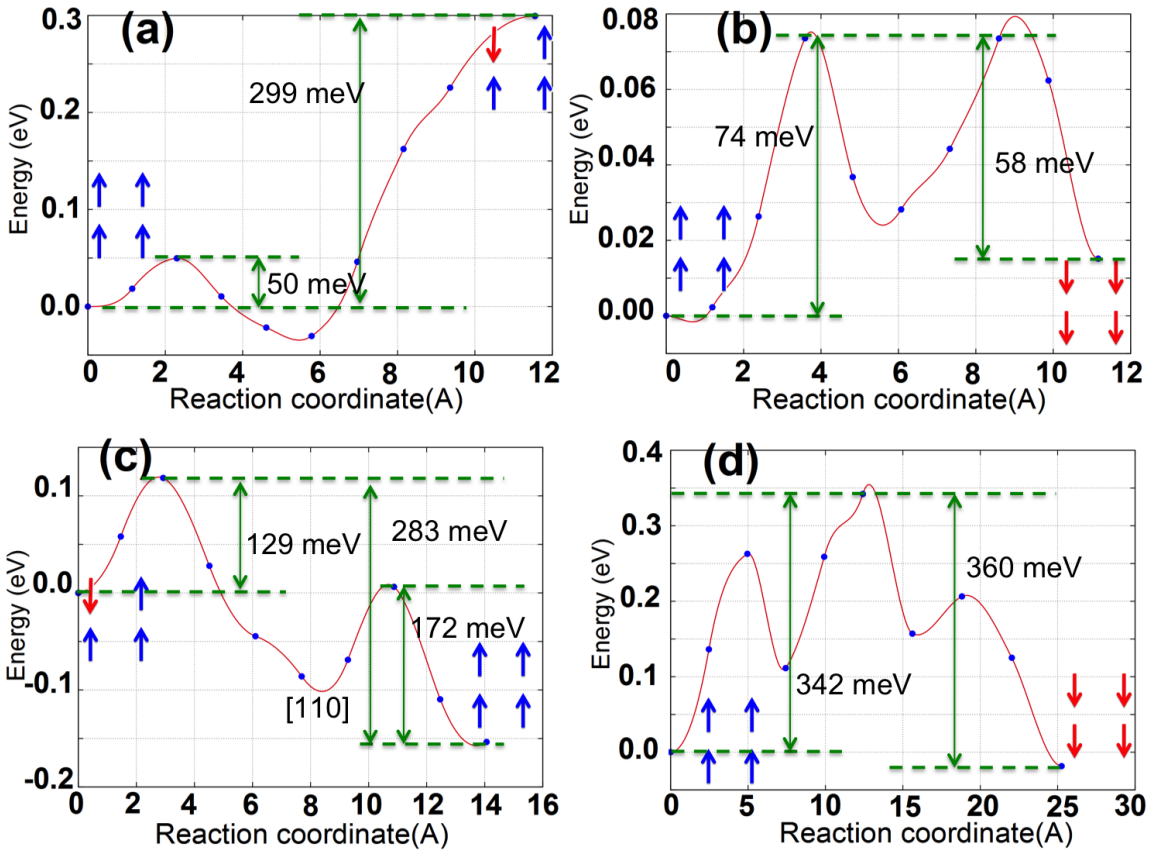

Figure 2.6: The energy landscape of MA^+ ion flip over c axis in α and β phase. The energy landscape of independent MA^+ ion rotation of α phase (a) and of β phase (c); The energy landscape of collective MA^+ ion rotation of α phase (b) and of β phase (d). The energy in (b) is the energy landscape per MA^+ ion. Arrows in the figure represent MA^+ orientations.

energy barrier is only four times higher than kT, so the MA^+ can rotate collectively at room temperature.

Ferroelectric response favours collective polarization, and so we also calculate the energy barrier of orientations of a single MA^+ ion with either its neighbours fixed or moving in parallel. This comparison is shown for both the α and β phases in Figure 2.6. We choose the MA^+ ion rotation from [001] to [00$\bar{1}$]. For the α phase, the collective energy barrier for one MA^+ ion is 74 meV, as shown in Figure 2.6(b). For independent rotation, the barriers are about zero if the start MA^+ ion configuration anti-parallel to surrounding MA^+, where the reaction coordinate(RC) $\approx$ 12 Å. If MA^+ ion starting configuration is parallel to surrounding MA^+ (RC $\approx$ 0 Å), the barrier is about 300 meV, as shown in Figure 2.6(a). These results suggest that MA^+ in the α-phase have a kinetic preference to be arranged in parallel.

For independent rotation in the β phase, as shown in Figure 2.6(c), the MA^+ ion rotates from [001] ($RC \approx 14$ Å) to about [110] ($RC \approx 8$ Å), with an energy barrier of 172 meV. If this MA^+ ion rotates further to $[00\bar{1}]$ ($RC \approx 0$ Å), the total energy barrier is as high as 283 meV. While if the MA^+ ion was oriented to $[00\bar{1}]$ ($RC = 0$ Å) and the neighbouring MA^+ vectors are [001], the energy barrier is smaller, but still high compared to that of the α phase. Hence, the energy barrier to flip a MA^+ ion is 129 meV if the MA^+ ion is initially anti-parallel to the neighbouring MA^+, and becomes as high as 283 meV if the MA^+ ion is initially parallel to the neighbouring MA^+. The concerted rotation barrier for one MA^+ ion is 80-90 meV, which is higher than that (60 -70 meV) rotated in the α phase. We expect collective reorientation to be slower in the β phase in agreement with experiment.[161]

These results show MA^+ ions are coupled each other. On one hand, the energy barriers in the α are lower than these in the β phase, which is likely due to the inorganic framework is smaller in the β phase.[8] On the other hand, energy barriers of independent rotations in the β phase are higher than energy barriers of collective rotation per MA^+ ion, which indicates that MA^+ kinetically prefer the parallel arrangement in both phases.

These low energy barriers also indicate that MA^+ ion orientation responds to the external field. An energy barrier of 100 meV corresponds to 9.6 kJ/mol, which is in agreement with the low-temperature experimental activation energy 9.7 kJ/mol.[170] The dipole moment of the MA^+ ion in the gas phase is estimated at $\mathbf{M} = 2.29$ D.[69] We find a change in polarization on rotation of the MA^+ ion from [001] to $[\bar{1}\bar{1}0]$ is about $\Delta\mathbf{M} \approx 5$ D (shown in Table 2.7, it is 20 D for four MA^+). This includes the response of all the electrons, and the relaxations of the ions described above. The energy change on rotating a dipole by 90° in an electric field $\mathbf{E}$ is $|\Delta\mathbf{E}| = |\mathbf{M}|\cdot|\mathbf{E}|$. The barriers of rotation are not exactly at 90°, but this provides a convenient comparison of energy magnitudes. The field required to change the energy of a 2.29 D dipole by 100 meV on 90° is 2.1×10^7 V/cm, and for a 5 D dipole 1.0×10^7 V/cm. Note that these fields are the 'cavity' fields experienced by the MA^+ ion or the unit cell. For comparison the fields experienced by the perovskite layer at various times in its history are close to 1.0 V/300 nm = 3.3×10^4 V/cm. Here, we assume the probability of a MA^+ to rotate is the exponential of $\frac{E_d - E_b}{kT}$, where E_d is the energy of dipole moment change, E_b is the energy barrier and the kT is its thermal energy. If there energy barrier is 100 meV and kT= 25 meV and E_d=1 meV for 5 D dipole moment in a field of 3.3×10^4 V/cm, the probability is 1.9 %. For smaller energy barriers, the probability is larger. This is the first point arguing that MA+ can rotate under

operating field conditions. We conclude that significant electric fields, or sufficient times to overcome barriers, are needed to produce a polarization that may influence performance.[37, 36] This is consistent with the observed slow hysteresis behaviour discussed above.

2.3.9 Polarization, efficiency and hysteresis

We have found above relatively modest changes in electronic structure with MA^+ rotation. This argues against the first possible mechanism that reorientation of the MA^+ ion affects performance by direct modification of electronic structure. The more likely macroscopic mechanism coupling polarization to performance is illustrated in Figure 2.1. We examine here this macroscopic mechanism, that accumulated charges in charge transfer layers can induce a field that hinders charge transport, and that performance is improved when the polarization screens this hindering field, denoted above $\mathbf{E}_0$. The field produced by the polarization of $MAPbI_3$ (red in Figure 2.1), together with the capacitive charge (blue in Figure 2.1) induced field, counteract the hindering field, promoting charge transport, and improving PCE. The slow polarization rates contribute to slow hysteresis behaviors.

In the α phase, energy differences between the 001-, 110- and 111- $MAPbI_3$ structures are lower than 20 meV, and energy barriers for collective MA^+ ion reorientation are smaller than 100 meV, shown in Table 2.1. Based on these results, under normal conditions, the MA^+ in the α phase $MAPbI_3$ are likely disordered overall.[159] For the β phase, both energy differences and energy barriers become slightly higher, so that MA^+ rotate less freely and more slowly. At room temperature, experiments show MA^+ ions are dynamically disordered,[159, 160, 161] but the material is ferroelectric.[8, 108, 78] The low energy barriers mean that applied fields could rearrange MA^+ ions. As MA^+ controls the dipole moment of unit cell both of the α and β phase, an external field rearranging MA^+ ions can tune the polarization of $MAPbI_3$.

Here we examine whether or not the polarization field is strong enough to cause hysteresis in hybrid perovskite solar cells. If we take the polarization difference from MA^+ rotation ($\Delta\mathbf{P}$) as the polarization (shown in Table 2.7) induced by external fields, then the polarized field should be $\mathbf{E} = \frac{\Delta\mathbf{P}}{\epsilon_0(\epsilon_r-1)} = 3.6 \times 10^8$ V/m, where ϵ_r is the low-frequency relative dielectric constant, about 25.[63] This field is about 100 times higher than the hindering field ($\mathbf{E}_0 \approx 3.3\times10^6$ V/m) under operating conditions. This suggests that only a few part of polarized MA^+ is enough to screen the hindering field. Assuming MA^+ ion alignment follows the Boltzmann distribution, the number

of aligned MA^+ is related to its potential energy, $-\mathbf{M}\cdot\mathbf{E}$, where $\mathbf{M}$ is the dipole-moment of the MA^+. We assume only six orientations (one parallel to the field, four perpendicular, and one antiparallel) are possible. Assuming it is measured at 1 V/s scanning speed, in Ref [70] Figure 1a, as an example, trapped charges are able to de-trap, and the capacitive screening field is able to respond to the hindering field. Energies for MA^+ aligning along six directions are $|\mathbf{M}|\cdot|\mathbf{E}|$, zero and $-|\mathbf{M}|\cdot|\mathbf{E}|$ respectively. If the total field $\mathbf{E} = 5.67\times10^5$ V/m, Boltzmann ratios are then $\exp(2|\mathbf{M}|\cdot|\mathbf{E}|/kT) : 4\times\exp(|\mathbf{M}|\cdot|\mathbf{E}|/kT) : 1.00 = 1.005 : 4\times1.002 : 1.00$. The net percentage of the polarized MA^+ is therefore about $\frac{1.005-1.00}{1.005+4\times1.002+1} = 0.08\%$. The net polarized charge density ρ is about 6.4 μC/cm^2 $\times$ 0.07 % = 0.0048 μC/cm^2. In a parallel-plate capacitor, the field can be estimated as $\mathbf{E}_p = \rho/\epsilon_0\epsilon_r = 2.58\times10^5$ V/m, which is about half of the total field of 5.67×10^5 V/m For the same reason, we estimated screening field is about 5.61×10^5V/m for the operating hindering field of 2.17 $\times10^6$ V/m. The screening field can screen about one fourth of the total field.

The mechanism illustrated in Figure 2.1 requires that ferroelectric polarization cancels partly the hindering field. The polarization changes calculated here are consistent with this mechanism, and we conclude from these calculations that rotation of the MA^+ is likely responsible for the hysteresis and performance characteristics. We note also that the dipole moment is not limited to the MA^+, and includes contributions from inorganic ions and electron rearrangement. This is third point, that polarization can induce a screening field that agrees with a measured compensated field.

Based on three points, the compensated field observed in experiment comes from the polarization of MA+ ions and capacitive charges. Normal hysteresis, seen for example in a DSC, increases with shorter delay times, due to the relaxation of capacitive charges accumulated at interfaces (including trapping and de-trapping). Both capacitive charges and bound charges play roles in hybrid perovskite solar cells. On the increase of scanning speed, hysteresis appears when the charge structure cannot relax quickly enough to keep up with the scan, and then disappears when the charge structure changes hardly during the scan. The collective rotation of MA^+ is low (at that time, we don't which one is faster and which one is slower. Now it is proved that the capacitive charge relaxed more slowly than polarization.), and when the scanning speed high, the polarization bound charge cannot respond, so capacitive charge dominates hysteresis. For such scanning rates, shorter delay times lead to stronger hysteresis, in agreement with experiment.[36, 37, 142, 50, 70] The capacitive charge relaxation times are usually between 1 ms to 100 ms in silicon based solar cells

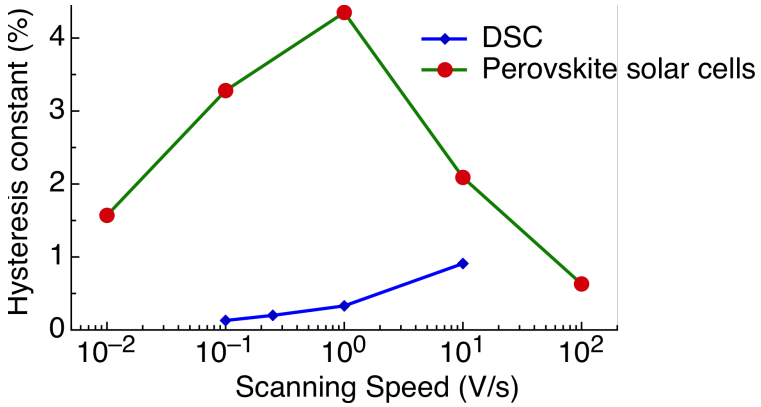

Figure 2.7: The dependence of the hysteresis of solar cells' performance and scanning speed. Hysteresis constant is defined as $PCE_{max}^{backward} - PCE_{max}^{forward}$. A peak hysteresis is exist when scanning speed increases.

(around 1 ms) and DSC (around 1-100 ms).[138, 139, 171, 140, 141] No hysteresis occurs when the delay times are significantly larger than this relaxation.

A long delay time, such as 1 s, eliminates the hysteresis induced by capacitive charges, but MA^+ ions are still unable to be fully polarized under this delay time due to the large polarization relaxation time of 1-100 s.[70, 50, 41, 51, 48] In this case, the polarization charges dominate their hysteresis. Hence, for scanning delay times longer than capacitive charge relaxation time, and shorter than the relaxation time of polarization charges, we expect significant hysteresis in agreement with experiments.[70, 51] Figure 2.7 shows a measured[70] peak in hysteresis for $MAPbI_3$ cells near the relaxation time seen in experiments, at 1 s to 100 s, along with analogous data for a DSC.[138] We conclude that the slower hysteresis, seen to grow with lower scan rates,[51, 70] is due to polarization by reorientation of MA^+, and the faster hysteresis, seen to grow at higher scan rates,[36, 37, 142, 50, 70] is due to the same capacitive charge that produces hysteresis in DSCs.

Figure **1a** in the paper by Tress *et al.*[70] shows a series of J-V curves of a hybrid perovskite solar cell under different scan rates. They illustrate the connection between relaxations and PCEs. They start measurement with the voltage of 1 V, where the cell is fully polarized in the direction promoting charge transport. For fast scanning, 10 V/s and 100 V/s, the polarization field is unable to decay. Therefore, higher PCEs occur with higher scanning speeds. When the voltage reaches -1 V and then increases to 1 V, for a high scanning speed, the polarization state is unaltered, so there is no change for its performance. For a slow scan speed, the relaxation is able to respond. The polarization field prefer to align in the direction hindering charge transport when

the voltage reaches -1 V and then increases to 0 V. Thus, lower PCEs are expected in the sweep direction from -1 V to 1 V. Hysteresis will be observed, as illustrated in Figure 2.7.

2.4 Conclusions

We calculated electronic properties with MA^+ oriented to three representative directions, in phases above and below the phase transition, and the heights of energy barriers between these structures. Little change was found between the two phases near room temperature. Thus $MAPbI_3$ solar cells work stably near or through phase transition point. We compared collective reorientation of all MA^+ in the crystal, as in a ferroelectric's spontaneous, macroscopic polarization, to the reorientation of a single MA^+ ion with its neighbours fixed. Two possible mechanisms for the influence of MA^+ orientation in $MAPbI_3$ on photovoltaic performance are examined.

The first possible mechanism is that reorientation of MA^+ directly affects the electronic structure, and so directly affects the creation and transport of electronic excitations. We found only modest changes in their band gap, relative permittivity, and most other electronic properties on rotation of MA^+. We do see that some of the effective masses vary a lot due to the conduction band bottoms change drastically as the MA^+ ion rotates, but found the overall pattern of effective masses changes little.

The second possible mechanism is that bound charges due to the polarization of perovskite, controlled by the collective orientation of MA^+ in part cancels the hindering field due to the accumulation of carriers at charge transfer layers. This 'macroscopic' mechanism is illustrated in Figure 2.1. The field arising from polarization, together with that of charge carriers accumulated at interfaces, counteracts the hindering field, and promotes charge transport. Capacitive charges and polarization bound charges are also observed in experiments and proved to promote charge transport.[137, 70]

We found significant polarization changes on reorientations of MA^+. Though not all changes in dipole moment are due to the reorientation of these cations, their configuration does dominate the polarization. Relaxation of lead ions contributes less than one half of the change produced by MA^+ reorientation. The calculated polarization changes are large enough to influence charge transport and so performance of a photovoltaic. The rotation energy barrier of a MA^+ ion, in the α or β phase of $MAPbI_3$, depends on orientations of neighbouring MA^+. If all the MA^+ ions rotate in concert, rotation barriers are lower than 100 meV per ion. If only one ion rotates

with its neighbours fixed, the energy barrier can be as low as 10 meV, also can be as high as 300 meV, depending on the direction of rotation. The MA^+ in $MAPbI_3$ prefer to rotate collectively, and to be parallel to their neighbours. These results are consistent with the measured ferroelectricity of the materials.[8, 108, 78] We further found that energy differences between states of different polarization, and energy barrier heights between different states, are low enough that reorientation is possible under the operating conditions of a photovoltaic with $MAPbI_3$ as the absorbing layer, and on relevant time scales.

We interpreted the anomalous hysteresis in hybrid perovskite solar cells due to relaxations of polarization and capacitive charges. The overall hysteresis is dominated by the time scales of the scanning rate of measurement, the relaxation time of polarization and the relaxation time of ion migration. In Chapter 5, the dynamic simulation of MA^+ polarization and ion migration were designed and performed. Results show that the relaxation time of ion migration is in the range of ms to s with good agreement with experiments. However, the relaxation time of MA^+ polarization is approximately μs, which is much shorter than the delay time in experiments. Hence, we could say that the hysteresis in PSCs is produced by ion migration.

Taken together with the experimental observation of slow relaxation times, and of hysteresis, our calculations of the MA^+ rotation energy changes, barrier heights, and polarization responses show that collective MA^+ rearrangement and ion migration strongly influences power conversion efficiency.

Chapter 3

A numerical model for charge transport and energy conversion of PSCs

3.1 Introduction

In chapter 2, basic electronic properties of the β and α phase $MAPbI_3$ have been systematically discussed. However, how these basic electronic parameters affect output characters is unknown. To connect the basic electronic parameters to the output performance, a numerical model is required. Structural and electronic properties of different phases of $MAPbI_3$ also have been discussed.[64, 67, 63, 52] They attribute the high performance to the low band gap and large static dielectric constant. Frost *et al.* have suggested that transport along domain boundaries makes polarization improve performance.[104, 69] We studied the energy landscape of $MAPbI_3$ and found that polarization makes a positive contribution through screening.[52] Although these theories have shown that perovskite materials have good electronic properties, it is still not fully understood how these properties affect light harvest and charge movement in its solar cells. To make this clear, numerical simulations are needed. Using the numerical model reported below, we can analyze how basic electronic parameters directly and quantitatively play roles in solar cells.

Numerical simulations for silicon solar cells have been used for more than 40 years.[172, 173, 81] In the late 1970's, computer-aided numerical analysis of silicon solar cells was developed by solving Poisson's equation and the hole and electron continuity equations.[172] The effect of interface states on high-performance amorphous silicon solar cells[174] and the effect of electrical mismatches in photovoltaic cell interconnection circuits have been discussed in detail.[175] The PC1D program

was distributed by UNSW,[173, 81] it is widely used for silicon solar cell analysis and optimization, such as modeling of free-carrier absorption,[81] enhancement of optical absorption,[82] wafer thickness optimization[83] and optimization of device structure.[84] Numerical models for Dye Sensitized Solar Cell (DSCs) and Bulk Heterojunction (BHJ) organic solar cells are also developed.[85, 86, 87, 88, 89, 90, 91, 92, 93] With these numerical methods, details of charge movement in solar cells and how a factor affects solar cells performance are revealed. These models help us to understand its mechanism and optimize its fabrications.

However, these models for silicon solar cells and DSCs are unable to describe the mechanism in PSCs. The model developed for silicon solar cells is based on doping that forms a p-n junction. Dopant density and its distribution determine solar cell's performance, especially the output voltage.[93] The model for DSCs involves solvent, which conducts ions and current. Additionally, its output voltage depends on the redox level in electrolytes.[90] For PSCs, the output voltage is dependent on the electron and hole quasi-Fermi energy levels at corresponding electrodes, with no relation to dopants nor redox level. Its charge carriers are photon-generated holes and electrons, no solvent ion migration contributes to current. The applied voltage is determined by the difference of quasi-Fermi energy levels at perovskite two sides.

There has been a number of recent developments for numerical simulation of PSCs. Liu *et. al*, using a general solar cell simulation program – AMPS-1D, show PSC's PCE dependence on thickness, defect density and charge mobility of its perovskite layer.[94] As we have discussed, a general model is unable to describe the charge transport behavior and mechanism in PSCs exactly. Assuming the electric field in the whole solar cell is constant and using general equations, Sun *et. al* obtain an analytical solution.[95] But their assumption contradicts the fact that the electric field in a real solar cell is not constant. Additionally, though they obtain analytic solutions, parameters they used are obtained from the fitting of experiment I-V curves, which is more about fitting rather than prediction. Foster *et. al* developed a numerical model with specific parameters and physics for PSCs.[96] It is perhaps the best model up to now, but it has problem in solving equations. Not only are many parameters unable to be obtained from experiment directly, but also they meet the difficulty of solving their equations with physically realistic parameter values. Reenen *et. al* proposed a model to explain the hysteresis in PSCs based on time evolution.[77] Although they could explain the hysteresis, their results are in poor agreement with quantitative measurements in Tress' experiments.[70] Here, we are going to introduce a new model for PSCs. Most of our equations are the same with Foster's models, but

non-uniform generation and more recombination mechanisms are implemented in our model. Most importantly, there is not any problem with solving our equations with physically realistic parameter values.

In this part, we build up a numerical solar cell model for PSCs based on the Continuity equations and the Poisson's Equation. Most of our equations are the same with Foster's models, but also includes non-uniform charge carrier generation, more reasonable output potential, and more recombination mechanisms. Most importantly, the model is compatible with solving our equations with physically realistic parameter values. We first describe our equations and methods. Very specific details are given in the Methods section and Appendix B. Using this model, we studied PSC performance's dependencies of various factors, such as light intensity, charge carrier's lifetime and mobility, to their performances including V_{oc}, J_{sc} and PCEs. These dependencies give us guidelines on how to design and optimize PSCs.

3.2 Methods

3.2.1 Semiconductor physics in PSCs

In PSCs, charge carriers include electrons and holes. Both of their diffusion and their drift contribute to the output current. For hole transport, if the hole density is p, the current induced by hole is given by:

$$J_p = J_{diffusion} + J_{drift} = -eD_p\frac{\partial p}{\partial x} + ep\mu_p F \tag{3.1}$$

where e is the elementary charge, F is the electric field and D_p is the hole diffusion coefficient, μ_p is the hole mobility. In this work, we estimate mobilities from diffusion coefficients through Einstein relation ($\mu = \frac{eD}{kT}$). For electron transport, we have

$$J_n = eD_n\frac{\partial n}{\partial x} + en\mu_n F \tag{3.2}$$

where, n is the electron density. D_n is the diffusion coefficient of electrons. In this part, 0.017 cm^2s^{-1} and 0.011 cm^2s^{-1} are used for D_n and D_p, which come from Stranks' experiment[29]. There are different diffusion coefficient reported in other experiments, such as 0.036 cm^2s^{-1} and 0.022 cm^2s^{-1}.[28] The diffusion coefficient in optimized solar cells can be as high as 1.5 cm^2s^{-1} according to the mobility of 60 $cm^2s^{-1}V^{-1}$.[176, 177, 178, 179] For mobility dependence calculation, D_n and D_p are set at certain times higher than 0.017 cm^2s^{-1} and 0.011 cm^2s^{-1}.

Conservation of charge carriers leads to the Continuity equation:

$$e\frac{\partial n}{\partial t} = \frac{\partial J_n}{\partial x} + eG - eR \tag{3.3}$$

For a steady state, charge density is constant: $\partial n/\partial t$=0. Therefore, we have:

$$\frac{\partial J_n}{\partial x} = -eG + eR \tag{3.4}$$

$$\frac{\partial J_p}{\partial x} = eG - eR \tag{3.5}$$

where G and R are the generation rate and recombination rate, respectively. The electric field is solved by Poisson's equation,

$$\frac{\partial F}{\partial x} = e\frac{p-n}{\varepsilon\varepsilon_0} \tag{3.6}$$

Generally, we have five equations: Equation (3.1), (3.2), (3.4), (3.5) and (3.6). These five equations are used to solve five parameters: n, p, J_p, J_n and F. As all of these equations are the first order differential, five boundary conditions are needed. At the photon-anode, $x = 0$, TiO_2 layer side, only electron can get out, thus $J_p|_{x=0} = 0$. For the same reason, we have $J_n|_{x=d} = 0$ for photon-cathode. Then, the current boundary conditions are,

$$\begin{aligned} J_n|_{x=d} &= 0 \\ J_p|_{x=0} &= 0 \end{aligned} \tag{3.7}$$

Other boundary conditions are electric field strengths at two boundaries and the applied voltage between two boundaries.

$$\begin{aligned} F_{x=0} &= F_0 \\ F_{x=d} &= F_d \end{aligned} \tag{3.8}$$

A built-in electric field reduces overall electric field within dielectric itself, when a dielectric matter is placed in an external field. A screening field is built up by capacitive charges, such as charged defects and charge in traps. It is difficult to determine the specific boundary field due to the presence of TiO_2 and Spiro-OMeTAD layers and interface states. There are two extreme cases. One extreme case is that the built-in and screening field is stronger enough, F_0=F_d=0. The other extreme case is that there is no built-in and screening field at all, F_0=F_d=V/d, if the field in perovskite is uniformly distributed. For a real solar cell, boundary fields should be between zero and V/d. In this paper, without specific notation, the field boundary conditions are F_0=F_d=V/d. For more complex situations, we will discuss it elsewhere.

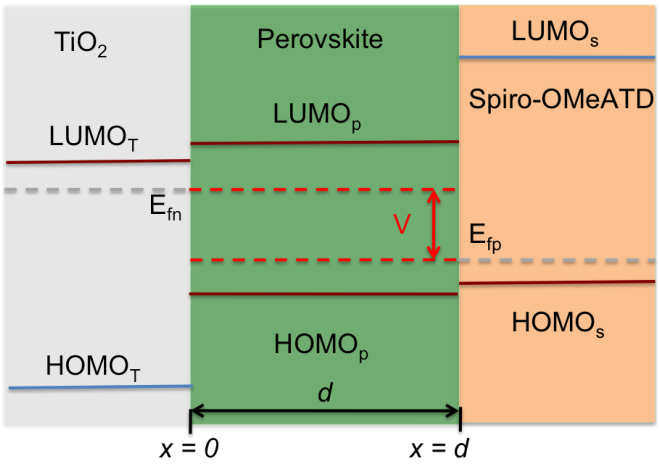

Figure 3.1: Energy levels of TiO_2/$MAPbI_3$/Spiro-MeOTAD solar cells. The output voltage of a solar cell is the potential difference between the electron Quasi-Fermi level at $x = 0$ and the hole Quasi-Fermi level at $x = d$. $V = E_{fn}|_{x=0} - E_{fp}|_{x=d}$. The electron Quasi-Fermi level in TiO_2 layer is the same with it in perovskite layer. The hole Quasi-Fermi level in the Spiro-OMeATD layer is the same with it in perovskite layer.

The output voltage of a PSC is the potential difference between the electron Quasi-Fermi level at $x = 0$ and the hole Quasi-Fermi level at $x = d$. $eV = E_{fn}|_{x=0} - E_{fp}|_{x=d}$ (Figure 3.1), where these Fermi levels satisfy: $n|_{x=0} = N_c e^{\frac{E_c - E_{fn}}{-kT}}$ and $p|_{x=d} = N_v e^{\frac{E_v - E_{fp}}{kT}}$, where N_c and N_v are the DOS of the conduction band and the valence band, respectively. Hence, the applied voltage can be expressed as:

$$\begin{aligned} eV &= E_{fn} - E_{fp} = E_c + kTln(\frac{n|_{x=0}}{N_c}) - (E_v - kTln(\frac{p|_{x=d}}{N_v})) \\ &= E_{bgap} + kTln(\frac{n|_{x=0}}{N_c}) + kTln(\frac{p|_{x=d}}{N_v}) \end{aligned} \tag{3.9}$$

For an intrinsic semiconductor, its Fermi level locates at the center of the gap between the conduction band and the valence band. It requires $N_c = N_v$ to keep semiconductor neutral. In our simulation, $N_c = N_v = 3.97 \times 10^{18}$ cm^{-3}, which is estimated from our DFT DOS calculation.[52] The calculation details will be given in Chapter 6. Therefore, the applied voltage is implemented as charge densities at two boundaries:

$$n|_{x=0} p|_{x=d} = N_c N_v e^{\frac{E_{bgap} - eV}{-kT}} \tag{3.10}$$

With these five equations and five boundary conditions, the solution is determined.

3.2.2 Generation rate and recombination rate

The first process in solar cells is the photon absorption–exciton formation–exciton separation. We name this process as photon-induced charge carrier generation, which can be expressed as $G = IPCE \times I_0$, where IPCE is the Incident Photon-to-Current Efficiency and I_0 is the light incident density. Incident density decreases as photons going through a medium. The generation rate is a function of depth (x) from the surface:

$$G(x) = \int_0^{\lambda_0} G(\lambda, x)d\lambda = \int_0^{\lambda_0} IPCE(\lambda) \times I(\lambda) \times \alpha(\lambda) \times e^{-\alpha(\lambda)x}d\lambda \tag{3.11}$$

where λ is the wavelength and λ_0 is the absorption edge. α is the absorption coefficient, which is set as 5.7×10^4 cm^{-1} for photons with wavelength shorter than λ_0. It is the experimental value at λ= 500 nm.[28]. For good PSCs, $IPCE$s for photons with wavelength shorter than λ_0 are usually higher than 80%.[24, 37, 180, 34] It is worth noticing that the $IPCE$ difference between experiment and Equation (3.11). In the calculation of experiment $IPCE(\lambda) = \frac{Current}{Incident\ light\ density(\lambda)}$, which counts unabsorbed photons in. The relation between experiment and our $IPCE$ is $IPCE(\lambda)_{exp} = IPCE(\lambda)_{theory} \times \int_0^d \alpha(\lambda)e^{-\alpha(\lambda)x}dx < IPCE(\lambda)_{theory}$. Without an infinite thickness perovskite layer, $IPCE$ in theory should be higher than experimental $IPCE$. Hence, it is reasonable to set theoretical $IPCE(\lambda) = 100\%$ based on experiment value of 80%. This assumption means each absorbed photon transferred into one pair of electron and hole.

Experimental band gap of $MAPbI_3$ differs in experiments, it is in the region from 1.45 eV to 1.70 eV.[58, 25, 8, 1, 59, 60] To have a direct comparison with Zhou's experiment I-V curve, a band gap of 1.55 eV from Zhou's experiment is used.[1] $I(\lambda)$ is calculated from AM 1.5 spectrum provided by NREL.

When charges move, electrons and holes attract each other and try to combine. Recombination of free charge carriers in materials with low defects concentration and low mobility is often described with direct recombination. According to Langevin theory, the charge recombination rate is proportional to the electron density and the hole density:[181, 96, 182]

$$R = r \times (n \times p - n_i^2) \tag{3.12}$$

r is the recombination coefficient and $n_i = N_c \times exp(\frac{-E_{gap}}{2kT})$, is the intrinsic carrier concentration. As the band gap is big comparing to thermal energy (kT), the intrinsic charge carrier density is very low compared to photon generated charge carrier

densities. Recombination also could happen through traps and defects, which can be described by the Shockley-Read-Hall (SRH) theory: [183, 184, 93]

$$R = \frac{np - n_i^2}{\tau_p(n + n_1) + \tau_n(p + p_1)} \tag{3.13}$$

τ_p and τ_n are lifetimes for hole and electron, respectively. While, n_1 and p_1 are dependent on the energy levels of the recombination centers: $n_1 = N_c exp[-(E_C - E_d)/(kT)]$ and $p_1 = N_v exp[(E_V - E_d)/(kT)]$. They are equilibrium electron and hole concentrations in a sample whose Fermi level coincides with the position of recombination centers. Due to its large band gap ($np >> n_i^2$) and benign defects ($n_1 << n$, $p_1 << p$), Equation (3.13) goes to:

$$R = \frac{n \times p}{\tau_p n + \tau_n p} \tag{3.14}$$

which is also used in DSCs modeling.[87, 90] In our model, we assume that lifetimes of hole and electron are the same due to limited experiment values.

3.2.3 Methods to solve partial differential equations

The numerical solution is computed using the method recommended for 'Two Point Boundary Value Problems' in *Numerical Recipes in Fortran*.[185] It should be noted that the simple shooting method with classical Runge-Kutta yields poor convergence and performance, as the charge density ranges across several magnitudes from 10^{10} cm^{-3} to 10^{18} cm^{-3}. The method set out in *Numerical Recipes* is further adapted so that the array *scalv* is variable rather than constant, to accommodate the range of charge density. For more details, please refer to information provided in Appendix B and the Chapter 17 in *Numerical Recipes in Fortran*.

3.3 Results

3.3.1 Comparison of two typical recombination mechanisms

There are two possible recombination mechanisms, one is direct recombination, which follows Equation (3.12); another is indirect recombination through defects, which follows the SRH model, shown as Equation (3.14). Direct recombination happens in intrinsic bulk materials without defects, while, indirect recombination happens at bulk defects or surfaces and interfaces. In Xing's experiment, the lifetime is measured to be about 5 ns without charge transport layer, it decreases to 0.37 ns and 0.64 ns by

Table 3.1: Parameters used to simulate PSCs.

Symbol	Meaning	Value
$IPCE$	IPCE	100%
E_{bgap}	Band gap	1.55 eV[1]
T	Temperature	300 K
τ	Lifetime	736 ns [1]
τ_{intf}	Interface lifetime	6 ns
I_l	Light intensity	1.5 AM
d	Perovskite thickness	350 nm[1]
F_0, F_d	Boundary Field	V/d
N_c, N_v	Density of States	$3.97 \times 10^{18} cm^{-3}$.[52]
α	Absorption coefficient	$5.7 \times 10^{4} cm^{-1}$.[28]
D_n	Electron diffusion coefficient	0.017 $cm^2 s^{-1}$. [29]
D_p	Hole diffusion coefficient	0.011 $cm^2 s^{-1}$. [29]
r	Recombination coefficient	$1.03 \times 10^{-9} cm^3 s^{-1}$*

*For direct recombination. The recombination coefficient (r) is estimated by fitting the experimental Photoluminescence decay, more details are available in Appendix B.

adding a PCBM or a Spiro-OMeTAD layer respectively.[28] In Stranks' experiment, the thin film thickness is 180 nm, which is about three times thicker than Xing's (65 nm), carrier's lifetime increases to 9.6 ns. The presence of interface in their experiment also decreases its lifetime to 3.17 ns or 4.2 ns.[29] Improved methods usually give longer lifetime. For a modified two-step deposited 280 nm thickness $MAPbI_3$ film without or with infiltrated mesoporous TiO_2, the measured lifetimes are about 200 ns (without) and 6 ns (with).[186] All of these experiments suggest that the presence of interface reduces lifetime significantly, especially in a very thin film. These experiments imply fast recombination occur at interfaces. Therefore, it is promising to refine interfaces states to increase PCEs. Zhou's work confirms our understanding.[1] They engaged with interface engineering and made solar cells with PCEs up to 19.3%, which was the highest PCE at that time. In their experiment, a thin film deposed on glass substrate shows lifetime about 382 ns and 736 ns. With this fact, the lifetime of intrinsic direct recombination should be about 736 ns. While the lifetime of interface recombination should be in the range of 0.1-10 ns, which is dependent on fabrication conditions, as illustrated in Ref[28, 29, 186].

Here, we simulate the highest performance solar cell in Ref 1 with these two recombination mechanisms. The first model is implemented with SRH mechanism. Its lifetime is set as 736 ns.[1] The second model, the recombination in solar cells is direct recombination, $R = rnp$. Parameters we used are shown in Table 3.1. Most of parameters come from the experiment did by Zhou *et al.*[1] Diffusion coefficients are

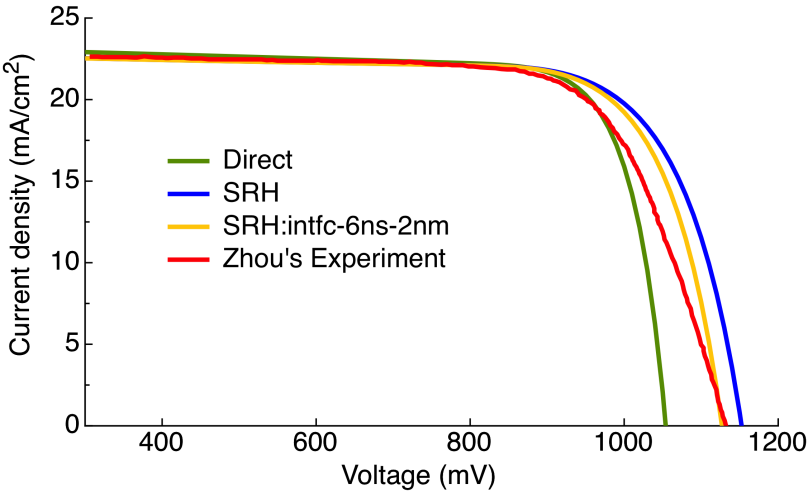

Figure 3.2: Comparison of experiment with direct recombination and SRH models. The red line is the experiment performance;[1] Direct recombination model result is noted as green line; Result of SRH model without interface recombination is shown in blue; Result of SRH model with interface recombination is shown in yellow. The thickness of interface is 1 nm. Parameters are listed in Table 3.1.

taken from Stranks' experiment.[29]

As shown in Table 3.2 and Figure 3.2, J_{sc} are 22.93 mAcm^{-2} and 23.28 mAcm^{-2} for the SRH and the direct recombination model, respectively. They are close to the experiment value of 22.75 mAcm^{-2}. The direct recombination model gives a larger filled factor (FF) of 79.89%. FF of the SRH model is 76.15%, which is closer to the FF (75.07%) in experiments. The most significant difference between experiment and simulations is V_{oc}. V_{oc} for the direct model is 1054 mV, varies away from the experimental value of 1130 mV. V_{oc} of the SRH model is 1153 mV, closer to experiment. Implementing of an interface region with 1 nm thickness with 6 ns lifetime gives better agreement on V_{oc}. Hence, the performance reproduced by the SRH model is more accurate than the direct recombination model compared to experiments. The FF of direct recombination model is larger than that of the model with charge combined through defects. This indicates defects in thin film may lead to low FF. Charges densities, currents densities, and electric field in these simulated PSCs are shown in Figure B.3 in Appendix B.

From these simulations, we draw two conclusions. The first conclusion is that the SRH model is better than the direct recombination model to describe the recombination in PSCs. This conclusion indicates that most recombination in perovskite happens through defects rather direct intrinsic recombination. Together with the fact that defects in the bulk of $MAPbI_3$ perovskite are benign,[63] it suggests that the re-

Table 3.2: Comparison of experiment performance and various simulation models

Source	V_{oc} **(mV)**	J_{sc} **(mA)**	**PCEs (%)**	**FF**
Direct recombination	1054	23.28	19.61	0.7989
SRH model without interface	1153	22.93	20.12	0.7615
SRH model with interface	1130	22.90	20.03	0.7743
Experiment[1]	1130	22.75	19.30	0.7507

combination of charge carriers might mainly happen at domain surfaces and interfaces. This suggestion is verified by experiments that the lifetime of perovskite without an interface is much higher than that of perovskite film with interfaces.[28, 29, 1, 186] The second conclusion is that in a real PSC, interface region with shorter charge carrier's lifetime is confirmed. This interface recombination leads to low V_{oc}. For this sake, a PSC with high J_{sc} and FF, and low V_{oc} can be further improved by interface engineering. It is one of the key reason for Zhou *et. al.* achieving high V_{oc}.[1]

3.3.2 Charge carrier lifetime dependence

Higher charge collection efficiencies and PCEs are expected with longer charge carrier lifetimes. This expectation is confirmed by our simulation results in Figure 3.3. PCEs increase with carrier lifetimes. Without interface recombination, V_{oc} shows a certain relation with lifetime:

$$V_{oc}(mV) = A \times ln(\tau - \tau_0) + V_0 \tag{3.15}$$

for results calculated with boundary conditions of $F_0 = F_d = 0$, V_0 is 900.1 mV, $\tau_0 = 0.209$ ns and A = 52.354 mV, which agrees well with approximated analytical models ($2kT = 52$ meV) for DSCs. [187, 188, 189]. If we use diffusion coefficients with 0.034 cm^2s^{-1} and 0.022 cm^2s^{-1}, parameters change very little: $V_0 = 902.902$ mV, A = 51.810 mV. While for simulation results with boundary conditions of $F_0 = F_d = V/d$, $V_0 = 622.286$ mV, $\tau_0 = 3.635$ ns and A = 80.633 mV, which varies a lot from $2kT$. Therefore, approximated analytical models are correct only when boundary fields are zero.

The presence of interface breaks this relation. No matter how many fitting parameters are used, fitting curves vary away from simulation points, as shown in Figure B.7 in Appendix B. All of the V_0, J_{sc}, FF and PCEs increase with charge carrier lifetime no matter whether there is or not an interface. The V_{oc} difference between models with and without interface is 70 mV when the carrier lifetime is 700 ns. While, the J_{sc} difference is only 1 $mAcm^{-2}$. The presence of a thin interface decreases a lot in

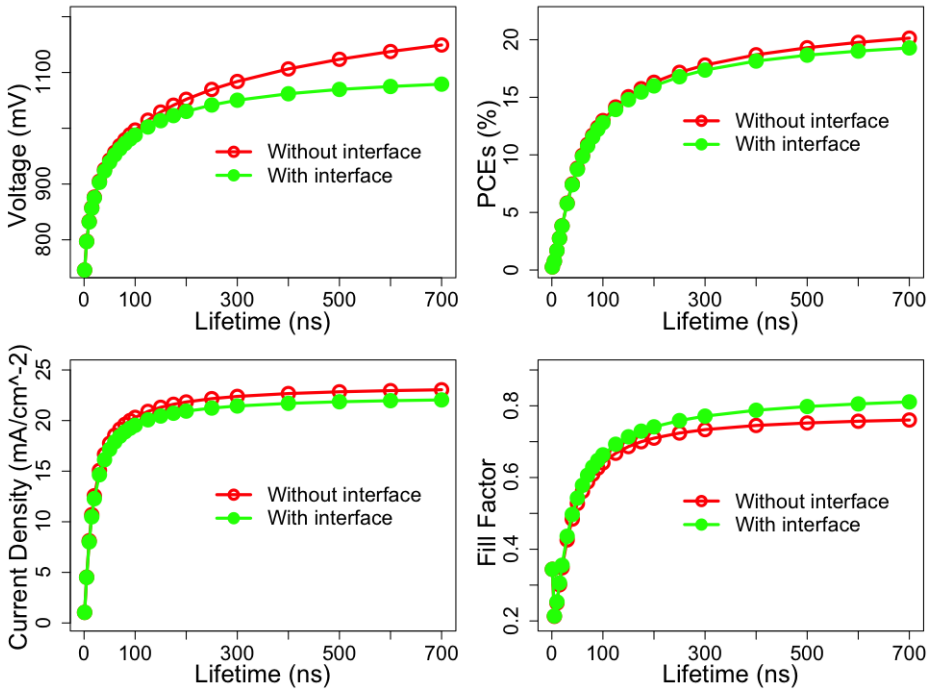

Figure 3.3: Solar cells' performances with different charge carrier's lifetimes from 1 ns to 700 ns. Other parameters are shown in Table 3.1.

V_{oc} and a little in J_{sc} for a solar cell with long diffusion length. J-V curves of these simulations are shown as in Figure B.8 and B.9, in Appendix B.

3.3.3 Mobility dependence

It is well known that a solar cell with high charge carrier mobilities should have high charge collection efficiency and large current. Here, we made a set of simulations with series mobilities. If the charge carrier lifetime is set at 736 ns, performance is almost constant when mobilities change. This is because the diffusion length is much longer than cell's thickness. Therefore, we set the lifetime as 20 ns for mobility dependence calculations. Mobilities were multiplied with respect to the mobilities of 0.65 and 0.42 cm^2/Vs, which are calculated from the diffusion coefficients of 0.017 cm^2s^{-1}(electron) and 0.011 cm^2s^{-1} (hole). As shown in Figure B.10, there is not much difference between performances of models with and without interfaces. This is because the interface carrier lifetime is comparable to the short carrier lifetime of bulk. V_{oc} differences among these simulations are within 4 mV, relative differences are within 0.5%. Therefore, mobilities are not reckoned as a factor affecting V_{oc}. While, it does change J_{sc} and PCEs very much. J_{sc} is improved from 12.6 $mAcm^{-2}$ to 23.3 $mAcm^{-2}$ and PCEs are improved from 3.8% to 14.5%, if mobilities increase from 0.65

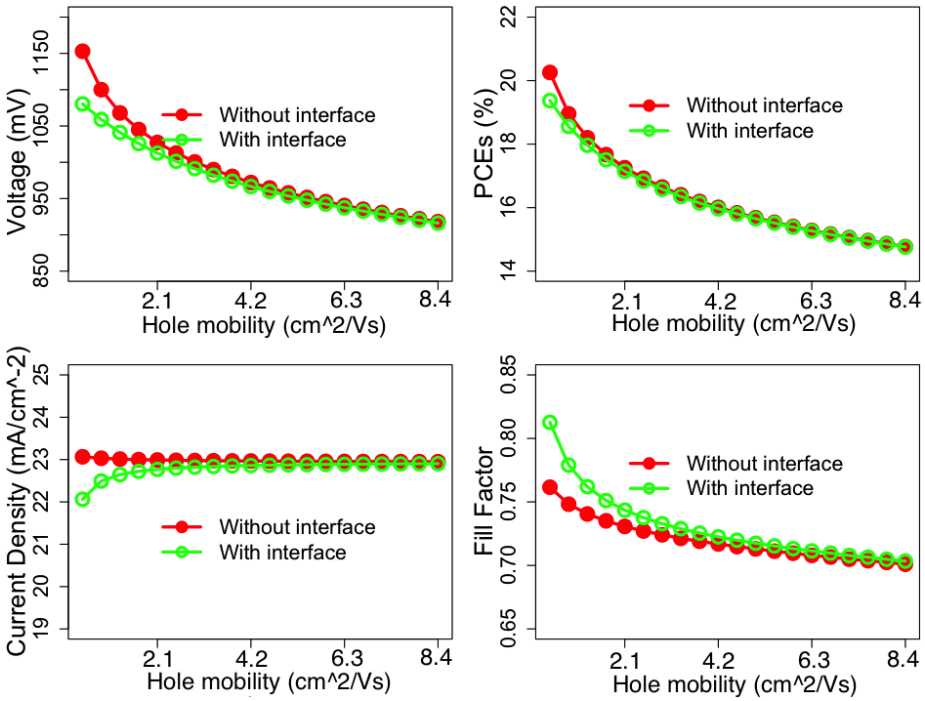

Figure 3.4: Solar cells' performances with various mobilities and lifetimes. Diffusion lengths are kept at 1.12 μm and 900 nm for electron and hole, respectively. Both of the electron and hole mobilities increase, at the same lifetime decreases. The interface recombination width is 1 nm with 1 ns lifetime. Other parameters are listed in Table 3.1.

and 0.42 cm^2/Vs to 13.08 (electron) and 8.46 (hole) cm^2/Vs. Both J_{sc} and PCEs increase significantly with mobilities increasing if the diffusion length ($L = \sqrt{D \times \tau}$) is shorter than the length of 3 times of solar cell thickness. When the diffusion length is 3 times longer than the solar cell thickness, further increasing of mobility gives little improvement.

3.3.4 Diffusion length dependence

Diffusion length is one of the most important parameters of solar cells. It represents overall charge transport character of a semiconductor. It is determined by charge carrier's lifetime and diffusion coefficient: $L_e = \sqrt{D_e \times \tau_e}$. Figure 3.4 shows performances of solar cells with various D_e and D_h, while the diffusion length is fixed. In these simulations, τ decreases in order to keep diffusion length constant. The diffusion lengths are 1.12 μm and 900 nm for electron and hole, respectively. V_{oc} and PCEs decrease as D_e increases due to τ decreasing. J_{sc} has not much change, especially for the results of a solar cell without interfaces. Almost constant J_{sc} suggests that

J_{sc} is only determined by carrier's diffusion length. With diffusion length increasing (diffusion coefficient or lifetime increasing), J_{sc} increases very fast at the beginning, as shown in Figure B.10 in Appendix B. It almost reaches saturated value of 23.3 mAcm^{-2} when the diffusion length is about 1.7 μm, which is about 5 times thicker than the thickness of perovskite layer.

3.3.5 Light intensity dependence

The toxicity of lead compound limits the wide usage of PSCs. To avoid pollution, additional packaging is needed to seal whole solar cells. For large-scale solar cell fabrications, large packing area increases the cost significantly. To reduce packing cost requires small packing area. Here is the concentrator solar cell. As its inner active part is much smaller than that of the non-concentrator solar cell, this will save lots of packaging materials. Not only does it decrease the packaging materials, but also reduce the usage of perovskite. Hence, concentrator solar cells are very promising to reduce cost. The other motivation of concentrator solar cells is that it usually has higher PCEs than that of non-concentrator solar cells. For example, according to the data provided by NREL,[190] the PCE record of single junction crystal GaAs solar cells is 26.4%. However, the record for its concentrator solar cell is 29.1%, about 10 percentage is improved.

Here, we discuss the possibility of making concentrator PSCs. Various light intensities are implemented in simulations. J_{sc} is almost proportional to the light intensity. The normalized J_{sc} per Sun light intensity keeps constant or varies very little. As shown in Figure 3.5, when light intensities increase from 1 to 1000 Suns light intensity, the normalized J_{sc} increases slightly from 23.07 mAcm^{-2} to 23.19 mAcm^{-2} for models without interfaces, from 22.06 mAcm^{-2} to 22.49 mAcm^{-2} for models with interfaces. High light intensity produces high V_{oc} in PSCs as well as in other types of solar cells.[191, 192] Without interfaces, V_{oc} increases from 1153 mV to 1542 mV for irradiation intensity increasing from 1 to 600 Suns. The constant normalized J_{sc} and increasing V_{oc} with light intensity are in good agreement with the experiment.[193] For 700 Suns irradiation, V_{oc} is larger than its band gap 1.55 eV. This is due to the photon generated charge carrier concentration being higher than the DOS of perovskite, which never happens in real cases. Saturable absorption happens when the irradiation light intensity becomes extreme. In this case, absorption does not increase with light increasing. FF increases from 81.3% to 86.7% (with interfaces) or from 76.2% to 85.6% (without interfaces). The most impressive is the improvement of PCEs, which increases from 20.3% to 30.6% for models without interfaces when the

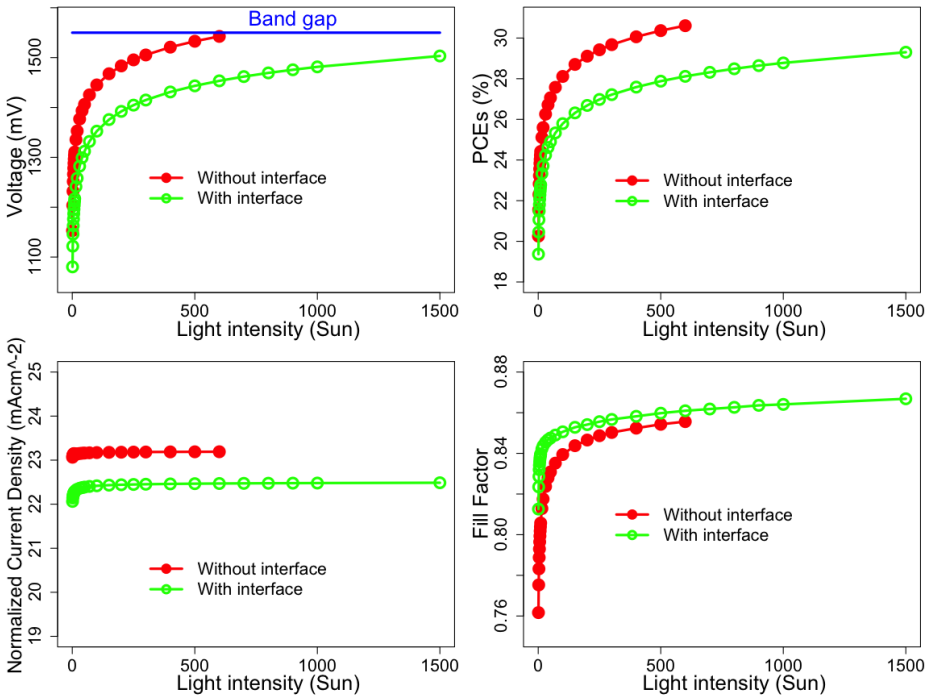

Figure 3.5: Light intensity dependence. The interface recombination width is 1 nm and its lifetime is 1 ns. Other parameters are shown in Table 3.1.

light intensity increases from 1 to 600 Suns. For models with interface, it raises from 19.4% to 29.3%, when the light intensity increases from 1 to 1000 Suns. Under high incident light intensity, high-density charge carriers are generated and transported to the two ends of perovskite layer, and then, higher V_{oc} and PCEs are expected.

In experiments, one-junction GaAs cells show a logarithmic relation for the efficiency and concentration, if the concentration is lower than 500 times.[194] This trend is in good agreement with our simulation result, as shown in Figure 3.6. When the incident light becomes extremely intensive, PCE no longer increases and even decreases.[195, 192] We interpret two reasons contribute the discrepancy at extreme light intensities. The first is the saturable absorption, which refers to light absorption does not increase with light intensity. The second reason is heat accumulation at high light intensity. Heat accumulation increases solar cell's temperature and then lowers its performance. For a solar cell with interfaces, works at 300 K under 800 Suns, its PCE is 28.5%. It decreases to 27.6% when it works at 350 K, shown as the blue cycle in Figure 3.6. For a solar cell works under 1000 Suns, its PCE decreases from 28.8% to 27.2% when the working temperature increases from 300 K to 400 K. For a solar cell works under 1500 Suns, its PCE decreases from 29.3% to 26.6% when the working temperature increases from 300 K to 500 K. Therefore, for $MAPbI_3$ concentrator

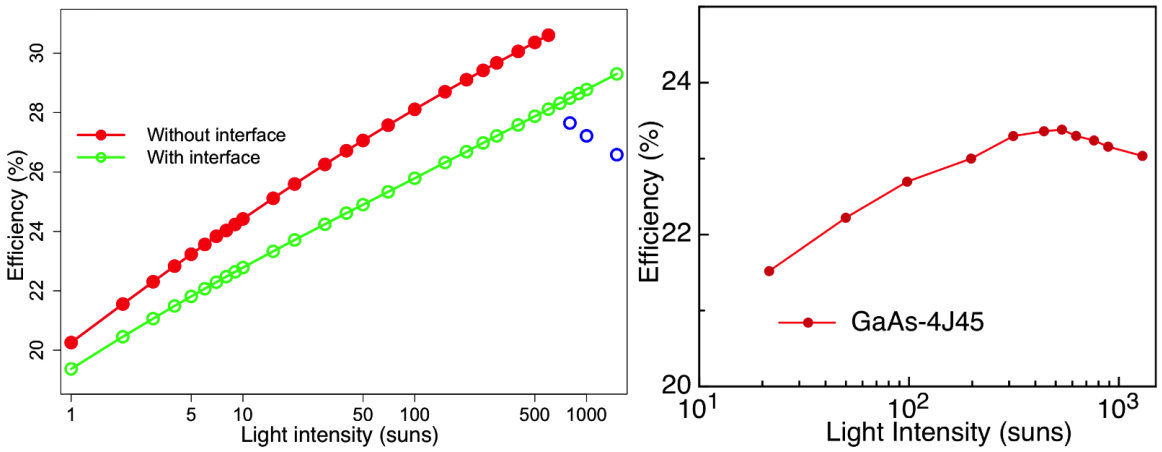

Figure 3.6: Light intensity dependence tendency compares to experiment of GaAs solar cells. Left are simulation results, right are results from experiment.[194] For simulation, the interface recombination width is 1 nm and its lifetime is 1 ns. PCEs of PSCs simulated under 300 K is shown in red or green. Blue points are results simulated with temperature of 350 K, 400 K and 500 K, from left to right, respectively. Other parameters are shown in Table 3.1.

solar cells, a cooling system is very crucial, as shown in Fig. 3.7 and Fig. 3.6. There is another problem of heat accumulation for PSCs: phase transition. The β phase $MAPbI_3$ will go to its α phase when the temperature is above 330 K. Fortunately, their electronic properties change little between the α and β phases as we have shown in Chapter 2. Thus, phase transition hardly affects solar cells performance.

3.3.6 Temperature dependence

Temperature dependent performance is investigated in order to maximize solar cells output under optimum conditions. It is found that the working temperature does not alter J_{sc} in a significant manner. It decreases from 23.08 $mAcm^{-2}$ to 23.05 $mAcm^{-2}$, when the temperature increases from 200 K to 400 K, as shown in Figure 3.7. For solar cells with interfaces, J_{sc} drops from 22.11 $mAcm^{-2}$ to 22.03 $mAcm^{-2}$. However, V_{oc} significantly decreases from 1272 meV to 1037 meV as the temperature rising from 200 K to 400 K. The PCE reduces from 24% to 17.5% as temperature raising from 200 K to 400 K. Without phase transition, PSCs working at lower temperature give higher PCEs.

A phase transition happens at 330.15 K, where $MAPbI_3$ goes from the β phase to the α phase. According to Landau-Ginzburg theory of fluctuations, the correlation length near the transition temperature (T_c) is proportional to $1/\sqrt{|T - T_c|}$. Long correlation length gives high mobility and long diffusion length. If we assume that,

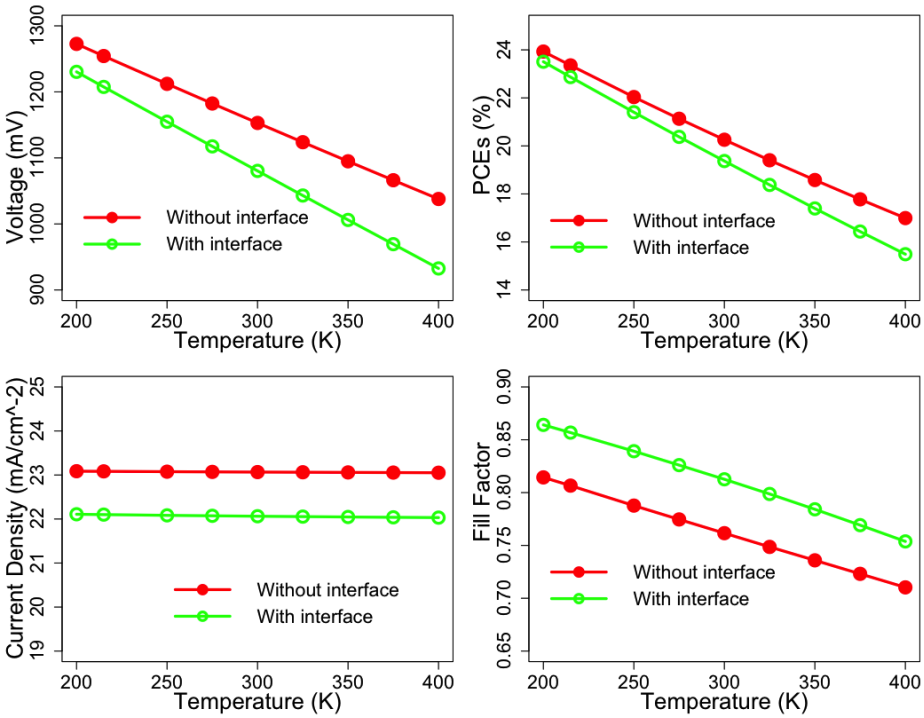

Figure 3.7: Performances of PSCs under temperature from 200 to 400 K. The interface recombination width is 1 nm and its lifetime is 1 ns. Other parameters are shown in Table 3.1.

diffusion coefficients can be calculated by $D = \frac{D^0}{|T-T_c|}$. Considering electron and hole diffusion coefficients are 0.017 and 0.011 cm^2s^{-1} at 300 K, D^0 for electron and hole should be 0.51 and 0.33 cm^2s^{-1}, respectively. In this case, the highest performance is found at low temperature or near T_c. V_{oc} continuously decreases as temperature rises. FF and J_{sc} show a 'transition point' at T_c. J_{sc} increases with temperature increasing when the temperature is below T_c. It decreases when the temperature is higher than T_c. The highest PCE in these simulations is 22.02%, which is at the lowest temperature. Below T_c, PCEs decrease at first and then increase when the temperature is near T_c. It decreases again when the temperature continues to rise. Actually, different devices show different performance dependence. For a PSC with very short diffusion length, the maximum PCE is found at 330 K, as shown Figure B.11 in Appendix B.

3.3.7 Thickness dependence

Perovskite thin film thickness is one of the crucial parameters to make high performance solar cells. On one hand, the perovskite layer needs to be thick in order to absorb more possible photons. On the other hand, the perovskite layer needs to be

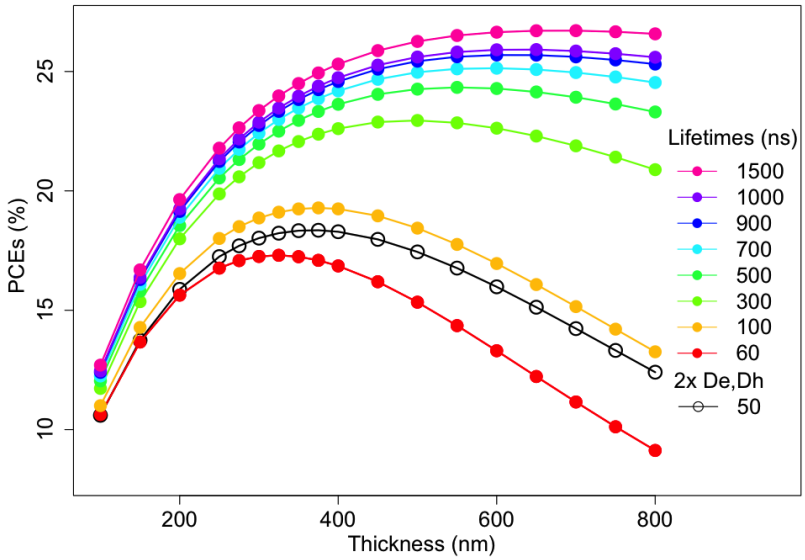

Figure 3.8: The thickness dependent PCEs. The optimum thickness is determined by the diffusion length. Simulations are carried out with boundary fields $F_0 = F_d = 0$. The simulation results with boundary fields of $F_0 = F_d = V/D$ are shown in Appendix B. Lifetime changed in order to change the diffusion length. Other parameters are listed in Table 3.1.

thin in order to collect more charge carriers. It is difficult for photon generated charge carriers to be efficiently collected in very thick films. Hence, the optimum thickness should be in a balance of its absorption length and diffusion length. For models with boundary conditions of $F_0 = F_d = 0$ and without interface recombination, solar cells with a lifetime of 100 ns the optimum thickness is about 375 nm, as shown in Figure 3.8. If the lifetime increases to 300 ns, the optimum thickness is around 500 nm. For lifetimes of 700 ns, 1000 ns and 1500 ns, optimum thicknesses are 600 nm, 650 nm and 700 nm, respectively. When we model it with interfaces, as shown in Figure B.12, the optimum thickness are 375 nm, 500 nm, 550 nm, 550 nm and 600 nm for lifetimes of 100 ns, 300 ns, 700 ns, 1000 ns and 1500 ns. Based on these trends, we draw a conclusion that the upper limit of the optimum perovskite layer thickness is 600 nm with interface recombination. For models with $F_0 = F_d = V/d$, results are shown in Figure B.13 and Figure B.14 in Appendix B.

Figure 3.8 shows the thickness dependence of the model with 100 ns lifetime and diffusion coefficients of 0.017 and 0.011 cm^2s^{-1}, is the same with that of the model with 50 ns lifetime and diffusion coefficients of 0.034 and 0.022 cm^2s^{-1}. This fact suggests that optimum thickness is solely dependent on the diffusion length. As the absorption coefficient of perovskite thin film is $5.7 \times 10^4/cm$, the absorption length is 175 nm. Shown in Figure 3.8, when the diffusion length is shorter than or close

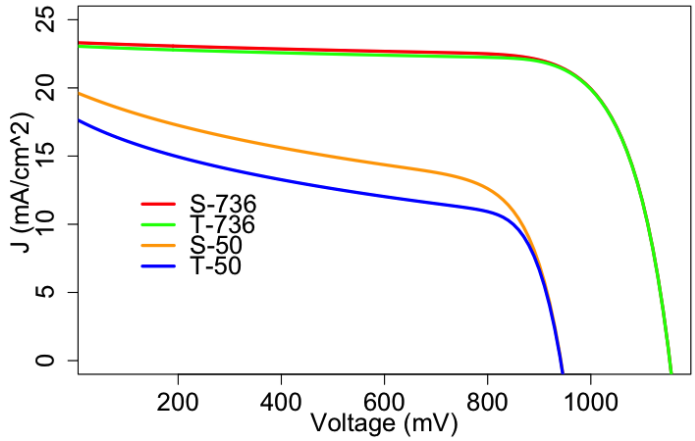

Figure 3.9: Performances of solar cells with two type structures and different lifetimes. Boundary fields are $F_{x=0} = F_{x=d} = \frac{V}{d}$. Results with boundary field $F_0 = F_d = 0$ are shown in Appendix B.

to the absorption length, the optimum length is about the diffusion length. For the diffusion length much longer than absorption length, the optimum length is still near the magnitude of the absorption length.

3.4 Discussion

Sunlight may enter the perovskite layer either through the TiO_2 layer or the Spiro-MeOTAD layer. The question is which structure can make higher PCE solar cells? Due to large band gaps of TiO_2 and Spiro-MeOTAD, it is reasonable to neglect the absorption of these two layers. The model with light coming from TiO_2 layer is noted as T model. While, the model with light coming from Spiro-MeOTAD layer is noted as S model. The difference between them is where the high-density charge carrier generates. For S model, light in perovskite near Spiro-MeOTAD side is more intensive than that near TiO_2 side. Hence, more charge carriers are generated near Spiro-MeOTAD side. In this model, electrons need travel a long distance from Spiro-MeOTAD side to TiO_2 side. In T model, for the same reason, holes need to travel a long distance from TiO_2 side to Spiro-MeOTAD side. As electron's mobility is higher than hole's in $MAPbI_3$, it is easier for electron traveling far distance. Therefore, S model should exhibit better performance than T model could do.

Simulations give the same result as we analyzed. V_{oc} is nearly the same. What's different is the J_{sc}. They are 23.07 $mAcm^{-2}$ and 23.32 $mAcm^{-2}$ for T and S model with the lifetime of 736 ns, respectively. PCEs are 20.25 and 20.30%, not much differ-

ence, which is due to the diffusion length being much longer than the perovskite layer's thickness. For a solar cell with shorter lifetime, these two structures show larger difference. As demonstrated in Figure 3.9, J_{sc} of solar cells with lifetime of 50 ns are 19.70 mAcm^{-2} and 17.75 mAcm^{-2} for S and T models, respectively. Corresponding PCEs are 10.13% and 8.77%, more than 2% PCEs is improved if we use S model. Models with interface and different boundary conditions show the same results. Details are provided in Appendix B. Generally, as the electron mobility is higher than hole's, it is better to fabricate solar cells with light coming from Spiro-MeOTAD side.

As we have shown in Results, short diffusion length leads to low V_{oc} and small J_{sc}. For such a solar cell, increasing of charge carrier's mobility and lifetime improves its performance. Therefore, a cell with low V_{oc} and small J_{sc} can be improved by the engineering of perovskite thin film. When should we focus on the interface engineering? Figure 3.2 and Figure B.7 in Appendix B show that the presence of a very thin interface reduces J_{sc} little, but reduces V_{oc} significantly. Therefore, for a cell with large J_{sc} and small V_{oc}, we should refine its interface states. This conclusion was confirmed by the experiment did by Zhou *et. al.*[1] In their work, interface engineering improves interface states and avoids high interface recombination, and then yields unusual high V_{oc}.

3.5 Conclusion

In this part of work, we built a numerical model with two different recombination mechanisms and methods. The model with SRH recombination is in better agreement with experiment than the model with direct recombination, which indicates that the recombination in hybrid PSCs is mainly through defects and traps. It is found that PCEs are determined by charge carrier's lifetimes, diffusion coefficients and diffusion lengths. J_{sc} is solely determined by charge carrier's diffusion lengths, and V_{oc} depends on the charge carrier's lifetime. The temperature dependencies are discussed based on two different assumptions. If the mobility is constant, performance decreases as temperature increases. The other assumption is that mobilities may change near phase transition point. The correlation length near the transition temperature (T_c) is, we expect, proportional to $1/\sqrt{|T - T_c|}$. Long correlation length leads to high mobility and long diffusion length. Then, we expect to find the best performance near T_c or at the lowest accessible temperature. Lastly, simulations show that the presence of interface decreases V_{oc}, J_{sc} and PCEs.

We demonstrated how to use our model to provide guidelines for PSC design and optimization. Firstly, for a material with electron mobility higher than hole mobility, the cell with hole transport layer facing the sun has a higher PCE than the cell with electron transport layer facing the sun. Secondly, the optimum thickness of the active layer is dependent on its absorption length and its diffusion length. When the diffusion length is shorter than the absorption length, the optimum length is about the diffusion length. But for the diffusion length far longer than absorption length, the optimum length is still in the magnitude of absorption length. Thirdly, a solar cell with a thin rapid interface recombination shows a low V_{oc} and high J_{sc}. It suggests that solar cell with low V_{oc} and high J_{sc} can be improved by interface engineering. A solar cell with both low V_{oc} and low J_{sc}, is mainly due to poor charge transport ability in perovskite layer. Enhancing the quality of perovskite thin film is crucial. Lastly, the light dependence of PSCs indicated perovskite concentrator solar cells is the possible new developing direction for PSCs.

These equations and methods we have reported and tested provide a framework for numerical modeling of perovskite-based cells and the optimization of their performance.

Chapter 4

Numerical analysis of a hysteresis model in PSCs

4.1 Introduction

Perovskite solar cells have achieved PCEs up to 22% in just five years.[23, 24, 4] They attract great attention due to their high performance and anomalous hysteresis. It is believed that the large charge carrier diffusion lengths and the compensated field are two key factors for high performances of hybrid PSCs.[28, 29, 176, 177, 178, 179] In experiments, it was observed that the slowly built compensated field contributes to the anomalous hysteresis.[70, 49] The compensated field is thought to be induced by ion migration and electronic charge traps.[70, 49, 77] The compensated field works as a screening effect resulting in a high dielectric constant, which has been observed up to 1000 for $MAPbI_3$.[97, 196] According to the experimental compensated field, we use the numerical model developed in the last chapter to analyze the screening effect and hysteresis behaviors.

At high frequencies, only electronic orbitals are able to respond and become polarized, whereas all of the electronic orbitals, defect charges and ions are able to respond at low frequencies. As a result, the high-frequency dielectric constants are observed as low as 6-7,[52, 97] compared to the approximately 100 times higher low-frequency dielectric constants. [97] This frequency dependent dielectric constant behaviour is consistent with the compensated field and the extremely slow photo-conductivity response in $MAPbI_3$ solar cells.[41] We argue that both the compensated field and the slow photo-conductivity come from certain slow relaxations. This relaxation screens external fields and increases the dielectric constant. Ion migration is believed to be one of the possible reasons for this relaxation.[49, 75, 76, 51, 70, 77] But the slow response experiments carried out by Gottesman *et al.* shows two opposite behaviours of

decreased/increased photoconductivity in identically constructed devices. This cannot be explained by ion migration.[41] Hence, ion migration is not the only origin of hysteresis. Van Reenen *et al.* modeled this hysteresis and found the combination of ion migration and electronic traps brings about hysteresis.[77]

Besides ion migration, polarization is the other possible reason for hysteresis. Beilsten-Edmands *et al.* claimed that there is no ferroelectric nature contribution to hysteresis due to the intrinsic polarization being too small.[75] They treated the polarization at very high frequency ($f \to \infty$) as its intrinsic polarization. However, for any ferroelectric polarizations under an extremely high frequency, the polarization should be zero as the electronic orbitals and ions are unable to respond. Up to now, there is no direct evidence to deny ferroelectric polarization in PSCs. Additionally, Kutes *et al.* showed a direct observation of ferroelectric polarizations.[108] The debate of ferroelectric polarization in PSCs and their hysteresis continues.

From a theoretical aspect, most research supports the existence of polarization. First-principles studies have shown that the energy barriers for defect migrations are from 0.08 eV to 0.40 eV depending on ion types[197, 198] These energy barriers are low enough to be crossable at room temperature. We also reported the energy barrier for MA^+ reorientation is about 0.01 eV to 0.098 eV, which depends on the initial and final MA^+ orientations and neighboring MA^+ orientations.[52] From the base of their energy landscapes, polarization is easier to respond and screen external fields. As we showed in Ref. 52 MA^+ ions are able to be rotated collectively under an applied external field, which then polarizes $MAPbI_3$ crystals or thin films. This collective reorientation and polarization combined with capacitive charges screen external hindering field and promote power conversion efficiency. Hence, the other slow relaxation should be polarization relaxation. Our argument is in good agreement with Sanchez's experiment that the slow dynamic process depends strongly on the organic cation, MA^+ or $HC(NH_2)_2$ (FA^+).[50] The rotation of MA^+ ions and migration of I^- ions are systemically discussed by Frost *et al.*[104, 98, 199] They argued that the internal electrical fields associated with polarization contribute to hysteresis in J-V curves.[104] They also observed that a single cation rotation and anion migration take several picoseconds.[98, 199] Hence, we argue here that polarization and ion migration are both possible to induce screening fields and contribute to hysteresis.

We propose here that the screening charge contains two components: one is the polarization charge resulted from MA^+ reorientation and inorganic frame; the other is capacitive charges from defects and trapped charges including ions. For normal PSCs without polarization, photon generated charge carriers accumulate in defects

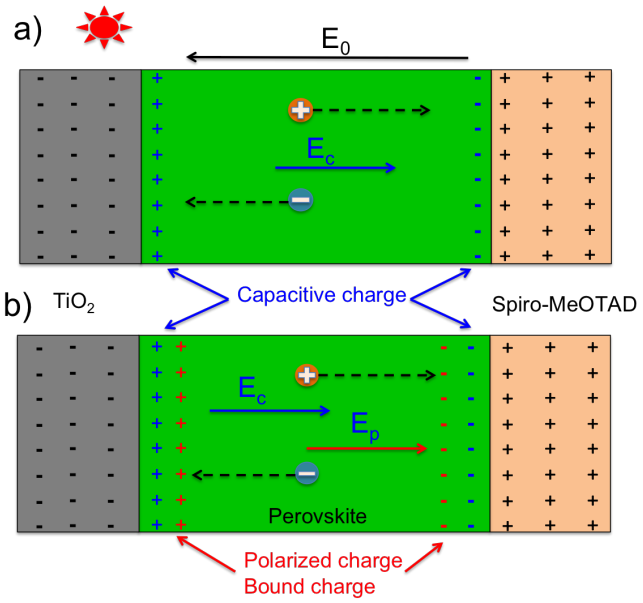

Figure 4.1: Our proposed mechanism of PSCs

near interfaces, shown as the blue charge in Figure 4.1. These accumulated charges induce a field that counteracts the applied hindering field. We name the applied field hindering field because it is opposite to the work current vector. For PSCs, polarization charges can further counteract the hindering field and promote charge carrier transport. Due to these capacitive and polarization screening effects, high PCEs are expected for hybrid PSCs. This is the first hypothesis we are going to test.

The second hypothesis we are going to test is that hysteresis in J-V curves come from these two kinds of slow relaxations. As their relaxations are slow, screening fields fall behind the applied hindering field if the measurement scanning is fast enough. This delay induces hysteresis. We apply numerical simulations to reproduce and explain the anomalous hysteresis effect in PSCs. Our results show both capacitive charge and polarization charge could contribute to hysteresis effects. Relaxation times of these two charges determine the overall behaviour of scan rate dependent hysteresis.

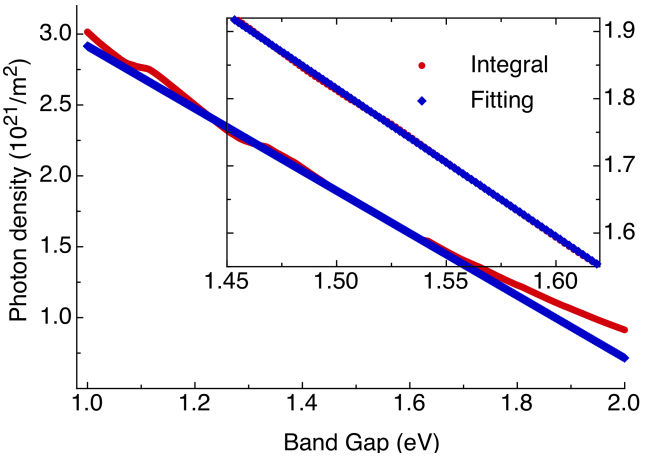

Figure 4.2: Integral and fitting incident photon density of AM 1.5 Standard Spectrum. The insert shows the integral and the fitting result of photon density with band gaps between 1.45 eV and 1.62 eV. Error in this region is smaller than 2%.

4.2 Methods

4.2.1 Equations and boundary conditions

Our model is based on the continuity equations and Poisson's equation in one dimension, adapted for PSCs:[57]

$$\begin{aligned} J_n &= eD_n\frac{\partial n}{\partial x} + n\mu_n F \\ J_p &= -eD_p\frac{\partial p}{\partial x} + p\mu_p F \\ \frac{\partial J_n}{\partial x} &= -eG + eR \\ \frac{\partial J_p}{\partial x} &= eG - eR \\ \frac{\partial F}{\partial x} &= \frac{p-n}{\varepsilon\varepsilon_0} \end{aligned} \tag{4.1}$$

where, J_n and J_p are the electron current and the hole current respectively; n is the electron density and p is the hole density; μ and D are the charge carrier mobility and the diffusion coefficient respectively; footnote symbols $_n$ and $_p$ mean they belong to the electron and the hole respectively; G and R are the generation rate and the recombination rate; F is the external applied electric field. Boundary conditions and parameters are shown in reference 57.

4.2.2 Generation rate

Light harvest and charge generation are expressed as $G = IPCE \times N$, where $IPCE$ is Incident Photon-to-Current Efficiency. N is the incident photon density calculated by $\int \frac{I(\lambda)}{hc/\lambda} d\lambda$, where $I(\lambda)$ is the incident light density, h is the Plank constant, c is the speed of light and λ is the photon's wavelength. According to the Beer-Lambert law, light intensity inside a material decays exponentially from the surface as: $I(\lambda, x) = I(\lambda, 0)e^{-\alpha(\lambda)x}$, where x is the incident depth from the surface and $\alpha(\lambda)$ is the absorption coefficient. Therefore, the charge generation rate becomes:

$$G(x) = \int_0^{\lambda_0} G(\lambda, x) d\lambda = \int_0^{\lambda_0} IPCE(\lambda) \times \frac{I(\lambda, 0) \times \alpha(\lambda) \times e^{-\alpha(\lambda)x}}{hc/\lambda} d\lambda \tag{4.2}$$

λ_0 is the absorption edge, corresponding to the band gap. After a photon is absorbed, an exciton formed by a hole and electron pair is generated. The hole and the electron attract each other and try to combine. We assume each exciton separates to one pair of free hole and electron, which means $IPCE(\lambda) = 100\%$.[57] Then the charge generation rate becomes:

$$G(x) = \int_0^{\lambda_0} IPCE(\lambda) \times \frac{I(\lambda, 0) \times \alpha(\lambda) \times e^{-\alpha(\lambda)x}}{hc/\lambda} d\lambda = \alpha N_0 e^{-\alpha x} \tag{4.3}$$

where, $N_0 = \int_0^{\lambda_0} \frac{I(\lambda,0)}{hc/\lambda} d\lambda$; $I(\lambda, 0)$ is the AM1.5 Standard Solar Spectra. The experiment band gap of $MAPbI_3$ is in the region from 1.45 eV to 1.70 eV.[58, 25, 8, 1, 59, 60] In our simulations, we use a linear fitting to estimate incident photon density near 1.55 eV. $N_0 = -2.20 \times 10^{17} \times E_{bgap}$ (eV)$+5.12 \times 10^{17}$ (cm^{-2}), where E_{bgap} is the band gap of the perovskite thin film. As shown in Figure 4.2, for the band gap in the range of 1.45 eV to 1.62 eV, the accurate integral density and the fitted density are nearly the same. The incident photon density is calculated to be 1.59×10^{17} cm^{-2}, if the band gap is 1.60 eV.

4.2.3 Boundary field conditions: Potential and field distributions in solar cells

A planar PSC has a sandwich structure. Two electrodes clip a compact (TiO_2) layer, a perovskite layer and a hole transport layer (Spiro-OMeTAD layer). Electrodes are conductors and the potential in a conductor is constant, hence we neglect their potential drop in this discussion. The active parts are the clipped compact layer, perovskite layer and hole transport layer. Under light irradiation, charge carriers are generated and flow. If we describe the resistances of the compact layer, perovskite

layer and hole transport layer as R_t, R_p and R_s respectively. Based on Ohm's law, the voltage drop in the perovskite layer is $V_p = \frac{V_0 \times R_p}{R_t + R_p + R_s}$, where V_0 is the applied voltage. However, two facts refute this assumption. The first is that Ohm's law only refers to drift current, in which case the current is in the same direction as the field, while current in solar cells is opposite to the applied field. The second is that the diffusion current, which is beyond the Ohm's law and the Drude model description, is larger than the drift current. Hence, it is much more reasonable to consider them as dielectric materials. Then the voltage drop across the perovskite layer is:

$$V_p = \frac{V_0 \times \epsilon_t \times \epsilon_s \times d_p}{(\epsilon_t \times \epsilon_s \times d_p + \epsilon_t \times \epsilon_p \times d_s + \epsilon_s \times \epsilon_p \times d_t)} = A \times V_0 \tag{4.4}$$

where ϵ and d are dielectric constant and thickness of corresponding layers, footnote $_t$ for TiO_2, $_p$ for perovskite and $_s$ for Spiro-OMeTAD. A is the percentage of applied voltage drop across the perovskite layer, which equals $\frac{\epsilon_t \times \epsilon_s \times d_p}{(\epsilon_t \times \epsilon_s \times d_p + \epsilon_t \times \epsilon_p \times d_s + \epsilon_s \times \epsilon_p \times d_t)}$. When ϵ_t, ϵ_p and ϵ_s are 100,[200] 1000,[97] and 3,[30] and their corresponding layers thickness are 50, 380 and 200 nm,[1] then the voltage drop across the perovskite layer is A=0.56%. For the following simulations, the boundary field at the ends of the perovskite layer are $F(x = 0) = F(x = d) = \frac{V_p}{d_p}$.

4.2.4 Field relaxation of screening capacitive charge and polarization charge.

Defects and traps in semiconductor interfaces are able to charge and discharge as capacitors do. Hence, we name these charges the capacitive charge. In our previous work,[52] we also showed that $MAPbI_3$ can be polarized by external fields through rotating MA^+ ions and tilting inorganic frames. Due to energy barriers, MA^+ ions need some time to respond. We name this response the polarization relaxation. Assume the polarization field relaxes (increases/decreases) exponentially with delay time (δt): $\delta\mathbf{F}[\delta t] = \delta\mathbf{F}[\infty] \times (1 - e^{-\delta t/\tau_c})$, where $\delta\mathbf{F}[\infty]$ is the field difference between the initial field and final field with infinite relaxation time.

The field in bulk materials within a static external field ($\mathbf{F}_0$) is $\mathbf{F} = \mathbf{F}_0 + \mathbf{F}_c$, where $\mathbf{F}_c = -S_c\mathbf{F}_0$ and S_c is the screening coefficient for capacitive charges. If there is a polarization field, then the total field becomes $\mathbf{F} = \mathbf{F}_0 + \mathbf{F}_c + \mathbf{F}_p$, where $\mathbf{F}_p = -S_p\mathbf{F}_0$ and S_p is the screening coefficient due to polarization. If the measurement voltage is applied step-by-step, then the field at time t with applied voltage V can be expressed:

$$\mathbf{F}[V, t] = \mathbf{F}_0[V, t] + \mathbf{F}_c[V, t] + \mathbf{F}_p[V, t], \tag{4.5}$$

where:

$$\mathbf{F}_c[V,t] = (\mathbf{F}_c[V,\infty] - \mathbf{F}_c[V-\delta V, t-\delta t])(1-e^{-\delta t/\tau_c}) + \mathbf{F}_c[V-\delta V, t-\delta t]$$

and

$$\mathbf{F}_p[V,t] = (\mathbf{F}_p[V,\infty] - \mathbf{F}_p[V-\delta V, t-\delta t])(1-e^{-\delta t/\tau_p}) + \mathbf{F}_p[V-\delta V, t-\delta t]$$

in which, $\mathbf{F}_c[V,\infty]$ and $\mathbf{F}_p[V,\infty]$ are screening fields under applied voltage V with infinite delay time for the capacitive charge and the polarization charge, respectively; δt is the measurement delay time and τ_c and τ_p are relaxation times of these two charges; $\mathbf{F}[V,t]$ and $\mathbf{F}_0[V,t]$ are the total field and the hindering field at time t with applied voltage V; $\mathbf{F}_c[V-\delta V, t-\delta t]$ and $\mathbf{F}_p[V-\delta V, t-\delta t]$ are the field of capacitive charge and the field of polarization charge of last step, respectively.

4.3 Results and discussion

4.3.1 Screening improvement from capacitive charge and polarization charge

According to Equation (4.4), the voltage drop across the perovskite layer is a function of dielectric constant and thickness of each layer. For quick scans, dielectric constants at high frequency are exhibited. The high-frequency dielectric constants of TiO_2, perovskite, Spiro-OMeTAD are 86,[200] 6,[97] and 3,[30] respectively. In this case, the potential drop across the perovskite layer is 43% of the applied voltage. At very slow scan rates (such as 25 mV/s), they exhibit low-frequency dielectric constants. The low-frequency dielectric constants of TiO_2 [200] and perovskite[97] have values of up to 173 and 1000 respectively. In this case, A is 0.5%. With a long delay time, screening fields of capacitive charge and polarization charge contribute to the large dielectric constant, and this leads to a small A–the percentage of applied voltage drop across the perovskite layer. We propose that the increased dielectric constant of perovskites come from the slow polarization relaxation and ion migration, which has been shown to be possible via DFT calculations.[52, 197, 198, 199]

Based on experimental parameters, the percentage of voltage drop across the perovskite layer is between 0.5% to 43%. Here, solar cell performance of A with values from 0 to 100% were simulated. The thicknesses of simulated solar cells are 350 nm.[1] Diffusion coefficients of the perovskite layer were set to be 0.017 cm^2s^{-1}(for electrons) and 0.011 cm^2s^{-1}(for holes).[29] The band gap is 1.55 eV.[1] Carrier lifetimes in bulk materials without interfaces are assumed to be 736 ns.[1] The presence

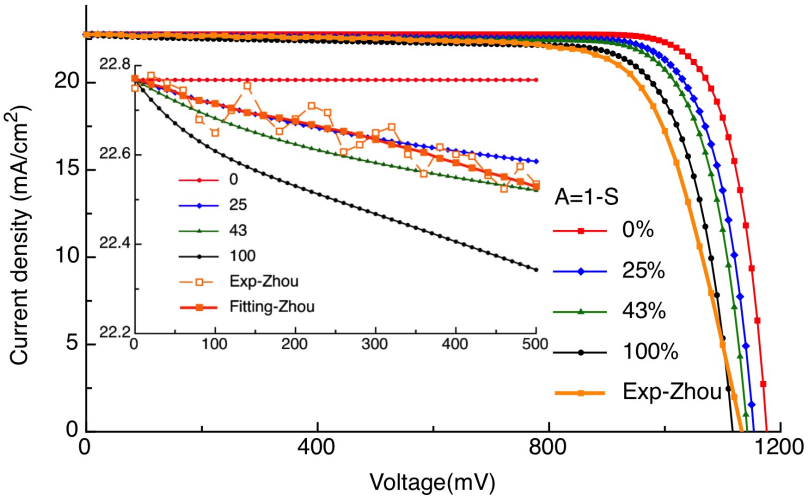

Figure 4.3: Performances of PSCs with different A (in Equation 4.4). A 2 nm thick interface with a lifetime of 7 ns is implemented. All of the J_{sc} are 22.77 mAcm^{-2}. The measurement delay time is assumed to be infinite.

Table 4.1: Performance of PSCs with different values of A.

A	V_{oc} **(mV)**	J_{sc} **(mA)**	**PCEs (%)**	**FF**
0	1176	22.77	22.44	0.8380
25	1154	22.77	21.36	0.8131
43	1142	22.77	20.93	0.8044
100	1117	22.77	19.90	0.7821
Experiment	1130	22.75	19.30	0.7507

of interfaces decreases charge carrier lifetime which indicates a high recombination rate at interfaces. More details have been discussed in reference 57. Thus, a 2 nm interface recombination region with charge carriers lifetime of 7 ns was implemented. The implement of this interface is determined according to experimental J_{sc}. In our simulation, for all values of A, J_{sc} is 22.77 mAcm^{-2}, which is close to the experimental value of 22.75 mAcm^{-2}. Figure 4.3 and Table 4.1 show experiment and simulation current density–voltage (J-V) curves of solar cells with various A. The orange square line is the experiment performance of a solar cell fabricated by Zhou.[1] Our simulated FFs are larger than the experiment value of 75%. V_{oc} in these simulations are around the experiment value of 1130 mV. When A is 100%, no screening effect is exhibited, and the J-V curve is closest to experiment. However, as shown in the insert of Figure 4.3, the experiment current decreases between theoretical lines with $A = 25\%$ and $A = 43\%$ between 0 - 500 mV and 22 - 23 mAcm^{-2}. Below 300 mV, the blue diamond line simulated with $A = 25\%$ is the closest to Zhou's experiment. The simulated V_{oc}, J_{sc}, FF and PCE are 1154 mV, 22.77 mA, 81.3% and 21.36%, respectively.

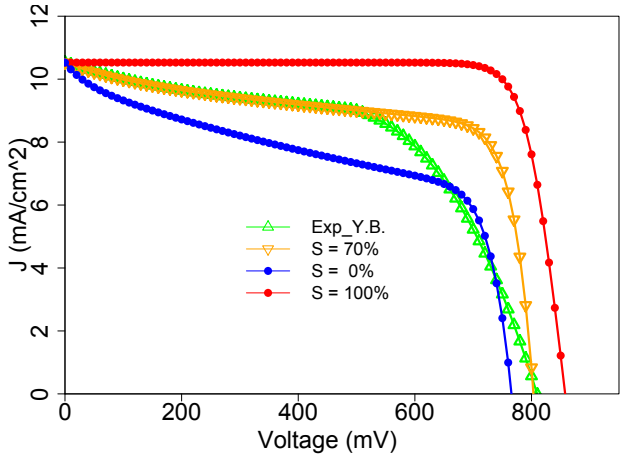

Figure 4.4: Performance of an unoptimized PSC and simulated PSCs with different screening coefficients, S=1-A. The thickness of the simulated solar cell is 350 nm. The diffusion coefficients of the perovskite layer were assumed to be 0.017 cm^2s^{-1} and 0.011 cm^2s^{-1} for electrons and holes respectively. The band gap is 1.45 eV. The lifetime in the cell is 57 ns. The working conditions were set to be at 300 K and 1 sun (1.5AM). The charge carrier lifetime in the perovskite layer is 57 ns. The interface region is set as 12 nm thick with an interface charge carrier lifetime of 0.37 ns.

As we proposed that polarization charges can further reduce the hindering field at very low scan rate, then the dielectric constant can be up to 1000.[97] In this case, the voltage drop across the perovskite layer is almost zero, which implies the hindering field has disappeared. With these parameters, our model gives a PCE of 22.4%. This suggests that by measuring with slow scan rate a high dielectric constant of the perovskite layer results, which reduces the voltage drop across the perovskite layer. Therefore, charge carriers are easier to transfer out, and a higher PCE is achieved. This conclusion is consistent with Sherkar's result that devices having polarizations in the plane of devices show high J_{sc} and FF.[201] The difference is that the screening effect in our simulation comes from both polarization and ion migration.[52]

The screening improvement is small for solar cells with very high mobilities and long lifetimes. But PCEs of solar cells with poor electron transport ability can be significantly improved through screening effects. A simply made, unoptimized PSC exhibits poor performance as shown by the green triangle in Figure 4.4. Its performance can be reproduced by our model with short charge carriers lifetime and a thick interface recombination. The simulated J_{sc} is 10.5 mA/cm^2, in agreement with experiment. For an ideally screened solar cell, its current is almost constant before 700 mV. Whereas, for a solar cell without screening effect its current decreases drastically near 0 mV then linearly with voltage until 700 mV.

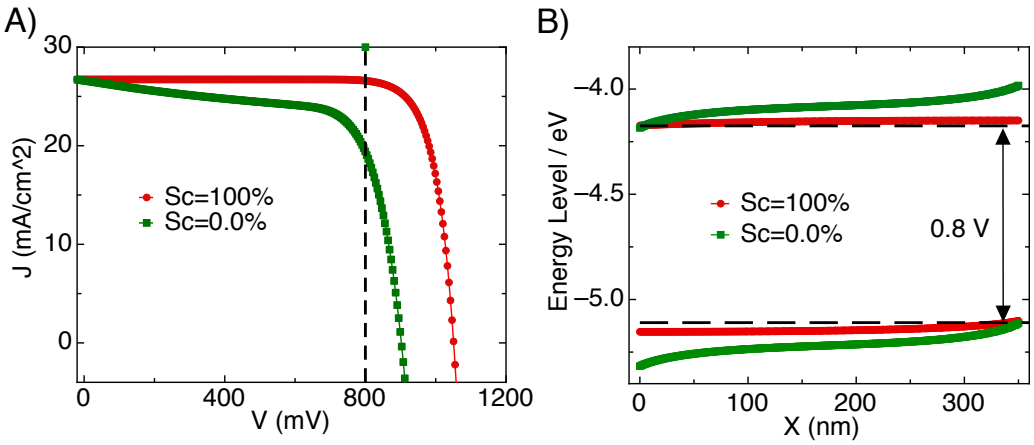

Figure 4.5: Quasi-Fermi levels for electron and hole in solar cell at oupput voltage of 800 meV with different screening coefficients. The thickness of the simulated solar cell is 350 nm. The diffusion coefficients of the perovskite layer were assumed to be 0.017 cm^2s^{-1} and 0.011 cm^2s^{-1} for electrons and holes respectively. The band gap is 1.55 eV. The lifetime is 736 ns. The working conditions were set to be at 300 K and 1 sun (1.5AM). The generation rate in PSC is uniform.

The simulated curve with 70% screen coefficient is in good agreement with the experimental curve when the output voltage is lower than 600 mV. The variation in high voltage is due to the higher fill factor of our idealized model. This implies the remaining percentage of the applied voltage in the experimental solar cell is about 30%, which is in good agreement with the range of 0.5% - 43% calculated from experimental parameters. This is the evidence that screening effects present in PSCs. The PCE of the solar cell without screening is 4.3%, which is improved to 5.9% if a 70% screening effect is present. With an ideal screening, the PCE would reach 7.5%. This results in a more than 70% improvement compared to the unscreened solar cell. The screening effect in solar cells improves PCE, especially in solar cells with poor charge carrier conductivity. Therefore, we draw a conclusion that the screening effect is the reason why simply made PSCs could achieve high performance.

In order to have a better understanding of the screening effect, models with different screening coefficients are simulated. Figure 4.5A) is the working J-V curves of these two models. The quasi-Fermi levels are shown in 4.5B). Since the quasi-Fermi levels are almost the same near the sunlit surface for different screening in the model with exponential generation due to high density of charge carriers are produced near there, the plotted quasi-Fermi levels for comparison are calculated by the model with uniform generation,[52] which gives more obvious band bending. The output voltage is the energy level difference between $E_{fn}(x = 0)$ and $E_{fp}(x = d)$, which is 800 meV.

For the model with ideal screening effect, the quasi-Fermi levels are little changed. However, for the non-screening effect model, the quasi-Fermi level is bended, which agrees with literatures.[55] The current of the model with $Sc = 100\%$ is higher than that of the model with $Sc = 0.0\%$ at 800 meV, this means more carriers are collected in the $Sc = 100\%$ model even the gradient of its quasi-Fermi level is smaller than that of the $Sc = 0.0\%$ model. It is shown that the quasi-Fermi level for the non-screen model is closer to the conduction band or the valence band. This suggests to realize a same output voltage, the non-screen model requires higher density of charge carriers.

In a normal solar cell without polarization, screening is also present. But all of the screening charges are capacitive charges due to defects and trapped charge carriers. These trapped charges will take part in charge recombination, which in turn reduces its current and PCE. For $MAPbI_3$, polarized charges cannot be combined unless polarizations become totally disordered. This also gives the benefit of a large current in the device. It is worth noticing that the polarization is not only from MA^+ ions but also from the inorganic frame. For perovskite materials, even there are no cations with dipoles, the materials can be ferroelectrically polarized as in $BaTiO_3$.[202] This means perovskite materials, such as $FAPbI_3$ and $C(NH_2)_3PbI_3$ also have the potential to make high performance solar cells.

In the above simulations, diffusion coefficients were assumed constant. Actually, screening fields also make charge carrier transport easier and then increase diffusion coefficients. Therefore, PCEs of PSCs can be further improved.

4.3.2 Numerical simulation of anomalous hysteresis

Capacitive charges are believed to be the main factor for hysteresis in silicon solar cells and DSCs.[138, 139, 140] When the measurement scan rate is too fast, capacitive charges are unable to catch up with the changing of scanning field and hysteresis is observed. Usually, more obvious hysteresis is observed with faster scanning. As charges are able to be trapped and de-trapped in silicon solar cells quickly, an extremely fast scan rate (short delay time) is required to observe hysteresis in silicon solar cells. The measurement delay time is estimated to be around 1 ms in order to observe hysteresis.[140] Charges in DSCs move slower and the trap and de-trap process take longer. Therefore, the relaxation time to see hysteresis in DSCs can be up to 100 ms. The corresponding scanning speed is about 100 mVs^{-1}.[138, 139]

What makes PSC hysteresis mysterious is not only its large relaxation time, but also the changing of hysteresis with scan rate. For silicon solar cells and DSCs, a shorter delay time (higher scan rate) brings about more obvious hysteresis.[138, 139,

140] In contrast, in PSCs, a shorter delay time can either induce a more or less obvious hysteresis.[49, 70, 51] Even in the same time region, some measurements indicate an increase whilst others show a decrease.[143, 70, 51] In this work, the hysteresis constant is defined as the difference between the maximum PCEs of forward and backward measurements. The presence of two peaks may reflect two different sources, polarization and ion migration. A single MA^+ ion takes several *ps* to rotate,[98, 199, 111] while, the slow charge relaxation time in PSCs is in the order of 1-30 s.[49, 51, 41, 70, 47] This may be because the collective relaxation of millions of ions should take much longer. The timescale for a domain wall to traverse a typical device is estimated to be about 0.1-1 ms.[111] For ion migration, it should take longer due to its larger energy barrier than MA^+ rotation. If we select a typical 0.2 eV [197, 198]energy barrier for I^- ion migration and 0.05 eV[52] for MA^+ rotation, and assume the relaxation time is proportional to $e^{-E_b/kT}$, where E_b is the energy barrier and kT is thermal energy, the relaxation time of I^- ions is about 320 times higher than the relaxation time of MA^+ ions polarization. Considering longer relaxation time for the experiment, we set capacitive charge relaxation time as 2.5 s and 250 ms for polarization in below simulations.

Lots of experiments have been designed to study hysteresis, the most systematic experiment is the work done by Tress *et al.*[70] They measured one PSC forward and backward with different scan rates from 10 to 100,000 mVs^{-1}. Every measurement begins with certain polarization states which are pre-polarized with the same condition.

As all the measurements were taken from a single solar cell with a certain initial state we could model their J-V curves under different scan rates with one set of basic parameters. Parameters used to model the work by Tress *et al.* are shown in Table 4.2. In Figure 4.6, experimental J-V curves are drawn with dashed lines, while simulated J-V curves are plotted with solid lines. The PCE is higher during backward scan. The voltage decreases during the backward scan, and the screening field falls behind. Hence, the actual screening field at a certain voltage is higher as the screening field is positive related to the previous applied field. For the same reason, the screening field at a certain voltage is lower during the forward scan. That means the screening field is higher during the backward scan than during the forward scan. Higher efficiency is achieved when the hindering field is screened to a greater extent during the backward scan.

Our simulated V_{oc} are about 915 mV, which are in good agreement with Tress's experiment. As we expected, the simulated performance of the backward scan is

Table 4.2: Assumed and experimental parameters used to simulate Tress' solar cells.

Symbol	Meaning	Value
E_{bgap}	Band gap	1.52 eV
T	Temperature	300 K
I_l	Light intensity	1.5 AM
$IPCE$	IPCE	100%
d	Perovskite thickness	350 nm
N_c,N_v	Density of States	$3.97 \times 10^{18} cm^{-3}$.[52]
α	Absorption coefficient	$5.7 \times 10^{4} cm^{-1}$.[28]
A	Voltage drop percentage	8.4%
D_n	Electron diffusion coefficient	0.030 $cm^2 s^{-1}$
D_p	Hole diffusion coefficient	0.063 $cm^2 s^{-1}$
τ_p	Polarization relaxation time	0.25 s
τ_c	Capacitive charge relaxation time	2.5 s
S_p	Polarization screen coefficient	50%
S_c	Capacitive charge screen coefficient	49%
τ	Charge carriers lifetime	10.2 ns

higher than that of the forward scan. The current at voltage of -1 V with scan rate of 100 Vs^{-1} is 22.10 $mAcm^{-2}$, which is close to the experimental value of 20.40 $mAcm^{-2}$. At -1 V, currents modeled with scan rates of 10 Vs^{-1}, 1 Vs^{-1}, 100 mVs^{-1} and 10 mVs^{-1} are 21.87 $mAcm^{-2}$, 20.18 $mAcm^{-2}$, 15.27 $mAcm^{-2}$ and 13.97 $mAcm^{-2}$, respectively. All of these current densities are close to the experiment 20.90 $mAcm^{-2}$, 19.4 $mAcm^{-2}$, 16.20 $mAcm^{-2}$ and 14.90 $mAcm^{-2}$ with errors smaller than 1.0 $mAcm^{-2}$. Not only do these typical values agree, but the J-V curves also have similar shapes. By applying one set of parameters for a certain solar cell, we reproduce its hysteresis J-V curves under different conditions. The agreement between Tress' experiment and our simulation suggests that our model and the proposed mechanism are correct.

For normal hysteresis from typical capacitive charges, as seen in DSCs made by Koide *et al.*[138, 139] it becomes more extreme when the scan rate increases, as shown in Figure 4.7. In contrast, Snaith *et al.* observed anomalous hysteresis, which becomes less extreme as the scan rate increase. Even at extremely slow scan rates, it is still significant.[51] We interpret this phenomenon as being a result of slower ion migration. As observed in experiments, the relaxation time can be as short as 1 s,[50] or alternatively as long as several tens of seconds.[49, 51, 41, 70, 47] The performance is similar in Tress' and Snaith's experiments which suggest their solar cells have similar electronic parameters. If we just change the capacitive relaxation time from 2.5 s to 50 s without changing other parameters, our simulations give hysteresis in good agreement with Snaith's experiment.[51] Jeon's solar cells show higher PCEs,

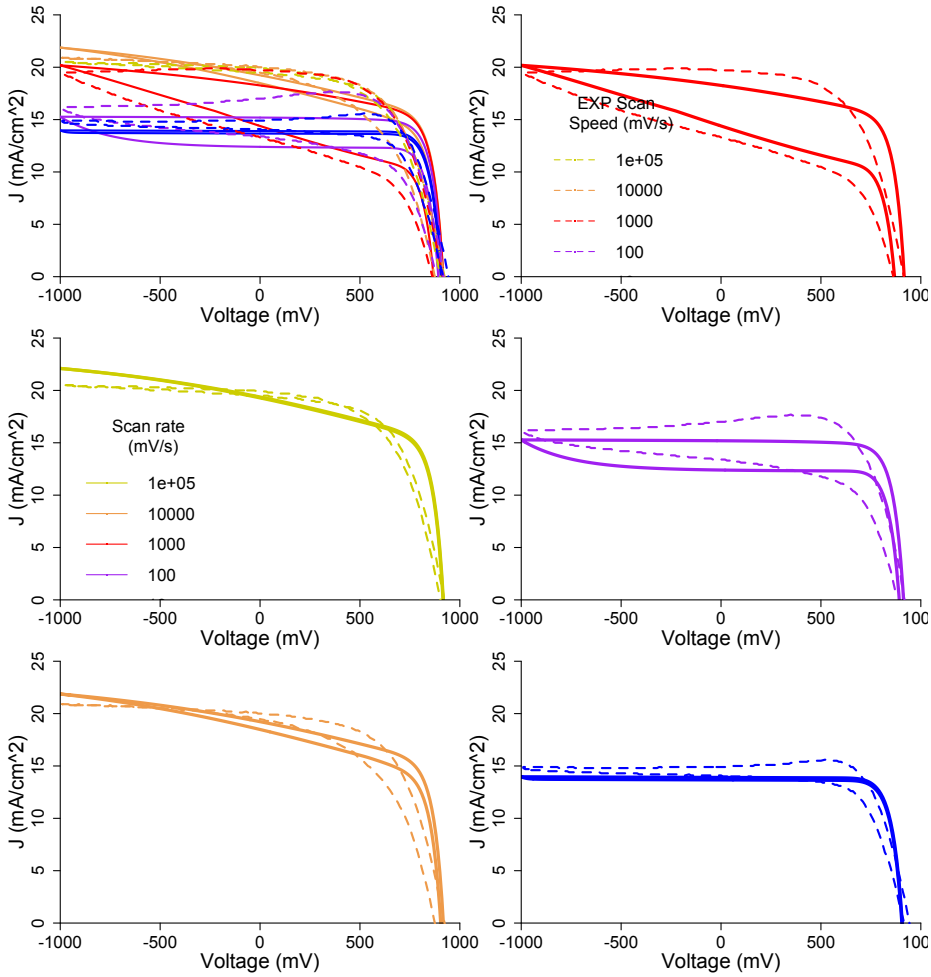

Figure 4.6: Performances of a solar cell measured forward and backward with different scan rates. Solid lines are simulation results. Dashed lines are results from Tress *et al.*'s experiment. We use direct recombination without an interface. Different color is for the different scan rates.

hence, their solar cells should have better electronic properties.[143] To model Jeon's solar cells, the charge carrier lifetime was increased to 80 ns and S_c was decreased to 10%. Hysteresis observed in Jeon's experiment is also repeated with a capacitive charge relaxation time of 0.9 s. All of the simulation and experimental hysteresis constants are shown in Figure 4.7. It is found that for very low or high scan rate measurements, the hysteresis decreases. This is due to the relaxation field undergoing little change under extremely high scan rates. The screening field is constant during a forward-backward measurement. No hysteresis is expected as there is no difference between forward and backward scans. While, for the case of very slow scans, there is enough time to relax. Hence, the screening field is always proportional to the external applied field. Screening fields are the same under a certain applied voltage no mater

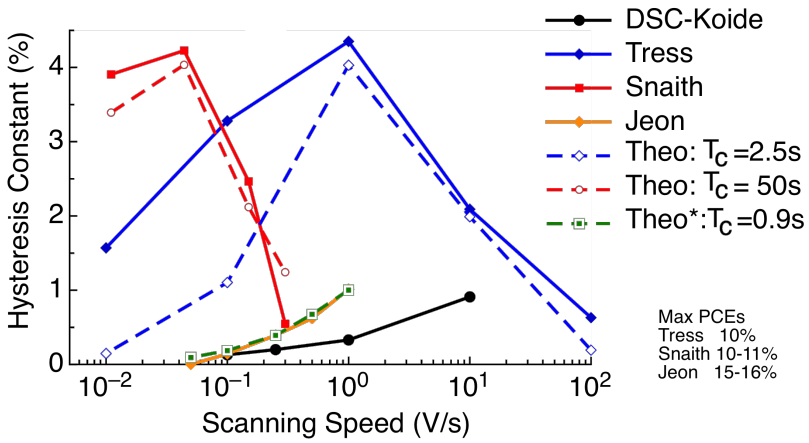

Figure 4.7: Scanning rate dependent hysteresis constants. The hysteresis constant is defined as the difference between the maximum PCEs of forward and reverse measurement. Experimental data is depicted by solid lines with filled points. Numerical simulation results are plotted as dashed lines with open points. T_c is the polarization relaxation time used in the model.

it is a forward or a backward scan. Therefore, hysteresis will not happen at very slow scan rate either.

4.3.3 To eliminate hysteresis

Hysteresis-free inverted PSCs have been made from interface engineering or using PCBM electron transfer layer.[203, 204, 205] We argue these hysteresis-free devices are due to the improvement of interface states rather than the inverted structure, because normal structure PSCs also have been made without large hysteresis by implementing C_{60}[206] or PCBM[16]. As illustrated in Figure 4.1, both the polarization charge and the ionic charge are accumulated near interfaces. These charges could be compensated or neutralized by contact layers. For an ideal crystal without any defects, ions cannot migrate because there is no vacancy to go. Whereas, defects exist at interfaces, such as dangling bonds. Therefore, it is possible to reduce and even to eliminate ion migration and the induced hysteresis through interface engineering or decreasing defects in thin films. For uniform polarizations, there is no net charge overall and also no net charge in the bulk. All of the polarization charges are near surfaces or interfaces. In PSCs, if polarizations are presented, net charges should be presented at interfaces between perovskite and contact layers: one end of perovskite is positive and the other is negative. If we impose a contact layer with negative charges at the surface on the end with positive charges, and a contact layer with positive charges at the surface on the end with negative charges, these polarization charges are neutralized.

Therefore, this part of the hysteresis also could be reduced or eliminated through interface engineering. The slowly relaxed polarization of perovskite is also possible to be compensated by the polarization of contact layers. Fullerene and its derivatives, such as C_{60}[207] and PCBM[208, 209] are polarisable. Hence they are good candidates to compensate the polarization of perovskite and eliminate hysteresis of PSCs. Some of these materials have been successfully applied to reduce or eliminate hysteresis, such as C_{60} in Ref.206 and PCBM in Ref.205, 203, 204, 16.

4.4 Conclusion

Using numerical simulations we have confirmed that the screening effect improves PSC performance. This improvement is more obvious in solar cells made from simple methods. On the basis of our previous DFT calculations, we argue that the screening field comes from both ion migration and polarization charge. This field weakens the hindering field, promotes charge transport and improve PCEs.

Due to slow polarization and ion relaxation, the screening field is delayed, which leads to hysteresis. As the relaxation time of capacitive and polarization charges are in different scales, rate dependent hysteresis behaviors become more complicated. With the relaxation of capacitive and polarization charges, we reproduced various measured hysteresis curves.[49, 70, 143] Using similar parameters and different scan rates, we also reproduced the hysteresis effects observed by Snaith *et al.* These results suggest that hysteresis is caused by two kinds of very slow relaxations. This agreement with measured hysteresis, in turn, supports our proposed mechanism that polarization and capacitive charge take part in the screening of the hindering field and improve its PCE. We show that not only can ion migration cause hysteresis, but also polarization can as well. Although, both ion migration and polarization are bulk properties, they could be affected by interface states and contact layers. Polarizable contact materials, such as fullerene and its derivatives, may be good candidates to compensate screening fields from polarization or ionic charges and eliminate hysteresis of PSCs.

In this paper we assumed that one of the relaxations is polarization based on Gottesman's experiment,[41] but this is not necessary. Any slow relaxation response with the ability to screen external hindering field could bring about hysteresis. This slow relaxation could also be different kinds of ion migration. As polarization relaxation and ion migration usually exhibit similar behaviors, such as thickness dependence.[210, 211] To determine whether these slow responses are polarization or ion migration, more experiments and theoretical works should be carried out further. Theoretical

works on dynamics of ion migration and polarization are shown in Chapter 5, which supports ion migration and refutes MA^+ polarization.

Chapter 5

Ion migration and polarization relaxations

5.1 Introduction

In Chapter 4, we showed that both ion migration and MA^+ polarization have the ability to bring about screening fields. MA^+ polarization relaxation and ion migration usually exhibit similar behaviors, such as thickness dependence.[210, 211] Lots of theoretical work has been done to illustrate the possible effects of ion migration and ferroelectric polarization, however it is unclear whether they really occur in PSCs. Many experiments claim that they observed ion migration [74, 212] or polarization,[78, 108] but they cannot distinguish the fundamental difference between these two mechanisms. In this chapter, we discuss the dynamic relaxation behaviors of ion migration and MA^+ polarization, and try to specify their contributions.

Most perovskites are ferroelectric. On the other hand, most ferroelectric materials are perovskites. Additionally, polarizations in organic solar cells have positive effects on their photovoltaic performances,[132, 133] Frost *et al.* assumed the presence of ferroelectric polarization and used it to explain hysteresis in PSCs.[104, 47] DFT work demonstrated that organic hybrid perovskites might be ferroelectrically polarized,[52, 69, 105, 106, 107] however, there are contrary results observed in experiments.

Kutes *et al.* claimed that they directly observed ferroelectric domains in $MAPbI_3$ thin films in 2014 and 2015.[108, 78, 71] In the same year, Beilsten-Edmands *et al.* demonstrated that there is no ferroelectricity in a $MAPbI_3$ perovskite-based photovoltaic device.[75] We found that the evidence in all of these experiments is not enough to support their conclusions. Kutes *et al.* showed the polarization of $MAPbI_3$ thin films under different biases,[108] but this polarization may also come from ion

migrations. In Beilsten-Edmands' experiment, they excluded ferroelectric polarization as there is no polarization at infinite high frequency.[75] However this argument fails to estimate the intrinsic polarization. For ferroelectric materials, the polarization should be near zero at an extremely high frequency as the electronic orbitals and ions are unable to catch up with the external field and respond. All of these ferroelectric polarizations show decreasing trends at very high frequency, such as experiments in reference [109] and [110]. Fan *et al.* reported that perovskites should have ferroelectric polarizations in theory, but at room temperature they didn't observe it.[107] They drew the conclusion by comparing the I-E curves of Au/$MAPbI_3$/ PEDOT:PSS/ITO and Au/$BiFeO_3$/$SrRuO_3$. There are two issues with their experiments. The first is that they used two different devices structures. The second is that they ignored the influence of applied voltage amplitude and frequency. The amplitude and frequency of applied voltage for perovskites were 1 V and 10 Hz, whereas, corresponding values for $BiFeO_3$ were 26 V and 1 kHz. Since ferroelectric polarization is frequency dependent, these two experiments with 100 times difference in frequency cannot be directly compared.

Azpiroz *et al.* estimated that the energy barriers of defect migrations are from 0.08 eV to 0.40 eV depending on ion type.[197, 198] We also reported the energy barrier for MA^+ reorientation is about 0.01 eV to 0.098 eV, depending on the initial and final MA^+ orientations and neighboring MA^+ orientations.[52] Single cation rotation and one anion migration step are observed to be several picoseconds.[213, 214] These studies show the possibility of ion migration and polarization, but whether they contribute to PSC's photovoltaic performance and hysteresis is unknown because PSC behaviors are influenced by the collective behaviors of ion migration and polarization not the single ion migration step or polarization step.

Frost *et al.* showed a dynamic polarization model and concluded that the internal electrical fields associated with microscopic polarization domains contribute to hysteresis J-V curves in PSCs.[104] The rotation of MA^+ and migration of I^- are systematically discussed.[98] These two theoretical studies are too general. They showed the result of possible mechanisms rather than a verification of their mechanism. Leguy *et al.* used quasi-elastic neutron scattering measurements to show that MA^+ reorientate with a residence time of approximately 14 ps at room temperature.[111] Their Monte Carlo simulations demonstrated MA^+ behave either as anti-ferroelectric or ferroelectric, which depends on the interaction of neighboring MA^+. However, they did not consider the polarization of the inorganic frame, which could also contribute to ferroelectricity, such as in $BiFeO_3$.[11] Therefore, we studied the independent and

collective movements of MA^+, and also the possible polarization originating from the inorganic frames. This work was shown in Chapter 2. More importantly, the fully periodic model they used to mimic the dynamic of polarizations is not reasonable, because the fully periodic model is unable to consider the effect of surface charges, which plays a very important role in polarizations. On the other hand, the 300 nm thick layers of perovskite in PSCs are more like a thin film rather than bulk materials. We found here that behaviors of thin films (two-dimensional periodic models) and bulk materials (three-dimensional periodic models) are totally different and even show opposite phenomenon. In this chapter, we set up two and three-dimensional periodic models to mimic relaxations of ion migration and polarization in perovskites. Our result show that the charge dynamic behaviors of thin films is much different to that of bulk materials. Additionally, we exclude the MA^+ polarization contribution to hysteresis J-V curves in PSCs.

5.2 Methods

5.2.1 Coulomb Hamiltonian

Ions are considered as point charges and only the Coulomb interactions were calculated. The MA^+ dipole moment was set as 0.25 eÅ, which is described by two opposite $0.25e$ charges with a fixed distance of 1 Å. With periodic boundary conditions, the Hamiltonian is described as

$$H = \sum_{i=1}^{n}\sum_{j=1}^{n}\sum_{lmk}\frac{q_i q_j}{\overrightarrow{r_{ij}} + l\overrightarrow{a} + m\overrightarrow{b} + k\overrightarrow{c}} + \sum_{i=1}^{n} q_i \overrightarrow{F_0}\overrightarrow{r} \tag{5.1}$$

Where, n is the number of charges; $\overrightarrow{a}, \overrightarrow{b}$ and $\overrightarrow{c}$ are unit cell basis vectors; r_{ij} is the displacement between charge i and charge j; l, m and k are integers for the Ewald summation; $\overrightarrow{F_0}$ is the external field, and $\overrightarrow{r}$ is the dipole moment. For the two dimensional model, $k = 0$. Because the interaction summation converges slowly in real space, it is usually split into a long range interaction term and a short range interaction term, which converge quickly in reciprocal and real space respectively. The specific method used here is FMM,[215] which is implemented in the library ScaFaCoS ("Scalable Fast Coulomb Solver").[216] Programs were written in FORTRAN. The electric convergence energy was set as 1.0 $\times 10^{-6}$ eV for static energy calculations. For dynamic simulations, the electric convergence energy was based on relative energy error, which is set as 1.0 $\times 10^{-6}$.

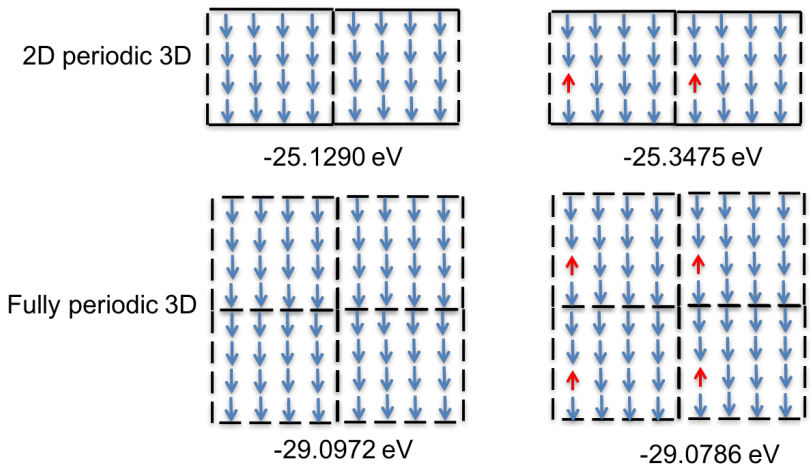

Figure 5.1: Energy cost of flipping one polar in the two and the three-dimensional periodic $4 \times 4 \times 4$ models.

5.2.2 The difference between two and three-dimensional periodic models

It is well known that polarization in a thin film induces surface charges. For the fully periodic model, there is no surface, not to mention a surface charge. Hence, polarization behaviors cannot be mimicked by the three-dimensional periodic model. In order to realize the surface charge, a two-dimensional periodic model is required. To confirm this hypothesis we built two $4 \times 4 \times 4$ grid models with all MA^+ aligned in one direction, as shown in Figure 5.1. Then we estimated energy costs for flipping a MA^+ in the two-dimensional and the three-dimensional periodic models. It is found the energy goes up when we flip a dipole in the fully periodic model, which agrees with our commonsense that dipoles prefer to align in the same direction. However, the energy goes down for flipping a MA^+ in two-dimensional periodic models. This result confirms our initial assumption. Because their behaviors differ, the result simulated with fully periodic models such as in Leguy *et al.*[111] are not reasonable as actual thin films in PSCs are very thin and have surface charges.

5.2.3 Ion migration dynamics

We made some reasonable assumptions in order to simulate ion dynamics: (1) only one defect is permitted in one inorganic cage, which is the unit cell of α phase; (2) the defect can hop from one cage to any of its six neighboring cages with one step, the hopping rate follows the Arrhenius equation. Figure 5.2A shows the α unit cell of $MAPbI_3$. The cage is colored with red lines; six possible hopping paths are shown

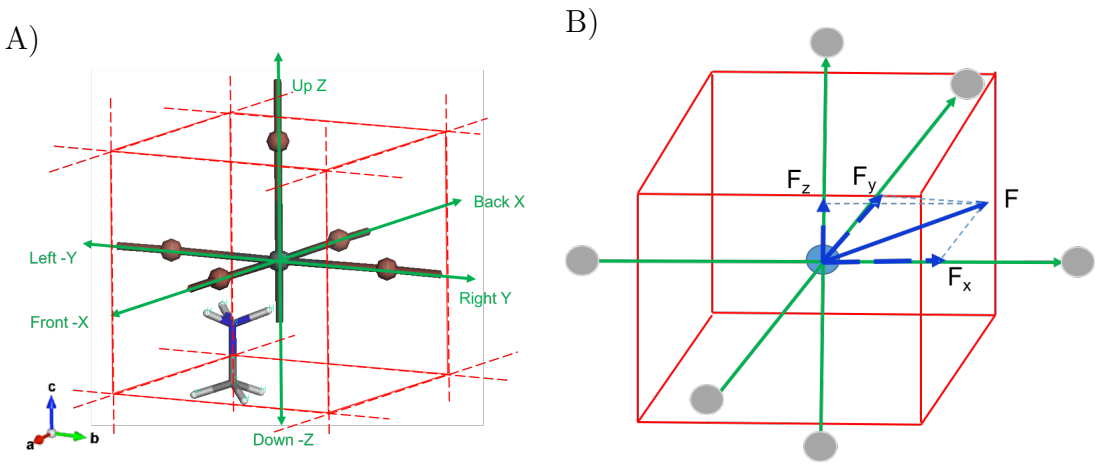

Figure 5.2: A), One grid in simulation compared to the α unit cell. Six possible hopping paths are shown in green arrows and text; B) the simplified grid and possible final locations of six possible hops.

as green arrows. These six hopping directions are x(100), -x(-100), y(010), -y(0-10), z(001) and -z(00-1). After one hop, the defect goes to one of the six sites (gray spheres) in Figure 5.2B. In our simulations, we calculate the relaxation steps rather than the relaxation time. The relaxation time can be estimated by $t = n * \delta$, where t is the relaxation time, n is the relaxation steps and δ is the time for one hop. In Figure 5.2A, lead (Pb) is shown at the center, but it is not only representative of a Pb ion, it could also be an iodine ion as the hopping behavior of $Pb_2{}^+$ and I^- should be similar.

The difference between $Pb_2{}^+$ and I^- is their hopping energy barriers, which determine the hopping time δ. According to the Arrhenius equation, the hopping rate $r = Ae^{-\frac{E_a}{kT}}$, where E_a is the activation energy. For ion migration the activation energy is the hopping energy barrier. Considering the energy barrier for MA^+ rotation is about 80 meV [52] and the energy barrier of iodine migration is about 300 meV,[197, 198] their hopping times should satisfy $\delta_{polar} : \delta_I = e^{\frac{80}{26}} : e^{\frac{300}{26}} = 1 : 4729$, where the thermal energy is 26 meV. The ion hopping time is estimated to be 66.2 ns as the MA^+ polarization rotation time is observed about 14 ps by Leguy *et al.*[**?**] The estimated ion migration time is in concert with experiments that no ion migration was observed within 200 ps.[111]

The process flow diagram of this program is shown in Figure 5.3. At first, an $x_n \times y_n \times z_n$ grid network is built. Each grid corresponds to an α unit cell. Ionic defects are randomly generated in grids with density of $1.0{\times}10^{18}$ cm^{-3}, which is high enough to make sure the external field could be screened. After defects are generated,

Kinetic Monte Carlo (KMC) dynamics was performed to reach equilibrium states. During these dynamics simulations, extra defects will be eliminated. We calculate the total energy and fields on each ion by FMM method at every step.[216] The hopping probability is $e^{\frac{-E_a}{kT}}$. We generate a random number (rdn), this ion is going to hop if $rdn < e^{\frac{-E_a}{kT}}$. If the force felt by the ion is $\overrightarrow{F}$, the ion prefers to move along the direction of $\overrightarrow{F}$. Thus, we call it the driving force. Due to this driving force, the energy barrier for the ion hopping along path j (j=1,6) with displace $\overrightarrow{R_j}$ lowers. It becomes $E_a - \overrightarrow{F}\overrightarrow{R_j}$. Then its hopping rate could be $r_j = A\ e^{\frac{-E_a + \overrightarrow{F}\overrightarrow{R_j}}{kT}}$. The hopping probability of a specific path P_j is calculated by $P_j = r_j / \sum_{i=1}^{6} r_i$. A random number ($rdn$) between 0 and 1 was generated for each hop, if $\sum_{i=1}^{j-1} P_i < rdn < \sum_{i=1}^{j} P_i$, the ion hops along path j.

Relaxation lifetimes are estimated from relaxations between the equilibrium state with certain external fields to the equilibrium state without external fields. In these simulations, we record net fields, non-combined defect charges and system Coulomb energy. The relaxation lifetime step is obtained by fitting the field in the z direction with the exponential decay function $Fz(i) = Fz_0 e^{-\frac{i}{\tau}}$, where i is the simulation step and τ is the relaxation lifetime step. The system was considered to have reached an equilibrium when $|\frac{E_i - E_{i-1}}{E_i}| < 10^{-6}$ during the last 200 steps, where E_i is the energy at the current step and E_{i-1} is the energy at the last step.

5.2.4 MA^+ dipole dynamics

Similar to ion migration dynamics, dipoles are randomly aligned in every grid and then a classic dynamic Monte Carlo simulation is run under a certain external field. When the system has reached an equilibrium state, we remove the external field and let the system relax to another equilibrium state without external fields. Due to the screening effect of inorganic frame, the dipole moment we used is 0.25 eÅ, which is smaller than the dipole moment of 0.477 eÅin its gas phase

The smaller dipole moment of 0.25 eÅ was used due to a screening effect when compared to the gas phase MA^+ dipole moment of 0.477 eÅ.[69]

MA^+ dipoles are described by two opposite 0.25 e charges with a fixed distance of 1 Å. Hence, Hamiltonian of polarizations also can be described by Equation 5.1. The overall flowchart is the same with the dynamic of ion migrations. Two types of dynamics were tried.

The first is that dipoles are allowed to align in every direction and move continuously. We calculate forces on each charge and torques of each dipole. The torque is

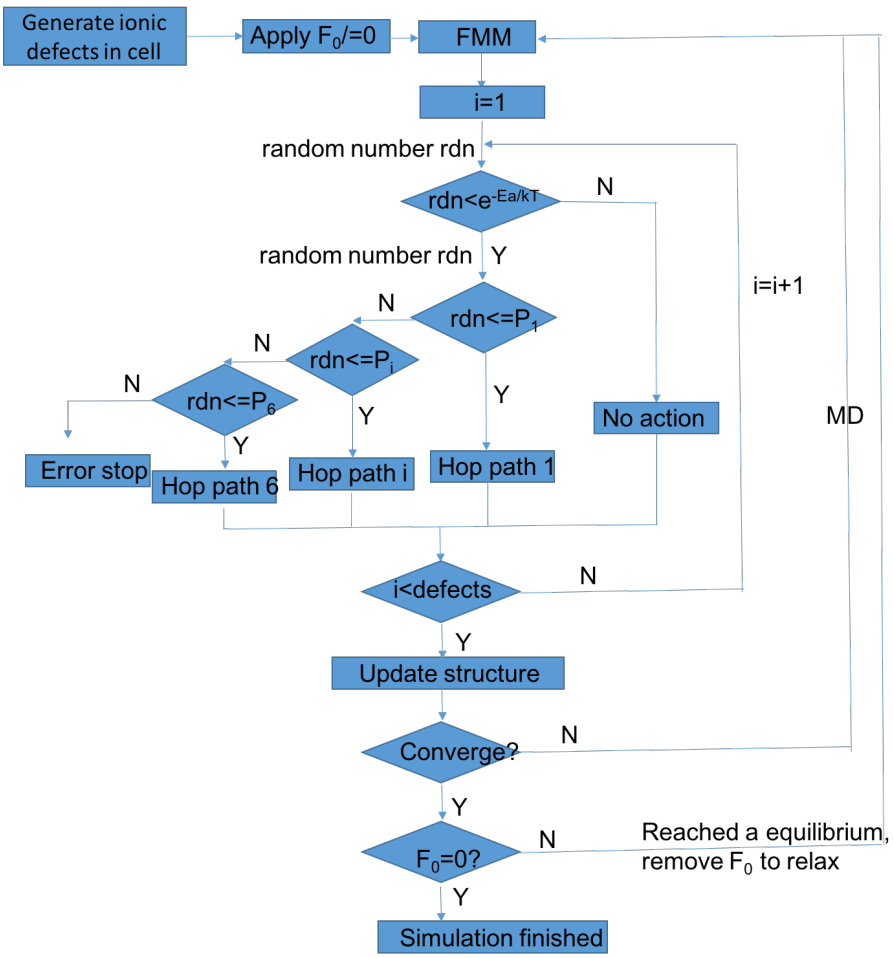

Figure 5.3: Flowchart of the Metropolis Monte Carlo dynamics of ion migrations. We first run dynamic to reach an equilibrium state with an external field. Then we remove the external field, and let it relax to an equilibrium state without external fields. The relaxation lifetime steps are estimated from the relaxation between these two equilibrium states.

estimated by $T = 0.25e\ \overrightarrow{r_+} \times \overrightarrow{F_+} - 0.25e\ \overrightarrow{r_-} \times \overrightarrow{F_-}$. The rotation angle is obtained by $\alpha = |T|dt$, where dt is the step scale. Physically, $dt = \delta t/M$, where M is the moment of inertia of MA^+ and δt is the time step. In this work, M was set as one unit and $dt = 10$. The rotation angle of each step is between 0 to 30 degree. The rotation probability is $e^{\frac{-E_a}{kT}}$.

The second is a hopping model. Only 26 possible alignments are allowed for MA^+ ions. There are 6 face centers (010), 8 corners (111) and 12 edges (110) of grids. The rotation probability is also defined by $e^{\frac{-E_a}{kT}}$, where E_a is the barrier energy for reorientation. The calculation difference between this dipole dynamic and the ion migrations dynamic is the probability calculation of each rotation. For ion migration,

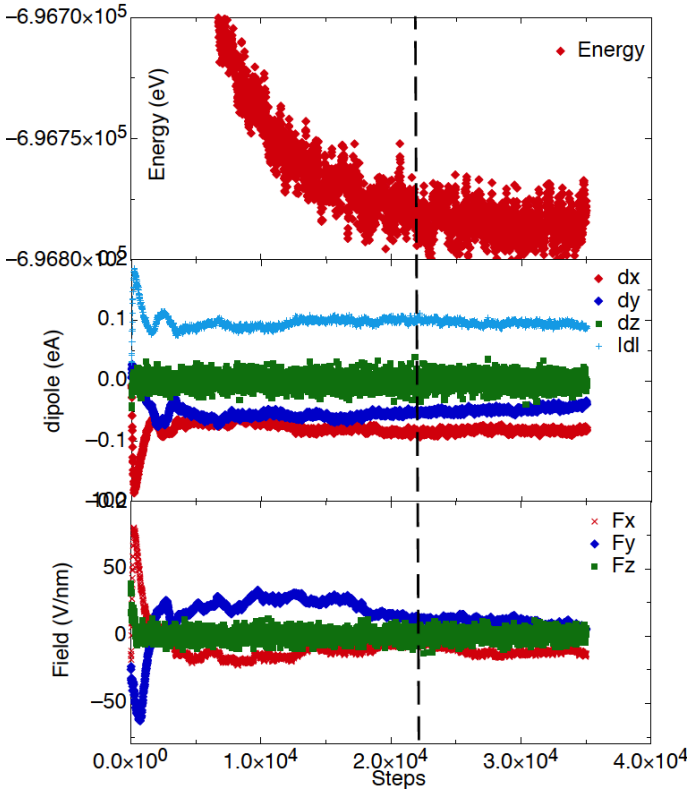

Figure 5.4: Dynamic energies, dipoles and fields in a two-dimensional periodic 50 ×50 ×20 grids (31.5 ×31.5 ×12.6 nm^3) model.

the driving energy is $q\overrightarrow{F}\overrightarrow{r}$, while it is $\overrightarrow{F}\delta\overrightarrow{p}$ for dipole rotation, where $\delta\overrightarrow{p}$ is the dipole moment change induced by the MA^+ reorientation.

5.2.5 Dynamics simulation convergence criteria

Figure 5.4 shows the dynamic simulation energies, dipoles and fields in a two dimensional 31.5 ×31.5 ×12.6 nm^3 model. Before the 22,000th step, energies, dipoles and fields are relaxing towards equilibrium states. It reached a stable state after the 25,000th step. Because these relaxations are Metropolis Monte Carlo dynamics, energies fluctuate during steps from 22,000 to 35,000. Even though we know the system reached equilibrium at step 22,000, there is no significant change in energy difference at each step from step 5,000 to step 35,000. Hence, there is no way to estimate the equilibrium state based on energy difference at each step. The dynamic energy difference in an equilibrium state and a non-equilibrium state is whether the averaged energy is decreasing. Therefore, we use the average energy of previous N steps. The

N steps average energy difference was calculated by:

$$DE = \overline{E_{n-N,n}} - \overline{E_{n,n+N}} \tag{5.2}$$

where $\overline{E_{n-N,n}}$ and $\overline{E_{n,n+N}}$ are the average energies of the previous N steps and the current N steps. We tried to use N=100, but it still failed to determine the convergence state. Sometimes the field has not arrived at relative stable value. Others will continue to run even after the system has reached a very stable state (the criteria aren't met). In our simulations, we set three criteria to determine the convergence state. The first criteria is the N-step average energy difference, which is set as $<= 0.02$ eV. The second is relative N-step average difference, $(\overline{E_{n-N,n}} - \overline{E_{n,n+N}})/\overline{E_{n,n+N}}$, which is set as $<= 1.0 \times 10^{-4}$. The last is the N-step average field, $(\overline{F_{n-N,n}} - \overline{F_{n,n+N}})/\overline{F_{n,n+N}}$, which is set as $<= 0.1\%$. When these three convergence criteria were continuously satisfied for 10 times, the system was considered to be reached the equilibrium state.

5.3 Result and discussion

5.3.1 Pre-relaxation of ion migration

Ionic defects are randomly generated in all grids. Relaxation lifetime is estimated from the relaxation between two equilibrium states. Therefore, a pre-relaxation to reach an equilibrium state is required. As shown in Figure 5.5A-C, total charges in half cells ($0 < z <= 0.5d$, where d is the cell thickness) decrease with relaxation. It is found that charges in thicker thin films decrease slower. This suggests that the screening field induced by ion migration relaxation relaxes slower in thicker thin films. After a long relaxation, net charges in half cells converge. The converged number of charges in each half cell is 76, 77 and 71 for the field of 1 V/300 nm with thicknesses of 63 nm, 126 nm and 189 nm grids respectively. For a stronger field 10 V/300 nm, these charges are 783, 784 and 812 for thicknesses of 63 nm, 126 nm and 189 nm grids respectively. For the initial field of 100 V/300 nm, the number of charges are 7300, 7314 and 7348 under equilibrium states. The net number of charges is approximately proportional to the applied external field. Meanwhile, there is no obvious thickness dependence. Figure 5.5D shows the field change in pre-relaxations. The initial field equals the applied external field. During relaxation, the applied field is screened by ions and decreases. At the equilibrium state, the average net fields are -2.235 $\times 10^{-4}$ V/nm, -6.272$\times 10^{-4}$ V/nm and -6.925$\times 10^{-4}$ V/nm for thickness of 63 nm, 126 nm and 189 nm, respectively, comparing to the external field of 33.333$\times 10^{-4}$ V/nm. Though the relaxation energy change at each step is very small, it is always lowering. Due to

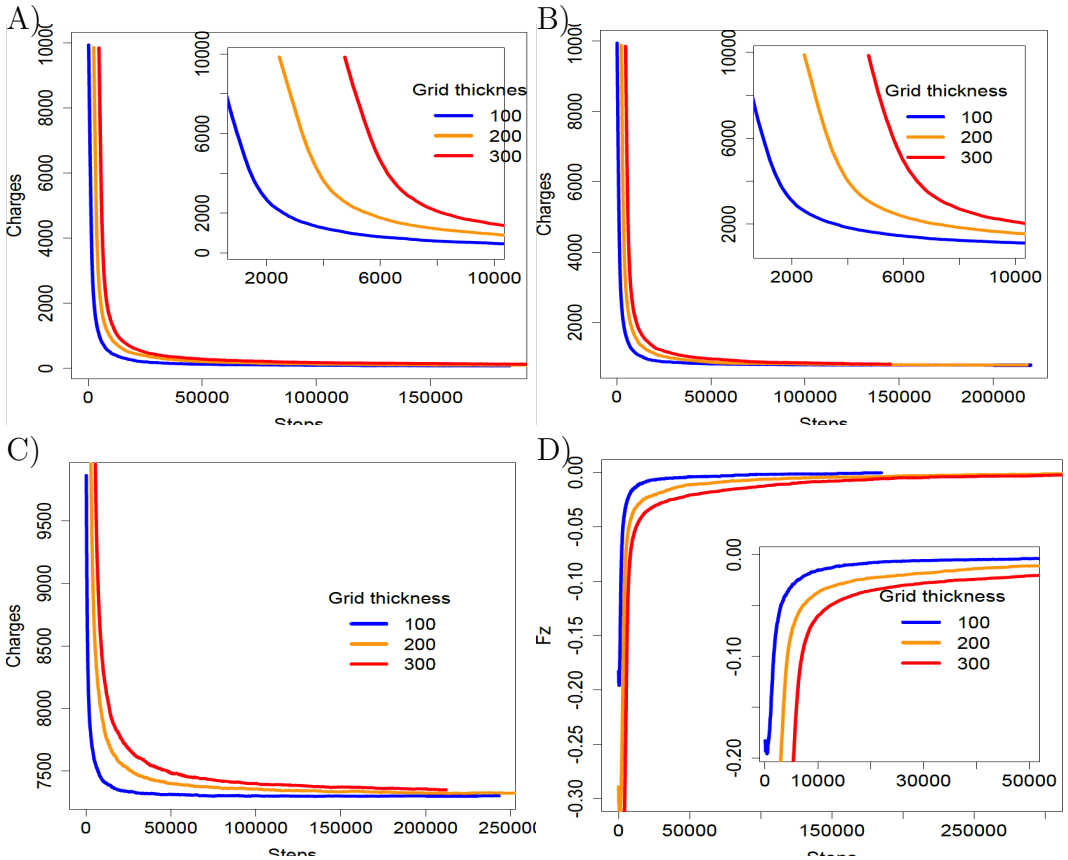

Figure 5.5: Pre-relaxation: number of charges in half cells of two-dimensional periodic models with sizes of 1000×1000×100 (≈ 630 nm × 630 nm× 63 nm), 1000×1000×200, 1000 × 1000 × 300 with fields of 1 V/300nm A); 10 V/300nm B) and 100 V/300nm C). D) The average z component field in cells with different thicknesses under the external field of 1 V/300nm.

extremely slow relaxation at the end, we set reasonable convergence criteria to save time.

5.3.2 Relaxation of ion migration between two equilibrium states

After pre-relaxation, ion diffusion models reach equilibrium states. We then remove the external field and let them relax again. This relaxation process will be used to estimate its relaxation lifetime. Figure 5.6A) shows the average fields in the z direction in thin film models. The simulated data is shown with points and fitting results are lined by curves. It is found that these fields decrease exponentially with relaxation steps. The thicker film decays slower. We fit these curves with the exponential decay function $F_z = A \times e^{-\frac{x}{\tau}} + C$, where τ is the relaxation lifetime steps and x is the

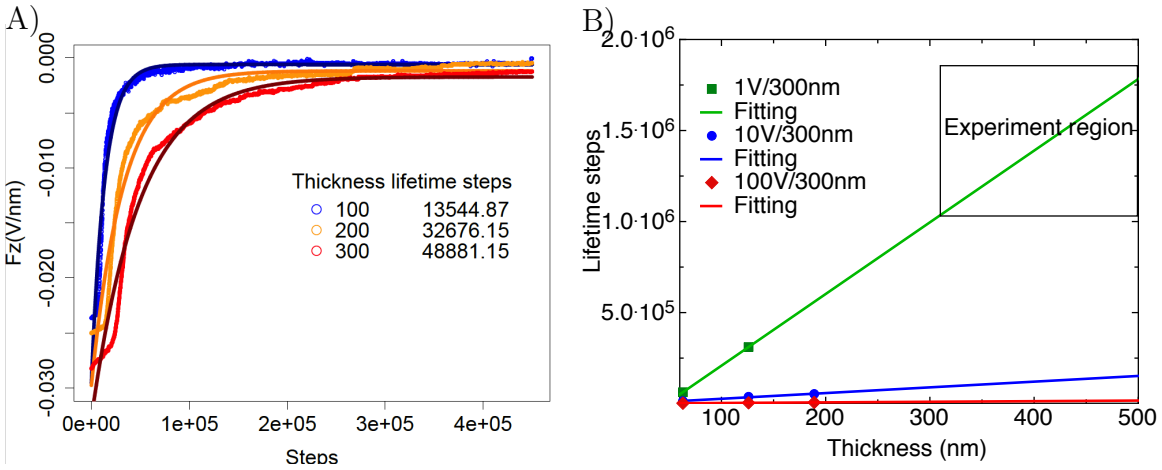

Figure 5.6: A), Fields decay in ion relaxation of two-dimensional periodic models with sizes of 1000 × 1000 × 100 (≈ 630nm × 630nm× 63nm), 1000 × 1000 × 200 (≈ 630nm × 630 nm× 126 nm), 1000 × 1000 × 300 (≈ 630nm × 630nm× 189 nm) with field of 10V/300nm; B) The relation between fitted relaxation lifetime step, thickness and applied external fields.

step. These estimated relaxation lifetimes are shown in Table 5.1. For these initial external field of 10 V/ 300 nm models, relaxation lifetime steps are 13,544, 32,676 and 48,881 for thicknesses of 63 nm, 126 nm and 189 nm grids respectively. Relaxations of these models with different initial external fields are also investigated. Figure 5.6B shows relaxation lifetime steps of models with different thickness and external fields. The relaxation lifetime steps increase linearly with the thin film thickness for the same initial external fields. It is also seen that the equilibrium state with a stronger initial external field decays more rapidly. As shown in Table 5.6, 10 times higher fields will roughly lead to 5 times faster decay. In experiments, thicknesses of typical PSCs are 300 nm - 500 nm and the external fields are 1 V/300 nm to 1 V/500 nm, the relaxation lifetime is in the region of 1 - 3 $\times 10^6$ steps. Assuming each step of ion migration and polarization are chemical reactions, their reaction rates follow the Arrhenius equation $k = Ae^{-E_a/k_BT}$, where E_a is the activation energy. For ion migration and polar rotation, these activation energies are equal to their energy barriers.[52] Therefore, the time per step of ion migration and polarization are $t_i : t_p = e^{-0.32/0.026} : e^{-0.08/0.026} \approx 1 : 10^4$. If the rotation time of polar is 0.3 ps - 50 ps,[111, 213, 214] the time for one step ion migration should be 3 ns - 500 ns. **Thus, the real relaxation lifetime of ion migration induced screening field is 3 ms - 1,500 ms, which is in good agreement with experimental delay times to produce hysteresis.[51, 70, 217]** Hence ion migration relaxation is a very possible source to induce hysteresis.

Table 5.1: Ion migration relaxation lifetimes of two-dimensional periodic models with different thicknesses and different external fields. Thin film areas are 630×630 nm^2. Different simulations produce different lifetime relaxations (most simulations within a relative error of 30%) due to the random process, thus, only the magnitude is meaningful.

Thickness	**Lifetime steps**		
Grids (nm)	**1V/300nm**	**10V/300nm**	**100V/300nm**
100 (63)	62,731	13,545	2,331
200 (126)	310,761	32,676	4,405
300 (189)	NA	48,881	6,508

5.3.3 Polarization relaxation in the continuous model

Figure 5.7A and Figure 5.7B show the total fields and dipole moments of $63 \times 63 \times 12.6$ nm^3 and $63 \times 63 \times 63$ nm^3 models in pre-relaxation. Initial net dipole moments in all directions are near zero as dipoles are randomly aligned. Average dipoles in the z direction are immediately polarized to respond the external field. It reaches a relative stable state after about 3,000 steps. **Whereas, average dipole moments in x and y directions are still relaxing even near equilibrium states. This finding suggests fields and dipoles relax slower on periodic directions.** Therefore, polarization relaxation lifetime was longer in Leguy's simulation[111] because their models are three-dimensionally periodic. In order to confirm this hypothesis, we also calculated dipoles relaxation in three-dimensional periodic models in Section 5.3.5. All of the fields and dipole moments are stable at the end of pre-relaxations. Figure 5.7C-D show the fields and dipole moments after removing external fields when they reached equilibrium states. Relaxations of z component fields and dipoles decay exponentially, while, these parameters in x and y directions decay slowly and linearly.

The fields in the z direction are fitted with the exponential decay functions (orange line). These fitted parameters give relaxation lifetime steps. These fitted functions are $Fz = -0.055\, e^{\frac{x-37510}{557.67}} - 0.0039$ and $Fz = -0.054\, e^{\frac{x-101610}{573.70}} - 0.0029$ for thicknesses of 12.6 nm and 63 nm, respectively. Hence, their lifetimes are 557.67 and 573.70 steps. If one step is the rotation of polar and the time for each rotation is 0.3 ps -50 ps[111, 213, 214], then the real relaxation time will be in the range of 170 ps to 28.5 ns. These relaxation lifetimes are too short compared to experiment delay times of 1 ms - 1 s. Thus, it is impossible for MA^+ polarization to induce hysteresis with experimental delay times.

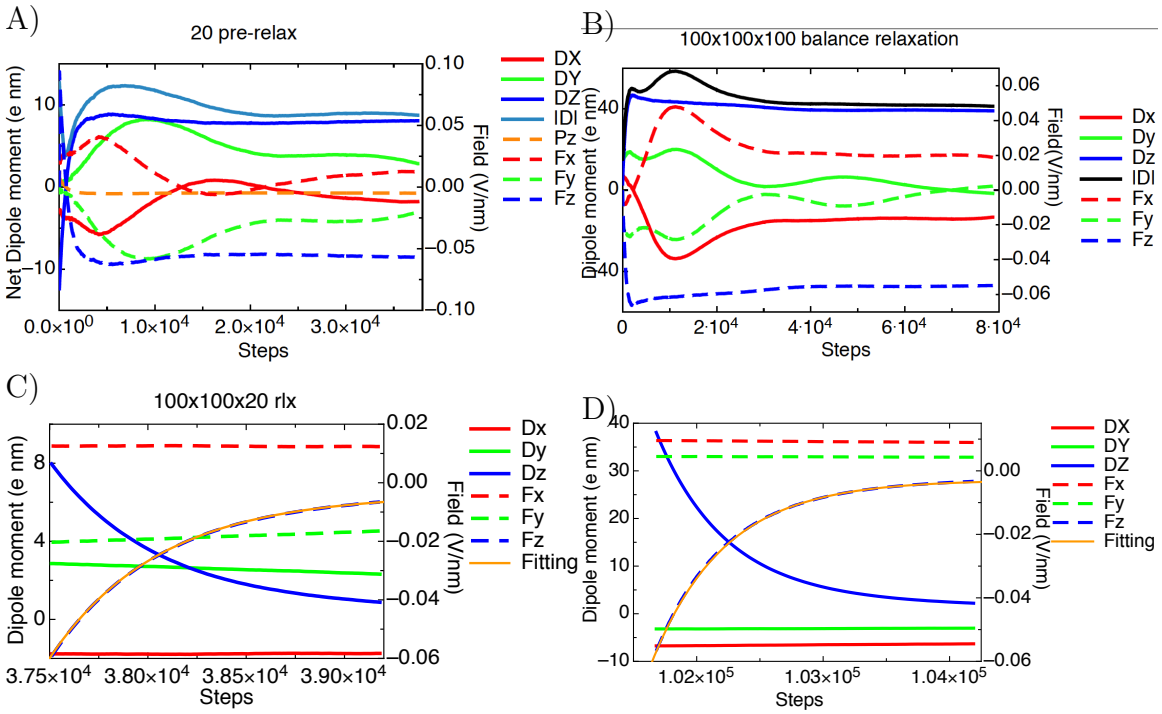

Figure 5.7: Fields and dipole moments during pre-relaxation of two-dimensional periodic model $63 \times 63 \times 12.6$ nm^3 A) and model $63 \times 63 \times 63$ nm^3 B); Fields and dipole moments during relaxation between two equilibrium states of model $63 \times 63 \times 12.6$ nm^3 C), and model $63 \times 63 \times 63$ nm^3 D).

5.3.4 Polarization relaxations in two-dimensional periodic hopping models

In the continuous model, the MA^+ is allowed to align along any directions. Due to non-uniform potential surfaces, MA^+s prefer to align on specific directions.[52, 218, 219] There are 6 face centers (010), 8 corners (111) and 12 edges (110) of grids. Three different thickness models were built with grids of $63\times63\times12.6$ nm^3, $63\times63\times31.5$ nm^3 and $63 \times 63 \times 63$ nm^3 and applied initial external fields of 1 V/300 nm, 10 V/300 nm and 100 V/300 nm. All of the dipoles were randomly aligned at the initial step. KMC dynamics simulations were then performed to reach equilibrium states. Figure 5.8A-C show the dipole moment in z directions at the initial state, the equilibrium state with the external field (100 V/300 nm) and the equilibrium state without external field of the in $63 \times 63 \times 63$ nm^3 cell. Figure 5.8A shows the initial randomly generated dipoles. Dipoles are uniformly aligned. At the equilibrium state with external fields, dipoles are positively polarized, as shown in Figure 5.8B. Dipoles prefer to align head-to-tail and form dipole lines. While, neighboring dipoles are aligned oppositely. The alignment is similar to the results of simulation done by others.[104] This polarization

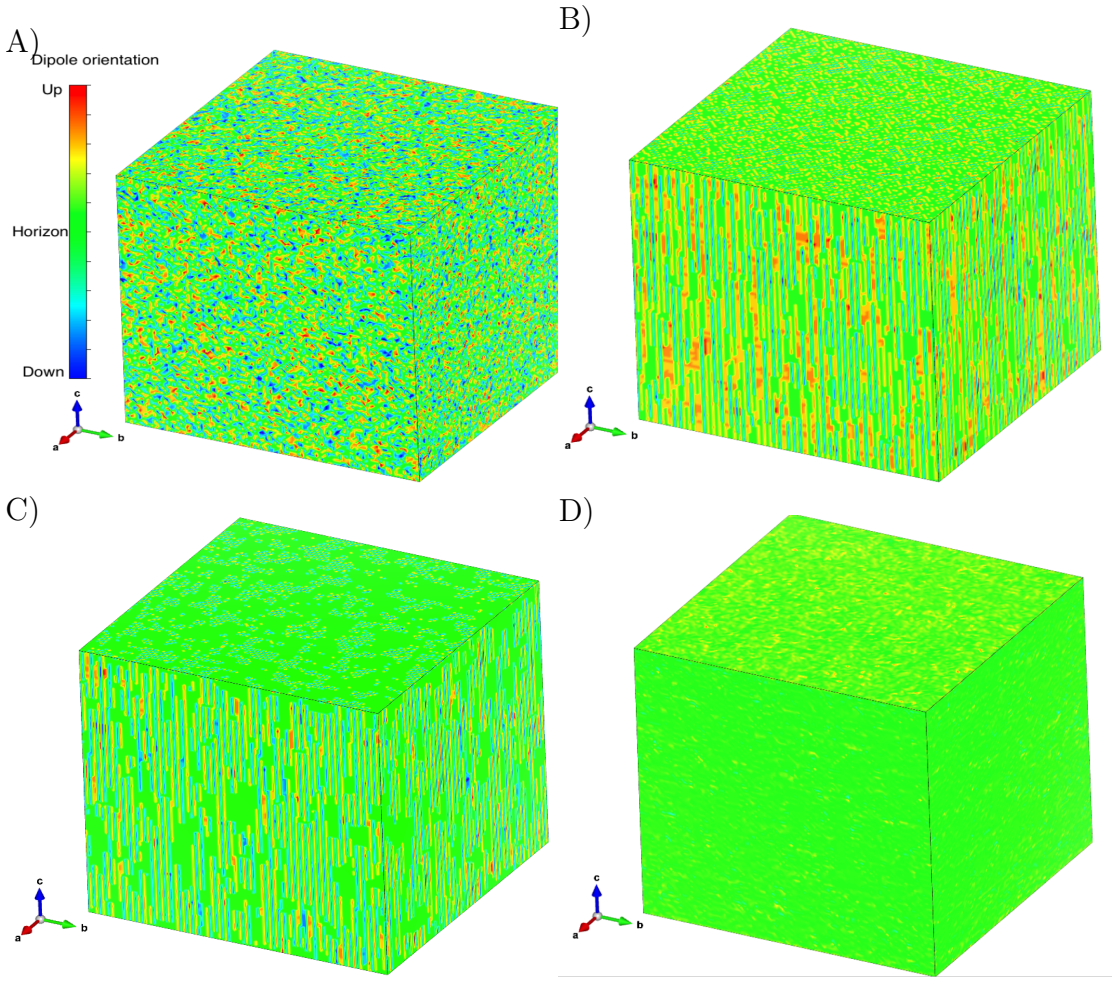

Figure 5.8: z component polarizations in $63 \times 63 \times 63$ nm^3 cell of two-dimensional periodic model with the applied initial external fields of 100 V/300 nm at initial state A), equilibrium state with external field B) and equilibrium state without external field C). D) is the total field in $63 \times 63 \times 63$ nm^3 cell at equilibrium state with external field.

screens the external field. Total fields in the thin film are nearly uniform, as shown in Figure 5.8D. The polarization will disappear during the relaxation after we remove the external fields. Figure 5.8C demonstrates the dipole alignment at the equilibrium state without external fields. Domains can be seen from the top. However, within a domain, dipoles aligned in lines opposite to neighboring lines, which produces zero polarization overall.

Figure 5.9A-B shows the dynamics of summation of fields in all grids during dynamic simulations with an initial external field of 10 V/300 nm. The average field can be calculated by dividing the summation of field with the number of grids. For the model of $63 \times 63 \times 12.6$ nm^3, at the beginning, z component total field is 1.24×10^4

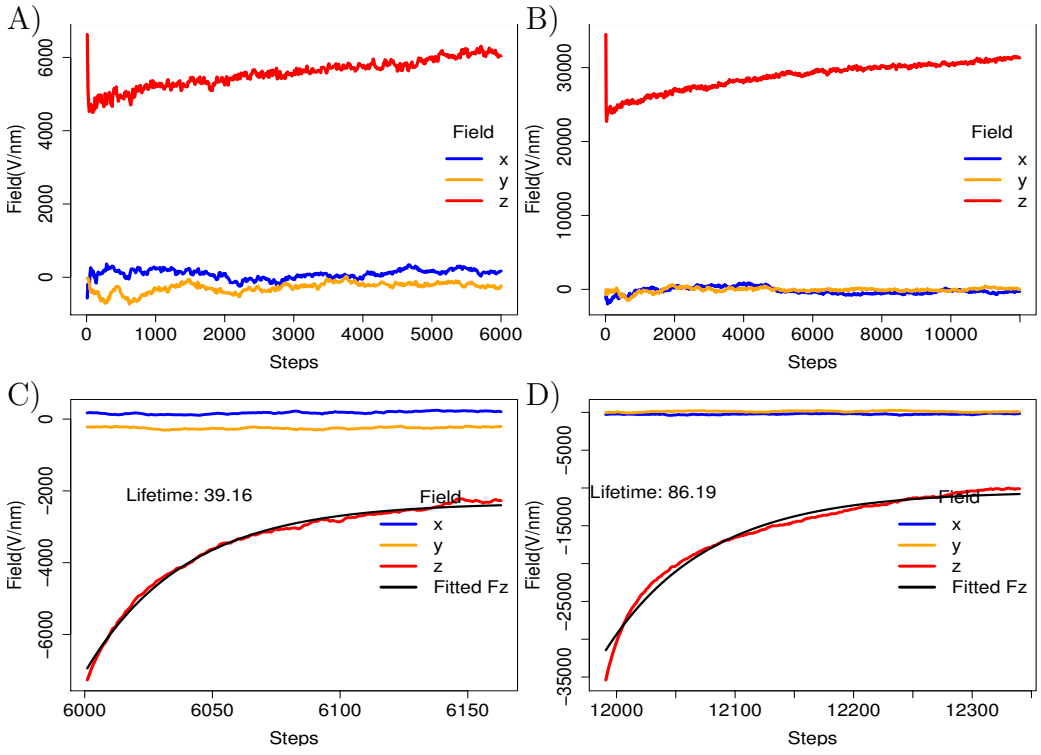

Figure 5.9: Total fields of polar dynamics model $63 \times 63 \times 12.6$ nm^3 A) and model $63 \times 63 \times 63$ nm^3 B) during pre-relaxation with the initial external field of 10 V/300 nm; Total fields of model $63 \times 63 \times 12.6$ nm^3 C), and model $63 \times 63 \times 63$ nm^3 D) during relaxation between two equilibrium states.

V/nm, then its average field is $\frac{1.24\times10^4}{2\times100\times100\times20}$= 0.031 V/nm, which is almost equal to the external applied field (10 V/300 nm = 0.033 V/nm). This is because dipoles are randomly aligned, the net dipole should be around zero without screening. In the next 20 steps, the external field is screened to one third of the original value. After that, the total field increases to 0.015 V/nm when the system reached equilibrium. At this time, the screening field is 0.033- 0.015= 0.018 V/nm. Then the external field is removed to let the dipoles relax again. The screening field decays. The relaxation lifetime is estimated by fitting with an exponential decay function. Their lifetimes are 39.16, 61.1 and 86.19 steps for thickness of 12.6 nm, 31.5 nm and 63 nm, respectively. They increase with thickness. For the stronger initial field of 100 V/ 300nm, all of them decay faster. The lifetime steps are 12.23, 13.40 and 13.87 for thickness of 12.6 nm, 31.5 nm and 63 nm, respectively. This indicates that dipoles relax faster under stronger initial fields. The experimental initial field is about 1 V/300 nm and their thickness is approximately 300- 500 nm, corresponding to 476-793 grids. We extrapolate the data simulated under a field of 1 V/300 nm to the experimental

Table 5.2: Polarization relaxation lifetimes of two-dimensional periodic hopping models with different thicknesses and different external fields.

Thickness	**Lifetime steps**		
Grids (nm)	**1V/300nm**	**10V/300nm**	**100V/300nm**
20 (12.6)	993*	39.16	12.23
50 (31.5)	319	61.01	13.40
100 (63)	472	86.19	13.87

*noise is too obvious to fit, not reliable.

thickness region, their lifetimes are estimated between 300- 1000 steps. Hence, the polarization relaxation lifetime is about 0.1 ns -50 ns if the time for each rotation is 0.3 ps - 50 ps[111, 213, 214]. Therefore, the polarization relaxation is excluded to be a source of hysteresis as the scale of its relaxation lifetime differ too much to the experimental delay time in hysteresis.

5.3.5 Polarization relaxations in three-dimensional periodic hopping models

To have a direct comparison, we also set up two three-dimensional models to perform dipole relaxations under two different external fields. Cell sizes are $31.5 \times 31.5 \times 31.5$ nm^3(A) and $63 \times 63 \times 63$ nm^3 and initial applied external fields are 10 V/ 300 nm and 1 V/ 300 nm. There are periodic conditions in all directions. Dipoles relax slower than two-dimensional periodic models under the same conditions. The lifetime in three-dimensional periodic models are several hundred times longer than that in two-dimensional periodic model. Additionally, lifetimes in two-dimensional periodic models are independent on the size of simulated unit cell, however, they do depend on the initial fields. The lifetime for 10 V/300 nm is about 5000 steps, while the lifetime for 1 V/500 nm (0.0020 V/nm) ranges from 50,000 to 200,000 steps. If the time for each rotation is 0.3 ps - 50 ps[111, 213, 214], then the collective relaxation lifetime is around 150 ns- 10 μs, which is shorter than Leguy's simulation of timescale for a domain wall to traverse a typical device to be 0.1- 1 ms. The discrepancy between us is due to the field influence, as we have shown that the dynamic relaxation is strongly dependent on initial fields. For a domain wall reverse in Leguy's experiment, the field is weaker than the field we applied. Hence, their estimated domain traverse time should be longer than our simulations.

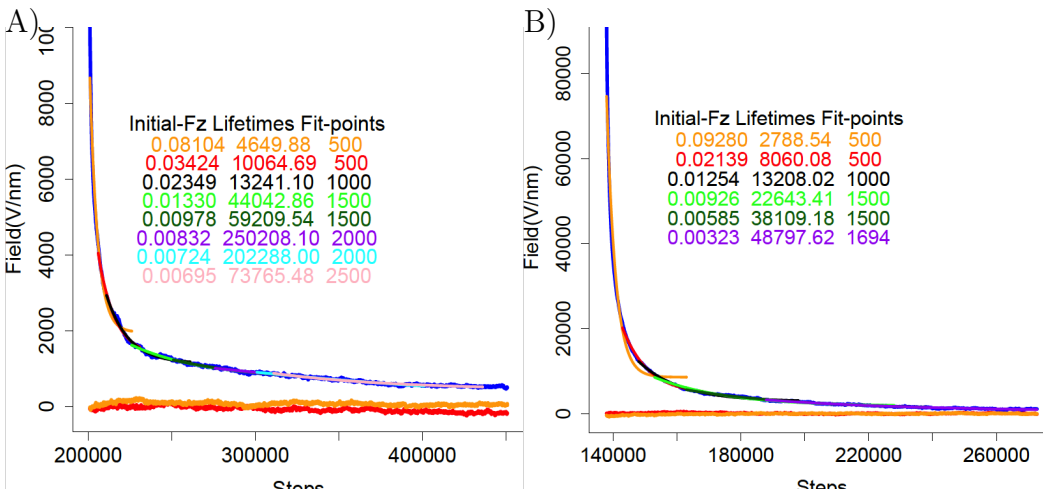

Figure 5.10: Field relaxations in the three-dimensional periodic 31.5 × 31.5 × 31.5 nm^3(A) and 63 × 63 × 63 nm^3 (B) models.

5.4 Conclusion

In this chapter, we revealed that dipole relaxation behaviors in two and three-dimensional periodic models are totally different. Because polarization induces surface charges, which cannot be implemented in the fully periodic model, conclusions of polarization relaxation behaviors simulated by three-dimensional periodic model are misleading. The polarization in PSCs should be mimicked with two-dimensional periodic model. Based on simulation results, we draw three conclusions. Firstly, both the ion migration and polarization could counteract with external fields and induce screening fields. This suggests both can possibly induce screening field and hysteresis based on the conclusion made in Chapter 4 that the slowly relaxed screening field induces hysteresis. Secondly, the relaxation processes of ion migration and polarization are dependent on the initial field strength and thin film thickness. The relaxation time increases linearly with thin film thickness, and it decreases drastically with increasing initial field. Lastly, the ion migration relaxation lifetime of experimental thin films are estimated in the region of 1 - 3 $\times 10^6$ steps corresponding to 3 ms - 1500 ms. This estimated region is in concert with experimental delay times to produce hysteresis.[51, 70, 217] However, the relaxation lifetime of polarization is estimated to be 50 ns, which is about six magnitudes smaller than experimental delay times. Hence, the polarization of MA^+ is not a plausible reason to induce hysteresis in PSCs.

Chapter 6

Low Density of States Contribute High Open Voltage in PSCs

6.1 Introduction

Open-circuit voltage (V_{oc}) of a solar cell is always lower than the absorber band gap. The difference between them is called open-circuit voltage deficit. A large V_{oc} deficit means large potential energy lost and leads to a lower performance. The effort to reduce the open-circuit voltage deficit never stops. Most of this kind of work is focusing on fabrication technics and methods,[220, 119, 221] a few of them focus on the influence from the intrinsic properties of perovskites. Here, we discuss the open-circuit voltage deficit from the aspect of material itself and propose that we can reduce the open-circuit voltage deficit by using materials with low DOS and small effective mass.

PSCs have realized Power Conversion Efficiencies (PCEs) up to 22 %.[33, 131, 24, 12, 1, 4] Excellent electron and hole diffusion ability[28, 29] and a very wide absorption wavelength range with high IPCE[34, 25, 62] are considered as two main factors for PSC's high performance. Both theoreticians[165, 64, 163, 149, 67] and experimentalists[28, 29, 222, 159] are trying to find more fundamental reasons. They attribute the high performance of PSC to its proper band gap and large static dielectric constant.[64, 67, 63, 52] Others believe that polarization of perovskite benefits its high PCEs through grain boundary[104, 69, 223, 105] or screening effect.[52] By careful examination, we found that the reason of excellent electronic properties found by both experimental and theoretical works only benefits the high output current, whereas the maximum J_{sc} (21 mA/cm^2) of PSCs[1] is much lower than the J_{sc} (30 mA/cm^2) of CdTe solar cells[224], which has similar band gaps. Therefore, there must be other reasons.

The other most possible reason is the high V_{oc}, which has not been fully discussed for PSCs. Before our investigation, we collected experimental band gaps and V_{oc} related data of different type solar cells. For amorphous silicon, its band gap ranges from 1.55 to 2.10 eV,[122] whereas its highest V_{oc} is only about 0.98V.[123] Its voltage deficit is 570 mV. For multi-crystalline silicon solar cells, the highest V_{oc} is 660 mV, which is 460 mV lower than its band gap at 1.12 eV.[124] The maximum V_{oc} of CdTe solar cells is 1.10 V,[225, 126, 226] which is 400 mV lower than its band gap of 1.5 eV at 300K.[125] However, the high V_{oc} in CdTe solar cell is obtained by sacrificing its PCE. For CdTe solar cells with V_{oc} larger than 1.0 V, the maximum PCE is 13.6%.[226] For the best performance CdTe solar cell the voltage deficit is 630 mV.[124] For a PSC, its V_{oc} reaches 1.14 V corresponding to the band gap of 1.57 V.[1] The voltage deficit is 430 mV. It is obvious that the PCE is higher when its voltage deficit is lower. Therefore, we are going to discuss some factors related to V_{oc} and check whether there is a rule governing solar cell's V_{oc} and performance.

Open-circuit voltage deficits were discussed in organic solar cells,[115, 116, 117, 118] quantum dot solar cells,[119] a-Si:H/c-Si heterojunction solar cells.[120, 121] In quantum dot solar cells, it was found that sub-bandgap states are the most likely origin of the high V_{oc} deficit.[119] For bulk heterojunction solar cells, theoretical works showed that the V_{oc} depends on (1) the donor-acceptor energy gap; (2) charge-carrier recombination rates; (3) illumination intensity; (4) the contact work functions (if not in the pinning regime); and (5) the amount of energetic disorder.[120, 121]

In 2013, Edri et al. showed that PSCs can realize high V_{oc} up to 1.3 V. While, this high V_{oc} is based on its large band gap of 2.3 eV, Its open-circuit voltage deficit is as large as 1.0 V. Shao's experiment showed that reducing the energy disorder in the fullerene electron transport layer through a simple solvent annealing process increases the V_{oc} from 1.04 V to 1.13 V.[227] It was also found that the tuning of the work function can improve V_{oc} in devices.[228] Chen et al. demonstrated that the limiting of V_{oc} of $CH_3NH_3PbBr_3$ PSCs is due to the interface loss induced by the charge extraction layer rather than by bulk dominated recombination losses.[129] In theory, Yang et al. illustrated that the reduced bimolecular recombination is the origin of high V_{oc}.[127] With numerical simulations, we also showed the inert interface defects, long charge carrier lifetime and strong incident light intensity increase V_{oc}.[57] Kirchartz et al. showed that photon recycling enhances the V_{oc} in the range of 10-100 mV.[229] The upper limit of V_{oc} was estimated to be 1.24-1.32 V based on different recombination mechanisms.[230]

For organic solar cells, Garcia-Belmonte et al. found that small tails of DOS distribution will lead to high V_{oc}.[115] Sulas et al. also showed that the increased density of charge-transfer states causes V_{oc} loss.[116] The same conclusion was observed by Collins et al.[118] So the question is whether DOSs in perovskite contribute to its solar cell high V_{oc}? Specially, there are some works reported that perovskites exhibit low DOSs at the edges of the valence and conduction band.[128, 231]

In this chapter, we show that besides the defects, charge carrier lifetime and incident light intensity, there are other parameters that affects V_{oc}. They are N_c and N_v. With two different methods based on *ab initio* calculations, we calculated the effective conduction band and valence band DOSs (N_c and N_v) of silicon, CdTe and typical hybrid perovskites, such as $CH_3NH_3PbI_3$[196, 232] and $HC(NH_2)_2PbI_3$,[142, 233, 234, 235, 236] which have been widely used in solar cells. It was found that N_c and N_v of hybrid perovskites and CdTe are several times lower than that of silicon. These low N_c and N_v are in good agreement with the low DOS observed by Endres et al.[128, 231] By implementing these N_c and N_v into the numerical model we developed for PSC,[57] we found that low N_c and N_v in perovskite materials could contribute 100 mV higher V_{oc} compared to the 'PSC' with silicon's N_c and N_v.

6.2 Methods

6.2.1 DFT calculation details

In this chapter, we calculated N_c and N_v of typical perovskites, silicon and CdTe in order to find out the effect of DOS on their power conversion performance. Perovskite structures came from Ref. 8. All of the calculations are performed by VASP.[144, 145] Silicon band structure based on GGA-PS functional,[151] GW method[237, 238] and HSE[239, 240] functional are carried out and compared in order to find the optimum method. It is found that the GW method and HSE functional do give correct band gaps of 1.10 eV and 1.14 eV comparing to 1.12 eV of experiments. Whereas, their effective masses are very similar to the masses from GGA-PS functional. Effective mass calculations in $MAPbI_3$ have been carried out with HSE functional and GW methods.[241, 149] The harmonic mean effective electron and hole masses of HSE+SOC calculations are 0.18 m_0 and 0.22 m_0 respectively.[241] Their average effective masses are 0.19 m_0 and 0.25 m_0 for the method of SOC+GW.[149] Both of these effective masses close to 0.192-0.199 m_0[52] and 0.21 m_0 (Shown in Table D.3) in our GGA-PS calculations. The effective mass error between our GGA-PS method and these two highly accurate methods is smaller than the error between these two

accurate methods themselves. This confirms that GW and HSE functional do give correct band gaps while their effective masses are the same with GGA-PS functional. For the sake of computational time limitation and little accuracy sacrifice, we use GGA-PS functional in this work. The effective masses are the quadratic coefficients of the fitting quadratic function with five points near the high-symmetry **k**-point. Fittings are performed by R code.[242] Detailed processes and methods are described in SI.

6.2.2 N_c and N_v calculation from DOS(E)

When the charge concentration is low, the interaction between charges is weak and can be neglected. We assume there is no interaction between charge carriers, the charge carrier density follows the Maxwell-Boltzmann distribution. It is expressed by: $f(E) = f_0 \exp(-\frac{E-E_f}{kT})$, where, E is the energy level of charges, E_f is the Fermi energy level, and f_0 is the charge density at Fermi level. Thus, the electron density in the conduction band is given by

$$\begin{aligned} n &= \int_{E_c}^{\infty} DOS(E) \times f(E) dE = \int_{E_c}^{\infty} DOS(E) \times e^{\frac{E-E_{fn}}{-kT}} dE/V_{cell} \\ &= \int_{E_c}^{\infty} DOS(E-E_c) e^{\frac{E-E_c}{-kT}} dE/V_{cell} \times e^{\frac{E_c-E_{fn}}{-kT}} = N_c \times e^{\frac{E_c-E_{fn}}{-kT}} \end{aligned} \tag{6.1}$$

where, E_c and E_{fn} are the lowest energy of the conduction band and quasi Fermi level, V_{cell} is the volume of the unit cell, T is the temperature and k is the Boltzmann constant, DOS(E) is shown in Figure 6.1. N_c is calculated by:

$$N_c = \int_{E_c}^{\infty} \frac{DOS(E-E_c)}{V_{cell}} e^{\frac{E-E_c}{-kT}} dE \tag{6.2}$$

The integration of DOS(E) is very sensitive to calculation methods, in this work we used tetrahedron method with Blochl corrections (ISMEAR=-5) as recommended by VASP for accurate electronic DOS calculation.

6.2.3 N_c and N_v calculation from effective mass

Theoretically, the density-of-states function is given by

$$DOS(E) = 2\left(\frac{1}{2\pi}\right)^3 \int \frac{dS_k}{|\nabla_k E|}, \tag{6.3}$$

where, 2 is for the spin, $dS_k = 4\pi k^2$ for the integral of the energy surface. For free electrons, its energy is calculated by $E = \frac{\hbar^2 k^2}{2m_0}$. Thus $\nabla_k E = \frac{\hbar^2 k}{m_0}$. Substituting them into Equation 6.3, we obtain

$$DOS(E) = \left(\frac{1}{4\pi^3}\right)\frac{4\pi k^2}{\hbar^2 k/m_0} = \left(\frac{4\pi}{h^3}\right)(2m_0)^{3/2}E^{1/2}. \tag{6.4}$$

Equation 6.4 is based on free electrons with parabolic energy band. This equation can also be used for semiconductors with parabolic energy bands by replacing the free electron mass with the effective mass of electron or hole.[243] Choosing the conduction band edge as the reference level, Equation 6.4 can be expressed by

$$DOS(E - E_c) = \left(\frac{4\pi}{h^3}\right)(2m^*)^{3/2}(E - E_c)^{1/2}. \tag{6.5}$$

Finally, the electron density can be calculated by[243, 244]

$$\begin{aligned} n &= \int_{E_c}^{\infty} f(E)DOS(E - E_c)dE = \int_{E_c}^{\infty} \frac{1}{[1 + e^{(E_f - E)/k_B T}]}DOS(E - E_c)dE \\ &= \left(\frac{4\pi}{h^3}\right)(2m^* k_B T)^{3/2}\int_{E_c}^{\infty} \frac{(E - E_c)^{1/2}dE}{[1 + e^{(E_f - E)/k_B T}]} \\ &= N_c F_{1/2}(\eta), \end{aligned} \tag{6.6}$$

where

$$N_c = 2(2\pi m^* k_B T/h^2)^{3/2} = 2.5409 \times 10^{19}\left(\frac{T m_c^*}{300 m_0}\right)^{3/2} \tag{6.7}$$

is the effective density of the conduction band states; $F_{1/2}(\eta) = \left(\frac{2}{\sqrt{\pi}}\right)\int_{E_c}^{\infty} \frac{(E-E_c)^{1/2}dE}{[1+e^{(E_f-E)/k_B T}]}$ is the Fermi integral.

For the non-spherical constant-energy surface, the effective mass is replaced by the reduced effective mass for DOS, which is given by

$$m^* = \sqrt[3]{g^2 m_l m_t m_t} \tag{6.8}$$

where g is the number of equivalent band minima, m_l and m_t are the longitudinal and transverse effective masses respectively. Equation 6.7 is calculated for the DOS calculation of materials with parabolic bands. The N_c and N_v are dominated by the bottom of the conduction band or the top of the valence band, the bottom and the top can be fitted by parabolic curves without bringing about significant errors. For hybrid perovskites, the conduction band bottom is strongly affected by MA^+ orientations.[52] Under certain cases,[164] hybrid perovskites can show two valleys. We think the N_c and N_v with and without disordered MA^+ should be similar. Hence, we use one valley band to calculate the effective mass. All fittings in this work are

reasonable without significant variation, as shown in Appendix D. For a material has several conduction bands with small energy difference, the total N_c is the summation of these conduction band N_c if their energy levels are the same. If their energy levels have small difference, the total DOS can be calculated by $N = \sum_{i=0}^{n} N_i \times e^{\frac{E_i - E_0}{-kT}}$, where N_i and E_i are the effective DOS and the energy level of the ith band.

6.3 Results

6.3.1 Known factors that influence V_{oc}

Open circuit voltages are always lower than their band gaps, which is due to charge carrier densities being lower than the effective DOSs of conduction band and valence band. In silicon solar cells, it was already found that V_{oc} is related to the charge density.[187, 188, 189] We point out that the output voltage of a solar cell is determined by its charge densities at two electrodes and N_c and N_v: [57, 230]

$$\begin{aligned} eV &= E_{fn} - E_{fp} = E_c + kT\ln(\frac{n|_{x=0}}{N_c}) - (E_v - kT\ln(\frac{p|_{x=d}}{N_v})) \\ &= E_{bgap} + kT\ln(\frac{n|_{x=0}}{N_c}) + kT\ln(\frac{p|_{x=d}}{N_v}) \\ &= E_{bgap} + kT\ln(n|_{x=0}p|_{x=d}) - kT\ln(N_cN_v) \end{aligned} \tag{6.9}$$

According to Equation (6.9), there are three approaches to reduce the voltage deficit. The first is operating solar cells at low temperature. If the working temperature is close to zero Kelvin, then $kT \approx 0$, which leads to $V \approx E_{bgap}$. But keeping solar cells working under low temperature may cost more. This conclusion agrees with experiment and theory done by Sachenko et al.[245] The second is increasing the charge carrier densities at two boundaries ($n|_{x=0}p|_{x=d}$). To do so, both increasing the generation rate by using concentrated incident light and efficient charge transport are feasible. Using high-density incident light source to generate high density charge carriers is already applied in concentrator solar cells that higher concentrated solar cells have higher V_{oc}.[246, 192, 193] We also verified this with numerical simulations.[57] The other method is to improve charge transfer efficiency by either reducing recombination or increasing carriers lifetime and mobility. Numerical simulations showed that the longer the lifetime the higher the V_{oc} outputs.[57] We also demonstrated that the presence of interface recombination lowers V_{oc},[57] which was verified by recent publications that V_{oc} is primarily limited by the interface losses.[127, 129] Here, we find that besides the light intensity, charge carries lifetime and mobility and recombination, there is another parameter controls V_{oc}.

Table 6.1: N_c and N_v calculated from integration of conduction and valence band DOS(E) of unit cells through Equation (6.2).

Compound	V (Å^3)	N_c-integral	N_v-integral	N_c (cm^{-3})	N_c (cm^{-3})	N_cN_v (cm^{-6})
α-$FAPbI_3$	765.85	4.55×10^{-3}	8.99×10^{-4}	5.94×10^{18}	1.17×10^{18}	6.97×10^{36}
$MAPbCl_3$	716.61	8.56×10^{-3}	3.11×10^{-4}	1.19×10^{19}	4.34×10^{17}	5.18×10^{36}
$MAPbI_3$	984.66	1.03×10^{-2}	6.26×10^{-4}	1.04×10^{19}	6.36×10^{17}	6.62×10^{36}
CdTe	271.72	8.19×10^{-6}	5.53×10^{-3}	3.00×10^{16}	2.03×10^{19}	6.09×10^{35}
Si	40.05	4.56×10^{-4}	6.17×10^{-5}	1.14×10^{19}	1.54×10^{18}	1.75×10^{37}

6.3.2 N_c and N_v from DOS(E)

The last approach to improve V_{oc} is using materials with low N_c and N_v. Here, we calculated DOS(E) of typical perovskites, CdTe and silicon by VASP. DOS(E) are displayed in Figure 6.1. N_c and N_v were then calculated by integrating these DOS(E), as illustrated by Equation (6.2). Table 6.1 shows N_c and N_v of these materials. It was found that all the perovskites have similar N_c and N_v, with product around 6×10^{36} cm^{-6}, which is about one third of silicons. CdTe has a very low N_c of 3.0×10^{16} cm^{-3} as a result of the very sharp DOS(E) at bottom of conduction (Figure 6.1D). While, its N_v is the largest. According to Equation (6.9), only the product of N_c and N_v influences V_{oc} as the output potential is the relative potential difference between quasi hole and electron Fermi levels. Among them, Si has the highest N_c and N_v product, which is up to 10^{37} cm^{-6}. The lower N_c and N_v in perovskite and CdTe are supposed to have higher V_{oc} than silicon under same parameters and conditions. The N_c and N_v calculated from DOS(E) integration is very sensitive to calculation methods, although we used recommended settings for accurate electronic DOS(E), the integration of discrete DOS(E) brings about errors as well. The accuracy of N_c and N_v calculated from DOS(E) integral here is poor. Only the relative magnitude of the calculated N_c and N_v are reliable.

6.3.3 N_c and N_v from effective mass

N_c and N_v calculated from effective mass are expected to be more accurate. The error comes from the evaluation of effective mass. Here, we calculated both N_c and N_v from effective electron mass and effective hole mass respectively. The effective mass is calculated according to its definition and estimated by fitting band curves near conduction band bottoms and valence band tops. Details about the calculation method can be found in Ref. 248 and 52. Related band structures and fittings are available in SI. The calculated reduced effective mass of $MAPbI_3$ for conductivity with

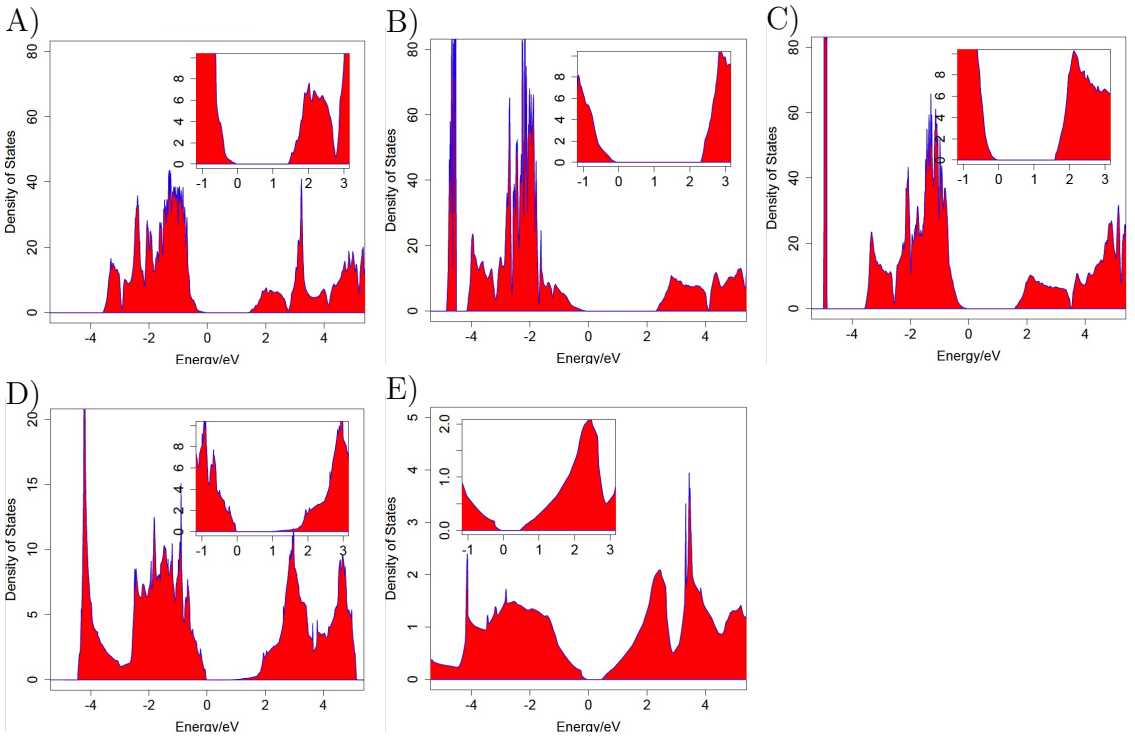

Figure 6.1: Density of states of A), α-$FAPbI_3$; B), $MAPbCl_3$; C), $MAPbI_3$; D), CdTe and E), Si respectively.

the same method is 0.09 m_0,[52] similar to experimental values ranging from 0.09-0.15. (0.09-0.12 m_0,[249] 0.12 m_0[167], 0.11 m_0[168], 0.10 m_0[250] and 0.15 m_0.[169]) This agreement confirms that our calculations are reliable.

The estimated silicon hole effective masses are 0.12-0.76 m_0, and effective electron mass is 1.20 m_0. Both the calculated N_c and N_v are comparable to reference data.[247] Effective electron masses of the lowest conduction bands are 0.31-0.70 m_0 and 0.17-0.53 m_0, for $MAPbCl_3$ and $MAPbI_3$. Both of them are similar to the SOC-GW calculated 0.28-0.40 m_0 and 0.18-0.30 m_0.[251] These comparisons suggest that our

Table 6.2: N_c, N_v and simulated solar cell performance parameters for α-$FAPbI_3$, $MAPbCl_3$, $MAPbI_3$, CdTe and silicon.

Compound	N_v (cm^{-3})	N_c (cm^{-3})	N_cN_v	V_{oc} (mV)	PCEs (%)
α-$FAPbI_3$	2.90×10^{18}	1.20×10^{19}	3.47×10^{37}	1132.02	19.70
$MAPbCl_3$	3.64×10^{18}	1.36×10^{19}	4.94×10^{37}	1123.32	19.53
$MAPbI_3$	2.49×10^{18}	6.98×10^{18}	1.74×10^{37}	1149.14	20.04
CdTe	4.54×10^{19}	4.25×10^{17}	1.93×10^{37}	1146.46	19.99
Si	2.32×10^{19}	3.35×10^{19}	7.76×10^{38}	1055.70	18.18
Si[247]	2.85×10^{19}	1.85×10^{19}	5.27×10^{38}	1065.21	18.37

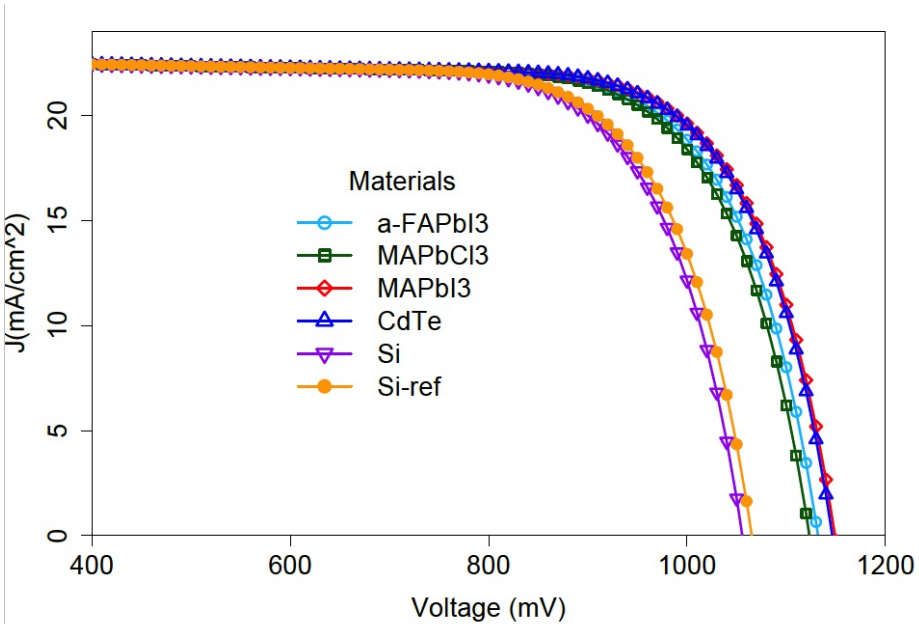

Figure 6.2: J-V curves of various materials with same electronic parameters except for N_c and N_v. The thickness of simulated solar cell is 350 nm. Diffusion coefficients of the perovskite were assumed to be 0.017 $cm^2 s^{-1}$ and 0.011 $cm^2 s^{-1}$.[29] The band gap is set as 1.55 eV.[1] The interface recombination width is 5 nm and its lifetime is 5 ns. The charge carrier lifetime is assumed to be 736 ns.[1] Cells operate at 300 K and 1 sun (1.5AM). More simulated details can be found in Ref. 57.

method is reliable. According to Equation (6.9), the product of N_c and N_v determines the voltage deficit from DOS. Therefore, N_c, N_v and their products are calculated in Table 6.2. The product sequence is Si > $MAPbCl_3$ ≈ α-$FAPbI_3$ ≈ $MAPbI_3$ ≈ CdTe, which is in concert with the result calculated from integration. The absolute value difference between the N_c and N_v from effective mass and the N_c and N_v from the integral is due to the poor accuracy of N_c and N_v from DOS(E) integral. Although CdTe has a very small N_c, its N_v is large as it has three flat valence bands. The N_c and N_v products of CdTe and perovskites are in the same scale, which is much smaller than that of silicon. Considering Equation (6.9), the voltage deficits of perovskites should be about 100 mV smaller than silicon's due to the products of hybrid perovskites are about 45 times lower than that of silicon.

6.3.4 Numerical simulations

In order to figure out how N_c and N_v influence solar cell performance and eliminate other parameters influences, such as band gap and carrier mobility influences, we assumed all of these materials have same parameters except for N_c and N_v. Several

other parameters are correlated with N_c and N_v, such as effective mass and absorption. A low N_c or N_v is related to the small effective electron or hole mass, which also contributes to the high performance. As the small effective mass produces high charge carrier mobility and small exciton separation energy,[52] mobilities and IPCEs are assumed the same in order to avoid the influence from the small effective mass. The low N_c and N_v may lead to low absorption. The absorption influence was excluded as we use same absorption coefficients. Using the numerical model we have developed for PSCs,[57] we simulated the working J-V curves of these materials. All of the simulated solar cells are 'perovskite' solar cells. For the simulated silicon and CdTe solar cells, they are not real silicon solar cells or CdTe solar cells, they are PSCs just with the N_c and N_v of silicon and CdTe. Figure 6.2 shows performances of their solar cells with different N_c and N_v. For the solar cell with silicon N_c and N_v, its $N_c \times N_v$ is 7.76×10^{38} cm^{-3}, the corresponding simulated V_{oc} is 1055.70 mV. For the $MAPbI_3$, its V_{oc} is calculated to be 1149.14 mV, which is about 93 mV higher than that of the silicon solar cell. If we lower the silicon N_c and N_v to the N_c and N_v of $MAPbI_3$, its PCEs will be improved from 18.18 % to 20.04 %. The relative improvement is about 10 %.

6.4 Discussion

Since the effective mass is calculated from the second derivative of bands, and number of K point in the band structure calculation are limited, this second derivative is not accurate. The error in effective mass evaluation is approximately 10 % in our calculations. , and the error for the reduced mass (m^*) is estimated to be approximately 15 %. The error in N_c or N_v is therefore approximately 23 %. The error in these two methods is obvious, but the sequence of N_c and N_v magnitude calculated from these two methods are the same. This confirms the low N_c and N_v in perovskite.

An important question is does low N_c and N_v lead to low charge density near electrodes ($n|_{x=0}p|_{x=d}$)? We find there will be no enhancement if the changing of $n|_{x=0}p|_{x=d}$ is the same as the changing of $N_c \times N_v$. Charge carriers are generated and then migrate to the electrodes. Hence, charge carrier densities at the two ends should increase with generation rate and mobilities, and decrease with thickness and recombination rate. The DOS has no effect on the recombination rate as the recombination rate is mostly dependent on the charge carrier density itself, defect density and defect energy levels according to the Shockley-Read-Hall Model.[243, 183, 184, 93] Low N_c and N_v are related with small effective masses according to Equation 6.7, and produce

high mobilities. The mobility effect was excluded in our simulations by using same mobilities. If take this into consideration, V_{oc} will be further improved.

The generation rate and thickness greatly influence each other. Theoretically, the generation rate is calculated from $G = \int_0^d \int_0^{\lambda_0} G(\lambda, x) d\lambda = \int_0^d \int_0^{\lambda_0} \eta_g [1 - R(\lambda)] \times I(\lambda) \times \alpha(\lambda) \times e^{-\alpha(\lambda)x} d\lambda dx = \int_0^{\lambda_0} I(\lambda) \times IPCE(\lambda, d) d\lambda$, where α is the absorption coefficient and I(λ) is incident photon density; $R(\lambda)$ is the reflect coefficient and η_g is the generation quantum efficiency; $IPCE(\lambda, d)$ is the quantum efficiency of a whole device, which is also called External Quantum Efficiency (EQE).[252] In some experiments, solar cells show $IPCE(\lambda)$ of approximately 80% in the visible light range.[253, 254, 13, 255, 24, 34] For a small α material, a thicker thin film is required to reach the same $IPCE$. The low N_c and N_v in perovskite might lead to low absorption, which will lower solar cell performance. As shown in Ref. 256, saturable absorption happens at extreme incident light intensities. The intensity to exhibit saturable absorption for Bi_2Se_3 is about 41-53 MW/cm^2,[257, 258] which is about 10^8 times strong than 100mW/cm^2 (the light intensity of AM1.5). There is no experimental saturable absorption data for perovskite materials, but the intensity should be of similar magnitude. Hence, the N_c and N_v's influence on absorption of sunlight is negligible for normal solar cells. Furthermore, the absorption of $MAPbI_3$ is higher than silicon as shown in Ref. 259. As such, to reach the same $IPCE$, PSC could be thinner. This thin film also leads to high $n|_{x=0}p|_{x=d}$. In summary, if we consider the N_c and N_v related parameter influences, higher $n|_{x=0}p|_{x=d}$ are expected. The high V_{oc} calculated from numerical models will be further improved.

6.5 Conclusion

In conclusion, using two different methods based on *ab initio* results, we estimated N_c and N_v of silicon, CdTe and typical perovskites. It was found that the DOSs of perovskites and CdTe are much lower than that of silicon. The low N_c and N_v consist with the small effective mass, which directly contributes to high mobility. To avoid the small effective mass induced improvement, the mobility in these simulations is fixed. Analytic and numerical results show that the material with lower N_c and N_v can realize higher open circuit voltage and higher PCEs. With systematic discussions, we determined how the N_c and N_v of material works on its solar cell performance. The lower N_c and N_v of perovskites lead to about 100 mV higher V_{oc} and 10 % (relative) higher PCEs. Considering low N_c and N_v consist with small effective masses, the performance of solar cells with low N_c and N_v will be further improved.

In this chapter, we show that besides inert interface defects,[129, 57] long charge carrier lifetime,[57] and reduced bimolecular recombination,[127] that low N_c and N_v in perovskites contribute to the high V_{oc} and high performance of PSCs. Therefore, the materials with low N_c and N_v should be good candidates for solar cells.

Chapter 7

Conclusion

In this thesis, I demonstrated that the influence of the orientation of MA^+ on the electronic properties of $MAPbI_3$ is strong along specific directions, while the influence on overall electronic properties is very little. The minor electronic property difference in the β and α phases explained why $MAPbI_3$ PSCs can work near its phase transition point. The small energy barriers for MA^+ rotations in different phases with different MA^+ neighboring alignment explained the nature of disorder in MA^+ ions. A numerical model for charge transport and energy conversion was developed for PSCs, and was used to analyze and optimize PSCs. Using numerical simulations of the dynamics including two mechanisms describing the slow relaxation of the screening field, experimental hysteresis in J-V curves was reproduced. With dynamic Monte Carlo simulations, we showed that the polarization of MA^+ is not ferroelectric but the possibility of ferroelectricity of Pb ions remains. The simulation of the relaxation dynamics suggests ion migration is the most likely cause of the observed hysteresis, while polarization is excluded. By combining DFT and numerical modeling, we showed perovskite materials display low N_cN_v and these DOSs lead to high V_{oc} and PCEs.

In Chapter 2, we studied the influence of the orientation of MA^+ on the electronic properties of $MAPbI_3$ in α and β phase. It was found that the structure with MA^+ orientating to [111] is the most stable configuration in the α phase, while [001] is the most stable in the β phase. The maximum energy difference in these configurations is smaller than 30 meV. Therefore, MA^+ ions should be totally disordered at room temperature. The conduction band minima and the valence band maxima are located at the R point in the α phase, whereas, they are located at the Γ point in the β phase. The MA^+ distorts the bottom of the conduction bands, effective masses on specific directions change a lot, while the band gaps and reduced effective masses do not change too much. The constant reduced effective mass indicates the rotation of

MA^+ has little impact on its photovoltaic phenomenon. Effective hole and electron masses are estimated to be about 0.17 m_0 and 0.20 m_0 respectively. We also found effective masses in the α phase are just slightly smaller than that in the β phase. This suggests that $MAPbI_3$ based solar cells can work near their phase transition point with no significant change in their performance. Lastly, the calculated large Born effective charge and large dielectric constant lead to a small exciton separation energy, which is about 30 meV. This small exciton separation energy enables efficient charge generation and improves PCE. Our results indicated that the rotation of MA^+ has little impact on the electronic properties of $MAPbI_3$.

In Chapter 2, it was also found that the unit cell dipole moment changes due to MA^+ rotation and lead ion displacement are about 6 - 8 μCcm^{-2} and 2 - 3 μCcm^{-2} respectively. This suggests both MA^+ reorientation and lead ion displacement could polarize $MAPbI_3$ in principle. The energy landscapes for MA^+ rotation are investigated in details. The rotation energy barrier of different MA^+ ranges from 0.01 eV to 0.30 eV, which depends on its phase and orientations of neighboring MA^+. It is found that MA^+ ions prefer to align in the same direction and rotate collectively. This indicates $MAPbI_3$ is very likely to be ferroelectric. Additionally, I showed that polarization of MA^+ is able to screen the hindering external field.

Chapter 3 shows a numerical model for PSCs. Advantages of our model are (1) no free parameters; (2) equations are solvable with every physical realistic parameter; (3) good agreement with experiments. Using this numerical model, it was found that performances of solar cells increase with charge carrier lifetimes, mobilities and diffusion lengths. The V_{oc} of a solar cell depends on light intensities and charge carrier lifetimes. Diffusion length and light intensity determine the J_{sc}. Additionally, three possible guidelines for the design and fabrication of perovskite solar cells are suggested by our calculations: (1) for a material with electron mobility higher than hole mobility, the cell with HTL facing the sun has a higher PCE compared to the cell with ETL facing the sun; (2) the optimum thickness of the active layer depends on its absorption length and its diffusion length. When the diffusion length is shorter than the absorption length, the optimum length is about the diffusion length. While, for the diffusion length far longer than the absorption length, the optimum length is still in the magnitude of absorption length; (3) solar cells with thin rapid interface recombinations show low V_{oc} and high J_{sc}. This suggests that a solar cell with low V_{oc} and high J_{sc} can be improved by interface engineering; a solar cell with both low V_{oc} and low J_{sc} is mainly due to the poor charge transport ability of the perovskite layer. Enhancing the quality of perovskite thin films is crucial. Lastly, the light

intensity dependence of PSCs indicates that concentrator perovskite solar cells are promising. These equations and methods we have reported and tested provide a framework for numerical modeling of perovskite-based cells and the optimization of their performance.

By implementing in our model two mechanisms describing the slow relaxation of the screening field assumed to originate ion migration and polarization, combined with the numerical model we developed in Chapter 3, we quantitatively reproduced the hysteresis in J-V curves in Tress's and Snaith's experiments. The agreement of the results of our simulations with experimental data suggests that the hysteresis in PSCs is due to two different relaxation mechanisms with different relaxation times. These two mechanisms could be ion migration and polarization, but they also may be due to migration of two different types of ions. Possible strategies to reduce hysteresis in PSCs are proposed. One consists of reducing defects in thin films and interfaces; the other consists of using polarizable materials as charge transfer layers to compensate the field induced by polarization and/or ion migration.

Although we showed that both the ion migration and polarization are possible to bring about hysteresis in J-V curves in Chapter 4, we cannot exclude or confirm any of them as we are unable to distinguish the difference between these two relaxations from mesoscopic simulations. Firstly, our simulation illustrated that the polarization of MA^+ is able to screen the external field, but it is dielectric rather ferroelectric. Secondly, lifetimes of these two relaxation mechanisms depends on the thin film thickness and initial applied external fields. It takes longer to relax in thicker thin films and films with weaker external fields. Lastly, the relaxation lifetime of ion migration is estimated in the range from 1 ms to 1.5 s, which are comparable to experimental delay times. On the other hand, the relaxation lifetimes of MA^+ are estimated to be several hundred ns to several μs, which significantly differ from experimental delay times. Therefore the hysteresis observed in the J-V curve in PSCs cannot be caused by MA^+ polarization but could be caused by the polarization of lead ions displacement.

Chapter 6 showed that N_c and N_v in perovskite and CdTe materials are much lower than that in silicon. Using numerical models, it was found that low N_cN_v in perovskite and CdTe produce higher V_{oc} and PCEs. The improvements of V_{oc} and PCE are about 100 meV and 10% (relative) respectively. This result explains the high V_{oc} in PSCs. It also points out a way to look for future solar cell materials.

In conclusion, by means of the results obtained in this thesis and outlined above, we believe we have provided new insight into the two main research questions stated in the introduction to this work.

The first main question is why PSCs can achieve high PCEs. We examined three possible reasons. (1) The first reason is related to the ferroelectric phase of perovskites and its consequence for the PSC performance. Our results indicate that the major part of polarization come from the rotation of MA^+. This polarization is dielectric rather ferroelectric. The dielectric polarization screens external hindering fields, promotes charge transfer and then improves PSC's PCE. The screening effect increases the dielectric constant at low frequencies, which has been observed in experiments. (2) The second reason is related to whether the orientation of MA^+ increases the electronic properties of $MAPbI_3$. It was found that the overall electronic properties of $MAPbI_3$ with differently orientated MA^+ are similar. This suggest the power conversion improvement from the enhancement of electronic properties from MA^+ rotation is small. (3) The third reason explored here investigates the influence of N_c and N_v on the high V_{oc} and high PCE. Low N_c and N_v are verified and their contribution to the improvement of PCEs is also confirmed.

The second main question is what causes hysteresis in PSCs. Numerical simulations showed that the hysteresis in PSCs was caused by two relaxation mechanisms with different relaxation time. Mesoscopic relaxation simulations of MA^+ polarization and ion migration demonstrated the relaxation of MA^+ is not the reason for hysteresis due to its short relaxation compared to experiments, while, ion migration is confirmed as its relaxation time is in agreement with experiments. I also put forward two possible strategies to eliminate hysteresis. My simulations contributed to a deeper understanding of hysteresis and attempted to suggest some guidelines to eliminate this problem.

My work is aimed to the understanding of perovskite materials and PSCs. These findings are expected to accelerate the development of PSCs and provide guidelines for the development of new photovoltaic materials.

Appendix A

Supplemental Information for Chapter 2

A.1 MA^+ orientations

Table A.1: Orientations of MA^+ ions in the β phase, which is calculated by: Coordinate of N atom − Coordinate of C atom.

MA vectors	MA	Lead fixed			Lead relaxed		
		X	Y	Z	X	Y	Z
00-1	1	0.70	0.70	-1.11	0.66	-0.69	-1.15
	2	-0.49	-0.49	-1.31	-0.72	-0.60	-1.16
	3	-0.49	-0.49	-1.31	0.66	-0.69	-1.15
	4	0.70	0.70	-1.11	-0.67	-0.65	-1.16
	Average	0.11	0.11	-1.21	-0.01	-0.66	-1.16
-110	1	-1.03	1.06	-0.06	-1.03	-0.95	0.48
	2	-0.76	0.98	-0.8	-0.96	-1.00	-0.54
	3	-0.72	0.70	-1.09	-1.02	-1.07	0.01
	4	-1.06	1.03	-0.10	-0.99	-1.08	0.07
	Average	-0.89	0.94	-0.52	-1.00	-1.02	0.00
1-1		0.88	0.96	-0.71	-0.97	-0.88	0.72
1	2	-0.57	0.76	-1.13	-1.16	0.27	0.89
	3	0.95	-0.57	-0.99	-1.09	-0.52	0.84
	4	0.75	0.73	-1.05	-1.08	-1.00	0.17
	Average	0.50	0.47	-0.97	-1.08	-0.53	0.66

A.2 Band structures of structures optimized with lead fixed

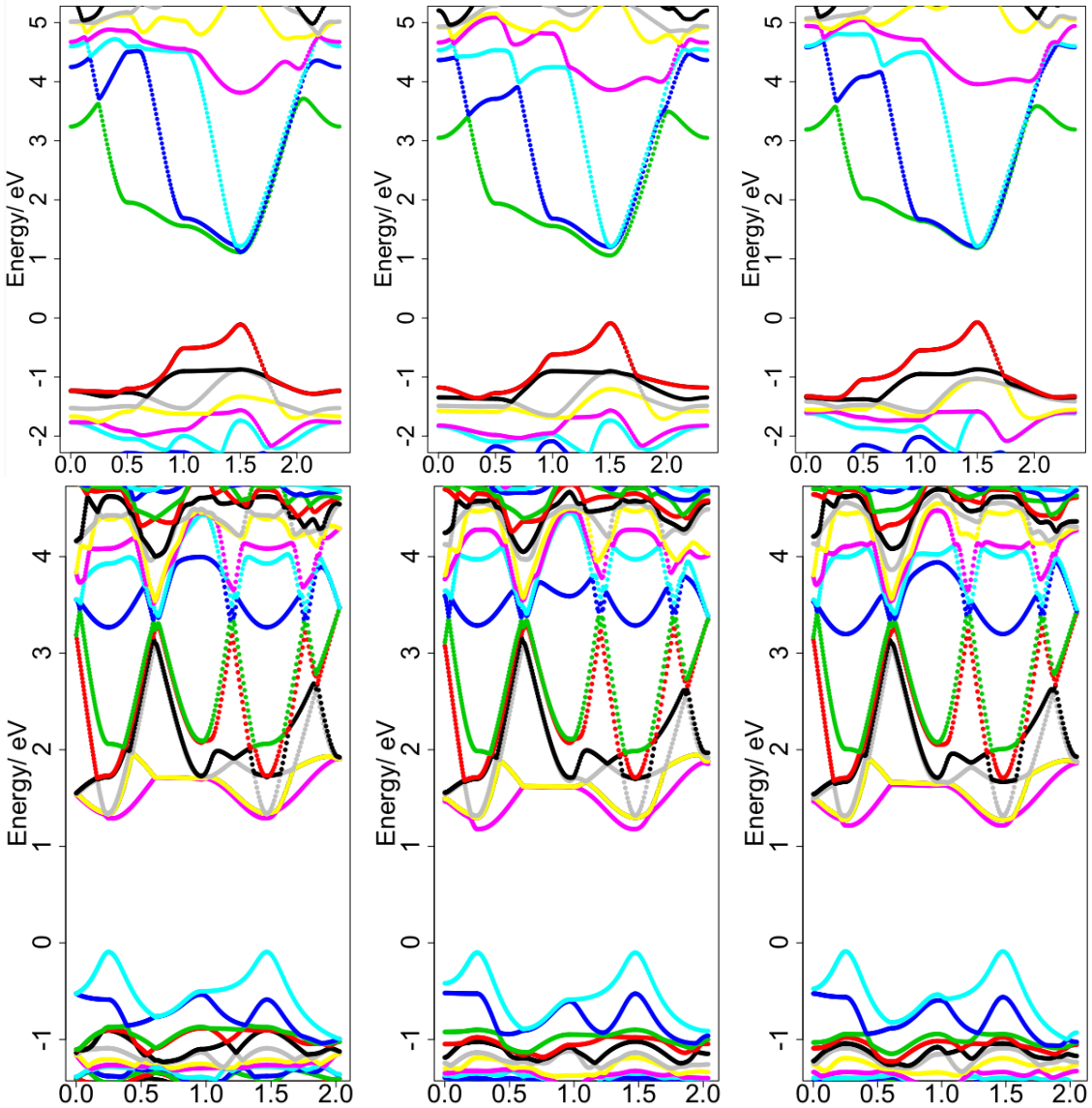

Figure A.1: The band structures of the α phase and the β phase with lead fixed. The upper three are the band diagrams (from left to right corresponding to 001-, 110- and 111-$MAPbI_3$, respectively) of the α phase. The band diagrams of β phase are shown at bottom (from left to right corresponding to 001-, 110- and 111-$MAPbI_3$, respectively).

A.3 Density of states of the structure of lead atom relaxed

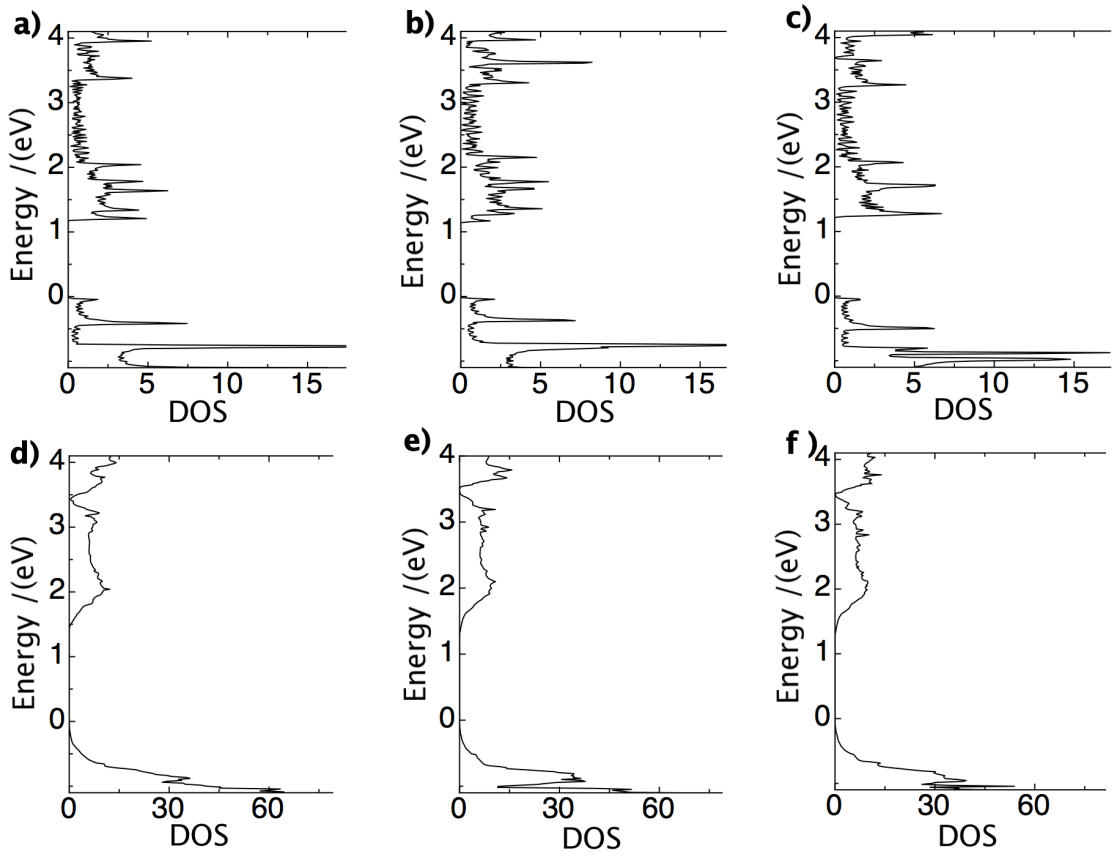

Figure A.2: Density of states of the structures with lead atom relaxed. a), b) and c) are DOS of α phase 001-,110-,111-$MAPbI_3$, respectively. d), e) and f) are the DOS of β phase 001-,110-,111-$MAPbI_3$, respectively.

A.4 Born Charge

Born charge tensors vary as MA^+ ions rotate. In optimized structures, MA^+ ions are not at the center of the inorganic cage, carbon atoms are always closer to the cage boundary. The no-diagonal elements of Born charge tensors close to zero. For lead atoms, the zz component born charge reduces from 5.15 to 5.01 to 4.78, as MA^+ ions rotate from [001] to [011] and to [111]. It is found that the born charge of iodine ions is very big only at one component. Among these three iodine ions, one maximum is at xx component, one takes yx component and the last one must take zz component.

Table A.2: Born charges of the lead and iodine ions in $MAPbI_3$ unit cells with differently orientated MA^+. (α phase, lead fixed)

MA orientation (accurate direction)	ION (coordinate)	DIRECTION	X	Y	Z
100 (0.0,0.0,0.24)	lead	X	4.688	0.007	-0.064
	(0.5 0.5 0.5)	Y	0.007	4.682	-0.06
		Z	-0.063	-0.059	5.146
	iodine	X	-0.723	-0.007	0.035
	(0.5 0.5 0)	Y	-0.007	-0.705	0.033
		Z	-0.007	-0.009	**-4.543**
	iodine	X	-0.905	0.010	-0.083
	(0.5 0.0 0.5)	Y	0.001	**-4.239**	-0.038
		Z	-0.087	0.018	-0.654
	iodine	X	**-4.063**	-0.002	-0.033
	(0.0 0.5 0.5)	Y	0.009	-0.882	-0.096
		Z	0.021	-0.100	-0.659
110(-0.01, 0.11, 0.20)	lead	X	4.995	0.007	-0.03
	(0.5 0.5 0.5)	Y	0.008	4.515	0.360
		Z	-0.030	0.372	5.000
	iodine	X	-0.801	0.012	0.010
	(0.5 0.5 0)	Y	0.008	-0.674	-0.230
		Z	0.001	-0.056	**-4.410**
	iodine	X	-0.991	0.015	-0.010
	(0.5 0.0 0.5)	Y	0.022	**-4.076**	-0.050
		Z	-0.010	-0.240	-0.710
	iodine	X	**-4.299**	0.000	0.000
	(0.0 0.5 0.5)	Y	0.000	-0.716	-0.030
		Z	0.018	-0.049	-0.740
111(0.13 0.14, 0.13)	lead	X	4.863	0.021	0.072
	(0.5 0.5 0.5)	Y	0.021	4.882	0.073
		Z	0.071	0.073	4.776
	iodine	X	-0.759	-0.113	-0.018
	(0.5 0.5 0)	Y	-0.111	-0.739	-0.015
		Z	-0.032	-0.030	**-4.198**
	iodine	X	-0.758	0.006	-0.114
	(0.5 0.0 0.5)	Y	-0.028	**-4.452**	-0.037
		Z	-0.109	-0.031	-0.745
	iodine	X	**-4.246**	-0.031	-0.042
	(0.0 0.5 0.5)	Y	0.004	-0.742	-0.108
		Z	-0.034	-0.104	-0.749

Table A.3: Born effective charges of the β phase 001-$MAPbI_3$ with lead fixed.

ION	DIRECTION	X	Y	Z
Pb(0.00, 0.00, 0.00)	X	4.581	-0.487	0.024
	Y	0.412	4.597	0.065
	Z	0.037	0.051	5.06
Pb(0.50, 0.50, 0.50)	X	4.581	-0.487	0.024
	Y	0.412	4.597	0.065
	Z	0.037	0.051	5.06
Pb(0.00, 0.00, 0.50)	X	4.597	0.412	0.065
	Y	-0.487	4.581	0.024
	Z	0.051	0.037	5.06
Pb(0.50, 0.50, 0.00)	X	4.597	0.412	0.065
	Y	-0.487	4.581	0.024
	Z	0.051	0.037	5.06
I(0.00, 0.00, 0.25)	X	-0.696	0.035	-0.041
	Y	0.014	-0.68	0.025
	Z	-0.079	0.016	-5.398
I(0.50, 0.50, 0.75)	X	-0.696	0.035	-0.041
	Y	0.014	-0.68	0.025
	Z	-0.079	0.016	-5.398
I(0.00, 0.00, 0.75)	X	-0.68	0.014	0.025
	Y	0.035	-0.696	-0.041
	Z	0.016	-0.079	-5.398
I(0.50, 0.50, 0.25)	X	-0.68	0.014	0.025
	Y	0.035	-0.696	-0.041
	Z	0.016	-0.079	-5.398
I(0.21, 0.71, 0.00)	X	-2.569	1.767	0.099
	Y	1.767	-2.569	0.099
	Z	0.088	0.088	-0.621
I(0.79, 0.29, 0.00)	X	-2.576	1.858	-0.031
	Y	1.858	-2.576	-0.031
	Z	-0.017	-0.017	-0.602
I(0.29, 0.21, 0.00)	X	-2.665	-1.761	-0.137
	Y	-1.754	-2.459	0.009
	Z	-0.082	0.012	-0.636
I(0.79, 0.71, 0.50)	X	-2.665	-1.761	-0.137
	Y	-1.754	-2.459	0.009
	Z	-0.082	0.012	-0.636
I(0.71, 0.79, 0.00)	X	-2.459	-1.754	0.009
	Y	-1.761	-2.665	-0.137
	Z	0.012	-0.082	-0.636
I(0.21, 0.29, 0.50)	X	-2.459	-1.754	0.009
	Y	-1.761	-2.665	-0.137
	Z	0.012	-0.082	-0.636
I(0.29, 0.79, 0.50)	X	-2.576	1.858	-0.031
	Y	1.858	-2.576	-0.031
	Z	-0.017	-0.017	-0.602
I(0.71, 0.21, 0.50)	X	-2.569	1.767	0.099
	Y	1.767	-2.569	0.099
	Z	0.088	0.088	-0.621

Table A.4: Born effective charges of the β phase 110-$MAPbI_3$ with lead fixed.

ION	DIRECTION	X	Y	Z
Pb(0.00, 0.00, 0.00)	X	4.690	0.506	0.169
	Y	-0.570	4.871	-0.033
	Z	0.138	-0.025	4.713
Pb(0.50, 0.50, 0.50)	X	4.592	0.567	0.150
	Y	-0.449	4.830	-0.012
	Z	0.127	-0.006	4.757
Pb(0.00, 0.00, 0.50)	X	4.752	-0.484	0.084
	Y	0.538	4.654	-0.100
	Z	0.082	-0.077	4.766
Pb(0.50, 0.50, 0.00)	X	4.824	-0.604	0.073
	Y	0.484	4.765	-0.100
	Z	0.087	-0.091	4.687
I(0.00, 0.00, 0.25)	X	-0.688	-0.141	-0.178
	Y	-0.119	-0.790	-0.002
	Z	-0.112	-0.007	-4.909
I(0.50, 0.50, 0.75)	X	-0.786	-0.093	-0.176
	Y	-0.062	-0.606	0.006
	Z	-0.120	-0.017	-5.007
I(0.00, 0.00, 0.75)	X	-0.653	-0.079	-0.060
	Y	-0.112	-0.733	0.129
	Z	0.010	0.099	-5.053
I(0.50, 0.50, 0.25)	X	-0.771	-0.104	-0.001
	Y	-0.127	-0.727	0.136
	Z	0.063	0.107	-4.905
I(0.21, 0.71, 0.00)	X	-2.821	1.958	0.048
	Y	1.932	-2.601	0.060
	Z	-0.001	0.100	-0.612
I(0.79, 0.29, 0.00)	X	-2.644	1.979	-0.023
	Y	2.037	-2.812	0.015
	Z	-0.082	0.052	-0.624
I(0.29, 0.21, 0.00)	X	-2.530	-1.931	-0.111
	Y	-1.969	-2.561	0.100
	Z	-0.141	0.084	-0.811
I(0.79, 0.71, 0.50)	X	-2.526	-1.903	-0.087
	Y	-1.926	-2.562	0.052
	Z	-0.102	0.065	-0.812
I(0.71, 0.79, 0.00)	X	-2.626	-1.990	-0.004
	Y	-1.987	-2.628	0.016
	Z	-0.024	-0.016	-0.645
I(0.21, 0.29, 0.50)	X	-2.640	-1.998	-0.009
	Y	-2.030	-2.667	-0.002
	Z	-0.026	-0.011	-0.639
I(0.29, 0.79, 0.50)	X	-2.490	1.839	-0.061
	Y	1.868	-2.717	-0.082
	Z	-0.146	-0.058	-0.630
I(0.71, 0.21, 0.50)	X	-2.700	1.846	0.073
	Y	1.873	-2.530	0.047
	Z	0.062	0.134	-0.627

Table A.5: Born effective charges of the β phase 111-$MAPbI_3$ with lead fixed.

ION	DIRECTION	X	Y	Z
Pb(0.00, 0.00, 0.00)	X	4.688	0.652	-0.203
	Y	-0.366	4.734	-0.063
	Z	-0.186	-0.073	4.832
Pb(0.50, 0.50, 0.50)	X	4.668	0.503	-0.163
	Y	-0.483	4.632	-0.076
	Z	-0.182	-0.034	4.953
Pb(0.00, 0.00, 0.50)	X	4.634	-0.504	-0.130
	Y	0.494	4.722	-0.145
	Z	-0.125	-0.121	4.865
Pb(0.50, 0.50, 0.00)	X	4.683	-0.375	-0.143
	Y	0.652	4.701	-0.142
	Z	-0.111	-0.149	4.943
I(0.00, 0.00, 0.25)	X	-0.831	0.018	0.075
	Y	0.043	-0.633	0.060
	Z	0.025	0.017	-5.110
I(0.50, 0.50, 0.75)	X	-0.683	0.001	0.126
	Y	0.035	-0.691	0.170
	Z	0.030	0.081	-5.339
I(0.00, 0.00, 0.75)	X	-0.781	-0.021	0.121
	Y	-0.074	-0.617	0.052
	Z	0.051	0.026	-5.159
I(0.50, 0.50, 0.25)	X	-0.609	0.057	0.179
	Y	0.034	-0.834	0.077
	Z	0.054	0.027	-5.229
I(0.21, 0.71, 0.00)	X	-2.621	1.838	0.154
	Y	1.830	-2.503	0.060
	Z	0.215	0.059	-0.691
I(0.79, 0.29, 0.00)	X	-2.445	1.735	-0.016
	Y	1.761	-2.641	-0.111
	Z	-0.017	-0.184	-0.611
I(0.29, 0.21, 0.00)	X	-2.829	-2.033	-0.057
	Y	-1.986	-2.666	0.056
	Z	-0.001	0.110	-0.574
I(0.79, 0.71, 0.50)	X	-2.646	-1.809	-0.050
	Y	-1.835	-2.496	0.031
	Z	-0.028	0.110	-0.664
I(0.71, 0.79, 0.00)	X	-2.601	-1.913	-0.003
	Y	-1.984	-2.731	0.026
	Z	0.062	0.092	-0.677
I(0.21, 0.29, 0.50)	X	-2.524	-1.888	0.081
	Y	-1.894	-2.703	-0.128
	Z	0.174	-0.093	-0.588
I(0.29, 0.79, 0.50)	X	-2.728	1.921	-0.066
	Y	1.897	-2.569	0.009
	Z	-0.095	0.006	-0.612
I(0.71, 0.21, 0.50)	X	-2.500	1.804	0.045
	Y	1.855	-2.681	0.114
	Z	0.048	0.140	-0.698

A.5 Estimation of screening field

Estimation of the hindering field($\mathbf{E}_0$) and the screen field in Tress' experiment. For the scanning rate of 1,000 meV/s, at the voltage of 0.65 V, the current are 15.72 mA/cm^2 and 9.04 mA/cm^2, from Figure 1a. The thickness of solar cell is about 300 nm, hence, the field can estimated as

$$\mathbf{E}_0 = 0.65V/300nm = 2.17 \times 10^6\ V/m.$$

If we assuming there is no power lost, the power of circuit are the same:

$$V * I_+ + V_s * I_+ = V * I_-$$

Where $_-$ and $_+$ is for the backward and forward measurement. V_s is the potential produced by the screen field. Then,

$$V_s = V * \frac{I_- - I_+}{I_+} = 0.65 * 0.74\ V = 0.48\ V$$

Therefore the screen field is $E_s = V_s/d = 0.48\ V/300\ nm = 1.6 \times 10^6$ V/m. The total field is $\mathbf{E} = \mathbf{E}_0 + \mathbf{E}_s = 5.67 \times 10^5$ V/m. Energies of the polarised MA^+ ions along six directions are $|\mathbf{M}||\mathbf{E}|$, zero and $-|\mathbf{M}||\mathbf{E}|$, respectively. The Boltzmann ratios are estimated as $\exp(2|\mathbf{M}||\mathbf{E}|/kT) : 4 \times \exp(|\mathbf{M}||\mathbf{E}|/kT) : 1.00 = 1.005 : 4 \times 1.009 : 1.00$. The net percentage of the polarised MA^+ ions is about $\frac{1.005-1.00}{1.005+4\times1.02+1} = 0.08\%$. The net polarised charge density ρ is the totally polarised charge density multiplying its polarisation percentage, about 6.4 μC/cm^2 $\times$ 0.08 % = 0.0048 μC/cm^2. In a parallel-plate capacitor, for this charge density on the two plate, the field in it can be estimated as $\mathbf{E}_p = \rho/\varepsilon_0\varepsilon_r = 2.58 \times 10^5$ V/m.

A.6 Calculation method benchmark

Some theoretical calculations show that van der Walls (vdW) force is very important for hybrid perovskite.[67, 260, 261, 262, 263] But all works are calculated on the level of PBE. They shown that the PBE+vdW method is better than that of the PBE method. Here, we use the PBE functional revised for solid. There are four papers using PBEsol without vdW.[164, 264, 64, 104] We show below that PBEsol is better than other methods with vdW. As shown in Table A.6, the sequence of lattice

parameters and volumes estimated by various methods is: PBE > optPBE-vdW > optB86b-vdW > PBE-vdw > PBEsol > Experimental > PBEsol-vdw. Parameters calculated by PBEsol are the closest parameters to experiments. If we consider the thermal expansion, lattice parameters get smaller. Hence, PBEsol is better than optB86b-vdW, optPBE-vdW and PBE-vdW.

Table A.6: Lattice parameters of tetragonal (β) phase $MAPbI_3$ calculated by various methods.

Method	a (Å)	b (Å)	c (Å)	V (Å^3)
PBE	9.074	9.029	13.175	1078.800
optPBE-vdW[265, 266]	9.007	9.015	13.010	1056.360
optB86b-vdW[265, 266]	8.891	8.869	12.811	1010.130
PBE-vdW[267, 268]	8.868	8.802	12.806	999.549
PBEsol	8.880	8.816	12.723	995.723
Exp[269]	8.855	8.855	12.659	992.600
Exp[8]	8.849	8.849	12.642	990.000
Exp[159]	8.860	8.860	12.453	975-987
PBEsol-vdW[267, 268]	8.544	8.642	12.048	888.578

Table A.7: Lattice parameters of orthorhombic (γ) phase $MAPbI_3$ calculated by various methods.

Method	a (Å)	b (Å)	c (Å)	V (Å^3)
PBE	9.075	12.838	8.698	1013.250
optPBE-vdW	8.980	12.821	8.699	1001.480
Exp3	8.861	12.620	8.581	959.500
optB86b+vdW	8.853	12.059	8.557	959.101
Exp2	8.836	12.580	8.555	951.010
PBEsol	8.855	12.573	8.474	943.523
PBE-vdW	8.707	12.579	8.522	933.338
PBEsol+vdW	8.435	12.256	8.388	867.038
PBE[67]	9.226	12.876	8.619	1023.880
optB86b+vdW[67]	8.831	12.648	8.570	957.180

Table A.7 shows the geometry parameters of the unit cell in orthorhombic phase optimized with different methods. Our calculations obtained geometries are closer to experiments than that of Wang's.[67] Both optB86b+vdW and PBEsol give good agreement. If we take the Exp3 as the standard, then optB86b+vdw gives better results in volume, but it gives a shorter b cell vector, the error is 0.57 Å. The largest difference for PBEsol is c cell vector, its error is only 0.11 Å. Thats to say, PBEsol gives a better shape. If we set the recent result Exp2 as standard, PBEsol gives

better results both in volume and shape. In general, the PBEsol method is better than optB86b+vdW, PBE+vdW, or optPBE+vdW.

Appendix B

Supplemental Information for Chapter 3

B.1 Numerical solution process details

B.1.1 Adapted equations and boundary conditions

The specific method we used to solve our equations are the relaxation method for 'Two Point Boundary Value Problems' in *Numerical Recipes in Fortran.*[185] Here, for convenience, we repeat these differential equations:

$$\begin{aligned} &J_p = -eD_p\frac{\partial p}{\partial x} + ep\mu_p F; \qquad J_n = eD_n\frac{\partial n}{\partial x} + en\mu_n F \\ &\frac{\partial J_n}{\partial x} = -eG + eR; \qquad \frac{\partial J_p}{\partial x} = eG - eR \\ &\frac{\partial F}{\partial x} = e\frac{p-n}{\varepsilon\varepsilon_0} \end{aligned} \tag{B.1}$$

and five boundary conductions:

$$\begin{aligned} &J_n|_{x=d} = 0; \qquad J_p|_{x=0} = 0; \qquad F_{x=0} = F_0 \\ &F_{x=d} = F_d; \qquad n|_{x=0}p|_{x=d} = N_cN_ve^{\frac{E_{bgap}-V}{-kT}} \end{aligned} \tag{B.2}$$

If we want to use the "Two point Boundary Value Problems" method in *Numerical Recipes in Fortran,*[185] all equations must be the first order differential and the boundary condition at two point is not coupled. As the last boundary condition in Equation B.2 is coupled. To decouple it, we add a new equation $n^0(x) = n|_{x=0}$, which is the electron density at x=0. It is a constant. For simple, we set $J_n = J_n/e$,$J_p = J_/e$, $n = ne$ and $p = pe$. We rewrite Equations B.1 in the form used in *Numerical Recipes in Fortran* ($\frac{\partial y}{\partial x} = g(x, y)$):

$$\begin{aligned} \frac{\partial p}{\partial x} &= (p\mu_p F - J_p)/D_p; & \frac{\partial n}{\partial x} &= (J_n - n\mu_n F)/D_n \\ \frac{\partial J_n}{\partial x} &= -G + R; & \frac{\partial J_p}{\partial x} &= G - R \\ \frac{\partial F}{\partial x} &= \frac{p-n}{\varepsilon\varepsilon_0}; & \frac{\partial n^0}{\partial x} &= 0 \end{aligned} \tag{B.3}$$

and boundary conditions:

$$\begin{aligned} J_p|_{x=0} &= 0; & F|_{x=0} &= F_0; & n|_{x=0} &= n^0|_{x=0} \\ F|_{x=d} &= F_d; & J_n|_{x=d} &= 0; & p|_{x=d} &= \frac{N_c N_v}{n^0|_{x=d}} e^{\frac{E_{bgap}-V}{-kT}} \end{aligned} \tag{B.4}$$

To implement these six (total number of equations, noted as N in *Numerical recipes*) equations into Fortran code, differential Equations B.3 are approximated by *finite-difference equations* (FDEs) on a grid of points (total point number, noted as M in *Numerical recipes*, we will discuss it in section B.1.7) that spans the whole perovskite layer:

$$\begin{aligned} & n^0(k) - n^0(k-1) = 0 \\ & J_p(k) - J_p(k-1) - h(G-R) = 0 \\ & F(k) - F(k-1) - h(\frac{\frac{p(k)+p(k-1)}{2} - \frac{n(k)+n(k-1)}{2}}{\varepsilon\varepsilon_0}) = 0 \\ & n(k) - n(k-1) - h(\frac{J_n(k)+J_n(k-1)}{2D_n} - \frac{\mu_n}{D_n}\frac{n(k)+n(k-1)}{2}\frac{F(k)+F(k-1)}{2}) = 0 \\ & p(k) - p(k-1) - h(\frac{\mu_p}{D_p}\frac{p(k)+p(k-1)}{2}\frac{F(k)+F(k-1)}{2} - \frac{J_p(k)+J_p(k-1)}{2D_p}) = 0 \\ & J_n(k) - J_n(k-1) - h(-G+R) = 0 \end{aligned} \tag{B.5}$$

where $h = x(k) - x(k-1)$. Then, the problem becomes FDEs on a mesh of M points, a solution consists of values for N dependent functions given at each of the M mesh points. In total there are $N \times M$ variables. The method determines the solution by starting with an initial guess and improving it iteratively. As the iterations improve the solution, the result will relax to the true solution.

B.1.2 General procedures

To simplify illustration, we set all these parameters as: $y_1 = n^0$; $y_2 = J_p$; $y_3 = F$; $y_4 = n$; $y_5 = p$; $y_6 = J_n$. We use the notation $\mathbf{y}_k$ to refer the entire set of

dependent variables y_1, y_2, . . ., y_6 at point x_k, and use the notation $\mathbf{g}_k$ to refer all the functions. Then Equation B.5 can be written:

$$0 = \mathbf{E}_k \equiv \mathbf{y}_k - \mathbf{y}_{k-1} - (x_k - x_{k-1})\mathbf{g}_k(x_k, x_{k-1}, \mathbf{y}_k, \mathbf{y}_{k-1}) \tag{B.6}$$

Where $\mathbf{E}_k$ is the errors of guessed solution. Equation B.6 provides six equations coupling twelve variables at point k, $k-1$. There are $M-1$ points, $k = 2, 3, ..., M$.

At the first boundary ($x = 0$) , we have three conditions (first three in Equation B.4)

$$0 = \mathbf{E}_1 \equiv \mathbf{B}(\mathbf{x}_1, \mathbf{y}_1) \tag{B.7}$$

while at the second boundary ($x = d$, last three in Equation B.4)

$$0 = \mathbf{E}_{M+1} \equiv \mathbf{C}(\mathbf{x}_M, \mathbf{y}_M) \tag{B.8}$$

The solution of Equation B.6, B.7 and B.8 consists of six variables y_j at the M points x_k. We give an **initial guess** (we will give it later), then corrections were applied to approximate to the solution. The correction is developed by expanding the FDEs in first-order Taylor series with respect to small changes $\Delta\mathbf{y}$. At an interior point ($2 < k < M$), this gives:

$$\mathbf{E}_k(\mathbf{y}_k + \Delta\mathbf{y}_k, \mathbf{y}_{k-1} + \Delta\mathbf{y}_{k-1}) \approx \mathbf{E}_k(\mathbf{y}_k, \mathbf{y}_{k-1}) + \sum_{i=1}^{N} \frac{\partial \mathbf{E}_k}{\partial y_{i,k-1}} \Delta y_{i,k-1} + \sum_{i=1}^{N} \frac{\partial \mathbf{E}_k}{\partial y_{i,k}} \Delta y_{i,k} \tag{B.9}$$

To approach a solution, $\mathbf{E}(\mathbf{y} + \Delta\mathbf{y})$ should be updated to be zero. The general set of equations at an interior point can be written in matrix form as

$$\sum_{i=1}^{6} S_{j,i} \Delta y_{i,k-1} + \sum_{i=6+1}^{12} S_{j,i} \Delta y_{i-6,k} = -E_{j,k}, \qquad j = 1, 2, ...6 \tag{B.10}$$

where, $S_{j,i} = \frac{\partial \mathbf{E}_k}{\partial y_{i,k-1}}$, $S_{j,i+6} = \frac{\partial \mathbf{E}_k}{\partial y_{i,k}}$. The dimension of $S_{j,i}$ is 6×12 at each k.

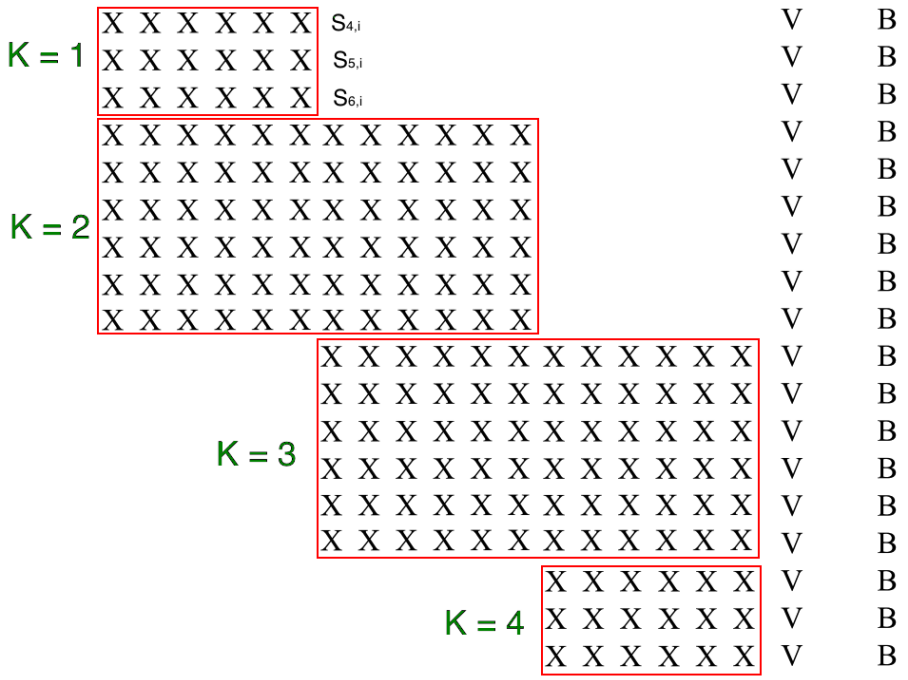

Figure B.1: Matrix structure of a set of linear six FDEs with three boundary conditions imposed at both endpoints. One X represents a coefficient of the FDEs, V represents a component of the unknown solution vector, and B is a component of boundary condition. Empty spaces represent zeros.

Similarly, the algebraic relations at the boundaries can be expanded in a first-order Taylor series for increments that improve the solution. Since $\mathbf{E}_1$ depends only on $\mathbf{y}_1$, we find at the first boundary:

$$\sum_{i=1}^{6} S_{j,i}\Delta y_{i,1} = -E_{j,1}, \qquad j = 4, 5, 6 \tag{B.11}$$

where $S_{j,i} = \frac{\partial E_{j,1}}{\partial y_{n,1}}$. At the second boundary,

$$\sum_{i=1}^{6} S_{j,i}\Delta y_{i,M} = -E_{j,M+1}, \qquad j = 1, 2, 3 \tag{B.12}$$

where $S_{j,i} = \frac{\partial E_{j,M+1}}{\partial y_{n,M}}$.

We thus have in Equations B.10, B.11 and B.12 a set of linear equations to be solved for the correction $\Delta\mathbf{y}$, iterating until the corrections are sufficiently small. The equations have a special structure, because each $S_{j,i}$ only couples with points k, $k-1$. Figure B.1 shows the structure of the complete matrix equation for the case of $M = 3$. There are three boundary conditions each boundary. The block boxed by red at left-up corner comes from the boundary condition $S_{j,i}$ at point $k = 1$. Next

two are $S_{j,i}$ from $k = 2$ and $k = 3$. The last block is corresponding to the three boundary conditions at the other boundary. This special form matrix is diagonalized by splitting into it M small matrix, and then diagonalize the matrix from the first point $k = 1$ to the last points $k = M + 1$. For more details, please check *Numerical recipes*.

B.1.3 S matrix

S matrix varies for different models. Here, we use direct recombination model ($R = r \times n \times p$, Equation 12 in main text) as an example. For SRH model and other models, the $S_{j,i}$ at each k points can be obtained by its definition in Equation B.6, B.7 and B.8. To simplify illustration, we set all these parameters as: $y_1 = n^0$; $y_2 = J_p$; $y_3 = F$; $y_4 = n$; $y_5 = p$; $y_6 = J_n$. Here, we only shows non-zero element. h is the size of discretion, $h = x(k) - x(k-1) = \frac{d}{M}$. We substitute μ with Einstein relation $\mu = \frac{eD}{kT} = \frac{D}{0.026}$ and R with rnp. Equation B.5 can be rewritten:

$$
\begin{aligned}
&y_1(k) - y_1(k-1) \equiv E_1 = 0 \\
&y_2(k) - y_2(k-1) - h(G - r\frac{y_5(k)+y_5(k-1)}{2}\frac{y_4(k)+y_4(k-1)}{2}) \equiv E_2 = 0 \\
&y_3(k) - y_3(k-1) - h(\frac{\frac{y_5(k)+y_5(k-1)}{2} - \frac{y_4(k)+y_4(k-1)}{2}}{\varepsilon\varepsilon_0}) \equiv E_3 = 0 \\
&y_4(k) - y_4(k-1) - h(\frac{y_6(k)+y_6(k-1)}{2D_p} - \frac{\mu_p}{D_p}\frac{y_4(k)+y_4(k-1)}{2}\frac{y_3(k)+y_3(k-1)}{2}) \equiv E_4 = 0 \\
&y_5(k) - y_5(k-1) - h(-\frac{y_2(k)+y_2(k-1)}{2D_n} + \frac{\mu_n}{D_n}\frac{y_5(k)+y_5(k-1)}{2}\frac{y_3(k)+y_3(k-1)}{2}) \equiv E_5 = 0 \\
&y_6(k) - y_6(k-1) - h(-G + r\frac{y_5(k)+y_5(k-1)}{2}\frac{y_4(k)+y_4(k-1)}{2}) \equiv E_6 = 0
\end{aligned}
\tag{B.13}
$$

For convenience's sake, we define $tmp1 = y(4,k) + y(4,k-1); tmp2 = y(5,k) + y(5,k-1); tmp = tmp1 + tmp2$. The S matrix is shown below written in Fortran. Here, LT is the charge carrier lifetime ans r is recombination coefficient, ne is the number of equations, noted as N in *Numerical recipes*. $S(i, jsf)$ is the last element for calculating E, then jsf= $2N + 1$.

For interior points $k = 2,\ 3,\ \ldots,M$

```
s(1,1)=-1;        s(1,ne+1)=1;        s(1,jsf)=y(1,k)-y(1,k-1)

s(2,4)=0.25*h*tmp2*LT;        s(2,ne+4)=s(2,4);        s(2,5)=0.25*h*tmp1*LT
s(2,ne+5)=s(2,5);             s(2,2)=-1.0 ;            s(2,ne+2)=1.0
```

s(2,jsf)=y(2,k)-y(2,k-1)+h*((0.25*tmp1*tmp2*LT-ni*ni)-g)

s(3,4)=0.5*h/($\varepsilon\varepsilon_0$); s(3,ne+4)=s(3,4)
s(3,5)=-0.5*h/($\varepsilon\varepsilon_0$); s(3,ne+5)=s(3,5)
s(3,3)=-1.0; s(3,ne+3)=1.0
s(3,jsf)=y(3,k)-y(3,k-1)-0.5*h*(tmp2-tmp1)/($\varepsilon\varepsilon_0$)

s(4,4)=-1.+h*(y(3,k)+y(3,k-1))/(4*kt); s(4,6)=-.5*h/de
s(4,ne+4)=1.+h*(y(3,k)+y(3,k-1))/(4*kt); s(4,ne+6)=-.5*h/de
s(4,3)=h*tmp1/(4*kt) ; s(4,ne+3)=h*tmp1/(4*kt)
s(4,jsf)=y(4,k)-y(4,k-1)-0.5*h*((y(6,k)+y(6,k-1))/de-tmp1*(y(3,k)+y(3,k-1))/(2*kt))

s(5,5)=-1.-h*(y(3,k)+y(3,k-1))/(4*kt); s(5,2)=0.5*h/dh
s(5,ne+5)=1.-h*(y(3,k)+y(3,k-1))/(4*kt); s(5,ne+2)=0.5*h/dh
s(5,3)=-h*tmp2/(4*kt) ; s(5,ne+3)=-h*tmp2/(4*kt)
s(5,jsf)=y(5,k)-y(5,k-1)+0.5*h*((y(2,k)+y(2,k-1))/dh-tmp2*(y(3,k)+y(3,k-1))/(2*kt))

s(6,6)=-1.0; s(6,ne+6)=1.0
s(6,4)=-0.25*h*tmp2*LT; s(6,ne+4)= s(6,4)
s(6,5)=-0.25*h*tmp1*LT ; s(6,ne+5)=s(6,5)
s(6,jsf)=y(6,k)-y(6,k-1)-h*((0.25*tmp1*tmp2*LT-ni*ni)-g)

At the first boundary(x=0, k=1)

s(4,ne+3)=1.0; s(5,ne+2)=1.0
s(6,ne+4)=1.0; s(6,ne+1)=-1.0
s(4,jsf)=y(3,1)-E0; s(5,jsf)=y(2,1); s(6,jsf)=y(4,1)-y(1,1)

At the second boundary(x=d, k=M)

s(1,ne+3)=1.0; s(2,ne+6)=1.0; s(3,ne+5)=1.0
s(3,ne+1)=exp(v/(kt))*n0*n0/(y(1,m)*y(1,m))
s(1,jsf)=y(3,m)-Ed; s(2,jsf)=y(6,m)
s(3,jsf)=y(5,m)-exp(v/(kt))*n0*n0/y(1,m)

B.1.4 Initial Guess

In our model, the applied voltage (V) is implemented as one boundary condition. The current density is obtained from solutions. We start with $V = 0V$, giving an initial

guess, solving equations. Then, the solution of $V = 0V$ will be used as the initial guess for the applied voltage $V = 10mV$. We increase the voltage with increment of 10 mV, until The desired voltage reached. The first initial guess are shown as below, where D is the thickness of perovskite layer. $myE0 = V/D$.
The first initial guess
do k=1,M
x(k)=(k-1)*h
y(1,k)=n0*exp(v/(2*kt))
y(2,k)=0.01*x(k)/D
y(3,k)=myE0
y(4,k)=n0*exp(v/(2*kt))*EXP(x(k)/D)
y(5,k)=n0*exp(v/(2*kt))*EXP(1-x(k)/D)
y(6,k)=(D-x(k))*0.01/D
end do

B.1.5 Error calculation and converged criteria

The total error is calculated by

$$Error = \frac{1}{6M} \sum_{k=1}^{M} \sum_{j=1}^{6} \frac{|\Delta y(j,k)|}{scalv(j)} \tag{B.14}$$

where $scalv(j)$ is the scale of variable $y(j)$. In *Numerical recipes*, the *scalv* vector is defined by a constant vector. In this numerical model, charge densities are in the scale of 10^{10} to 10^{18}. If we define the *scalv* as a constant, the error should in a very wide range. Therefore, we set $scalv(j)$ as the maximum value of previous $y(j,k)$. The convergence criteria (*conv*) is 1.0^{-20}. When error is smaller than *conv*, the solution was reached.

B.1.6 Charges densities, electric field and currents in perovskite solar cells

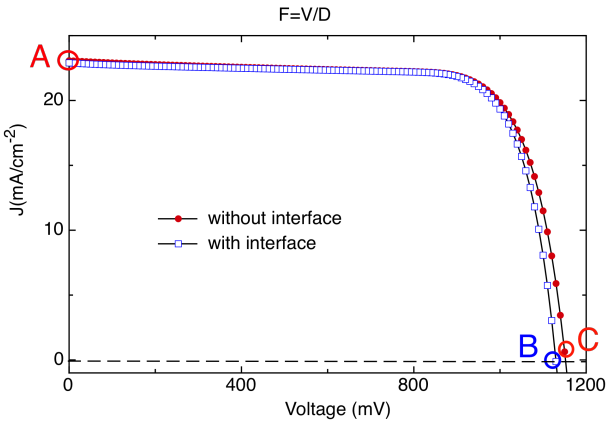

Figure B.2: J-V character curve simulated with boundary fields are $F(x = 0) = F(x = d) = V/d$. Other parameters are shown in Table 3.1. Charges densities, currents and field at A, B and C points are shown in Figure B.3.

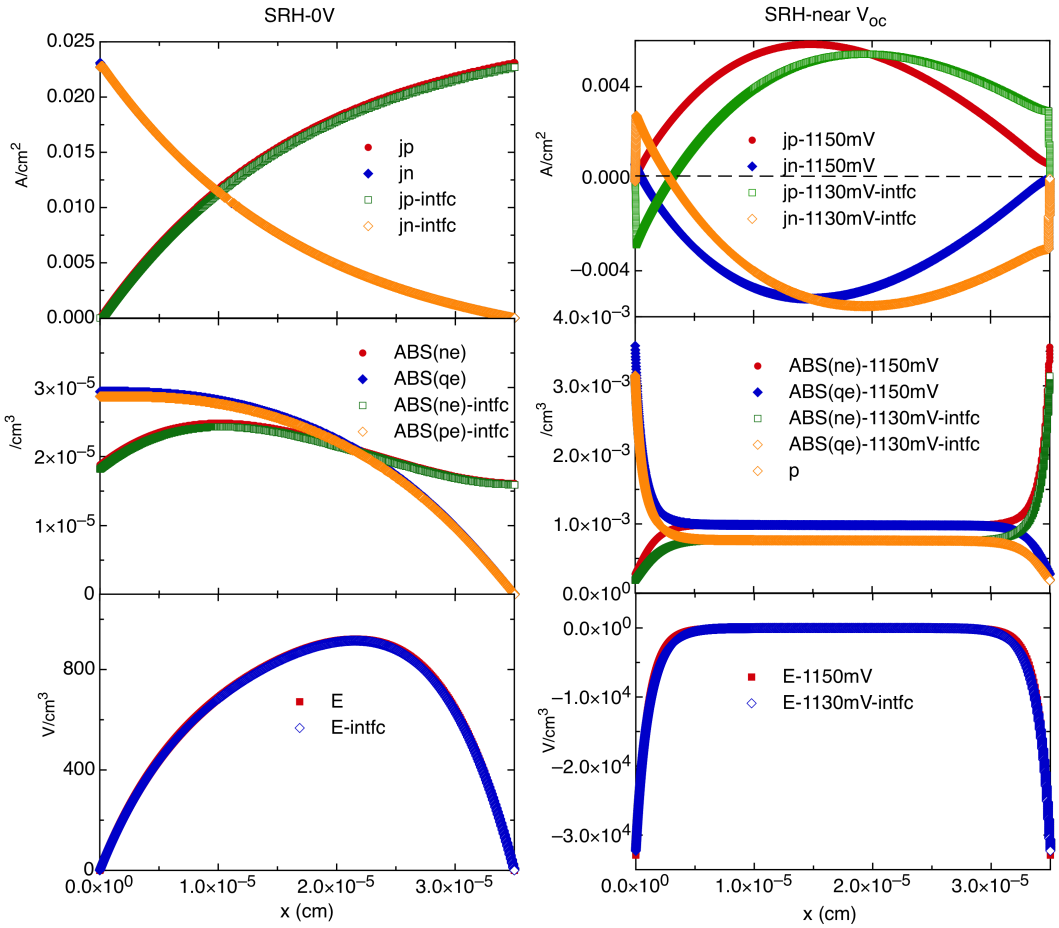

Figure B.3: Simulated charges densities, electric fields and currents in perovskite solar cells. Left shows parameters at short circuit, point A in Figure B.2. Right shows parameters near open circuit, point B and C in Figure B.2. Boundary fields are $F(x = 0) = F(x = d) = V/d$. Other parameters are shown in Table 3.1. The enlarged current distribution near TiO_2 side is shown in Figure B.4.

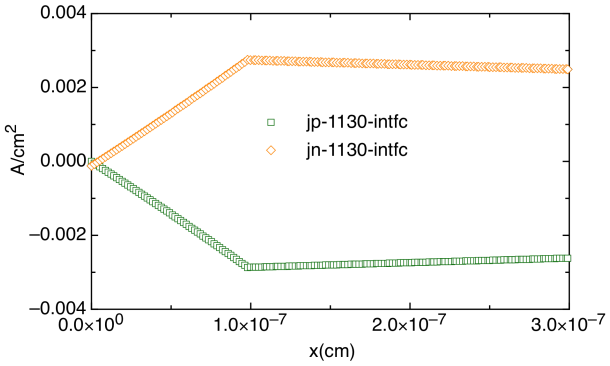

Figure B.4: Currents near TiO_2 side in perovskite solar cells near open circuit simulated with interfaces. Boundary fields are $F(x = 0) = F(x = d) = V/d$. Other parameters are shown in Table 3.1.

B.1.7 Mesh test

Here, we are going to test how many discretion points (M) are enough for our model. Models with and without interface recombination are carried out. As shown in Figure B.5, for model without interface recombination, 801 points is enough to get an accurate solution. For the sake of safety, we set $M = 3001$ for model without interface recombinations. While, for the model with interfaces, more points are required. We performed more test with an interface recombination with thickness of 2nm and charge carriers lifetime of 1 ns. It is found that there is no much difference between solutions solved with $M = 20001$ and $M = 300001$. As the computation time is proportional to the number of M points, high density points needs long time. Therefore, we choose $M = 20001$ for models with interface recombination.

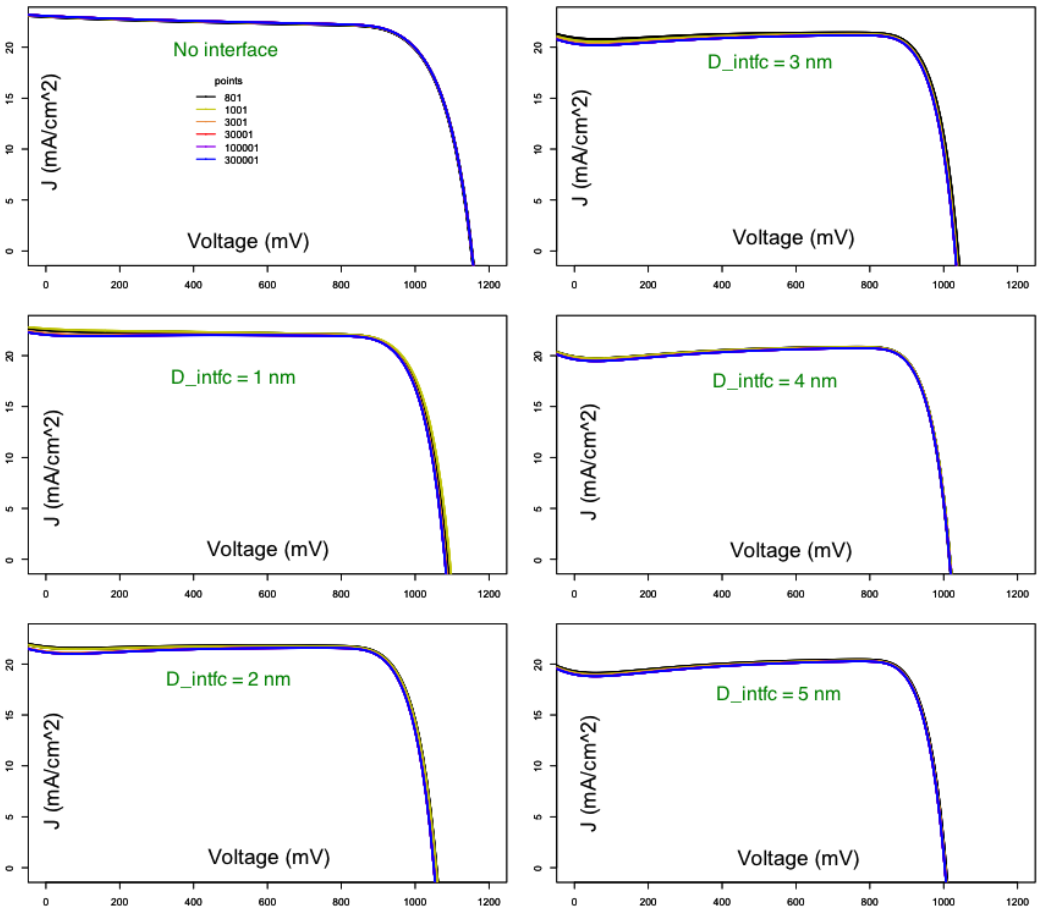

Figure B.5: J-V curves of a solar cell with different number of mesh points and interface recombination thickness. In the interface recombination region, charge carrier's lifetime is set as 1 ns. More parameters are shown in Table B.1

Table B.1: Parameters for M test.

α	Absorption coefficient	$5.7 \times 10^4 cm^{-1}$.[28]	T	Temperature	300 K
$IPCE$	IPCE	100 %	I_l	Light intensity	1.5 AM
N_c,N_v	Density of States	$3.97 \times 10^{18} cm^{-3}$.[52]	$Bgap$	Band gap	1.55 eV[1]
D_n	Electron diffusion coefficient	0.017 $cm^2 s^{-1}$. [29]	τ	Lifetime	736 ns [1]
D_p	Hole diffusion coefficient	0.011 $cm^2 s^{-1}$. [29]	F_0, F_d	Field at boundary	$\frac{V}{d}$
d	Perovskite thickness	350 nm[1]	τ_{intf}	Interface Lifetime	1 ns

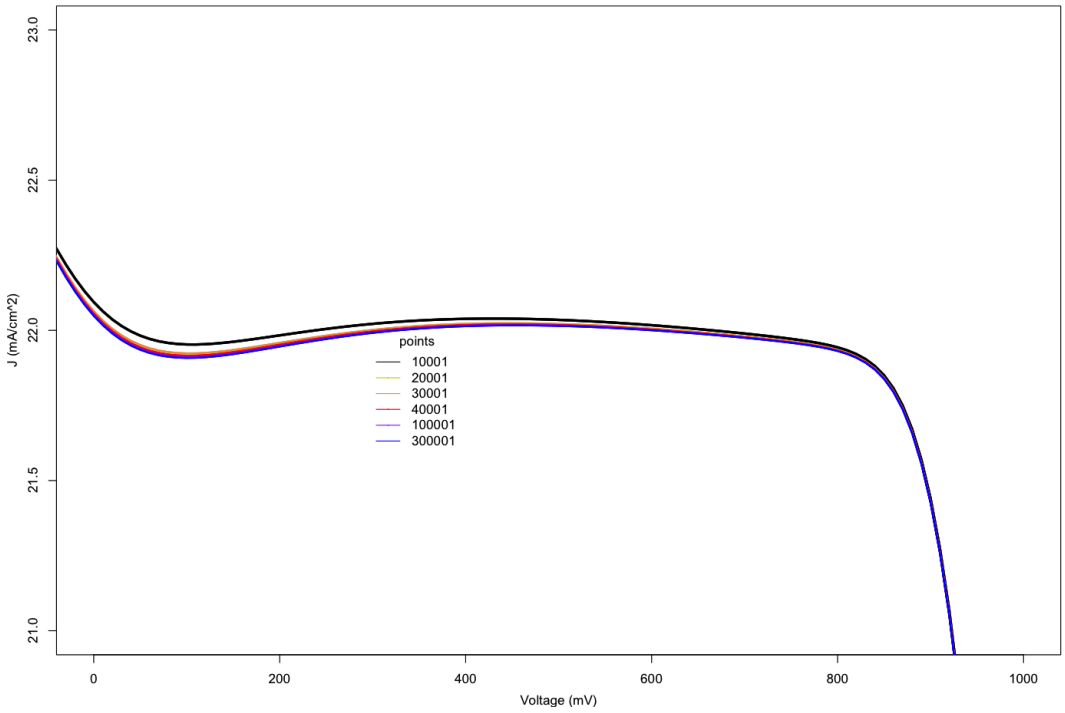

Figure B.6: J-V curves of a solar cell with different number of mesh. The interface recombination thickness is 2 nm. More parameters are shown in Table B.1

B.1.8 Parallelization

With a given V, J is determined by solving Equation B.3. Every solution only give one point in J-V curve of a solar cell. On the other hand, the mesh points need to be large in order to achieve accurate solutions. Hence, it is time-consuming to draw a J-V curve of a solar cell. Here, we implement MPI into our code for parallel calculations. The solution matrix is diagonalized by splitting it into M 6×13 submatrixs and diagonalizing the submatrix from $k = 1$ to $k = M$. It is not wise to divide this process into several parts and to diagonalize on separated CPUs. Therefore, we scatter all of the V array to every CPU, and then solve them separately. Lastly, all solutions are collected by MPI_GATHERV function.

B.2 Lifetime dependence:

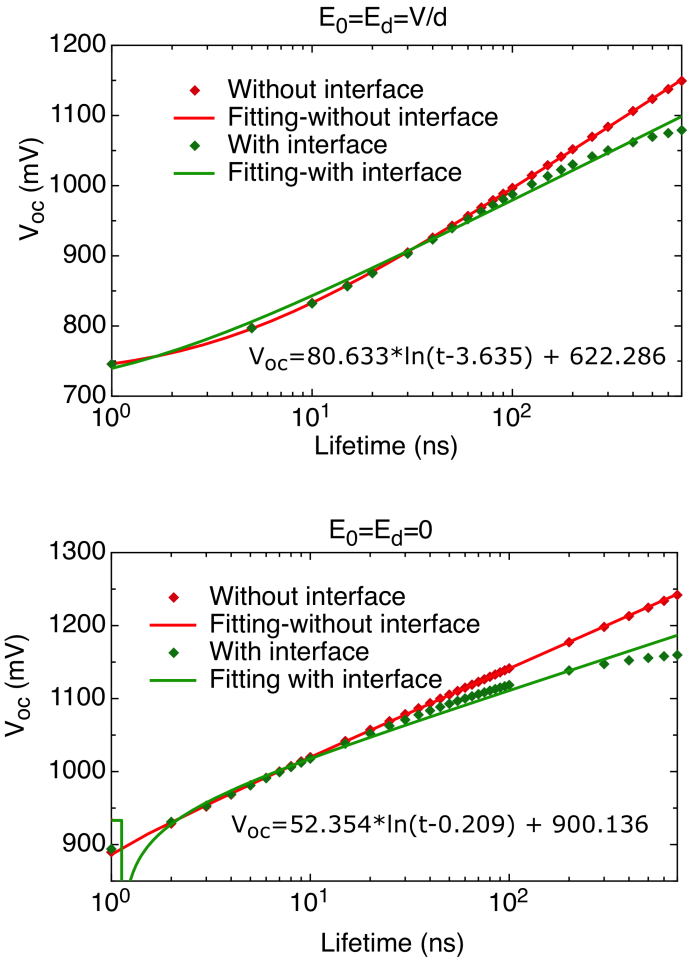

Figure B.7: V_{oc} lifetime dependence.

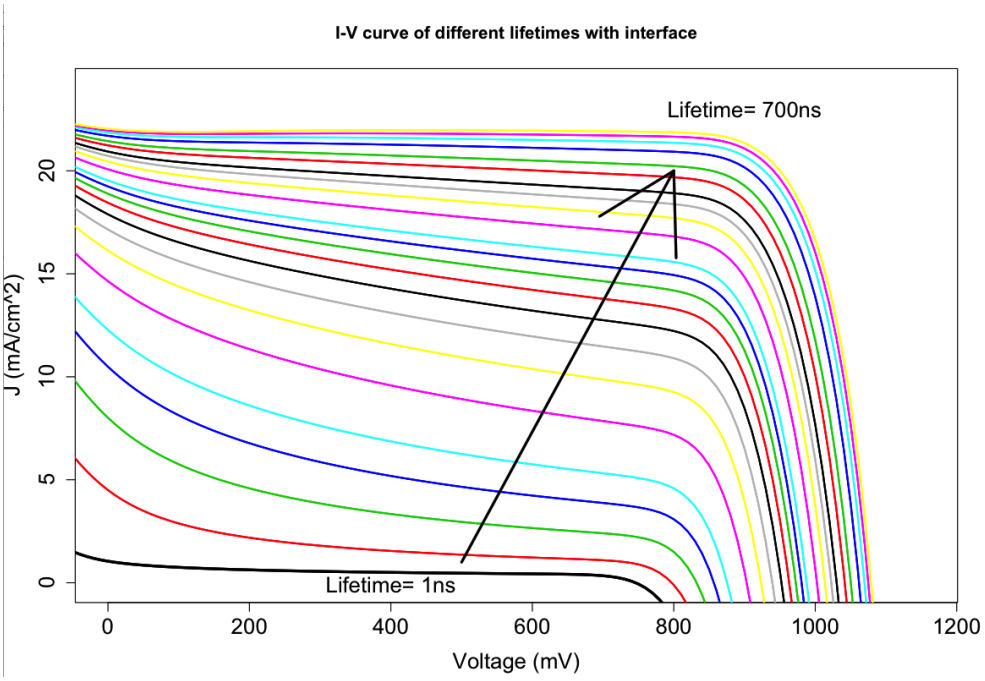

Figure B.8: Solar cell's performance with various lifetimes with interface recombination. F_0=F_d=V_0/d.

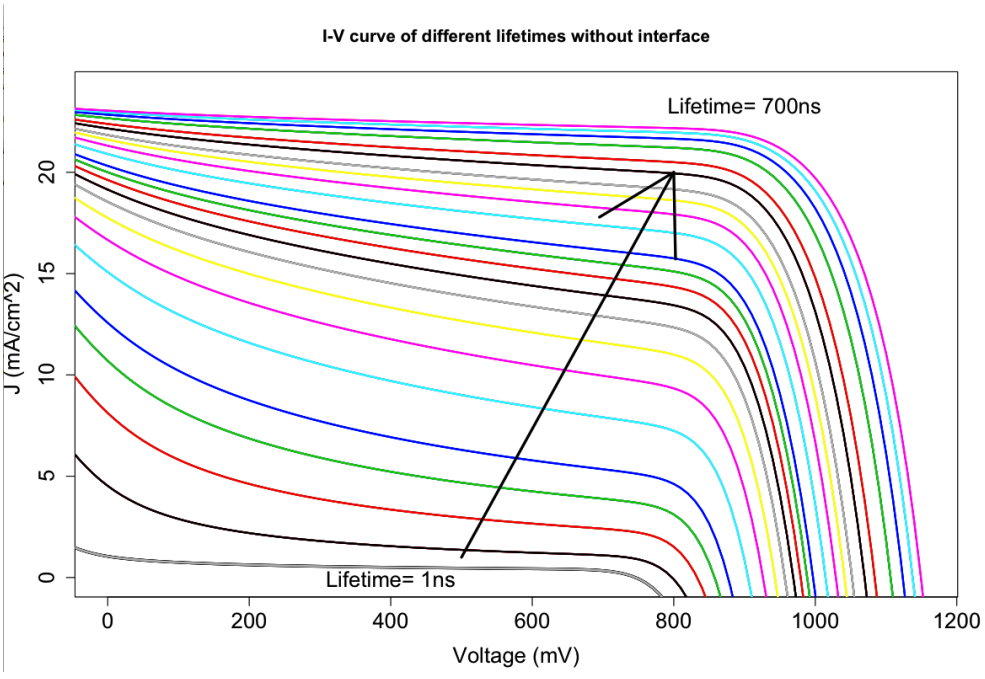

Figure B.9: Solar cell's performance with various lifetimes without interface recombination. F_0=F_d=V_0/d.

B.3 Mobility dependence:

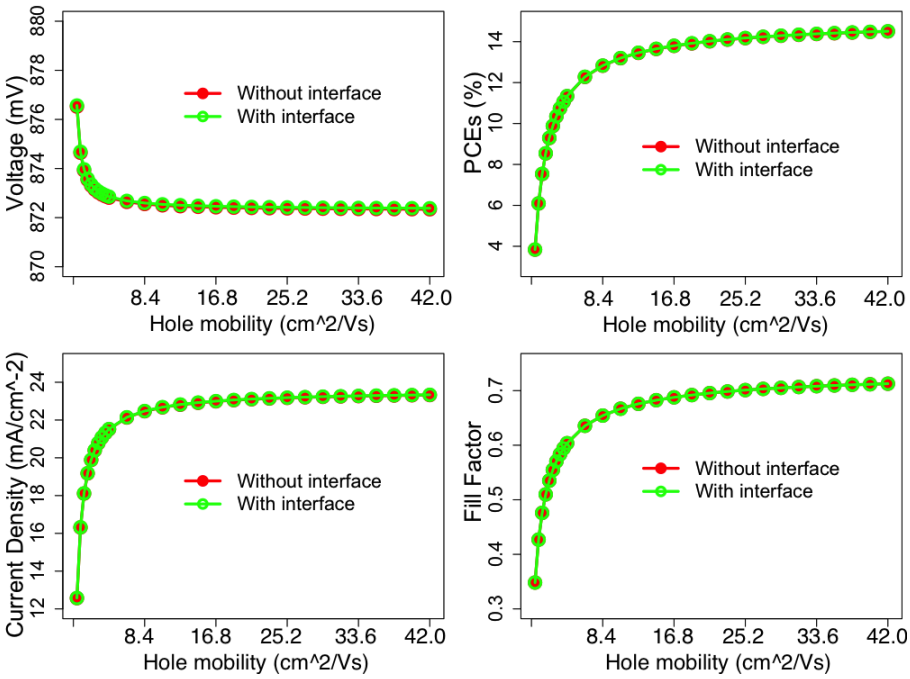

Figure B.10: Solar cell's performance with different mobilities. Both of the electron and hole mobilities increase to certain times of 0.65(electron) and 0.42 (hole) cm^2/Vs, the corresponding diffusion coefficients are $0.017cm^2/s$ and $0.011cm^2/s$. F_0=F_d=V_0/d.

B.4 Temperature dependence:

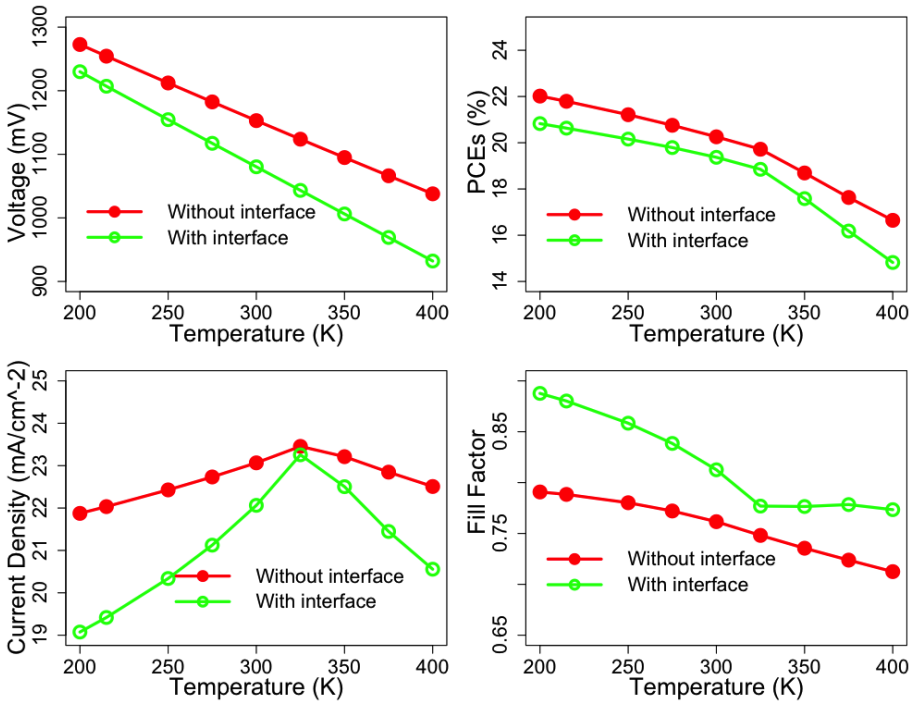

Figure B.11: Temperature dependence with different diffusion coefficients. The thickness of simulated solar cell is 350 nm. The band gap is 1.55 eV. The interface recombination width is 5 nm and its lifetime is 5 ns. The lifetime in cell is assumed to be 736 ns. The cells work under 1 sun (1.5AM).

B.5 Thickness depends performance

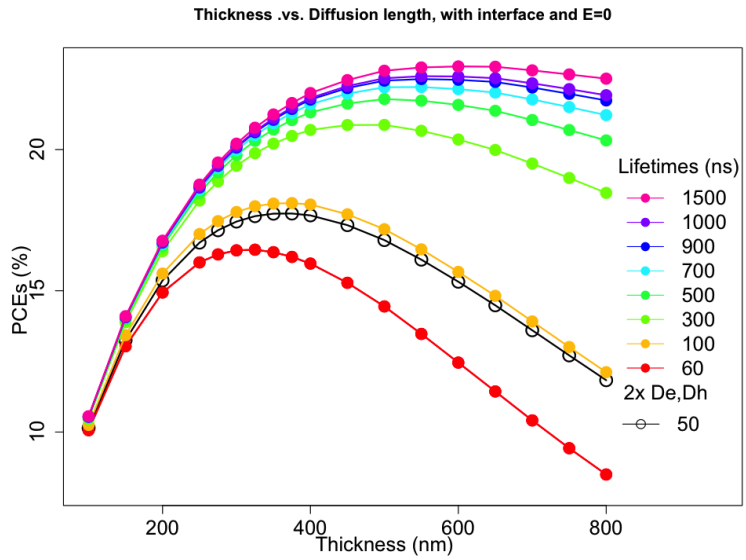

Figure B.12: The thickness dependence PCEs. The optimum thickness depends on the diffusion length. Modeled with interface. $F_0 = F_d = 0$

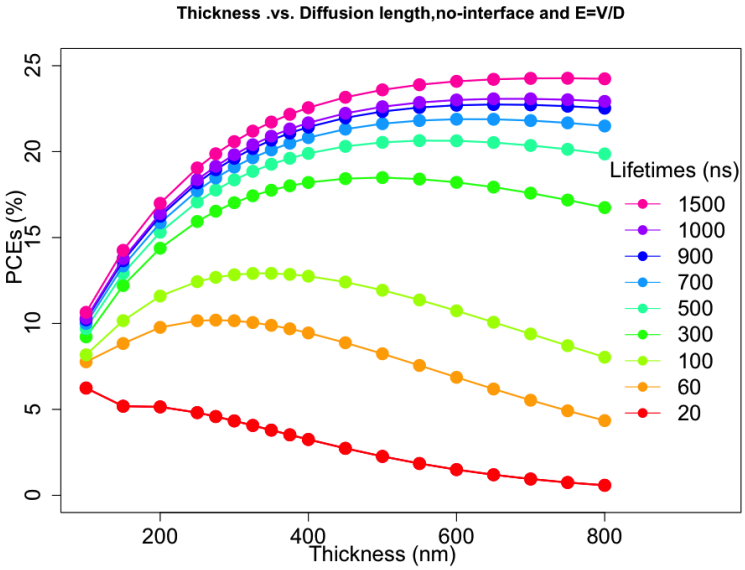

Figure B.13: The thickness dependence PCEs. The optimum thickness depends on the diffusion length. Modeled without interface. $F_0 = F_d = V/d$

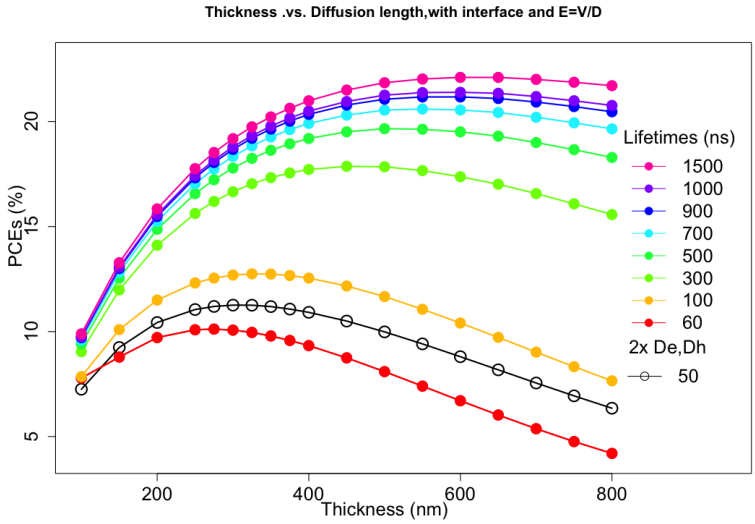

Figure B.14: The thickness dependence PCEs. The optimum thickness depends on the diffusion length. Modeled with interface. $F_0 = F_d = V/d$

B.6 Structure optimization

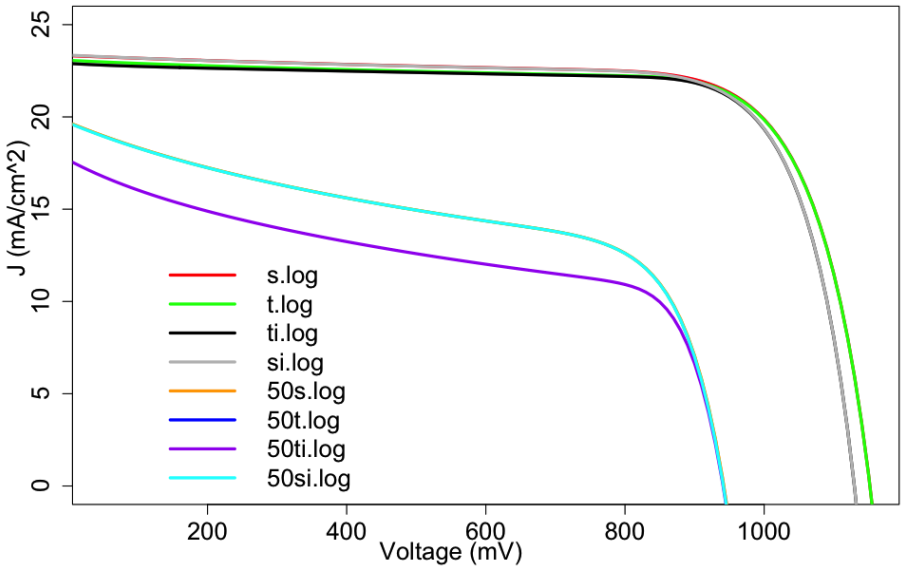

Figure B.15: Models comparison of T and S model with or without interface, with life time of 736 ns or 50 ns. $F_{x=0} = F_{x=d} = \frac{V}{d}$

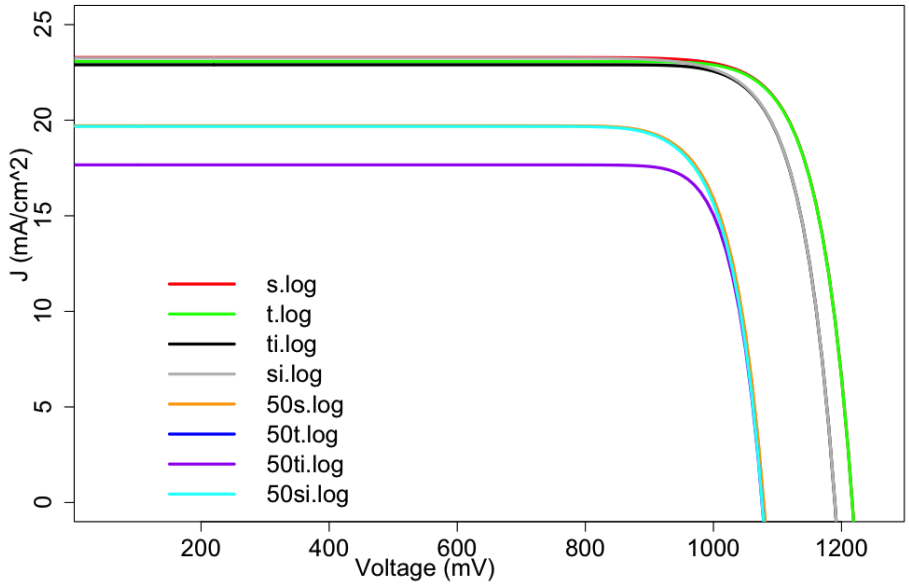

Figure B.16: Model comparisons of T and S model with or without interfaces, with life time of 736 ns or 50 ns. $F_{x=0} = F_{x=d} = 0$

B.7 Recombination coefficient estimation

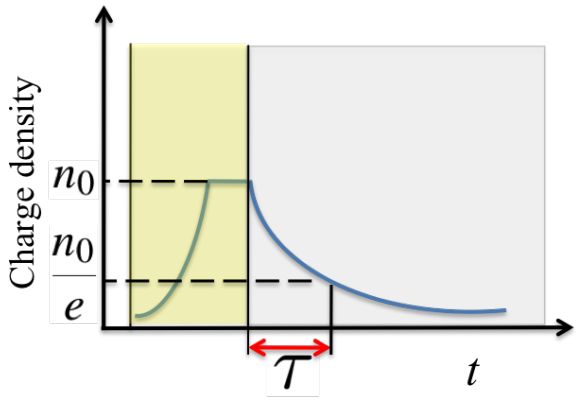

Figure B.17: Measurement of lifetime: In the yellow shadow region, the cell is irradiated by the pulse, in this region photon generate charge carriers become more and more until charges are saturated. Gray shadow covered region means the irradiation have been removed, the charge density decrease with time past.

As we have illustrated that Equation 3.14 is the charge carriers lifetime educe from Equation 3.12 under the condition of small charge injection under illumination.[87, 90] However, in real case, the condition of small injection is not satisfied. In experiments only the lifetime of charge carriers are available. Hence, we have to educe the recombination coefficients from charge carrier lifetimes. The lifetime measurement process

is [28, 29]: giving a short time illumination pulse, remove it, measure the charge density. Their processes are shown in Figure B.17. At first, the cell is irradiated by a pulse, during this period, photon generate charge carriers become more and more until charges are saturated. Then remove the pulse, the charge density decrease with time past. After a time of lifetime, the charge density become the $\frac{n_0}{e}$. Here, we will give the accurate relationship between the lifetime and recombination rate. It is assumed that the electron density is the same with the hole density ($n = p$). Then charge carriers recombination rate can be expressed as

$$\frac{dn}{dt} = -R = -r \times n \times p = -rn^2$$

then we have:

$$n = \frac{1}{r(t-c)}$$

As shown in Figure B.17, the charge density dynamics in solar cell has reached a balance when illumination is removed. The time of turn off the pulse is defined as zero. At $t = 0$, the charge density is n_0, then we can get $c = \frac{-1}{rn_0}$. Hence:

$$n = \frac{n_0}{rn_0 t + 1} \tag{B.15}$$

B.7.1 Uniformly distributed charge density

After the pulse removed, if the charge density in the device is uniformly distributed, at time τ, the charge density become $n = \frac{n_0}{e} = \frac{n_0}{rn_0\tau+1}$. Therefore, the lifetime can be expressed as:

$$\tau = \frac{e-1}{rn_0} \tag{B.16}$$

That's to say the charge carriers lifetime depends on the initial charge density rather than a certain value. Larger charge densities will lead to short lifetimes. If the charge density has reached a balance before remove the pulse, the charge generation rate should equal to the recombination rate: $G/d = r \times n_0^2$. Combining with equation (B.16), we can get

$$n_0 = \frac{G\tau}{L(e-1)} \tag{B.17}$$

Also we know the recombination coefficient:

$$r = \frac{L(e-1)^2}{G\tau^2} = 3.51499 \times 10^{-6} cm^3/s \tag{B.18}$$

These calculations is based on the assumption that carriers lifetime is 736 ns and charges are generated uniformly.

B.7.2 Estimation of the initial light intensity at $x = 0$

Before remove the pulse, the total generated carriers should be the same with the total recombined carriers. Hence:

$$\int_0^d \frac{I_0}{L} e^{-x/L} dx = \int_0^d r n_0^2 e^{-2x/L} dx$$

$$I_0 \left(1 - e^{-\frac{d}{L}}\right) = \frac{1}{2} L n_0^2 r \left(1 - e^{-\frac{2d}{L}}\right)$$

We get:

$$n_0 = \sqrt{\frac{2I_0(e^{-\frac{d}{L}} - 1)}{Lr(e^{-\frac{2d}{L}} - 1)}}$$

$$= \sqrt{\frac{2I_0}{Lr(e^{-\frac{d}{L}} + 1)}}$$

B.7.3 Decay exponentially-1

For a more accurate case, the charge density near the light surface is much higher than the charge density inside thin film. This high density will play a very important role in the process of recombination. If the generate rate is exponential decay, the lifetime become more complicated. Based on Equation B.16, the lifetime at x is

$$\tau(x) = \frac{e - 1}{r n_x} \tag{B.19}$$

Where $n_x = n_0 e^{\frac{-x}{L}}$, L is the decay depth. n_0 is the initial light intensity at $x = 0$. It will be estimated later. The charge density at x and time t is $n(x,t) = n_0 e^{\frac{-x}{L}} \times e^{\frac{-t}{\tau(x)}}$. Then the lifetime measured in experiment is the time make below equation true:

$$\frac{\int_0^d n_0 e^{\frac{-x}{L}} \times e^{\frac{-t}{\tau(x)}} dx}{\int_0^d n_0 e^{\frac{-x}{L}} dx} = \frac{1}{e} \tag{B.20}$$

We get,

$$\frac{(e-1)\left(e^{-\frac{r n_0 t e^{-\frac{d}{L}}}{e-1}} - e^{-\frac{r n_0 t}{e-1}}\right)}{r n_0 t (1 - e^{-\frac{d}{L}})} = \frac{1}{e} \tag{B.21}$$

If we use the data provided by Zhou [1], ($\tau = 736$ ns, d=350 nm, band gap = 1.55 eV), then r is calculated to be $1.23 \times 10^{-9} cm^3/s$. The decay curves from the experiment and decay estimated with $r = 1.23 \times 10^{-9} cm^3/s$ are shown in Figure B.18 left. As this method is an approximation, if we change r to $1.03 \times 10^{-9} cm^3/s$, its fit better, as shown in Figure B.18 right.

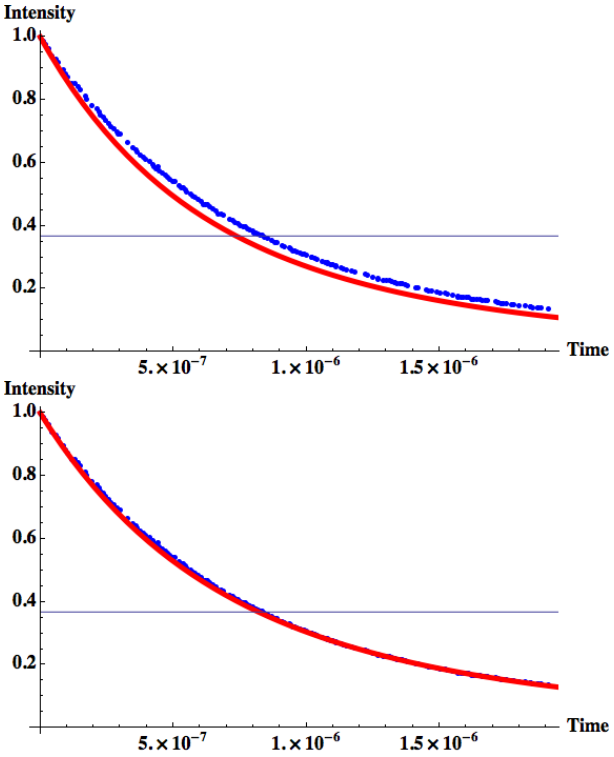

Figure B.18: Coefficient estimation. Decay exponentially-1

B.7.4 Decay directly-2

Rewrite the equation B.15, the carriers density at x and time t is

$$n(x) = \frac{n_0(x)}{rn_0(x)t + 1}$$

If the charge carriers is exponentially occupied at $t = 0$, $n_0(x) = \frac{I_0}{L} e^{\frac{-x}{L}}$, then the total charge density at time t is

$$\int_0^d \frac{n_0 e^{-\frac{x}{L}}}{n_0 r t e^{-\frac{x}{L}} + 1}\, dx$$

$$= \frac{-L \log\left(e^{d/L} + n_0 r t\right) + d + L \log(n_0 r t + 1)}{rt}$$

The initial density is $\int_0^d n_0 e^{\frac{-x}{L}} dx$

$$\frac{-L \log\left(e^{d/L} + n_0 r t\right) + d + L \log(n_0 r t + 1)}{n_0 r t \left(L - L e^{-\frac{d}{L}}\right)} = \frac{1}{e} \tag{B.22}$$

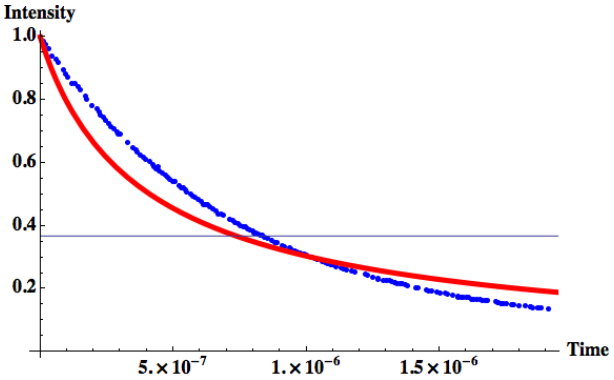

Figure B.19: Coefficient estimation. Decay directly-2

If we use the data provided by Zhou [1], (τ = 736 ns, d=350 nm, band gap = 1.55 eV), then r is calculated to be $1.33 \times 10^{-9} cm^3/s$. The decay curves from the experiment and decay estimated with $r = 1.33 \times 10^{-9} cm^3/s$ are shown in Figure B.19. Due to its poor agreement, this method is abandoned.

Appendix C

Supplemental Information for Chapter 4

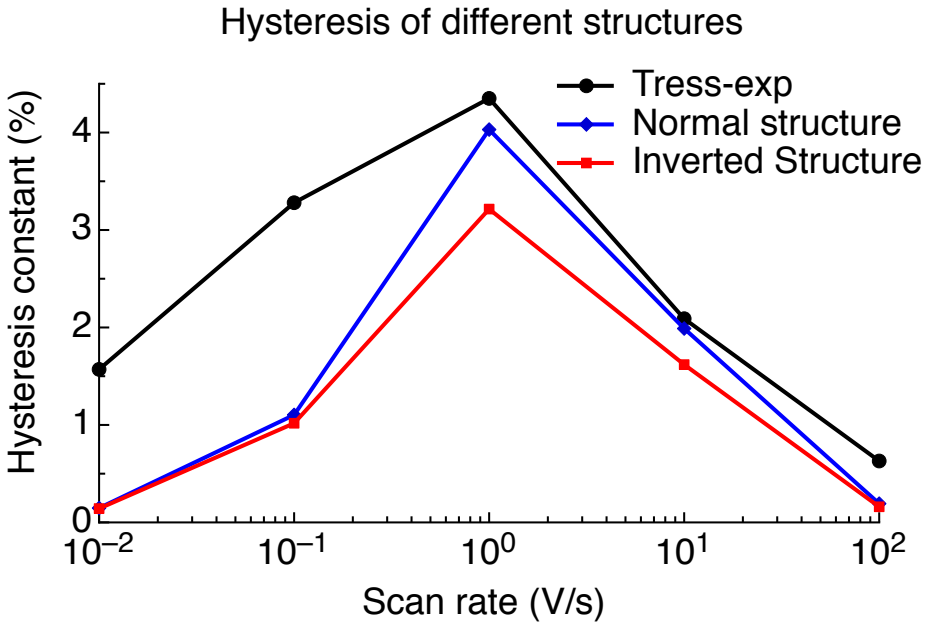

Figure C.1: Hysteresis constants of Tress's experiment, simulated normal structures and simulated inverted structure.

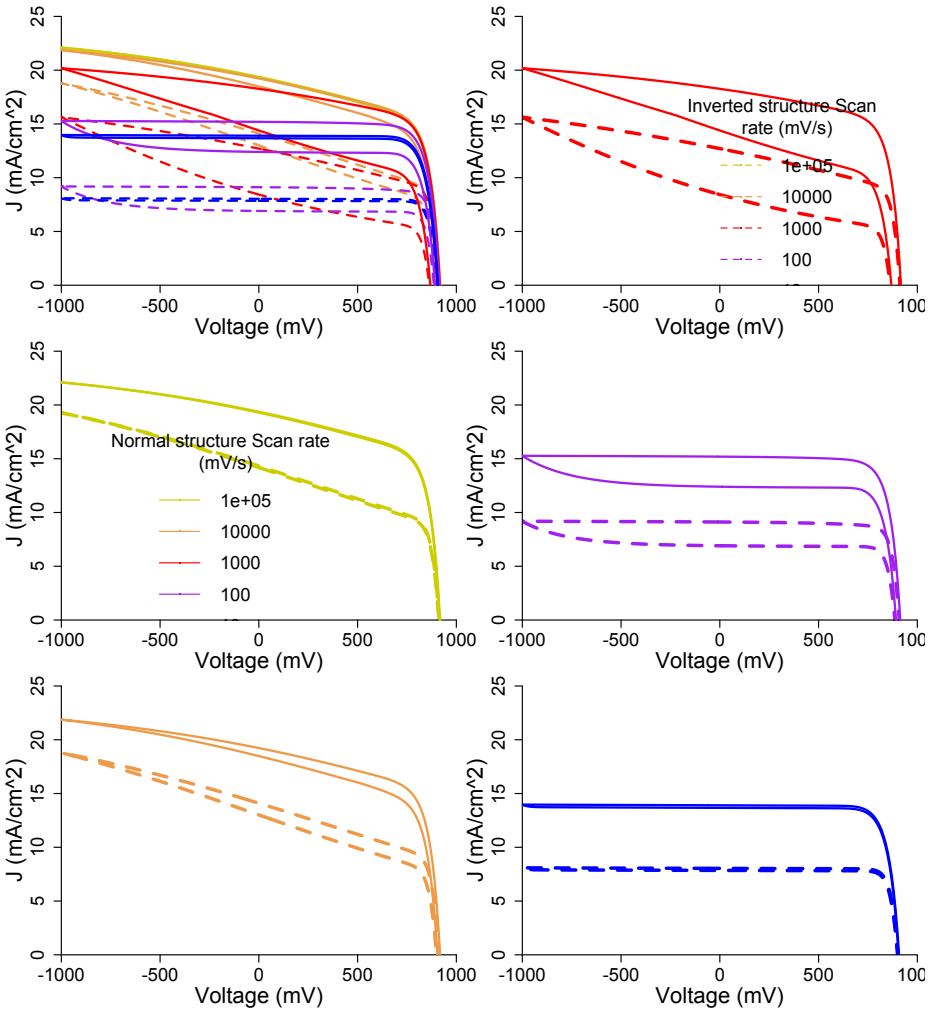

Figure C.2: Performances of a solar cell measured forward and backward with different scan rates. Solid lines are simulation results of normal structure perovskite solar cells. Dashed lines are simulation results of inverted structure perovskite solar cells. We use direct recombination without an interface. Parameters are shown in Table 4.2.

Appendix D

Supplemental Information for Chapter 6

D.1 Method choosing

In order to obtain relative more accurate DOS, GGA-PS,[151] GW[237, 238] and HSE06[239, 240] functions are carefully testified. GW and HSE06 functions could give accurate results. But the computational time is massive comparing to normal DFT calculation. Therefore, we will use normal DFT if its result is comparable to GW and HSE06. Table D.1 and Figure D.1 show the band structure and effective masses of silicon. It is found that there is a large difference for band gaps between different methods. We also found that their band structure, especially the sharp are very similar, which indicates that the effective mass maybe similar. We confirm it with calculations. The effective masses are shown in Table D.1. We found that the is very little differences between them. The error between GGA-PS and GW are about 10%. Therefore, we use GGA-PS function to perform our calculations.

The effective mass is calculated by fitting 5 points near the high-symmetry k-point with quadratic function. The reduced mass for silicon is defined as $m_r = (m_1 * m_2 * m_3 * .. * m_n)^{1/n}$. S points is where th the conduction band minimum locate. The band structure data was generated from Wannier90 program.[270, 271]

Table D.1: The effective masses of silicon on different directions calculated by GGA-PS, HSE06, GW methods. Unit is m_0, which is the free electron rest mass.

Method		GGA-PS	HSE06	GW
Band gap (eV)		0.44	1.14	1.10
G-S	CB	0.61	0.89	0.47
S-X	CB	0.58	1.14	0.43
Reduced mass	CB	0.59	1.01	0.45
L-Γ	VB1	-0.58	-0.42	-0.65
	VB2	-0.65	-0.68	-0.65
	VB3	-0.09	-0.12	-0.11
Γ-X	VB1	-0.45	-0.30	-0.35
	VB2	-0.27	-0.71	-0.29
	VB3	-0.14	-0.16	-0.15
K-Γ	VB1	-1.07	-0.71	-0.80
	VB2	-0.28	-0.61	-0.31
	VB3	-0.11	-0.13	-0.12
Reduced mass	VB1	0.65	0.45	0.57
	VB2	0.36	0.66	0.39
	VB3	0.12	0.14	0.12

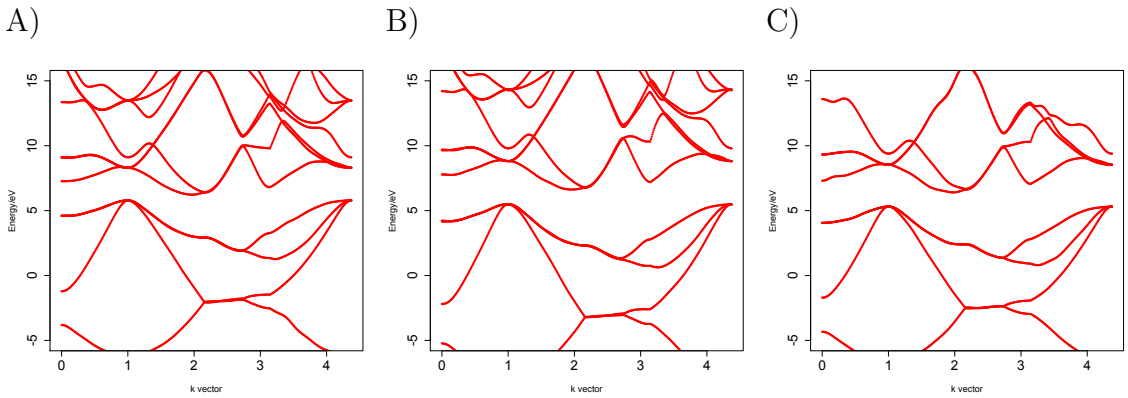

Figure D.1: Band structure of silicon calculated by different methods. A) Normal DFT with PBEsol exchange function, noted as PS; B) HSE method; C) GW method. The band gaps is 0.44 eV, 1.14 eV and 1.10 eV for GGA-PS, HSE06 and GW method respectively.

D.2 Effective mass and DOS of Silicon

Table D.2: Silicon effective masses for DOS and DOS.

K points	Coordinates	K points	Coordinates
Γ	(0,0,0)	Y	(0,0.5,0)
R	(-.5,-.5,-.5)	M	(.5,0,.5)
W	(.375,.375,.75)	S	(0.417391, 0, 0.417391)
N	(.5,0,-.5)		

Table D.3: Silicon effective masses for DOS and DOS.

Bands	Γ-S	S-N	S-Y	g	M_{eff}	DOS of band	Total DOS	Product
CB	1.04	0.19	0.25	6	1.20	3.35×10^{19}	3.35×10^{19}	
	R-G	G-M	W-G					
VB1	-0.64	-0.26	-2.70	1	0.76	1.69×10^{19}		7.76×10^{38}
VB2	-0.64	-0.26	-0.25	1	0.35	5.18×10^{18}	2.32×10^{19}	
VB3	-0.10	-0.17	-0.11	1	0.12	1.10×10^{18}		

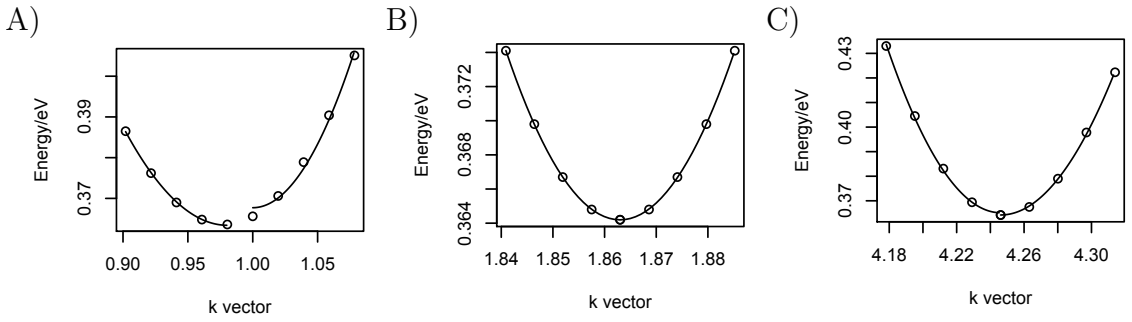

Figure D.2: Silicon Conduction band near S point on the direction of A) Γ-S; B) S-N; C) S-Y and its fitting for mass evaluation. Only left half is the wanted fitting. This plot calculation is specially performed for the effective mass calculation of S point. High density points near S points are implemented. Energy levels are raised.

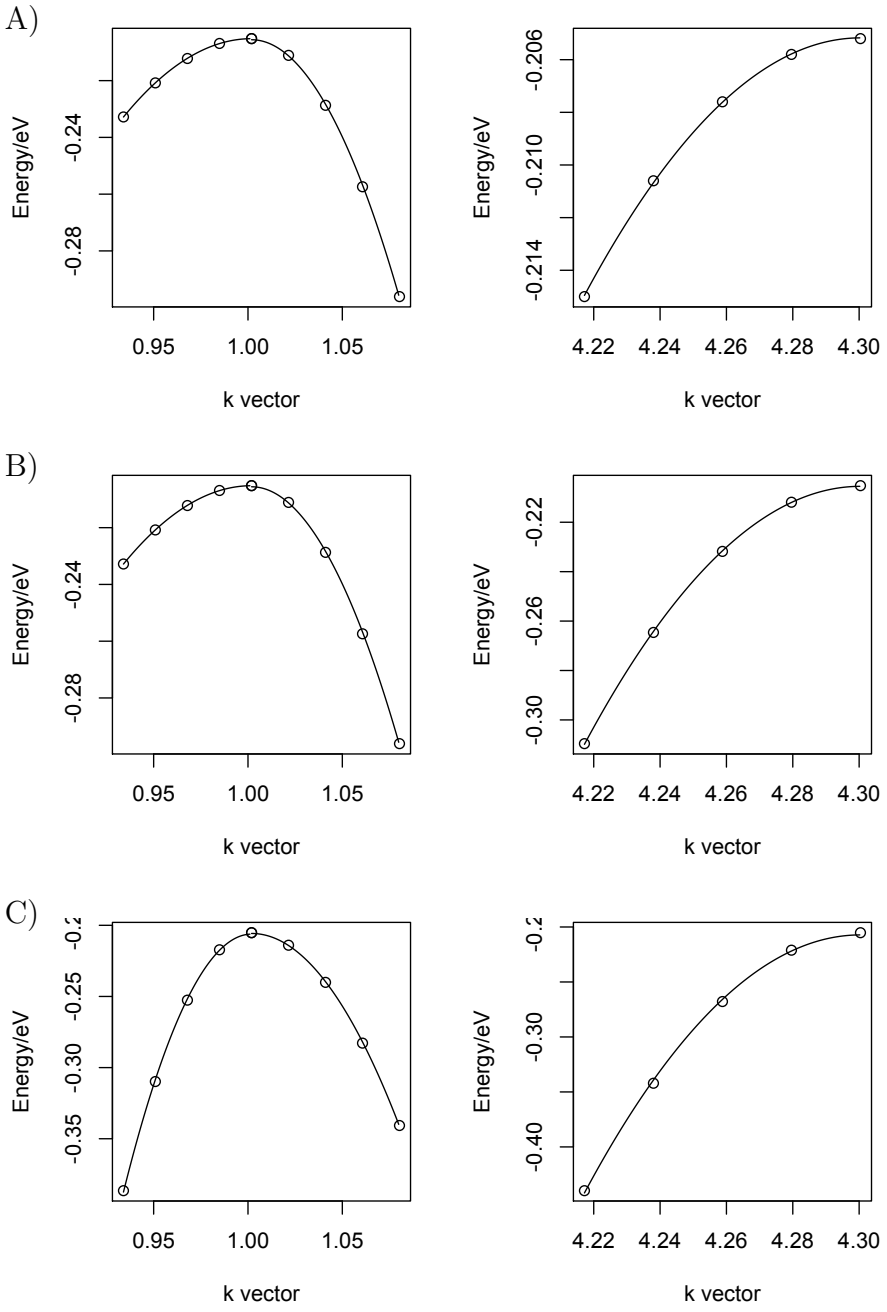

Figure D.3: Silicon Valence band near Γ point on the direction of R-Γ, Γ-M, W-Γ of A) VB1; B) VB2; C) VB3 and its fitting for mass evaluation.

D.3 Effective mass of α-$FAPbI_3$

Table D.4: α-$FAPbI_3$

Bands	M-Z	Z-Γ	Energy	g	M_{eff}	DOS of band	Total DOS	Product
CB3	0.12	0.17	0.77	2	0.21	2.51×10^{18}		
CB2	0.28	0.16	0.73	2	0.37	5.60×10^{18}	1.20×10^{19}	3.47×10^{37}
CB1	0.17	0.23	0.69	2	0.30	4.24×10^{18}		
VB	-0.14	-0.16	-0.68	2	0.24	2.90×10^{18}	2.90×10^{18}	

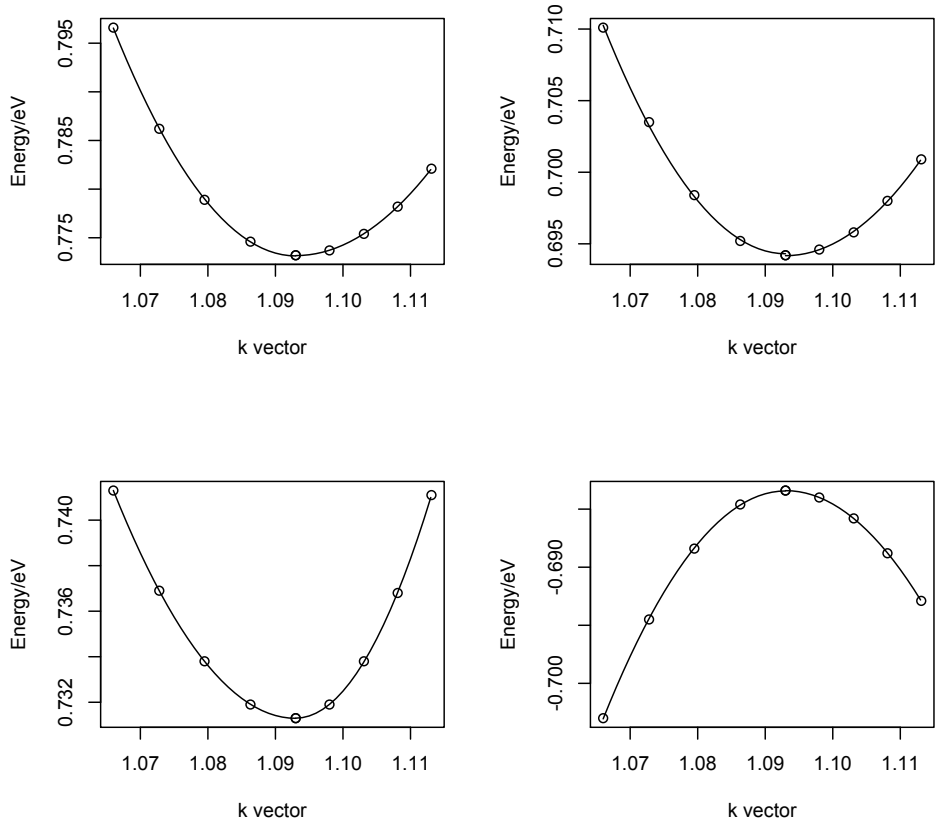

Figure D.4: α-$FAPbI_3$ CB3, CB2, CB1 and valence band near Z point on the direction of M-Z (left half), Z-Γ (right half) and its fitting for mass evaluation.

D.4 Effective mass of $MAPbCl_3$

Table D.5: $MAPbCl_3$

Bands	Z-Γ	Γ-X	Γ-R	Energy	g	M_{eff}	DOS of band	Total DOS	Product
CB3	0.11	0.30	0.19	1.63	1	0.18	2.00×10^{18}		
CB2	1.36	0.14	0.21	1.49	1	0.34	5.08×10^{18}	1.36×10^{19}	4.94×10^{37}
CB1	0.70	0.35	0.31	1.45	1	0.42	7.00×10^{18}		
VB	-0.32	-0.24	-0.26	-0.85	1	0.27	3.64×10^{18}	3.64×10^{18}	

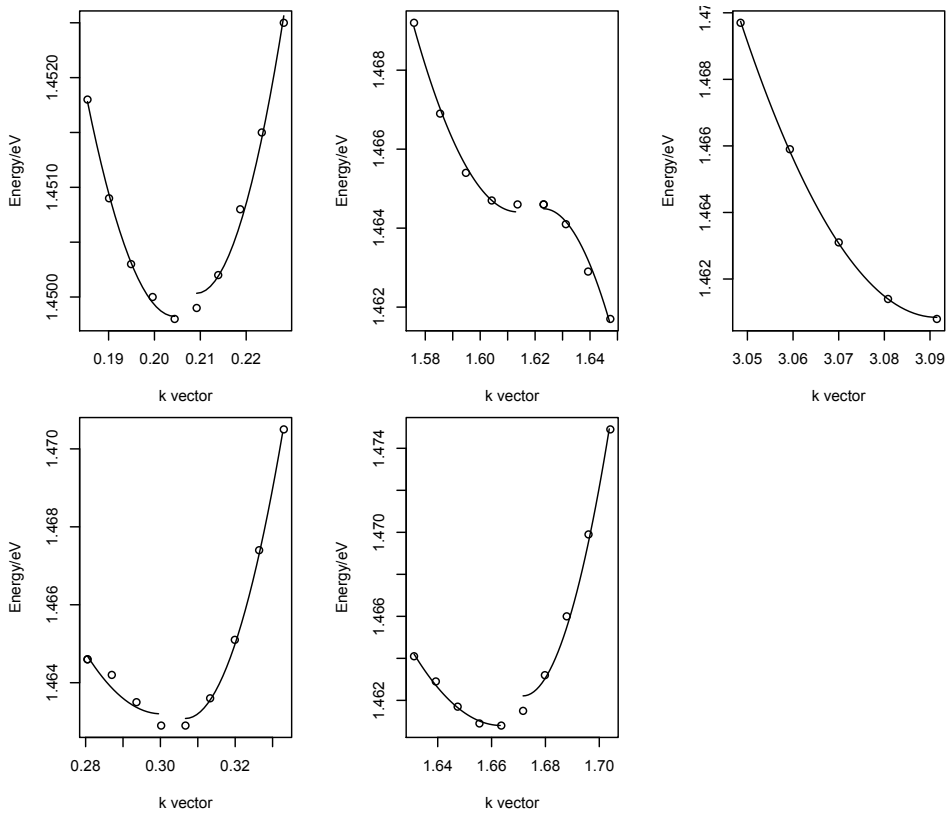

Figure D.5: $MAPbCl_3$ CB1 near Γ point on the direction of Z-Γ (left half of top-left), Γ-X(right half of bottom-left), M-Γ (left half of top-mid), Γ-R (right half of bottom-left), R'-Γ (top-right) and its fitting for mass evaluation.

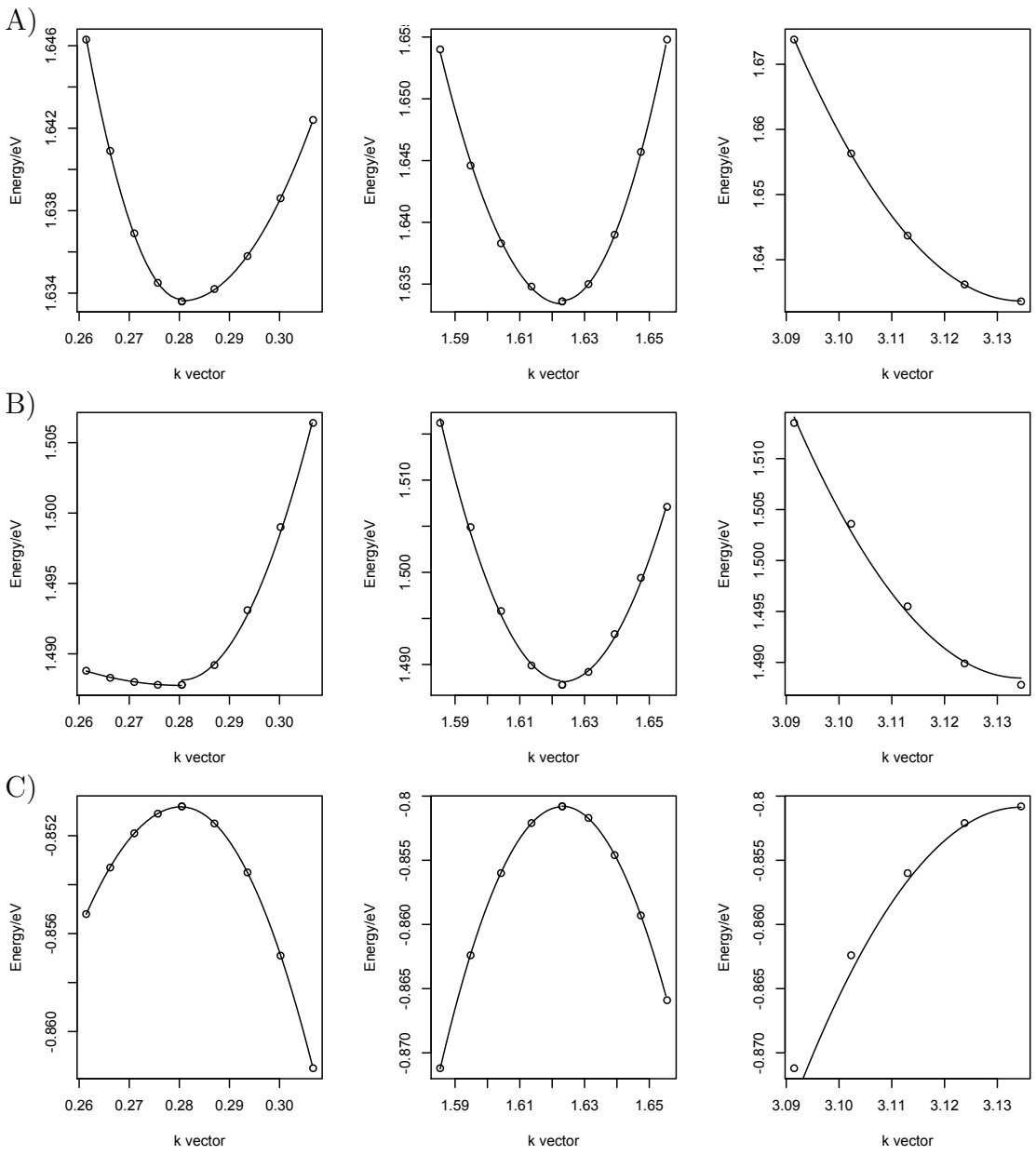

Figure D.6: $MAPbCl_3$ A) CB2; B) CB1; and C) valence band near Γ point on the direction of Z-Γ (left half of left figure), Γ-X(right half of left figure), M-Γ (left half of middle figure), Γ-R(right half of middle figure), R'-Γ (right figure) and its fitting for mass evaluation.

D.5 Effective mass of $MAPbI_3$

Table D.6: $MAPbI_3$

Bands	Z-Γ	Γ-X	Γ-R	Energy	g	M_{eff}	DOS of band	Total DOS	Product
CB3	0.08	0.13	0.13	0.86	1	0.11	8.90×10^{17}		
CB2	0.46	0.09	0.11	0.83	1	0.16	1.66×10^{18}	6.98×10^{18}	1.74×10^{37}
CB1	0.53	0.36	0.17	0.79	1	0.32	4.55×10^{18}		
VB	-0.23	-0.20	-0.21	-0.77	1	0.21	2.49×10^{18}	2.49×10^{18}	

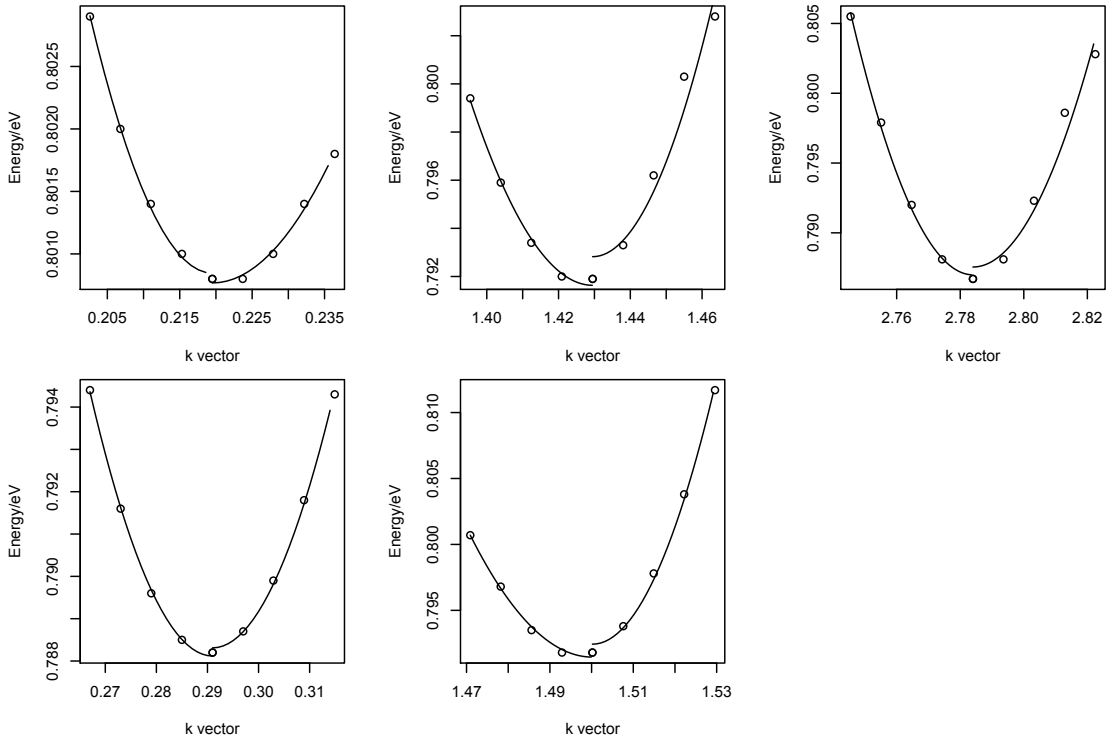

Figure D.7: $MAPbI_3$ CB1 near Γ point on the direction of Z-Γ, Γ-X, M-Γ, Γ-R, R'-Γ and its fitting for mass evaluation.

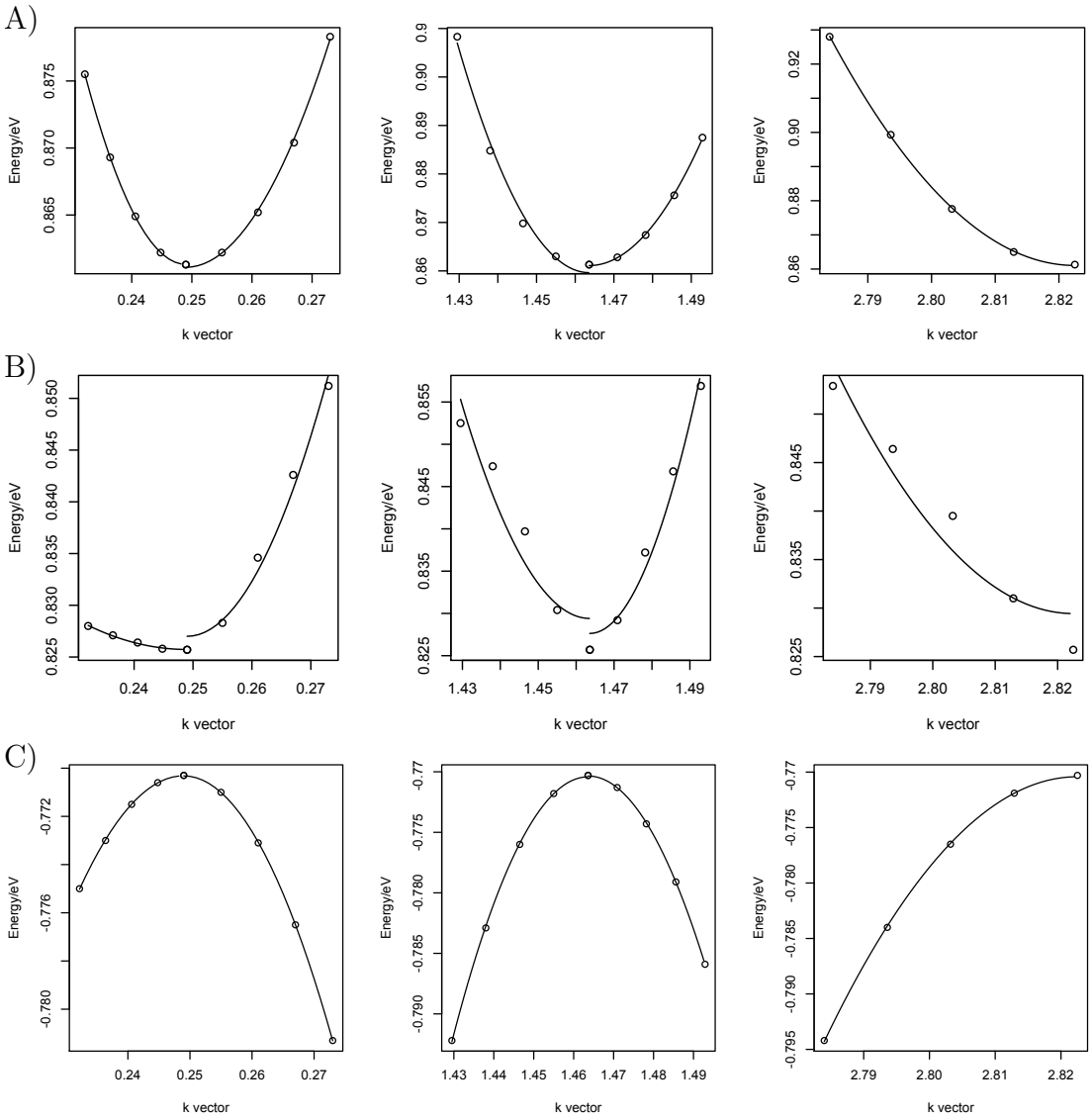

Figure D.8: $MAPbI_3$ A) CB2; B) CB1; and C) valence band near Γ point on the direction of Z-Γ (left half of left figure), Γ-X(right half of left figure), M-Γ (left half of middle figure), Γ-R(right half of middle figure), R'-Γ (right figure) and its fitting for mass evaluation.

D.6 Effective mass of CdTe

Table D.7: CdTe

Bands	Γ-X	M-Γ	Γ-R	g	M_{eff}	DOS of band	Total DOS	Product
CB	0.06	0.07	0.07	1	0.07	4.25×10^{17}	4.25×10^{17}	1.93×10^{37}
VB1	-0.51	-2.68	-1.11	1	1.15	3.14×10^{19}	4.54×10^{19}	
VB2	-0.51	-0.51	-1.11	1	0.66	1.37×10^{19}		
VB3	-0.06	-0.06	-0.06	1	0.06	3.86×10^{17}		

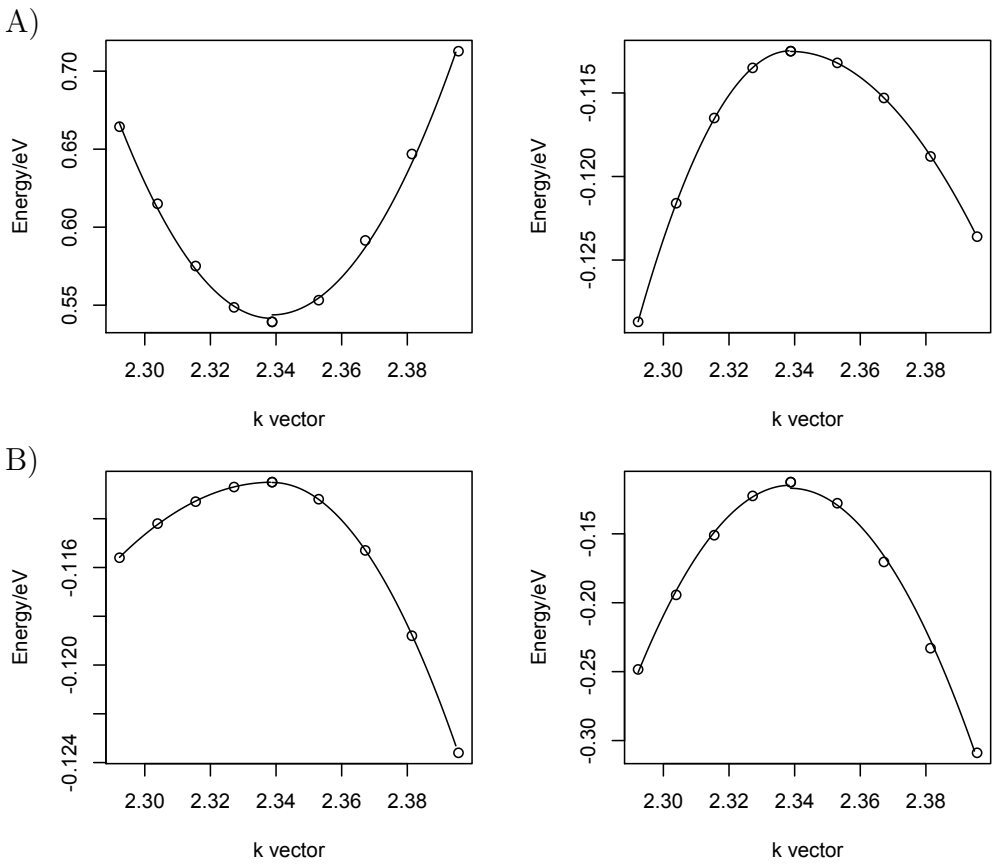

Figure D.9: CdTe valence (top-left) and conduction bands near Γ point on the direction of M-Γ, Γ-R and its fitting for mass evaluation.

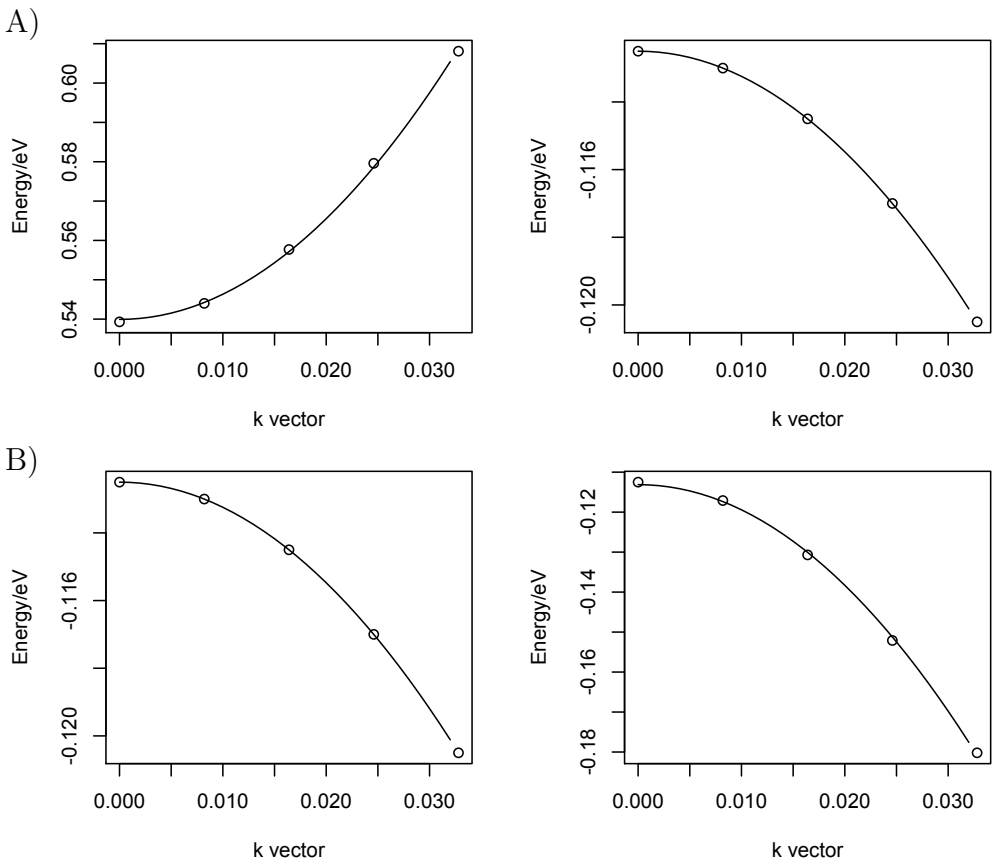

Figure D.10: CdTe Valence and conduction bands near Γ point on the direction of Γ-X and its fitting for mass evaluation.

Bibliography

[1] H. Zhou, Q. Chen, G. Li, S. Luo, T.-b. Song, H.-S. Duan, Z. Hong, J. You, Y. Liu, and Y. Yang. Interface engineering of highly efficient perovskite solar cells. *Science*, 345(6196):542–546, July 2014.

[2] Timeline of solar cells. `https://en.wikipedia.org/wiki/Timeline_of_solar_cells`, Accessed: 2016-06-21, November 2015.

[3] D. M. Chapin, C. S. Fuller, and G. L. Pearson. A New Silicon p-n Junction Photocell for Converting Solar Radiation into Electrical Power. *J. Appl. Phys.*, 25(5):676, 1954.

[4] Research cell efficiency records. `http://www.nrel.gov/ncpv/images/efficiency_chart.jpg`, Accessed: 2016-06-21. Accessed: 2016-06-29.

[5] Brian O'Regan and Michael Grätzel. A low-cost, high-efficiency solar cell based on dye-sensitized colloidal TiO2 films. *Nature*, 353(6346):737–740, oct 1991.

[6] Akihiro Kojima, Kenjiro Teshima, Yasuo Shirai, and Tsutomu Miyasaka. Organometal halide perovskites as visible-light sensitizers for photovoltaic cells. *J. Am. Chem. Soc.*, 131(17):6050–1, May 2009.

[7] Perovskite wikipedia. `https://en.wikipedia.org/wiki/Perovskite`, Accessed: 2016-06-21.

[8] Constantinos C Stoumpos, Christos D Malliakas, and Mercouri G Kanatzidis. Semiconducting tin and lead iodide perovskites with organic cations: phase transitions, high mobilities, and near-infrared photoluminescent properties. *Inorg. Chem.*, 52(15):9019–38, August 2013.

[9] Dragan Damjanovic. Ferroelectric, dielectric and piezoelectric properties of ferroelectric thin films and ceramics. *Reports Prog. Phys.*, 61(9):1267–1324, sep 1998.

[10] Na Sai, Alexie Kolpak, and Andrew Rappe. Ferroelectricity in ultrathin perovskite films. *Phys. Rev. B*, 72(2):020101, jul 2005.

[11] Kwi Young Yun, Dan Ricinschi, Takeshi Kanashima, Minoru Noda, and Masanori Okuyama. Giant Ferroelectric Polarization Beyond 150 C/cm 2 in BiFeO 3 Thin Film. *Jpn. J. Appl. Phys.*, 43(No. 5A):L647–L648, Apr 2004.

[12] Mingzhen Liu, Michael B Johnston, and Henry J Snaith. Efficient planar heterojunction perovskite solar cells by vapour deposition. *Nature*, 501(7467):395–8, September 2013.

[13] Zhicai He, Chengmei Zhong, Shijian Su, Miao Xu, Hongbin Wu, and Yong Cao. Enhanced power-conversion efficiency in polymer solar cells using an inverted device structure. *Nat. Photonics*, 6(9):593–597, aug 2012.

[14] Chun-Guey Wu, Chien-Hung Chiang, Zong-Liang Tseng, Md. K. Nazeeruddin, Anders Hagfeldt, and Michael Grätzel. High efficiency stable inverted perovskite solar cells without current hysteresis. *Energy Environ. Sci.*, 8(9):2725–2733, 2015.

[15] Lichen Zhao, Deying Luo, Jiang Wu, Qin Hu, Wei Zhang, Ke Chen, Tanghao Liu, Yi Liu, Yifei Zhang, Feng Liu, Thomas P. Russell, Henry J. Snaith, Rui Zhu, and Qihuang Gong. High-Performance Inverted Planar Heterojunction Perovskite Solar Cells Based on Lead Acetate Precursor with Efficiency Exceeding 18%. *Adv. Funct. Mater.*, pages 3508–3514, 2016.

[16] Jin Hyuck Heo, Hye Ji Han, Dasom Kim, Tae Kyu Ahn, and Sang Hyuk Im. Hysteresis-less inverted CH 3 NH 3 PbI 3 planar perovskite hybrid solar cells with 18.1% power conversion efficiency. *Energy Environ. Sci.*, 8(5):1602–1608, 2015.

[17] Min Hu, Linfeng Liu, Anyi Mei, Ying Yang, Tongfa Liu, and Hongwei Han. Efficient hole-conductor-free, fully printable mesoscopic perovskite solar cells with a broad light harvester NH2CH[double bond, length as m-dash]NH2PbI3. *J. Mater. Chem. A*, 2(40):17115–17121, 2014.

[18] Yunlong Li, Senyun Ye, Weihai Sun, Weibo Yan, Yu Li, Zuqiang Bian, Zhiwei Liu, Shufeng Wang, and Chunhui Huang. Hole-conductor-free planar perovskite solar cells with 16.0% efficiency. *J. Mater. Chem. A*, 3(36):18389–18394, 2015.

[19] Jiangjian Shi, Juan Dong, Songtao Lv, Yuzhuan Xu, Lifeng Zhu, Junyan Xiao, Xin Xu, Huijue Wu, Dongmei Li, Yanhong Luo, and Qingbo Meng. Hole-conductor-free perovskite organic lead iodide heterojunction thin-film solar cells: High efficiency and junction property. *Appl. Phys. Lett.*, 104(6), 2014.

[20] Anyi Mei, Xiong Li, Linfeng Liu, Zhiliang Ku, Tongfa Liu, Yaoguang Rong, Mi Xu, Min Hu, Jiangzhao Chen, Ying Yang, Michael Grätzel, and Hongwei Han. A hole-conductorfree, fully printable mesoscopic perovskite solar cell with high stability. *Science (80-.).*, 345(6194):295–298, 2014.

[21] Michael Grätzel. The light and shade of perovskite solar cells. *Nat. Mater.*, 13(9):838–842, aug 2014.

[22] Jeong-Hyeok Im, Chang-Ryul Lee, Jin-Wook Lee, Sang-Won Park, and Nam-Gyu Park. 6.5% Efficient Perovskite Quantum-Dot-Sensitized Solar Cell. *Nanoscale*, 3(10):4088–93, oct 2011.

[23] In Chung, Byunghong Lee, Jiaqing He, Robert P H Chang, and Mercouri G Kanatzidis. All-solid-state dye-sensitized solar cells with high efficiency. *Nature*, 485(7399):486–489, 2012.

[24] Michael M Lee, Joël Teuscher, Tsutomu Miyasaka, Takurou N Murakami, and Henry J Snaith. Efficient hybrid solar cells based on meso-superstructured organometal halide perovskites. *Science*, 338(6107):643–7, November 2012.

[25] Hui-Seon Kim, Chang-Ryul Lee, Jeong-Hyeok Im, Ki-Beom Lee, Thomas Moehl, Arianna Marchioro, Soo-Jin Moon, Robin Humphry-Baker, Jun-Ho Yum, Jacques E Moser, Michael Grätzel, and Nam-Gyu Park. Lead Iodide Perovskite Sensitized All-Solid-State Submicron Thin Film Mesoscopic Solar Cell with Efficiency Exceeding 9%. *Sci Rep.*, 2:591, August 2012.

[26] Lioz Etgar, Peng Gao, Zhaosheng Xue, Qin Peng, Aravind Kumar Chandiran, Bin Liu, Md. K. Nazeeruddin, and Michael Grätzel. Mesoscopic CH 3 NH 3 PbI 3 /TiO 2 Heterojunction Solar Cells. *J. Am. Chem. Soc.*, 134(42):17396–17399, oct 2012.

[27] Jun Hong Noh, Sang Hyuk Im, Jin Hyuck Heo, Tarak N. Mandal, and Sang Il Seok. Chemical Management for Colorful, Efficient, and Stable InorganicOrganic Hybrid Nanostructured Solar Cells. *Nano Lett.*, 13(4):1764–1769, Apr 2013.

[28] Guichuan Xing, Nripan Mathews, Shuangyong Sun, Swee Sien Lim, Yeng Ming Lam, Michael Grätzel, Subodh Mhaisalkar, Sum, and Tze Chien. Long-Range Balanced Electron- and Hole-Transport Lengths in Organic-Inorganic CH3NH3PbI3. *Science*, 342(6156):344–347, October 2013.

[29] Samuel D Stranks, Giles E Eperon, Giulia Grancini, Christopher Menelaou, Marcelo J P Alcocer, Tomas Leijtens, Laura M Herz, Annamaria Petrozza, and Henry J Snaith. Electron-hole diffusion lengths exceeding 1 micrometer in an organometal trihalide perovskite absorber. *Science*, 342(6156):341–4, October 2013.

[30] Henry J. Snaith and Michael Gratzel. Enhanced charge mobility in a molecular hole transporter via addition of redox inactive ionic dopant: Implication to dye-sensitized solar cells. *Appl. Phys. Lett.*, 89(26):262114, 2006.

[31] Edward J W Crossland, Nakita Noel, Varun Sivaram, Tomas Leijtens, Jack a Alexander-Webber, and Henry J Snaith. Mesoporous TiO2 single crystals delivering enhanced mobility and optoelectronic device performance. *Nature*, 495(7440):215–219, Mar 2013.

[32] Tomas Leijtens, Jongchul Lim, Joël Teuscher, Taiho Park, and Henry J Snaith. Charge density dependent mobility of organic hole-transporters and mesoporous TiO determined by transient mobility spectroscopy: implications to dye-sensitized and organic solar cells. *Adv. Mater.*, 25(23):3227–33, jun 2013.

[33] Pablo Docampo, James M Ball, Mariam Darwich, Giles E Eperon, and Henry J Snaith. Efficient organometal trihalide perovskite planar-heterojunction solar cells on flexible polymer substrates. *Nat. Commun.*, 4:2761, January 2013.

[34] Julian Burschka, Norman Pellet, Soo-Jin Moon, Robin Humphry-Baker, Peng Gao, Mohammad K Nazeeruddin, and Michael Grätzel. Sequential deposition as a route to high-performance perovskite-sensitized solar cells. *Nature*, 499(7458):316–9, July 2013.

[35] Dianyi Liu and Timothy L. Kelly. Perovskite solar cells with a planar heterojunction structure prepared using room-temperature solution processing techniques. *Nat. Photonics*, 8(2):133–138, dec 2013.

[36] Manda Xiao, Fuzhi Huang, Wenchao Huang, Yasmina Dkhissi, Ye Zhu, Joanne Etheridge, Angus Gray-Weale, Udo Bach, Yi-Bing Cheng, and Leone Spiccia. A Fast Deposition-Crystallization Procedure for Highly Efficient Lead Iodide Perovskite Thin-Film Solar Cells. *Angew. Chem. Int. Ed.*, 53(37):9898–9903, July 2014.

[37] Fuzhi Huang, Yasmina Dkhissi, Wenchao Huang, Manda Xiao, Iacopo Benesperi, Sergey Rubanov, Ye Zhu, Xiongfeng Lin, Liangcong Jiang, Yecheng Zhou, Angus Gray-Weale, Joanne Etheridge, Christopher R. McNeill, Rachel a. Caruso, Udo Bach, Leone Spiccia, and Yi-Bing Cheng. Gas-assisted preparation of lead iodide perovskite films consisting of a monolayer of single crystalline grains for High efficiency planar solar cells. *Nano Energy*, 10:10–18, sep 2014.

[38] Xiong Li, Dongqin Bi, Chenyi Yi, J.-D. Decoppet, Jingshan Luo, Shaik Mohammed Zakeeruddin, Anders Hagfeldt, and M. Gratzel. A vacuum flash-assisted solution process for high-efficiency large-area perovskite solar cells. *Science (80-.).*, 8060(June):1–10, 2016.

[39] Nam Joong Jeon, Jun Hong Noh, Woon Seok Yang, Young Chan Kim, Seungchan Ryu, Jangwon Seo, and Sang Il Seok. Compositional engineering of perovskite materials for high-performance solar cells. *Nature*, 517(7535):476–480, 2015.

[40] W. S. Yang, J. H. Noh, N. J. Jeon, Y. C. Kim, S. Ryu, J. Seo, and S. I. Seok. High-performance photovoltaic perovskite layers fabricated through intramolecular exchange. *Science (80-.).*, 348(6240):1234–1237, jun 2015.

[41] Ronen Gottesman, Eynav Haltzi, Laxman Gouda, Shay Tirosh, Yaniv Bouhadana, Arie Zaban, Edoardo Mosconi, and Filippo De Angelis. Extremely slow photoconductivity response of CH3NH 3PbI3 perovskites suggesting structural changes under working conditions. *J. Phys. Chem. Lett.*, 5:2662–2669, July 2014.

[42] Guangda Niu, Xudong Guo, and Liduo Wang. Review of recent progress in chemical stability of perovskite solar cells. *J. Mater. Chem. A*, 3(17):8970–8980, dec 2015.

[43] Yu Han, Steffen Meyer, Yasmina Dkhissi, Karl Weber, Jennifer M Pringle, Udo Bach, Leone Spiccia, and Yi-Bing Cheng. Degradation observations of

encapsulated planar CH 3 NH 3 PbI 3 perovskite solar cells at high temperatures and humidity. *J. Mater. Chem. A*, 3(15):8139–8147, 2015.

[44] Jinli Yang, Braden D Siempelkamp, Dianyi Liu, and Timothy L Kelly. Investigation of CH 3 NH 3 PbI 3 Degradation Rates and Mechanisms in Controlled Humidity Environments Using in Situ Techniques. *ACS Nano*, 9(2):1955–1963, feb 2015.

[45] Fukashi Matsumoto, Sarah M Vorpahl, Jannel Q Banks, Esha Sengupta, and David S Ginger. Photodecomposition and Morphology Evolution of Organometal Halide Perovskite Solar Cells. *J. Phys. Chem. C*, 119(36):20810–20816, sep 2015.

[46] Daniel Bryant, Nicholas Aristidou, Sebastian Pont, Irene Sanchez-Molina, Thana Chotchunangatchaval, Scot Wheeler, James R. Durrant, and Saif A. Haque. Light and oxygen induced degradation limits the operational stability of methylammonium lead triiodide perovskite solar cells. *Energy Environ. Sci.*, 9(5):1655–1660, 2016.

[47] Jing Wei, Yicheng Zhao, Heng Li, Guobao Li, Jinlong Pan, Dongsheng Xu, Qing Zhao, and Dapeng Yu. Hysteresis Analysis Based on the Ferroelectric Effect in Hybrid Perovskite Solar Cells. *J. Phys. Chem. Lett.*, 5:3937–3945, October 2014.

[48] Hui-Seon Kim and Nam-Gyu Park. Parameters Affecting I-V Hysteresis of CH3NH3PbI3 Perovskite Solar Cells: Effects of Perovskite Crystal Size and Mesoporous TiO2 Layer. *J. Phys. Chem. Lett.*, 5(17):2927–2934, August 2014.

[49] Eva Lisa Unger, Eric T Hoke, Colin D Bailie, William H Nguyen, Andrea Ruth Bowring, Thomas Heumuller, Mark Greyson Christoforo, and Michael D. McGehee. Hysteresis and transient behavior in current-voltage measurements of hybrid-perovskite absorber solar cells. *Energy Environ. Sci.*, 7:3690–3698, August 2014.

[50] Rafael S. Sanchez, Victoria Gonzalez-Pedro, Jin-Wook Lee, Nam-Gyu Park, Yong Soo Kang, Ivan Mora-Sero, and Juan Bisquert. Slow Dynamic Processes in Lead Halide Perovskite Solar Cells. Characteristic Times and Hysteresis. *J. Phys. Chem. Lett.*, 5(13):2357–2363, July 2014.

[51] Henry J Snaith, Antonio Abate, James M Ball, Giles E Eperon, Tomas Leijtens, Nakita K Noel, Samuel D Stranks, Jacob Tse-wei Wang, Konrad Wojciechowski, and Wei Zhang. Anomalous Hysteresis in Perovskite Solar Cells. *J. Phys. Chem. Lett.*, 5(9):1511–1515, May 2014.

[52] Yecheng Zhou, Fuzhi Huang, Yi-Bing Cheng, and Angus Gray-Weale. Photovoltaic performance and the energy landscape of CH 3 NH 3 PbI 3. *Phys. Chem. Chem. Phys.*, 17(35):22604–22615, 2015.

[53] Thomas Kietzke. Recent Advances in Organic Solar Cells. *Adv. Optoelectron.*, 2007:1–15, 2007.

[54] Juan Bisquert. *Nanostructured energy devices:Equilibrium Concepts and Kinetics*. CRC Press, Boca Raton, 2014.

[55] Daniel Abou-ras, Thomas Kirchartz, and Uwe Rau. Introduction to Thin-Film Photovoltaics. In *Advanced Characterization Techniques for Thin Film Solar Cells*, chapter 1, page 13. Wiley, Berlin, 2011.

[56] Thomas Kirchartz, Juan Bisquert, Ivan Mora-Sero, and Germà Garcia-Belmonte. Classification of solar cells according to mechanisms of charge separation and charge collection. *Phys. Chem. Chem. Phys.*, 17(6):4007–4014, 2015.

[57] Yecheng Zhou and Angus Gray-Weale. A numerical model for charge transport and energy conversion of perovskite solar cells. *Phys. Chem. Chem. Phys.*, 18(6):4476–4486, 2016.

[58] Wan-Jian Yin, Tingting Shi, and Yanfa Yan. Unique Properties of Halide Perovskites as Possible Origins of the Superior Solar Cell Performance. *Adv. Mater.*, 26(27):4653–4658, jul 2014.

[59] Yasuhiro Yamada, Toru Nakamura, Masaru Endo, Atsushi Wakamiya, and Yoshihiko Kanemitsu. Near-band-edge optical responses of solution-processed organicinorganic hybrid perovskite CH 3 NH 3 PbI 3 on mesoporous TiO 2 electrodes. *Appl. Phys. Express*, 7(3):032302, March 2014.

[60] Philip Schulz, Eran Edri, Saar Kirmayer, Gary Hodes, David Cahen, and Antoine Kahn. Interface energetics in organo-metal halide perovskite-based photovoltaic cells. *Energy Environ. Sci.*, 7(4):1377, 2014.

[61] William Shockley and Hans J. Queisser. Detailed Balance Limit of Efficiency of p-n Junction Solar Cells. *J. Appl. Phys.*, 32(3):510, 1961.

[62] Zhiliang Ku, Yaoguang Rong, Mi Xu, Tongfa Liu, and Hongwei Han. Full printable processed mesoscopic CHNHPbI/TiO heterojunction solar cells with carbon counter electrode. *Sci. Rep.*, 3:3132, January 2013.

[63] Mao Hua Du. Efficient carrier transport in halide perovskites: theoretical perspectives. *J. Mater. Chem. A*, 2(24):9091, 2014.

[64] Federico Brivio, Alison B. Walker, and Aron Walsh. Structural and electronic properties of hybrid perovskites for high-efficiency thin-film photovoltaics from first-principles. *APL Mater.*, 1(4):042111, 2013.

[65] Wan-Jian Yin, Tingting Shi, and Yanfa. Yan. Unusual defect physics in CH3NH3PbI3 perovskite solar cell absorber. *Appl. Phys. Lett.*, 104(6):063903/1–063903/4, 2014.

[66] Fan Zheng, Hiroyuki Takenaka, Fenggong Wang, Nathan Z Koocher, and Andrew M Rappe. First-Principles Calculation of the Bulk Photovoltaic Effect in CH 3 NH 3 PbI 3 and CH 3 NH 3 PbI 3 x Cl x. *J. Phys. Chem. Lett.*, 6(1):31–37, 2015.

[67] Yun Wang, Tim Gould, John F Dobson, Haimin Zhang, Huagui Yang, Xiangdong Yao, and Huijun Zhao. Density functional theory analysis of structural and electronic properties of orthorhombic perovskite CH3NH3PbI3. *Phys. Chem. Chem. Phys.*, 16(4):1424–9, December 2013.

[68] Dragan Damjanovic. Hysteresis in Piezoelectric and Ferroelectric Materials. In G.Bertotti, editor, *Sci. Hysteresis*, volume 3, pages 337–465. Elsevier, 2006.

[69] Jarvist Moore Frost, Keith Tobias Butler, Federico Brivio, Christopher Holman Hendon, Mark van Schilfgaarde, and Aron Walsh. Atomistic origins of high-performance in hybrid halide perovskite solar cells. *Nano letters*, 14(5):2584–90, May 2014.

[70] Wolfgang Tress, Nevena Marinova, Thomas Moehl, Shaik M Zakeeruddin, Mohammad Khaja Nazeeruddin, and Michael Grätzel. Understanding the rate-dependent JV hysteresis, slow time component, and aging in CH 3 NH 3 PbI 3 perovskite solar cells: the role of a compensated electric field. *Energy Environ. Sci.*, 8:995–1004, January 2015.

[71] Daehee Seol, Gill Sang Han, Changdeuck Bae, Hyunjung Shin, Hyun Suk Jung, and Yunseok Kim. Screening effect on photovoltaic performance in ferroelectric CH 3 NH 3 PbI 3 perovskite thin films. *J. Mater. Chem. A*, 3(40):20352–20358, 2015.

[72] Huimin Zhang, Chunjun Liang, Yong Zhao, Mengjie Sun, Hong Liu, Jingjing Liang, Dan Li, Fujun Zhang, and Zhiqun He. Dynamic interface charge governing the currentvoltage hysteresis in perovskite solar cells. *Phys. Chem. Chem. Phys.*, 17(15):9613–9618, 2015.

[73] Yecheng Zhou, Fuzhi Huang, Yi-Bing Cheng, and Angus Gray-Weale. Numerical analysis of a hysteresis model in perovskite solar cells. *Computational Materials Science*, 126:22–28, jan 2017.

[74] Bo Chen, Mengjin Yang, Shashank Priya, and Kai Zhu. Origin of J V Hysteresis in Perovskite Solar Cells. *J. Phys. Chem. Lett.*, 7(5):905–917, mar 2016.

[75] J. Beilsten-Edmands, G. E. Eperon, R. D. Johnson, H. J. Snaith, and P. G. Radaelli. Non-ferroelectric nature of the conductance hysteresis in CH3NH3PbI3 perovskite-based photovoltaic devices. *Appl. Phys. Lett.*, 106(17):173502, April 2015.

[76] Bin Yang, Ondrej Dyck, Jonathan Poplawsky, Jong Keum, Alexander Puretzky, Sanjib Das, Ilia Ivanov, Christopher Rouleau, Gerd Duscher, David Geohegan, and Kai Xiao. Perovskite Solar Cells with Near 100% Internal Quantum Efficiency Based on Large Single Crystalline Grains and Vertical Bulk Heterojunctions. *J. Am. Chem. Soc.*, 137(29):9210–9213, jul 2015.

[77] Stephan van Reenen, Martijn Kemerink, and Henry J. Snaith. Modeling Anomalous Hysteresis in Perovskite Solar Cells. *J. Phys. Chem. Lett.*, 6(19):3808–3814, oct 2015.

[78] Pengjun Zhao, Jinbao Xu, Chao Ma, Wei Ren, Lei Wang, Liang Bian, and Aimin Chang. Spontaneous polarization behaviors in hybrid halide perovskite film. *Scr. Mater.*, 102:51–54, June 2015.

[79] Yongbo Yuan, Timothy J Reece, Pankaj Sharma, Shashi Poddar, Stephen Ducharme, Alexei Gruverman, Yang Yang, and Jinsong Huang. Efficiency enhancement in organic solar cells with ferroelectric polymers. *Nat. Mater.*, 10(4):296–302, April 2011.

[80] Yongbo Yuan, Pankaj Sharma, Zhengguo Xiao, Shashi Poddar, Alexei Gruverman, Stephen Ducharme, and Jinsong Huang. Understanding the effect of ferroelectric polarization on power conversion efficiency of organic photovoltaic devices. *Energy Environ. Sci.*, 5(9):8558, 2012.

[81] D.A. Clugston and Paul A. Basore. PC1D version 5: 32-bit solar cell modeling on personal computers. In *Conf. Rec. Twenty Sixth IEEE Photovolt. Spec. Conf. - 1997*, pages 207–210. IEEE, 1997.

[82] Akihiko Nakajima, Takayuki Suzuki, Masashi Yoshimi, and Kenji Yamamoto. Enhancement of optical absorption for below 5 μm thin-film poly-Si solar cell on glass substrate. *Sol. Energy Mater. Sol. Cells*, 48(1-4):287–294, nov 1997.

[83] C.J.J. Tool, P. Manshanden, A.R. Burgers, and A.W. Weeber. Wafer thickness, texture and performance of multi-crystalline silicon solar cells. *Sol. Energy Mater. Sol. Cells*, 90(18-19):3165–3173, November 2006.

[84] G. Dingemans and W. M. M. Kessels. Status and prospects of Al2O3-based surface passivation schemes for silicon solar cells. *J. Vac. Sci. Technol. A Vacuum, Surfaces, Film.*, 30(4):040802, 2012.

[85] Akira Usami. Theoretical study of charge transportation in dye-sensitized nanocrystalline TiO2 electrodes. *Chem. Phys. Lett.*, 292(1-2):223–228, July 1998.

[86] Juan A. Anta, Fabiola Casanueva, and Gerko Oskam. A numerical model for charge transport and recombination in dye-sensitized solar cells. *J. Phys. Chem. B*, 110(11):5372–8, March 2006.

[87] Kei Ogiya, Chen Lv, Ai Suzuki, Riadh Sahnoun, Michihisa Koyama, Hideyuki Tsuboi, Nozomu Hatakeyama, Akira Endou, Hiromitsu Takaba, Momoji Kubo, Carlos A Del Carpio, and Akira Miyamoto. Development of Multiscale Simulator for Dye-Sensitized TiO2Nanoporous Electrode Based on Quantum Chemical Calculation. *Jpn. J. Appl. Phys.*, 47(4):3010–3014, 2008.

[88] Juan a. Anta. Random walk numerical simulation for solar cell applications. *Energy Environ. Sci.*, 2(4):387, 2009.

[89] Julio Villanueva, Juan A Anta, Elena Guillen, and Gerko Oskam. Numerical Simulation of the CurrentVoltage Curve in Dye-Sensitized Solar Cells. *J. Phys. Chem. C*, 113(45):3–4, November 2009.

[90] Mari Onodera, Kei Ogiya, Ai Suzuki, Hideyuki Tsuboi, Nozomu Hatakeyama, Akira Endou, Hiromitsu Takaba, Momoji Kubo, and Akira Miyamoto. Modeling of Dye-Sensitized Solar Cells Based on TiO2Electrode Structure Model. *Jpn. J. Appl. Phys.*, 49(4):04DP10, 2010.

[91] Jinhua Cai and Liyuan Han. Theoretical Investigation on Interfacial-Potential-Limited Diffusion and Recombination in Dye-Sensitized Solar Cells. *J. Phys. Chem. C*, 115(34):17154–17162, September 2011.

[92] Juan A Anta, Elena Guillén, and Ramón Tena-Zaera. ZnO-Based Dye-Sensitized Solar Cells. *J. Phys. Chem. C*, 116(21):11413–11425, May 2012.

[93] Pietro P. Altermatt. Models for numerical device simulations of crystalline silicon solar cellsa review. *J. Comput. Electron.*, 10(3):314–330, July 2011.

[94] Feng Liu, Jun Zhu, Junfeng Wei, Yi Li, Mei Lv, Shangfeng Yang, Bing Zhang, Jianxi Yao, and Songyuan Dai. Numerical simulation: Toward the design of high-efficiency planar perovskite solar cells. *Appl. Phys. Lett.*, 104(25):253508, jun 2014.

[95] Xingshu Sun, Reza Asadpour, Wanyi Nie, Aditya D Mohite, and Muhammad Ashraful Alam. A Physics-Based Analytical Model for Perovskite Solar Cells. *IEEE J. Photovolt.*, 5(5):1389–1394, sep 2015.

[96] J M Foster, H J Snaith, T Leijtens, and G Richardson. A Model for the Operation of Perovskite Based Hybrid Solar Cells: Formulation, Analysis, and Comparison to Experiment. *SIAM J. Appl. Math.*, 74(6):1935–1966, jan 2014.

[97] Emilio J. Juarez-Perez, Rafael S. Sanchez, Laura Badia, Germá Garcia-Belmonte, Yong Soo Kang, Ivan Mora-Sero, and Juan Bisquert. Photoinduced giant dielectric constant in lead halide perovskite solar cells. *J. Phys. Chem. Lett.*, 5(13):2390–2394, 2014.

[98] Jarvist M. Frost and Aron Walsh. What Is Moving in Hybrid Halide Perovskite Solar Cells? *Acc. Chem. Res.*, 49(3):528–535, Mar 2016.

[99] Ferroelectricity. `https://en.wikipedia.org/wiki/Ferroelectricity`, Accessed: 2016-07-4, June 2016.

[100] Yong Il Kim and Won Jong Lee. Modeling of hysteresis curves of ferroelectric capacitor with inhomogeneous charged defect density and polarization parameters in the ferroelectric film. *Japanese J. Appl. Physics, Part 1 Regul. Pap. Short Notes Rev. Pap.*, 39(3 A):1309–1319, 2000.

[101] S M Yang, J. Y. Jo, T H Kim, J.-G. Yoon, T K Song, H N Lee, Z Marton, S Park, Y Jo, and T. W. Noh. ac dynamics of ferroelectric domains from an investigation of the frequency dependence of hysteresis loops. *Phys. Rev. B*, 82(17):174125, nov 2010.

[102] Can Wang, Kui-juan Jin, Zhong-tang Xu, Le Wang, Chen Ge, Hui-bin Lu, Hai-zhong Guo, Meng He, and Guo-zhen Yang. Switchable diode effect and ferroelectric resistive switching in epitaxial BiFeO[sub 3] thin films. *Appl. Phys. Lett.*, 98(19):192901, 2011.

[103] Ian Swainson, Lisheng Chi, Jae Hyuk Her, Lachlan Cranswick, Peter Stephens, Björn Winkler, Daniel J Wilson, and Victor Milman. Orientational ordering, tilting and lone-pair activity in the perovskite methylammonium tin bromide, CH3NH3SnBr3. *Acta Crystallogr. B.*, 66(Pt 4):422–9, aug 2010.

[104] Jarvist M Frost, Keith T Butler, and Aron Walsh. Molecular ferroelectric contributions to anomalous hysteresis in hybrid perovskite solar cells. *APL Mater.*, 2(8):081506, aug 2014.

[105] Alessandro Stroppa, Claudio Quarti, Filippo De Angelis, and Silvia Picozzi. Ferroelectric Polarization of CH 3 NH 3 PbI 3 : A Detailed Study Based on Density Functional Theory and Symmetry Mode Analysis. *J. Phys. Chem. Lett.*, 6(12):2223–2231, jun 2015.

[106] Desiree Gentilini, Daniele Rossi, Matthias Auf der Maur, Aldo Di Carlo, and Alessandro Pecchia. Effect of ferroelectric nanodomains in perovskite solar cells. In *2015 IEEE 15th Int. Conf. Nanotechnol.*, pages 1382–1385. IEEE, jul 2015.

[107] Zhen Fan, Juanxiu Xiao, Kuan Sun, Lei Chen, Yating Hu, Jianyong Ouyang, Khuong P. Ong, Kaiyang Zeng, and John Wang. Ferroelectricity of CH3NH3PbI3 Perovskite. *J. Phys. Chem. Lett.*, 6(7):1155–1161, mar 2015.

[108] Yasemin Kutes, Linghan Ye, Yuanyuan Zhou, Shuping Pang, Bryan D Huey, and Nitin P Padture. Direct Observation of Ferroelectric Domains in Solution-Processed CH3NH3PbI3 Perovskite Thin Films. *J. Phys. Chem. Lett.*, 5:3335–3339, 2014.

[109] L. Pintilie, I. Vrejoiu, D. Hesse, G. LeRhun, and M. Alexe. Ferroelectric polarization-leakage current relation in high quality epitaxial Pb(Zr,Ti)O3 films. *Phys. Rev. B*, 75(10):104103, Mar 2007.

[110] Zhongbo Zhang, Morton H. Litt, and Lei Zhu. Unified Understanding of Ferroelectricity in n -Nylons: Is the Polar Crystalline Structure a Prerequisite? *Macromolecules*, 49(8):3070–3082, Apr 2016.

[111] Aurelien M A Leguy, Jarvist Moore Frost, Andrew P McMahon, Victoria Garcia Sakai, W Kochelmann, ChunHung Law, Xiaoe Li, Fabrizia Foglia, Aron Walsh, Brian C. O'Regan, Jenny Nelson, João T Cabral, and Piers R F Barnes. The dynamics of methylammonium ions in hybrid organicinorganic perovskite solar cells. *Nat. Commun.*, 6(May):7124, may 2015.

[112] Jin Hyuck Heo and Sang Hyuk Im. Highly reproducible, efficient hysteresis-less CH 3 NH 3 PbI 3x Cl x planar hybrid solar cells without requiring heat-treatment. *Nanoscale*, 8(5):2554–2560, 2016.

[113] Weijun Ke, Chuanxiao Xiao, Changlei Wang, Bayrammurad Saparov, Hsin-Sheng Duan, Dewei Zhao, Zewen Xiao, Philip Schulz, Steven P. Harvey, Weiqiang Liao, Weiwei Meng, Yue Yu, Alexander J. Cimaroli, ChunSheng Jiang, Kai Zhu, Mowafak Al-Jassim, Guojia Fang, David B. Mitzi, and Yanfa Yan. Employing Lead Thiocyanate Additive to Reduce the Hysteresis and Boost the Fill Factor of Planar Perovskite Solar Cells. *Adv. Mater.*, may 2016.

[114] Haixia Rao, Senyun Ye, Weihai Sun, Weibo Yan, Yunlong Li, Haitao Peng, Zhiwei Liu, Zuqiang Bian, Yongfang Li, and Chunhui Huang. A 19.0% efficiency achieved in CuOx-based inverted CH3NH3PbI3xClx solar cells by an effective Cl doping method. *Nano Energy*, 27:51–57, sep 2016.

[115] Germa Garcia-Belmonte, Pablo P. Boix, Juan Bisquert, Martijn Lenes, Henk J. Bolink, Andrea La Rosa, Salvatore Filippone, and Nazario Martin. Influence of the Intermediate Density-of-States Occupancy on Open-Circuit Voltage of Bulk Heterojunction Solar Cells with Different Fullerene Acceptors. *J. Phys. Chem. Lett.*, 1(17):2566–2571, sep 2010.

[116] Dana B. Sulas, Kai Yao, Jeremy J. Intemann, Spencer T. Williams, Chang-Zhi Li, Chu-Chen Chueh, Jeffrey J. Richards, Yuyin Xi, Lilo D. Pozzo, Cody W. Schlenker, Alex K.-Y. Jen, and David S. Ginger. Open-Circuit Voltage Losses in Selenium-Substituted Organic Photovoltaic Devices from Increased Density of Charge-Transfer States. *Chem. Mater.*, 27(19):6583–6591, oct 2015.

[117] Naveen Kumar Elumalai and Ashraf Uddin. Open circuit voltage of organic solar cells: an in-depth review. *Energy Environ. Sci.*, 9(2):391–410, 2016.

[118] Samuel D. Collins, Christopher M. Proctor, Niva A. Ran, and Thuc-Quyen Nguyen. Understanding Open-Circuit Voltage Loss through the Density of States in Organic Bulk Heterojunction Solar Cells. *Adv. Energy Mater.*, 6(4):1501721, feb 2016.

[119] Chia-Hao Marcus Chuang, Andrea Maurano, Riley E. Brandt, Gyu Weon Hwang, Joel Jean, Tonio Buonassisi, Vladimir Bulović, and Moungi G. Bawendi. Open-Circuit Voltage Deficit, Radiative Sub-Bandgap States, and Prospects in Quantum Dot Solar Cells. *Nano Lett.*, 15(5):3286–3294, may 2015.

[120] Chun-liang Zhong, Kui-wei Geng, Lan-e Luo, and Di-wu Yang. An analytical model to explore open-circuit voltage of a-Si:H/c-Si heterojunction solar cells. *J. Cent. South Univ.*, 23(3):598–603, mar 2016.

[121] James C. Blakesley and Dieter Neher. Relationship between energetic disorder and open-circuit voltage in bulk heterojunction organic solar cells. *Phys. Rev. B*, 84(7):075210, aug 2011.

[122] K Fukutani, M Kanbe, W Futako, B Kaplan, T Kamiya, C.M Fortmann, and I Shimizu. Band gap tuning of a-Si:H from 1.55 eV to 2.10 eV by intentionally promoting structural relaxation. *J. Non. Cryst. Solids*, 227-230:63–67, May 1998.

[123] Jianjun Liang, Eric A Schiff, S. Guha, B. Yan, and J. Yang. Light-Soaking Effects on the Open-Circuit Voltage of a-Si:H Solar Cells. *MRS Proceedings*, 862:A13.6, 2005.

[124] Martin A. Green, Keith Emery, Yoshihiro Hishikawa, Wilhelm Warta, and Ewan D. Dunlop. Solar cell efficiency tables (version 47). *Prog. Photovoltaics Res. Appl.*, 24(1):3–11, jan 2016.

[125] G. Fonthal, L. Tirado-Meja, J.I. Marn-Hurtado, H. Ariza-Calderón, and J.G. Mendoza-Alvarez. Temperature dependence of the band gap energy of crystalline CdTe. *J. Phys. Chem. Solids*, 61(4):579–583, apr 2000.

[126] Yuan Zhao, Mathieu Boccard, Shi Liu, Jacob Becker, Xin-Hao Zhao, Calli M. Campbell, Ernesto Suarez, Maxwell B. Lassise, Zachary Holman, and Yong-Hang Zhang. Monocrystalline CdTe solar cells with open-circuit voltage over 1 V and efficiency of 17%. *Nat. Energy*, 1(6):16067, may 2016.

[127] Wenchao Yang, Yao Yao, and Chang-Qin Wu. Origin of the high open circuit voltage in planar heterojunction perovskite solar cells: Role of the reduced bimolecular recombination. *J. Appl. Phys.*, 117(9):095502, mar 2015.

[128] James Endres, David A. Egger, Michael Kulbak, Ross A. Kerner, Lianfeng Zhao, Scott H. Silver, Gary Hodes, Barry P. Rand, David Cahen, Leeor Kronik, and Antoine Kahn. Valence and Conduction Band Densities of States of Metal Halide Perovskites: A Combined ExperimentalTheoretical Study. *J. Phys. Chem. Lett.*, 7(14):2722–2729, jul 2016.

[129] Shi Chen, Yi Hou, Haiwei Chen, Moses Richter, Fei Guo, Simon Kahmann, Xiaofeng Tang, Tobias Stubhan, Hong Zhang, Ning Li, Nicola Gasparini, Cesar Omar Ramirez Quiroz, Laraib S. Khanzada, Gebhard J. Matt, Andres Osvet, and Christoph J. Brabec. Exploring the Limiting Open-Circuit Voltage and the Voltage Loss Mechanism in Planar CH 3 NH 3 PbBr 3 Perovskite Solar Cells. *Adv. Energy Mater.*, page 1600132, jun 2016.

[130] Yecheng Zhou and Guankui Long. Low Density of Conduction and Valence Band States Contribute to the High Open-Circuit Voltage in Perovskite Solar Cells. *The Journal of Physical Chemistry C*, 121(3):1455–1462, jan 2017.

[131] Gary Hodes. Applied physics. Perovskite-based solar cells. *Science*, 342(6156):317–8, October 2013.

[132] Jianhua Huang, Hui Jia, Liangjie Li, Zhenhuan Lu, Wenqing Zhang, Weiwei He, Bo Jiang, Ailing Tang, Zhan'ao Tan, Chuanlang Zhan, Yongfang Li, and Jiannian Yao. Fine-tuning device performances of small molecule solar cells via the more polarized DPP-attached donor units. *Phys. Chem. Chem. Phys.*, 14(41):14238–42, November 2012.

[133] Charles Kiseok Song, Alicia C White, Li Zeng, Benjamin J Leever, Michael D Clark, Jonathan D Emery, Sylvia J Lou, Amod Timalsina, Lin X Chen, Michael J Bedzyk, and Tobin J Marks. Systematic investigation of organic photovoltaic cell charge injection/performance modulation by dipolar organosilane interfacial layers. *ACS Appl. Mater. Interfaces*, 5(18):9224–40, sep 2013.

[134] Q. Liu, I. Khatri, R. Ishikawa, a. Fujimori, K. Ueno, K. Manabe, H. Nishino, and H. Shirai. Improved photovoltaic performance of crystalline-Si/organic Schottky junction solar cells using ferroelectric polymers. *Appl. Phys. Lett.*, 103(16):163503, 2013.

[135] Yu-Che Hsiao, Huidong Zang, Ilia Ivanov, Tao Xu, Luyao Lu, Luping Yu, and Bin Hu. Dielectric Interface Effects on Surface Charge Accumulation and Collection towards High-Efficiency Organic Solar Cells. *J. Appl. Phys.*, 115(15):154506, April 2014.

[136] Shi Liu, Fan Zheng, Nathan Z. Koocher, Hiroyuki Takenaka, Fenggong Wang, and Andrew M. Rappe. Ferroelectric Domain Wall Induced Band Gap Reduction and Charge Separation in Organometal Halide Perovskites. *J. Phys. Chem. Lett.*, 6(4):693–699, February 2015.

[137] Ye Zhang, Mingzhen Liu, Giles E. Eperon, Tomas C. Leijtens, David McMeekin, Michael Saliba, Wei Zhang, Michele de Bastiani, Annamaria Petrozza, Laura M. Herz, Michael B. Johnston, Hong Lin, and Henry J. Snaith. Charge selective contacts, mobile ions and anomalous hysteresis in organicinorganic perovskite solar cells. *Mater. Horiz.*, 1:96, 2015.

[138] Naoki Koide and Liyuan Han. Measuring methods of cell performance of dye-sensitized solar cells. *Rev. Sci. Instrum.*, 75(9):2828, 2004.

[139] Naoki Koide, Yasuo Chiba, and Liyuan Han. Methods of Measuring Energy Conversion Efficiency in Dye-sensitized Solar Cells. *Jpn. J. Appl. Phys.*, 44(6A):4176–4181, June 2005.

[140] Matic Herman, Marko Jankovec, and Marko Topič. Optimal I-V curve scan time of solar cells and modules in light of irradiance level. *Int. J. Photoenergy*, 2012:1–11, 2012.

[141] Wolfgang Brütting, editor. *Physics of Organic Semiconductors*. Wiley-VCH Verlag GmbH & Co. KGaA, Weinheim, FRG, May 2005.

[142] Jin-Wook Lee, Dong-Jin Seol, An-Na Cho, and Nam-Gyu Park. High-Efficiency Perovskite Solar Cells Based on the Black Polymorph of HC(NH2)2 PbI3. *Adv. Mater.*, 6:4991–4998, June 2014.

[143] Nam Joong Jeon, Jun Hong Noh, Young Chan Kim, Woon Seok Yang, Seungchan Ryu, and Sang Il Seok. Solvent engineering for high-performance inorganicorganic hybrid perovskite solar cells. *Nat. Mater.*, 13(9):897–903, July 2014.

[144] Georg Kresse and Jürgen Furthmüller. Efficiency of ab-initio total energy calculations for metals and semiconductors using a plane-wave basis set. *Comput. Mater. Sci.*, 6(1):15–50, 1996.

[145] Georg Kresse, J Furthmuller, and Jürgen Furthmüller. Efficient iterative schemes for ab initio total-energy calculations using a plane-wave basis set. *Phys. Rev. B*, 54(16):11169–11186, 1996.

[146] P. E. Blöchl. Projector augmented-wave method. *Phys. Rev. B*, 50(24):17953–17979, December 1994.

[147] Giacomo Giorgi, Jun-ichi Fujisawa, Hiroshi Segawa, and Koichi Yamashita. Cation Role in Structural and Electronic Properties of 3D OrganicInorganic Halide Perovskites: A DFT Analysis. *J. Phys. Chem. C*, 118(23):12176–12183, June 2014.

[148] Giacomo Giorgi, Jun-Ichi Fujisawa, Hiroshi Segawa, and Koichi Yamashita. Small Photocarrier Effective Masses Featuring Ambipolar Transport in Methylammonium Lead Iodide Perovskite: A Density Functional Analysis. *J. Phys. Chem. Lett.*, 4(24):4213–4216, December 2013.

[149] Paolo Umari, Edoardo Mosconi, and Filippo De Angelis. Relativistic GW calculations on CH3NH3PbI3 and CH3NH3SnI3 perovskites for solar cell applications. *Sci. Rep.*, 4:4467, January 2014.

[150] Xueyuan Wu, M C Vargas, S Nayak, V Lotrich, and G Scoles. Towards extending the applicability of density functional theory to weakly bound systems. *J. Chem. Phys*, 115(19):8748–8757, 2001.

[151] John P Perdew, Adrienn Ruzsinszky, Gábor I Csonka, Oleg A Vydrov, Gustavo E Scuseria, Lucian A Constantin, Xiaolan Zhou, and Kieron Burke. Restoring the Density-Gradient Expansion for Exchange in Solids and Surfaces. *Phys. Rev. Lett.*, 100(13):136406, April 2008.

[152] David Vanderbilt and R D King-Smith. Electric polarization as a bulk quantity and its relation to surface charge. *Phys. Rev. B*, 48(7):4442–4455, August 1993.

[153] R. Resta. Theory of the electric polarization in crystals. *Ferroelectrics*, 136(1):51–55, November 1992.

[154] Raffaele Resta. Macroscopic polarization in crystalline dielectrics: the geometric phase approach. *Rev. Mod. Phys.*, 66(3):899–915, July 1994.

[155] R D King-Smith and David Vanderbilt. Theory of polarization of crystalline solids. *Phys. Rev. B*, 47(3):1651–1654, January 1993.

[156] Xifan Wu, David Vanderbilt, and D. Hamann. Systematic treatment of displacements, strains, and electric fields in density-functional perturbation theory. *Phys. Rev. B*, 72(3):035105, July 2005.

[157] Gregory Mills, Hannes Jónsson, and Gregory K Schenter. Reversible work transition state theory: application to dissociative adsorption of hydrogen. *Surf. Sci.*, 324(2-3):305–337, February 1995.

[158] Graeme Henkelman, Blas P. Uberuaga, and Hannes Jonsson. A climbing image nudged elastic band method for finding saddle points and minimum energy paths. *J. Chem. Phys.*, 113(22):9901, 2000.

[159] Tom Baikie, Yanan Fang, Jeannette M. Kadro, Martin Schreyer, Fengxia Wei, Subodh G. Mhaisalkar, Michael Graetzel, and Tim J. White. Synthesis and crystal chemistry of the hybrid perovskite (CH3NH3)PbI3 for solid-state sensitised solar cell applications. *J. Mater. Chem. A*, 1(18):5628, 2013.

[160] Yukihiko Kawamura, Hiroyuki Mashiyama, and Katsuhiko Hasebe. Structural Study on Cubic-Tetragonal Transition of CH3NH3PbI3. *J. Phys. Soc. Jpn.*, 71(7):1694–1697, July 2002.

[161] RE Wasylishen, O Knop, and JB Macdonald. Cation rotation in methylammonium lead halides. *Solid State Commun.*, 56(7):581–582, 1985.

[162] Jacky Even, Laurent Pedesseau, Eric Tea, Samy Almosni, Alain Rolland, Cédric Robert, Jean-Marc Jancu, Charles Cornet, Claudine Katan, Jean-François Guillemoles, and Olivier Durand. Density Functional Theory Simulations of Semiconductors for Photovoltaic Applications: Hybrid Organic-Inorganic Perovskites and III/V Heterostructures. *Int. J. Photoenergy*, 2014:1–11, 2014.

[163] Jacky Even, Laurent Pedesseau, Jean-Marc Jancu, and Claudine Katan. Importance of SpinOrbit Coupling in Hybrid Organic/Inorganic Perovskites for Photovoltaic Applications. *J. Phys. Chem. Lett.*, 4(17):2999–3005, September 2013.

[164] Federico Brivio, Keith T. Butler, Aron Walsh, and Mark van Schilfgaarde. Relativistic quasiparticle self-consistent electronic structure of hybrid halide perovskite photovoltaic absorbers. *Phys. Rev. B*, 89(15):155204, April 2014.

[165] Ivo Borriello, Giovanni Cantele, and Domenico Ninno. Ab initio investigation of hybrid organic-inorganic perovskites based on tin halides. *Phys. Rev. B*, 77(23):235214, June 2008.

[166] Mao Hua Du and David J. Singh. Enhanced Born charge and proximity to ferroelectricity in thallium halides. *Phys. Rev. B*, 81:1–5, 2010.

[167] M Hirasawa, T Ishihara, T Goto, K Uchida, and N Miura. Magnetoabsorption of the lowest exciton in perovskite-type compound (CH3NH3)PbI3. *Phys. B Condens. Matter*, 201:427–430, jul 1994.

[168] Teruya Ishihara. Optical properties of PbI-based perovskite structures. *J. Lumin.*, 60-61:269–274, April 1994.

[169] Kenichiro Tanaka, Takayuki Takahashi, Takuma Ban, Takashi Kondo, Kazuhito Uchida, and Noboru Miura. Comparative study on the excitons in lead-halide-based perovskite-type crystals CH3NH3PbBr3 CH3NH3PbI3. *Solid State Commun.*, 127(9-10):619–623, September 2003.

[170] Noriko Onoda-Yamamuro, Takasuke Matsuo, and Hiroshi Suga. Dielectric study of CH3NH3PbX3 (X = Cl, Br, I). *J. Phys. Chem. Solids*, 53(7):935–939, July 1992.

[171] N. Taylor. *PV Power Measurement Compiled by partners in the Performance FP6 Integrated Project.* JRC Scientific and Technical Report EUR, Luxembourg, 2010.

[172] Jerry G. Fossum. Computer-aided numerical analysis of silicon solar cells. *Solid. State. Electron.*, 19(4):269–277, Apr 1976.

[173] P. A. Basore. Numerical modeling of textured silicon solar cells using PC-1D. *IEEE Trans. Electron Devices*, 37(2):337–343, 1990.

[174] H. Tasaki, W. Y. Kim, M. Hallerdt, M. Konagai, and K. Takahashi. Computer simulation model of the effects of interface states on high-performance amorphous silicon solar cells. *J. Appl. Phys.*, 63(2):550, 1988.

[175] J.W. Bishop. Computer simulation of the effects of electrical mismatches in photovoltaic cell interconnection circuits. *Sol. Cells*, 25(1):73–89, oct 1988.

[176] Tomas Leijtens, Samuel D. Stranks, Giles E. Eperon, Rebecka Lindblad, Erik M J Johansson, Ian J. McPherson, Hå kan Rensmo, James M. Ball, Michael M. Lee, and Henry J. Snaith. Electronic Properties of Meso-Superstructured and Planar Organometal Halide Perovskite Films: Charge Trapping, Photodoping, and Carrier Mobility. *ACS Nano*, 8(7):7147–7155, July 2014.

[177] Hikaru Oga, Akinori Saeki, Yuhei Ogomi, Shuzi Hayase, and Shu Seki. Improved Understanding of the Electronic and Energetic Landscapes of Perovskite Solar Cells: High Local Charge Carrier Mobility, Reduced Recombination, and Extremely Shallow Traps. *J. Am. Chem. Soc.*, 136(39):13818–13825, October 2014.

[178] Nam-Gyu Park. Perovskite solar cells: an emerging photovoltaic technology. *Mater. Today*, 18(2):65–72, March 2015.

[179] Q. Dong, Y. Fang, Y. Shao, P. Mulligan, J. Qiu, L. Cao, and J. Huang. Electron-hole diffusion lengths > 175 m in solution-grown CH3NH3PbI3 single crystals. *Science (80-.).*, 347(6225):967–970, feb 2015.

[180] Hua Zhang, Xianfeng Qiao, Yan Shen, Thomas Moehl, Shaik M. Zakeeruddin, Michael Grätzel, and Mingkui Wang. Photovoltaic behaviour of lead methylammonium triiodide perovskite solar cells down to 80 K. *J. Mater. Chem. A*, 3(22):11762–11767, 2015.

[181] Dominique J. Wehenkel, L. Jan Anton Koster, Martijn M. Wienk, and René a J Janssen. Influence of injected charge carriers on photocurrents in polymer solar cells. *Phys. Rev. B*, 85:1–12, 2012.

[182] L. J. A. Koster, V. D. Mihailetchi, R. Ramaker, and P. W. M. Blom. Light intensity dependence of open-circuit voltage of polymer:fullerene solar cells. *Appl. Phys. Lett.*, 86(12):123509, 2005.

[183] W. Shockley and W. Read. Statistics of the Recombinations of Holes and Electrons. *Phys. Rev.*, 87(5):835–842, September 1952.

[184] R. Hall. Electron-Hole Recombination in Germanium. *Phys. Rev.*, 87(2):387–387, July 1952.

[185] WH Press, SA Teukolsky, WT Vetterling, and BP Flannery. *Numerical Recipes in FORTRAN, vol. 1.* Cambridge University Press, New York, second edition, 1992.

[186] Jiangjian Shi, Yanhong Luo, Huiyun Wei, Jianheng Luo, Juan Dong, Songtao Lv, Junyan Xiao, Yuzhuan Xu, Lifeng Zhu, Xin Xu, Huijue Wu, Dongmei Li, and Qingbo Meng. Modified Two-Step Deposition Method for High-Efficiency TiO2/CH3NH3PbI3 Heterojunction Solar Cells. *ACS Appl. Mater. Interfaces*, 6(12):9711–8, jun 2014.

[187] Francisco Enrique Gálvez, Erno Kemppainen, Hernán Míguez, and Janne Halme. Effect of Diffuse Light Scattering Designs on the Efficiency of Dye Solar Cells: An Integral Optical and Electrical Description. *J. Phys. Chem. C*, 116(21):11426–11433, May 2012.

[188] Sven Soedergren, Anders Hagfeldt, Joergen Olsson, and Sten-eric Lindquist. Theoretical Models for the Action Spectrum and the Current-Voltage Characteristics of Microporous Semiconductor Films in Photoelectrochemical Cells. *J. Phys. Chem.*, 98(21):5552–5556, May 1994.

[189] Janne Halme, Paula Vahermaa, Kati Miettunen, and Peter Lund. Device physics of dye solar cells. *Adv. Mater.*, 22(35):E210–34, September 2010.

[190] National renewable energy laboratory (nrel), research cell efficiency records, November 2015.

[191] E Guillén, L M Peter, and J A Anta. Electron Transport and Recombination in ZnO-Based Dye-Sensitized Solar Cells. *J. Phys. Chem. C*, 115(45):22622–22632, 2011.

[192] R.a. Sinton, Young Kwark, J.Y. Gan, and R.M. Swanson. 27.5-percent silicon concentrator solar cells. *IEEE Electron Device Lett.*, 7(10):567–569, oct 1986.

[193] Dongqin Bi, Lei Yang, Gerrit Boschloo, Anders Hagfeldt, and Erik M J Johansson. Effect of Different Hole Transport Materials on Recombination in CH 3 NH 3 PbI 3 Perovskite-Sensitized Mesoscopic Solar Cells. *J. Phys. Chem. Lett.*, 4(9):1532–1536, May 2013.

[194] Masafumi Yamaguchi and Antonio Luque. High efficiency and high concentration in photovoltaics. *IEEE Trans. Electron Devices*, 46(10):2139–2144, 1999.

[195] Masafumi Yamaguchi, Tatsuya Takamoto, and Kenji Araki. Super high-efficiency multi-junction and concentrator solar cells. *Sol. Energy Mater. Sol. Cells*, 90(18-19):3068–3077, nov 2006.

[196] Qianqian Lin, Ardalan Armin, Ravi Chandra, Raju Nagiri, Paul L Burn, and Paul Meredith. Electro-optics of perovskite solar cells. *Nat. Photonics*, 9(2):106–112, 2014.

[197] Jun Haruyama, Keitaro Sodeyama, Liyuan Han, and Yoshitaka Tateyama. First-Principles Study of Ion Diffusion in Perovskite Solar Cell Sensitizers. *J. Am. Chem. Soc.*, 137(32):10048–10051, aug 2015.

[198] Jon M. Azpiroz, Edoardo Mosconi, Juan Bisquert, and Filippo De Angelis. Defect migration in methylammonium lead iodide and its role in perovskite solar cell operation. *Energy Environ. Sci.*, 8(7):2118–2127, 2015.

[199] Mark T Weller, Oliver J. Weber, Jarvist M. Frost, and Aron Walsh. Cubic perovskite structure of black formamidinium lead iodide, α-[HC(NH2)2]PbI3, at 298 K. *J. Phys. Chem. Lett.*, 6:3209–3212, aug 2015.

[200] Relative permittivity. `https://en.wikipedia.org/wiki/Relative_permittivity`, Accessed: 2016-06-21. Accessed: 2016-06-21.

[201] Tejas S. Sherkar and L. Jan Anton Koster. Can ferroelectric polarization explain the high performance of hybrid halide perovskite solar cells? *Phys. Chem. Chem. Phys.*, 18(1):331–338, nov 2016.

[202] Relative permittivity. `https://en.wikipedia.org/wiki/Barium_titanate`, Accessed: 2016-06-21. Accessed: 2016-06-21.

[203] Hui-Seon Kim, In-Hyuk Jang, Namyoung Ahn, Mansoo Choi, Antonio Guerrero, Juan Bisquert, and Nam-Gyu Park. Control of I V Hysteresis in CH 3 NH 3 PbI 3 Perovskite Solar Cell. *J. Phys. Chem. Lett.*, 6(22):4633–4639, nov 2015.

[204] Kenjiro Miyano, Neeti Tripathi, Masatoshi Yanagida, and Yasuhiro Shirai. Lead Halide Perovskite Photovoltaic as a Model p i n Diode. *Acc. Chem. Res.*, 49(2):303–310, feb 2016.

[205] Yi Hou, Wei Chen, Derya Baran, Tobias Stubhan, Norman A Luechinger, Benjamin Hartmeier, Moses Richter, Jie Min, Shi Chen, Cesar Omar Ramirez Quiroz, Ning Li, Hong Zhang, Thomas Heumueller, Gebhard J Matt, Andres Osvet, Karen Forberich, Zhi-Guo Zhang, Yongfang Li, Benjamin Winter, Peter Schweizer, Erdmann Spiecker, and Christoph J Brabec. Overcoming the Interface Losses in Planar Heterojunction Perovskite-Based Solar Cells. *Adv. Mater.*, 28(25):5112–5120, jul 2016.

[206] Dewei Zhao, Weijun Ke, Corey R. Grice, Alexander J. Cimaroli, Xinxuan Tan, Mengjin Yang, Robert W. Collins, Hongmei Zhang, Kai Zhu, and Yanfa Yan. Annealing-free efficient vacuum-deposited planar perovskite solar cells with evaporated fullerenes as electron-selective layers. *Nano Energy*, 19:88–97, jan 2016.

[207] Vitaly V. Chaban and Eudes Eterno Fileti. Strong electronic polarization of the C 60 fullerene by imidazolium-based ionic liquids: accurate insights from BornOppenheimer molecular dynamic simulations. *Phys. Chem. Chem. Phys.*, 17(24):15739–15745, 2015.

[208] Akira Tada, Yanfang Geng, Qingshuo Wei, Kazuhito Hashimoto, and Keisuke Tajima. Tailoring organic heterojunction interfaces in bilayer polymer photovoltaic devices. *Nat. Mater.*, 10(6):450–455, jun 2011.

[209] Sean M. Ryno, Yao-Tsung Fu, Chad Risko, and Jean-Luc Brédas. Polarization Energies at OrganicOrganic Interfaces: Impact on the Charge Separation Barrier at DonorAcceptor Interfaces in Organic Solar Cells. *ACS Appl. Mater. Interfaces*, 8(24):15524–15534, jun 2016.

[210] D J Kim. Thickness-Dependent Retention Properties in Polycrystalline Pb (Zr , Ti) O 3 Capacitors Thinner than 100 nm. *J. Korean Phys. Soc.*, 51(October):75–78, 2007.

[211] Martin Z. Bazant, Katsuyo Thornton, and Armand Ajdari. Diffuse-charge dynamics in electrochemical systems. *Phys. Rev. E*, 70(2):021506, aug 2004.

[212] Michele De Bastiani, Giorgio Dell'Erba, Marina Gandini, Valerio D'Innocenzo, Stefanie Neutzner, Ajay Ram Srimath Kandada, Giulia Grancini, Maddalena Binda, Mirko Prato, James M. Ball, Mario Caironi, and Annamaria Petrozza. Ion Migration and the Role of Preconditioning Cycles in the Stabilization of the J - V Characteristics of Inverted Hybrid Perovskite Solar Cells. *Adv. Energy Mater.*, 6(2):1501453, jan 2016.

[213] Tianran Chen, Benjamin J. Foley, Bahar Ipek, Madhusudan Tyagi, John R. D. Copley, Craig M. Brown, Joshua J. Choi, Seung-Hun Lee, Photophysical Properties, Marina K Kuimova, Hazel A Collins, Milan Balaz, Emma Dahlstedt, James A Levitt, Nicolas Sergent, Klaus Suhling, Mikhail Drobizhev, Aleksander Rebane, Harry L Anderson, David Phillips, and Exhibition Road. Rotational dynamics of organic cations in the CH 3 NH 3 PbI 3 perovskite. *Phys. Chem. Chem. Phys.*, 0078(46):31278–31286, 2015.

[214] Artem A. Bakulin, Oleg Selig, Huib J. Bakker, Yves L. A. Rezus, Christian Müller, Tobias Glaser, Robert Lovrincic, Zhenhua Sun, Zhuoying Chen, Aron Walsh, Jarvist M. Frost, and Thomas L. C. Jansen. Real-Time Observation of Organic Cation Reorientation in Methylammonium Lead Iodide Perovskites. *J. Phys. Chem. Lett.*, 6:3663–3669, sep 2015.

[215] Fast multipole method. `https://en.wikipedia.org/wiki/Fast_multipole_method`, Accessed: 2016-08-21.

[216] Scafacos - scalable fast coulomb solvers. `www.scafacos.de`, Accessed: 2016-08-21.

[217] Zhenxuan Zhao, Xiangyu Chen, Huaqiang Wu, Xiaoming Wu, and Guozhong Cao. Probing the Photovoltage and Photocurrent in Perovskite Solar Cells with Nanoscale Resolution. *Adv. Funct. Mater.*, 26(18):3048–3058, may 2016.

[218] A. Mattoni, A. Filippetti, M. I. Saba, and P. Delugas. Methylammonium Rotational Dynamics in Lead Halide Perovskite by Classical Molecular Dynamics: The Role of Temperature. *J. Phys. Chem. C*, 119(30):17421–17428, jul 2015.

[219] Jonathan Lahnsteiner, Georg Kresse, Abhinav Kumar, D D Sarma, Cesare Franchini, and Menno Bokdam. Room temperature dynamic correlation between methylammonium molecules in lead-iodine based perovskites: An ab-initio molecular dynamics perspective. *arXiv:1608.04991 [cond-mat.mtrl-sci]*, pages 1–11, aug 2016.

[220] James Sites and Jun Pan. Strategies to increase CdTe solar-cell voltage. *Thin Solid Films*, 515(15):6099–6102, may 2007.

[221] Stéphane Bourdais, Christophe Choné, Bruno Delatouche, Alain Jacob, Gerardo Larramona, Camille Moisan, Alain Lafond, Fabrice Donatini, Germain Rey, Susanne Siebentritt, Aron Walsh, and Gilles Dennler. Is the Cu/Zn Disorder the Main Culprit for the Voltage Deficit in Kesterite Solar Cells? *Adv. Energy Mater.*, 6(12):1502276, jun 2016.

[222] Henry J. Snaith. Perovskites: The Emergence of a New Era for Low-Cost, High-Efficiency Solar Cells. *J. Phys. Chem. Lett.*, 4(21):3623–3630, November 2013.

[223] Claudio Quarti, Edoardo Mosconi, and Filippo De Angelis. Interplay of Orientational Order and Electronic Structure in Methylammonium Lead Iodide: Implications for Solar Cells Operation. *Chem. Mater.*, 26(22):6557–6569, October 2014.

[224] Martin A. Green, Keith Emery, Yoshihiro Hishikawa, Wilhelm Warta, and Ewan D. Dunlop. Solar cell efficiency tables (version 42). *Prog. Photovoltaics Res. Appl.*, 21(5):827–837, aug 2013.

[225] Darius Kuciauskas, Pat Dippo, Ana Kanevce, Zhibo Zhao, Long Cheng, Andrei Los, Markus Gloeckler, and Wyatt K. Metzger. The impact of Cu on recombination in high voltage CdTe solar cells. *Appl. Phys. Lett.*, 107(24):0–5, 2015.

[226] J. M. Burst, J. N. Duenow, D. S. Albin, E. Colegrove, M. O. Reese, J. A. Aguiar, C.-S. Jiang, M.K. Patel, M. M. Al-Jassim, D. Kuciauskas, S. Swain, T. Ablekim, K. G. Lynn, and W. K. Metzger. CdTe solar cells with open-circuit voltage breaking the 1 V barrier. *Nat. Energy*, 1(3):16015, feb 2016.

[227] Yuchuan Shao, Yongbo Yuan, and Jinsong Huang. Correlation of Energy Disorder and Open-Circuit Voltage in Hybrid Perovskite Solar Cells. *Nature Energy*, 1(1):15001, jan 2016.

[228] Weibo Yan, Yunlong Li, Senyun Ye, Yunlong Li, Haixia Rao, Zhiwei Liu, Shufeng Wang, Zuqiang Bian, and Chunhui Huang. Increasing Open Circuit Voltage by Adjusting Work Function of Hole-transporting Materials in Perovskite Solar Cells. *Nano Research*, 9(6):1600–1608, jun 2016.

[229] Thomas Kirchartz, Florian Staub, and Uwe Rau. Impact of Photon Recycling on the Open-Circuit Voltage of Metal Halide Perovskite Solar Cells. *ACS Energy Letters*, 1(4):731–739, oct 2016.

[230] Florian Staub, Hannes Hempel, Jan-Christoph Hebig, Jan Mock, Ulrich W. Paetzold, Uwe Rau, Thomas Unold, and Thomas Kirchartz. Beyond Bulk Lifetimes: Insights into Lead Halide Perovskite Films from Time-Resolved Photoluminescence. *Physical Review Applied*, 6(4):044017, oct 2016.

[231] Hiroki Kawai, Giacomo Giorgi, Andrea Marini, and Koichi Yamashita. The Mechanism of Slow Hot-Hole Cooling in Lead-Iodide Perovskite: First-Principles Calculation on Carrier Lifetime from ElectronPhonon Interaction. *Nano Letters*, 15(5):3103–3108, may 2015.

[232] Weidong Xu, Lijia Liu, Linju Yang, Pengfei Shen, Baoquan Sun, and John A. McLeod. Dissociation of Methylammonium Cations in Hybrid OrganicInorganic Perovskite Solar Cells. *Nano Lett.*, 16(7):4720–4725, jul 2016.

[233] Yuanyuan Zhou, Mengjin Yang, Joonsuh Kwun, Onkar S. Game, Yixin Zhao, Shuping Pang, Nitin P. Padture, and Kai Zhu. Intercalation crystallization of phase-pure α-HC(NH 2) 2 PbI 3 upon microstructurally engineered PbI 2 thin films for planar perovskite solar cells. *Nanoscale*, 8(12):6265–6270, 2016.

[234] Zaiwei Wang, Yuanyuan Zhou, Shuping Pang, Zewen Xiao, Jiliang Zhang, Wenqiang Chai, Hongxia Xu, Zhihong Liu, Nitin P Padture, and Guanglei Cui. Additive-Modulated Evolution of HC(NH 2) 2 PbI 3 Black Polymorph for Mesoscopic Perovskite Solar Cells. *Chem. Mater.*, 27(20):7149–7155, oct 2015.

[235] Jiaxing Song, Weidong Hu, Xiao-Feng Wang, Gang Chen, Wenjing Tian, and Tsutomu Miyasaka. HC(NH 2) 2 PbI 3 as a thermally stable absorber for

efficient ZnO-based perovskite solar cells. *J. Mater. Chem. A*, 4(21):8435–8443, 2016.

[236] Jincheol Kim, Jae S. Yun, Xiaoming Wen, Arman Mahboubi Soufiani, Cho Fai Jonathan Lau, Benjamin Wilkinson, Jan Seidel, Martin A. Green, Shujuan Huang, and Anita W. Y. Ho-Baillie. Nucleation and Growth Control of HC(NH 2) 2 PbI 3 for Planar Perovskite Solar Cell. *J. Phys. Chem. C*, 120(20):11262–11267, may 2016.

[237] F. Aryasetiawan and O. Gunnarsson. The GW method. *Reports Prog. Phys.*, 61(3):237–312, 1998.

[238] Lars Hedin. New Method for Calculating the One-Particle Green's Function with Application to the Electron-Gas Problem. *Phys. Rev.*, 139(3A):A796–A823, aug 1965.

[239] Juan E. Peralta, Jochen Heyd, Gustavo E. Scuseria, and Richard L. Martin. Spin-orbit splittings and energy band gaps calculated with the Heyd-Scuseria-Ernzerhof screened hybrid functional. *Phys. Rev. B*, 74(7):073101, aug 2006.

[240] Jochen Heyd, Gustavo E. Scuseria, and Matthias Ernzerhof. Hybrid functionals based on a screened Coulomb potential. *J. Chem. Phys.*, 118(18):8207, 2003.

[241] E. Menéndez-Proupin, P. Palacios, P. Wahnón, and J. C. Conesa. Self-Consistent Relativistic Band Structure of the $CH_3NH_3PbI_3$ Perovskite. *Phys. Rev. B*, 90(4):045207, jul 2014.

[242] R Core Team. *R: A Language and Environment for Statistical Computing*. R Foundation for Statistical Computing, Vienna, Austria, 2016.

[243] Li Sheng. *Semiconductor Physical Electronics*. Springer, Berlin, 2 edition, 2006.

[244] Simon M. Sze. *Physics of Semiconductor Devices*. Wiley, New York, 2nd edition, 1981.

[245] A V Sachenko, Yu V Kryuchenko, V P Kostylyov, A V Bobyl, E I Terukov, S N Abolmasov, A S Abramov, D. A. Andronikov, M. Z. Shvarts, I. O. Sokolovskyi, and M. Evstigneev. Temperature dependence of photoconversion efficiency in silicon heterojunction solar cells: Theory vs experiment. *J. Appl. Phys.*, 119(22):225702, jun 2016.

[246] R. R. King, D. C. Law, K. M. Edmondson, C. M. Fetzer, G. S. Kinsey, H. Yoon, R. A. Sherif, and N. H. Karam. 40% efficient metamorphic GaInPGaInAsGe multijunction solar cells. *Appl. Phys. Lett.*, 90(18):183516, 2007.

[247] Principles of electronic devices: Effective mass in semiconductors. `http://ecee.colorado.edu/~bart/book/effmass.htm`, Accessed: 2016-08-21.

[248] Ye-Cheng Zhou, Hao-li Zhang, and Wei-Qiao Deng. A 3N rule for the electronic properties of doped graphene. *Nanotechnology*, 24(22):225705, jun 2013.

[249] Krzysztof Galkowski, Anatolie Mitioglu, Atsuhiko Miyata, Paulina Plochocka, Oliver Portugall, Giles E. Eperon, Jacob Tse-Wei Wang, Thomas Stergiopoulos, Samuel D. Stranks, Henry J. Snaith, and Robin J. Nicholas. Determination of the Exciton Binding Energy and Effective Masses for Methylammonium and Formamidinium Lead Tri-halide Perovskite Semiconductors. *Energy Environ. Sci.*, 9(3):962–970, 2016.

[250] Atsuhiko Miyata, Anatolie Mitioglu, Paulina Plochocka, Oliver Portugall, Jacob Tse-Wei Wang, Samuel D. Stranks, Henry J. Snaith, and Robin J. Nicholas. Direct Measurement of the Exciton Binding Energy and Effective Masses for Charge Carriers in OrganicInorganic tri-halide Perovskites. *Nature Physics*, 11(7):582–587, jun 2015.

[251] Edoardo Mosconi, Paolo Umari, and Filippo De Angelis. Electronic and optical properties of MAPbX 3 perovskites (X = I, Br, Cl): a unified DFT and GW theoretical analysis. *Phys. Chem. Chem. Phys.*, 18(39):27158–27164, 2016.

[252] Chetan Singh Solanki. *Solar Photovoltaics: Fundamentals, Technologies And Applications*. PHI Learning, 3 edition, 2015.

[253] Qian Zhang, Bin Kan, Feng Liu, Guankui Long, Xiangjian Wan, Xiaoqing Chen, Yi Zuo, Wang Ni, Huijing Zhang, Miaomiao Li, Zhicheng Hu, Fei Huang, Yong Cao, Ziqi Liang, Mingtao Zhang, Thomas P Russell, and Yongsheng Chen. Small-molecule solar cells with efficiency over 9%. *Nat. Photonics*, 9(1):35–41, nov 2014.

[254] Xiaoyu Zhang, Long Chen, Xin Li, Jiangyi Mao, Wenjun Wu, Hans Ågren, and Jianli Hua. Photovoltaic properties of bis(octyloxy)benzo-[c][1,2,5]thiadiazole sensitizers based on an N,N-diphenylthiophen-2-amine donor. *J. Mater. Chem. C*, 2(20):4063, 2014.

[255] Pratap M Rao, Lili Cai, Chong Liu, In Sun Cho, Chi Hwan Lee, Jeffrey M Weisse, Peidong Yang, and Xiaolin Zheng. Simultaneously Efficient Light Absorption and Charge Separation in WO 3 /BiVO 4 Core/Shell Nanowire Photoanode for Photoelectrochemical Water Oxidation. *Nano Lett.*, 14(2):1099–1105, feb 2014.

[256] Shuqing Chen, Chujun Zhao, Ying Li, Huihui Huang, Shunbin Lu, Han Zhang, and Shuangchun Wen. Broadband Optical and Microwave Nonlinear Response in Topological Insulator. *Opt. Mater. Express*, 4(4):587, 2014.

[257] Shunbin Lu, Chujun Zhao, Yanhong Zou, Shuqing Chen, Yu Chen, Ying Li, Han Zhang, Shuangchun Wen, and Dingyuan Tang. Third Order Nonlinear Optical Property of Bi_2Se_3. *Opt. Express*, 21(2):2072, jan 2013.

[258] Liping Sun, Zhiqin Lin, Jian Peng, Jian Weng, Yizhong Huang, and Zhengqian Luo. Preparation of Few-Layer Bismuth Selenide by Liquid-Phase-Exfoliation and Its Optical Absorption Properties. *Sci. Rep.*, 4:4794, apr 2014.

[259] Martin A. Green, Anita Ho-Baillie, and Henry J. Snaith. The emergence of perovskite solar cells. *Nat. Photonics*, 8(7):506–514, jun 2014.

[260] Carlo Motta, Fedwa El-Mellouhi, Sabre Kais, Nouar Tabet, Fahhad Alharbi, and Stefano Sanvito. Revealing the role of organic cations in hybrid halide perovskite CH3NH3PbI3. *Nat. Commun.*, 6:7026, apr 2015.

[261] Jun Haruyama, Keitaro Sodeyama, Liyuan Han, and Yoshitaka Tateyama. Termination Dependence of Tetragonal CH 3 NH 3 PbI 3 Surfaces for Perovskite Solar Cells. *J. Phys. Chem. Lett.*, 5(16):2903–2909, aug 2014.

[262] Khuong P. Ong, Teck Wee Goh, Qiang Xu, and Alfred Huan. Mechanical Origin of the Structural Phase Transition in Methylammonium Lead Iodide CH 3 NH 3 PbI 3. *J. Phys. Chem. Lett.*, 6(4):681–685, feb 2015.

[263] David A. Egger and Leeor Kronik. Role of Dispersive Interactions in Determining Structural Properties of OrganicInorganic Halide Perovskites: Insights from First-Principles Calculations. *J. Phys. Chem. Lett.*, 5(15):2728–2733, aug 2014.

[264] Jiawang Hong, Alessandro Stroppa, Jorge Íñiguez, Silvia Picozzi, and David Vanderbilt. Spin-phonon coupling effects in transition-metal perovskites: A

DFT + U and hybrid-functional study. *Phys. Rev. B*, 85(5):054417, February 2012.

[265] M. Dion, H. Rydberg, E. Schröder, D. C. Langreth, and B. I. Lundqvist. Van der Waals Density Functional for General Geometries. *Phys. Rev. Lett.*, 92(24):246401, jun 2004.

[266] Jií Klimeš, David R. Bowler, and Angelos Michaelides. Van der Waals density functionals applied to solids. *Phys. Rev. B*, 83(19):195131, may 2011.

[267] X. Wu, M. C. Vargas, S. Nayak, V. Lotrich, and G. Scoles. Towards extending the applicability of density functional theory to weakly bound systems. *J. Chem. Phys.*, 115(19):8748, 2001.

[268] Stefan Grimme. Semiempirical GGA-type density functional constructed with a long-range dispersion correction. *J. Comput. Chem.*, 27(15):1787–1799, nov 2006.

[269] A. Poglitsch and D. Weber. Dynamic disorder in methylammoniumtrihalogenoplumbates (II) observed by millimeter-wave spectroscopy. *J. Chem. Phys.*, 87(11):6373, 1987.

[270] Nicola Marzari, Arash A. Mostofi, Jonathan R. Yates, Ivo Souza, and David Vanderbilt. Maximally Localized Wannier Functions: Theory and Applications. *Rev. Mod. Phys.*, 84(4):1419–1475, oct 2012.

[271] Arash A. Mostofi, Jonathan R. Yates, Young-Su Lee, Ivo Souza, David Vanderbilt, and Nicola Marzari. Wannier90: A Tool for Obtaining Maximally-Localised Wannier Functions. *Comput. Phys. Commun.*, 178(9):685–699, may 2008.

Appendix E

Forms of Agreement and Declaration

E.1 Forms of Chapter 2

Co-author authorisation form

THE UNIVERSITY OF MELBOURNE

All co-authors must complete this form. By signing below co-authors agree to the listed publication being included in the student's thesis and that the student contributed greater than 50% of the content of the publication and is the "primary author" ie. the student was responsible primarily for the planning, execution and preparation of the work for publication.

In cases where all members of a large consortium are listed as authors of a publication, only those that actively collaborated with the student on material contained within the thesis should complete this form. This form is to be used in conjunction with the *Declaration for a thesis with publication form*.

Students must submit this form, along with the *Declaration for thesis with publication form*, when the thesis is submitted to the Thesis Examination System: *https://tes.app.unimelb.edu.au/*

Further information on this policy and the requirements is available at:
gradresearch.unimelb.edu.au/preparing-my-thesis/thesis-with-publication

A. PUBLICATION DETAILS *(to be completed by the student)*

Full title	Photovoltaic performance and the energy landscape of $CH_3NH_3PbI_3$	
Authors	Yecheng Zhou, Fuzhi Huang, Yi-Bing Cheng, Angus Gray-Weale	
Student's contribution (%)	75%	
Journal or book name	Physical Chemistry Chemical Physics	
Volume/page numbers	17/22604-22615	
Status	☐ Accepted and In-press ☒ Published	Date accepted/published 28-Jul-2015

B. CO-AUTHOR'S DECLARATION *(to be completed by the collaborator)*

I authorise the inclusion of this publication in the student's thesis and certify that:

- the declaration made by the student on the *Declaration for a thesis with publication form* correctly reflects the extent of the student's contribution to this work;
- the student contributed greater than 50% of the content of the publication and is the "primary author" ie. the student was responsible primarily for the planning, execution and preparation of the work for publication.

Co-author's name	Co-author's signature	Date *(dd/mm/yy)*
Fuzhi Huang	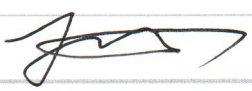	22/09/16

Co-author authorisation form

THE UNIVERSITY OF MELBOURNE

All co-authors must complete this form. By signing below co-authors agree to the listed publication being included in the student's thesis and that the student contributed greater than 50% of the content of the publication and is the "primary author" ie. the student was responsible primarily for the planning, execution and preparation of the work for publication.

In cases where all members of a large consortium are listed as authors of a publication, only those that actively collaborated with the student on material contained within the thesis should complete this form. This form is to be used in conjunction with the *Declaration for a thesis with publication form*.

Students must submit this form, along with the *Declaration for thesis with publication form*, when the thesis is submitted to the Thesis Examination System: *https://tes.app.unimelb.edu.au/*

Further information on this policy and the requirements is available at:
gradresearch.unimelb.edu.au/preparing-my-thesis/thesis-with-publication

A. PUBLICATION DETAILS *(to be completed by the student)*

Full title	Photovoltaic performance and the energy landscape of $CH_3NH_3PbI_3$	
Authors	Yecheng Zhou, Fuzhi Huang, Yi-Bing Cheng, Angus Gray-Weale	
Student's contribution (%)	75%	
Journal or book name	Physical Chemistry Chemical Physics	
Volume/page numbers	17/22604-22615	
Status	☐ Accepted and In-press ☒ Published	Date accepted/published 28-Jul-2015

B. CO-AUTHOR'S DECLARATION *(to be completed by the collaborator)*

I authorise the inclusion of this publication in the student's thesis and certify that:

- the declaration made by the student on the *Declaration for a thesis with publication form* correctly reflects the extent of the student's contribution to this work;
- the student contributed greater than 50% of the content of the publication and is the "primary author" ie. the student was responsible primarily for the planning, execution and preparation of the work for publication.

Co-author's name	Co-author's signature	Date *(dd/mm/yy)*
Yi-Bing Cheng	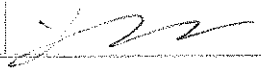	04/10/16

Co-author authorisation form

THE UNIVERSITY OF MELBOURNE

All co-authors must complete this form. By signing below co-authors agree to the listed publication being included in the student's thesis and that the student contributed greater than 50% of the content of the publication and is the "primary author" ie. the student was responsible primarily for the planning, execution and preparation of the work for publication.

In cases where all members of a large consortium are listed as authors of a publication, only those that actively collaborated with the student on material contained within the thesis should complete this form. This form is to be used in conjunction with the *Declaration for a thesis with publication form*.

Students must submit this form, along with the *Declaration for thesis with publication form*, when the thesis is submitted to the Thesis Examination System: *https://tes.app.unimelb.edu.au/*

Further information on this policy and the requirements is available at:
gradresearch.unimelb.edu.au/preparing-my-thesis/thesis-with-publication

A. PUBLICATION DETAILS *(to be completed by the student)*

Full title	Photovoltaic performance and the energy landscape of $CH_3NH_3PbI_3$	
Authors	Yecheng Zhou, Fuzhi Huang, Yi-Bing Cheng, Angus Gray-Weale	
Student's contribution (%)	75%	
Journal or book name	Physical Chemistry Chemical Physics	
Volume/page numbers	17/22604-22615	
Status	☐ Accepted and In-press ☒ Published	Date accepted/published 28-Jul-2015

B. CO-AUTHOR'S DECLARATION *(to be completed by the collaborator)*

I authorise the inclusion of this publication in the student's thesis and certify that:

- the declaration made by the student on the *Declaration for a thesis with publication form* correctly reflects the extent of the student's contribution to this work;
- the student contributed greater than 50% of the content of the publication and is the "primary author" ie. the student was responsible primarily for the planning, execution and preparation of the work for publication.

Co-author's name	Co-author's signature	Date *(dd/mm/yy)*
ANGUS GRAY-WEALE		28/9/2016

Declaration for a thesis with publication

THE UNIVERSITY OF MELBOURNE

PhD and MPhil students may include a primary research publication in their thesis in lieu of a chapter if:

- The student contributed greater than 50% of the content in the publication and is the "primary author", ie. the student was responsible primarily for the planning, execution and preparation of the work for publication
- It has been peer-reviewed and accepted for publication
- The student has approval to include the publication in their thesis from their Advisory Committee
- It is a primary publication that reports on original research conducted by the student during their enrolment
- The initial draft of the work was written by the student and any subsequent editing in response to co-authors and editors reviews was performed by the student
- The publication is not subject to any obligations or contractual agreements with a third party that would constrain its inclusion in the thesis

Students must submit this form, along with *Co-author authorisation forms* completed by each co-author, when the thesis is submitted to the Thesis Examination System: *https://tes.app.unimelb.edu.au/*. If you are including multiple publications in your thesis you will need to complete a separate form for each publication. Further information on this policy is available at: *gradresearch.unimelb.edu.au/preparing-my-thesis/thesis-with-publication*

A. PUBLICATION DETAILS *(to be completed by the student)*

Full title	Photovoltaic performance and the energy landscape of $CH_3NH_3PbI_3$	
Authors	Yecheng Zhou, Fuzhi Huang, Yi-Bing Cheng, Angus Gray-Weale	
Student's contribution (%)	75%	
Journal or book name	Physical Chemistry Chemical Physics	
Volume/page numbers	17/22604-22615	
Status	☐ Accepted and In press ☒ Published	Date accepted/ published 28 Jul 2015

B. STUDENT'S DECLARATION

I declare that the publication above meets the requirements to be included in the thesis

Student's name	Student's signature	Date *(dd/mm/yy)*
Yecheng Zhou	Yecheng Zhou	28/09/2016

C. PRINCIPAL SUPERVISOR'S DECLARATION

I declare that:

- the information above is accurate
- The advisory committee has met and agreed to the inclusion of this publication in the student's thesis
- All of the co-authors of the publication have reviewed the above information and have agreed to its veracity
- 'Co-Author Authorisation' forms for each co-author are attached.

Supervisor's name	Supervisor's signature	Date *(dd/mm/yy)*
ANGUS GRAY-WEALE	Angus Gray-Weale	28/9/2016

E.2 Forms of Chapter 3

Co-author authorisation form

THE UNIVERSITY OF MELBOURNE

All co-authors must complete this form. By signing below co-authors agree to the listed publication being included in the student's thesis and that the student contributed greater than 50% of the content of the publication and is the "primary author" ie. the student was responsible primarily for the planning, execution and preparation of the work for publication.

In cases where all members of a large consortium are listed as authors of a publication, only those that actively collaborated with the student on material contained within the thesis should complete this form. This form is to be used in conjunction with the *Declaration for a thesis with publication form*.

Students must submit this form, along with the *Declaration for thesis with publication form*, when the thesis is submitted to the Thesis Examination System: *https://tes.app.unimelb.edu.au/*

Further information on this policy and the requirements is available at:
gradresearch.unimelb.edu.au/preparing-my-thesis/thesis-with-publication

A. PUBLICATION DETAILS *(to be completed by the student)*

Full title	A numerical model for charge transport and energy conversion of perovskite solar cells	
Authors	Yecheng Zhou, Angus Gray-Weale	
Student's contribution (%)	85%	
Journal or book name	Physical Chemistry Chemical Physics	
Volume/page numbers	18/4476-4486	
Status	☐ Accepted and In-press ☒ Published	Date accepted/published 07-Dec-2015

B. CO-AUTHOR'S DECLARATION *(to be completed by the collaborator)*

I authorise the inclusion of this publication in the student's thesis and certify that:

- the declaration made by the student on the *Declaration for a thesis with publication form* correctly reflects the extent of the student's contribution to this work;
- the student contributed greater than 50% of the content of the publication and is the "primary author" ie. the student was responsible primarily for the planning, execution and preparation of the work for publication.

Co-author's name	Co-author's signature	Date *(dd/mm/yy)*
A. Gray-Weale	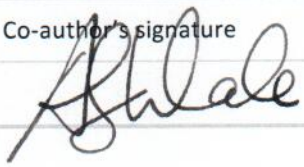	20/10/2016

Declaration for a thesis with publication

THE UNIVERSITY OF MELBOURNE

PhD and MPhil students may include a primary research publication in their thesis in lieu of a chapter if:

- The student contributed greater than 50% of the content in the publication and is the "primary author", ie. the student was responsible primarily for the planning, execution and preparation of the work for publication
- It has been peer-reviewed and accepted for publication
- The student has approval to include the publication in their thesis from their Advisory Committee
- It is a primary publication that reports on original research conducted by the student during their enrolment
- The initial draft of the work was written by the student and any subsequent editing in response to co-authors and editors reviews was performed by the student
- The publication is not subject to any obligations or contractual agreements with a third party that would constrain its inclusion in the thesis

Students must submit this form, along with *Co-author authorisation forms* completed by each co-author, when the thesis is submitted to the Thesis Examination System: *https://tes.app.unimelb.edu.au/*. If you are including multiple publications in your thesis you will need to complete a separate form for each publication. Further information on this policy is available at: *gradresearch.unimelb.edu.au/preparing-my-thesis/thesis-with-publication*

A. PUBLICATION DETAILS *(to be completed by the student)*

Full title	A numerical model for charge transport and energy conversion of perovskite solar cells	
Authors	Yecheng Zhou, Angus Gray-Weale	
Student's contribution (%)	85%	
Journal or book name	Physical Chemistry Chemical Physics	
Volume/page numbers	18/4476-4486	
Status	☐ Accepted and In press ☒ Published	Date accepted/ published 07-Dec-2015

B. STUDENT'S DECLARATION

I declare that the publication above meets the requirements to be included in the thesis

Student's name	Student's signature	Date *(dd/mm/yy)*
Yecheng Zhou	Yecheng Zhou	28/09/2016

C. PRINCIPAL SUPERVISOR'S DECLARATION

I declare that:

- the information above is accurate
- The advisory committee has met and agreed to the inclusion of this publication in the student's thesis
- All of the co-authors of the publication have reviewed the above information and have agreed to its veracity
- 'Co-Author Authorisation' forms for each co-author are attached.

Supervisor's name	Supervisor's signature	Date *(dd/mm/yy)*
ANGUS GRAY-WEALE	A Gray-Weale	28/09/2016

E.3 Forms of Chapter 4

Co-author authorisation form

THE UNIVERSITY OF MELBOURNE

All co-authors must complete this form. By signing below co-authors agree to the listed publication being included in the student's thesis and that the student contributed greater than 50% of the content of the publication and is the "primary author" ie. the student was responsible primarily for the planning, execution and preparation of the work for publication.

In cases where all members of a large consortium are listed as authors of a publication, only those that actively collaborated with the student on material contained within the thesis should complete this form. This form is to be used in conjunction with the *Declaration for a thesis with publication form*.

Students must submit this form, along with the *Declaration for thesis with publication form*, when the thesis is submitted to the Thesis Examination System: *https://tes.app.unimelb.edu.au/*

Further information on this policy and the requirements is available at:
gradresearch.unimelb.edu.au/preparing-my-thesis/thesis-with-publication

A. PUBLICATION DETAILS *(to be completed by the student)*

Full title	Numerical analysis of a hysteresis model in perovskite solar cells	
Authors	Yecheng Zhou, Fuzhi Huang, Yi-Bing Cheng, Angus Gray-Weale	
Student's contribution (%)	85%	
Journal or book name	Computational Materials Science	
Volume/page numbers	126/22-28	
Status	☐ Accepted and In-press ☒ Published	Date accepted/published 21-SEP-2016

B. CO-AUTHOR'S DECLARATION *(to be completed by the collaborator)*

I authorise the inclusion of this publication in the student's thesis and certify that:

- the declaration made by the student on the *Declaration for a thesis with publication form* correctly reflects the extent of the student's contribution to this work;
- the student contributed greater than 50% of the content of the publication and is the "primary author" ie. the student was responsible primarily for the planning, execution and preparation of the work for publication.

Co-author's name	Co-author's signature	Date *(dd/mm/yy)*
Fuzhi Huang		22/09/16

Co-author authorisation form

THE UNIVERSITY OF MELBOURNE

All co-authors must complete this form. By signing below co-authors agree to the listed publication being included in the student's thesis and that the student contributed greater than 50% of the content of the publication and is the "primary author" ie. the student was responsible primarily for the planning, execution and preparation of the work for publication.

In cases where all members of a large consortium are listed as authors of a publication, only those that actively collaborated with the student on material contained within the thesis should complete this form. This form is to be used in conjunction with the *Declaration for a thesis with publication form*.

Students must submit this form, along with the *Declaration for thesis with publication form*, when the thesis is submitted to the Thesis Examination System: *https://tes.app.unimelb.edu.au/*

Further information on this policy and the requirements is available at:
gradresearch.unimelb.edu.au/preparing-my-thesis/thesis-with-publication

A. PUBLICATION DETAILS *(to be completed by the student)*

Full title	Numerical analysis of a hysteresis model in perovskite solar cells		
Authors	Yecheng Zhou, Fuzhi Huang, Yi-Bing Cheng, Angus Gray-Weale		
Student's contribution (%)	85%		
Journal or book name	Computational Materials Science		
Volume/page numbers	126/22-28		
Status	☐ Accepted and In-press	☒ Published	Date accepted/published 21-SEP-2016

B. CO-AUTHOR'S DECLARATION *(to be completed by the collaborator)*

I authorise the inclusion of this publication in the student's thesis and certify that:

- the declaration made by the student on the *Declaration for a thesis with publication form* correctly reflects the extent of the student's contribution to this work;
- the student contributed greater than 50% of the content of the publication and is the "primary author" ie. the student was responsible primarily for the planning, execution and preparation of the work for publication.

Co-author's name	Co-author's signature	Date *(dd/mm/yy)*
Yi-Bing Cheng	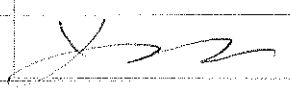	04/10/16

Declaration for a thesis with publication

THE UNIVERSITY OF MELBOURNE

PhD and MPhil students may include a primary research publication in their thesis in lieu of a chapter if:

- The student contributed greater than 50% of the content in the publication and is the "primary author", ie. the student was responsible primarily for the planning, execution and preparation of the work for publication
- It has been peer-reviewed and accepted for publication
- The student has approval to include the publication in their thesis from their Advisory Committee
- It is a primary publication that reports on original research conducted by the student during their enrolment
- The initial draft of the work was written by the student and any subsequent editing in response to co-authors and editors reviews was performed by the student
- The publication is not subject to any obligations or contractual agreements with a third party that would constrain its inclusion in the thesis

Students must submit this form, along with *Co-author authorisation forms* completed by each co-author, when the thesis is submitted to the Thesis Examination System: *https://tes.app.unimelb.edu.au/*. If you are including multiple publications in your thesis you will need to complete a separate form for each publication. Further information on this policy is available at: *gradresearch.unimelb.edu.au/preparing-my-thesis/thesis-with-publication*

A. PUBLICATION DETAILS *(to be completed by the student)*

Full title	Numerical analysis of a hysteresis model in perovskite solar cells	
Authors	Yecheng Zhou, Fuzhi Huang, Yi-Bing Cheng, Angus Gray-Weale	
Student's contribution (%)	85%	
Journal or book name	Computational Materials Science	
Volume/page numbers	126/22-28	
Status	☐ Accepted and In press ☒ Published	Date accepted/ published 21-SEP-2016

B. STUDENT'S DECLARATION

I declare that the publication above meets the requirements to be included in the thesis

Student's name	Student's signature	Date *(dd/mm/yy)*
Yecheng Zhou	Yecheng Zhou	28/09/2016

C. PRINCIPAL SUPERVISOR'S DECLARATION

I declare that:

- the information above is accurate
- The advisory committee has met and agreed to the inclusion of this publication in the student's thesis
- All of the co-authors of the publication have reviewed the above information and have agreed to its veracity
- 'Co-Author Authorisation' forms for each co-author are attached.

Supervisor's name	Supervisor's signature	Date *(dd/mm/yy)*
ANGUS GRAY-WEALE	A Gray-Weale	28/9/16

Co-author authorisation form

THE UNIVERSITY OF MELBOURNE

All co-authors must complete this form. By signing below co-authors agree to the listed publication being included in the student's thesis and that the student contributed greater than 50% of the content of the publication and is the "primary author" ie. the student was responsible primarily for the planning, execution and preparation of the work for publication.

In cases where all members of a large consortium are listed as authors of a publication, only those that actively collaborated with the student on material contained within the thesis should complete this form. This form is to be used in conjunction with the *Declaration for a thesis with publication form*.

Students must submit this form, along with the *Declaration for thesis with publication form*, when the thesis is submitted to the Thesis Examination System: *https://tes.app.unimelb.edu.au/*

Further information on this policy and the requirements is available at:
gradresearch.unimelb.edu.au/preparing-my-thesis/thesis-with-publication

A. PUBLICATION DETAILS *(to be completed by the student)*

Full title	Numerical analysis of a hysteresis model in perovskite solar cells	
Authors	Yecheng Zhou, Fuzhi Huang, Yi-Bing Cheng, Angus Gray-Weale	
Student's contribution (%)	85%	
Journal or book name	Computational Materials Science	
Volume/page numbers	126/22-28	
Status	☐ Accepted and In-press ☒ Published	Date accepted/published 21-SEP-2016

B. CO-AUTHOR'S DECLARATION *(to be completed by the collaborator)*

I authorise the inclusion of this publication in the student's thesis and certify that:

- the declaration made by the student on the *Declaration for a thesis with publication form* correctly reflects the extent of the student's contribution to this work;
- the student contributed greater than 50% of the content of the publication and is the "primary author" ie. the student was responsible primarily for the planning, execution and preparation of the work for publication.

Co-author's name	Co-author's signature	Date *(dd/mm/yy)*
A. Gray-Weale	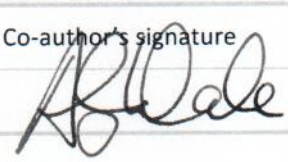	20/10/2016

E.4 Forms of Chapter 6

THE UNIVERSITY OF MELBOURNE

All co-authors must complete this form. By signing below co-authors agree to the listed publication being included in the student's thesis and that the student contributed greater than 50% of the content of the publication and is the "primary author" ie. the student was responsible primarily for the planning, execution and preparation of the work for publication.

In cases where all members of a large consortium are listed as authors of a publication, only those that actively collaborated with the student on material contained within the thesis should complete this form. This form is to be used in conjunction with the *Declaration for a thesis with publication form*.

Students must submit this form, along with the *Declaration for thesis with publication form*, when the thesis is submitted to the Thesis Examination System: *https://tes.app.unimelb.edu.au/*

Further information on this policy and the requirements is available at:
gradresearch.unimelb.edu.au/preparing-my-thesis/thesis-with-publication

A. PUBLICATION DETAILS *(to be completed by the student)*

Full title	Low Density of Conduction and Valence Band States Contribute to the High Open-Circuit Voltage in Perovskite Solar Cells	
Authors	Yecheng Zhou, Guankui Long	
Student's contribution (%)	95%	
Journal or book name	J. Phys. Chem. C	
Volume/page numbers	na, DOI: 10.1021/acs.jpcc.6b10914	
Status	☒ Accepted and In-press ☐ Published	Date accepted/published 4.Jan.2017

B. CO-AUTHOR'S DECLARATION *(to be completed by the collaborator)*

I authorise the inclusion of this publication in the student's thesis and certify that:

- the declaration made by the student on the *Declaration for a thesis with publication form* correctly reflects the extent of the student's contribution to this work;
- the student contributed greater than 50% of the content of the publication and is the "primary author" ie. the student was responsible primarily for the planning, execution and preparation of the work for publication.

Co-author's name	Co-author's signature	Date *(dd/mm/yy)*
Guankui Long	Guankui Long	15/01/2017